Colloidal 2D Lead Chalcogenide Near-Infrared Emitters: From Chemical Tailoring to Optical Functionality

Dissertation

der Mathematisch-Naturwissenschaftlichen Fakultät
der Eberhard Karls Universität Tübingen
zur Erlangung des Grades eines
Doktors der Naturwissenschaften
(Dr. rer. nat.)

vorgelegt von
M. Sc. Leon Biesterfeld
aus Hannover

Tübingen
2025

Gedruckt mit Genehmigung der Mathematisch-Naturwissenschaftlichen Fakultät der Eberhard Karls Universität Tübingen.

Tag der mündlichen Qualifikation:	16.03.2026
Dekan:	Prof. Dr. Thilo Stehle
1. Berichterstatterin:	Jun.-Prof. Dr. Jannika Lauth
2. Berichterstatter:	Prof. Dr. Reinhold Fink
3. Berichterstatterin:	Prof. Dr. Sandrine Ithurria Lhuillier

This dissertation was conducted in the group of Jun.-Prof. Jannika Lauth at the Institute of Physical and Theoretical Chemistry of the Eberhard Karls University of Tübingen between April 2022 and September 2025 and at the Institute of Physical and Electrochemistry at the Leibniz University Hannover between November 2021 and April 2022.

Zusammenfassung

Halbleiter-Nanokristalle (engl. *nanocrystals*, NCs) sind nanoskalige, kristalline Partikel, deren Eigenschaften aufgrund quantenmechanischer Effekte maßgeblich durch ihre Größe bestimmt sind. Derartige größenquantisierte Kristalle können nasschemisch durch kolloidale Synthese hergestellt werden, eine Methode, die den Zugang zu einer großen Vielfalt von Halbleitermaterialien mit präziser Kontrolle über ihre Zusammensetzung, Größe und Form ermöglicht. Zweidimensionale (2D) kolloidale NCs haben sich als besonders interessante Klasse dieser größenquantisierten Materialien erwiesen, da sie faszinierende optoelektronische Eigenschaften aufweisen, die sich von denen sphärischer Quantenpunkte (engl. *quantum dots*, QDs) unterscheiden. Vor allem 2D Nanoplättchen (engl. *nanoplatelets*, NPLs), die Strahlung des sichtbaren elektromagnetischen Spektrums des Lichts absorbieren und emittieren und beispielsweise aus CdSe oder Bleihalogenid-Perowskiten bestehen, wurden intensiv untersucht. 2D Materialien, die die verlustarmen optischen Übertragungsfenster von Glasfasern im nahen Infrarot (engl. *near-infrared*, NIR) erreichen können (z. B. Bleichalkogenide), sind hingegen vergleichsweise wenig erforscht, obwohl sie für künftige glasfaserbasierte Technologien als klassische Licht- oder quantenoptische Einzelphotonenquellen geeignet sind. Frühe Arbeiten zu kolloidalen 2D Bleichalkogeniden haben sich auf die Synthese vergleichsweise dicker PbS Nanoblättchen konzentriert, während dünne und stark größenquantisierte PbS und PbSe NPLs erst kürzlich realisiert wurden. Im Mittelpunkt dieser Arbeit stehen daher die zielgerichtete Synthese und postsynthetische Modifikation von ultradünnen 2D Bleichalkogenid PbX (X = S, Se, Te) NCs mit maßgeschneiderten optischen Eigenschaften sowie die Untersuchung und das Verständnis ihrer Photophysik.

Kapitel 1 und 2 bieten einen Einstieg in das Thema kolloidale 2D NIR Emitter und geben einen Überblick über die grundlegenden Konzepte auf denen die folgenden Kapitel aufbauen und führen die im Verlauf der Arbeit verwendeten Fachbegriffe ein. In Kapitel 3 wird eine Methode zur Oberflächenpassivierung und Erhöhung der Photolumineszenz-Quantenausbeute (engl. *photoluminescence quantum yield*, PLQY) von 2D PbSe NPLs erarbeitet. Anschließend wird unter Verwendung eines neuen Aminophosphin-Vorläufers eine Synthese von 2D PbTe

NPLs entwickelt (Kapitel 4). In Kapitel 5 wird ein Wassertransfer von 2D PbX NPLs vorgestellt, bei dem ihre NIR Photolumineszenz (PL) erhalten bleibt, wodurch neue Wege zu funktionalen Festkörper-Nanokompositen eröffnet werden. In den folgenden zwei Kapiteln rücken spektroskopische Messungen an den selbst synthetisierten 2D Strukturen in den Fokus. In Kapitel 6 wird die PL einzelner 2D PbS NPLs bei kryogenen Temperaturen charakterisiert. Hierbei finden sich extrem schmale PL Signale mit einer Halbwertsbreite unter 1 meV, die einen hohen linearen Polarisationsgrad aufweisen und das Potenzial von 2D PbS NPLs für quantenoptische Anwendungen unterstreichen. Im folgenden Kapitel wird die sehr starke Größenquantisierung in flachen 2D PbSe QDs (engl. *flat quantum dots*, fQDs) mittels Rastertunnelmikroskopie und -spektroskopie, kryogener PL Messungen und *tight-binding*-Berechnungen untersucht (Kapitel 7). Auf diese Weise werden verschiedene, durch ihre Lagenanzahl definierte, ultradünne fQD-Populationen mit einer Dicke von bis zu einer Monolage gefunden, welche den erste Nachweis von substratfreien PbSe-Monolagen darstellen. Diese flachen Quantenpunkte weisen eine extrem starke Größenquantisierung in ihrer Dicke auf und sind gleichzeitig durch ihre geringe laterale Ausdehnung größenquantisiert, und stellen somit eine neue Nanokristallklasse dar. In Kapitel 8 wird gezeigt, wie kolloidale PbSe fQDs mittels *stable jet electro spinning (SJES)* in Polymethylmethacrylat-Fasern eingebunden werden können. Die hergestellten anorganisch-organischen Hybridfasern sind parallel ausgerichtet, haben eine gut definierte glatte Oberfläche und weisen die optischen Eigenschaften der eingesponnenen PbSe fQDs auf. In Kapitel 7 wird abschließend der in den Kapiteln 3 bis 8 schrittweise präsentierte Weg von der anfänglichen kolloidalen Synthese von 2D PbX NCs über ihre ausführliche spektroskopische Untersuchung bis zur Integration von PbSe fQDs in leicht zu handhabende makroskopische Kompositmaterialien zusammengefasst. In Kapitel 10 werden zuletzt mögliche zukünftige Forschungsfragen aufgezeigt und diskutiert.

Abstract

Semiconductor nanocrystals (NCs) are nanoscaled crystalline particles with properties determined by their physical dimensions, resulting in unique light-matter interactions. Such quantum-confined crystals can be produced *via* colloidal synthesis, a method that allows for the preparation of a wide variety of semiconductors with precise control over their composition, size and shape. Two-dimensional (2D) colloidal NCs, in particular, have emerged as an interesting class of these materials and exhibit intriguing optoelectronic properties, which differ from those of their spherical quantum dot (QD) counterparts. Especially 2D nanoplatelets (NPLs), which absorb and emit light in the visible spectrum (*e.g.* of CdSe or lead halide perovskites), have been intensively studied. Meanwhile, materials that can reach the low-loss optical transmission windows of fiber optics (*e.g.* lead chalcogenides), located at near-infrared (NIR) wavelengths, remain comparatively less studied despite being sought after as classical or quantum emitters for future glass fiber-based technologies. Early work on colloidal 2D lead chalcogenides has been focused on synthesizing comparatively thick PbS nanosheets, while thin and strongly quantum confined PbS and PbSe NPLs were only recently implemented. This thesis is therefore centered around the target-oriented synthesis and post-synthesis modification of ultrathin 2D PbX (X = S, Se, Te) NCs with tailored optical properties, as well as the investigation and understanding of their photophysics.

Chapters 1 and 2 introduce the topic of colloidal 2D NIR emitters, providing an overview of the basic concepts on which the subsequent chapters are based, and defining the technical terms used throughout this work. In the 3rd chapter, a surface passivation method to increase the photoluminescence quantum yield (PLQY) of PbSe NPLs is established, which is followed by a new synthesis for 2D PbTe NPLs using aminophosphine precursor chemistry and giving access to the “elusive third family member” of 2D PbX (Chapter 4). Chapter 5 reports on a water transfer of 2D PbX NPLs, which preserves their telecom band-friendly NIR PL and opens new possible routes toward functional solid-state nanocomposites. In Chapter 6 and 7, the focus shifts to spectroscopic characterization of 2D PbX by first investigating the low-temperature PL of single 2D PbS NPLs. The cryogenic measurements reveal narrow PL with sub-meV linewidths and a high degree of linear polarization,

underscoring the potential of 2D PbS NPLs for quantum optical applications. In Chapter 7 the extreme quantum confinement in PbSe flat QDs (fQDs) is studied *via* scanning tunneling microscopy and spectroscopy, ensemble cryo-PL, and theoretical tight-binding calculations. Thereby, ultrathin single atomic layer-defined PbSe fQD populations with a thickness down to a monolayer are found, marking the first demonstration of substrate-free PbSe monolayers. These flat quantum dots exhibit extremely strong size quantization in their thickness dimension, while simultaneously being size-quantized by their small lateral extent, thus representing a new class of nanocrystals. Chapter 8 present a method to incorporate colloidal 2D PbSe fQDs into poly(methyl methacrylate) fibers using stable jet electro spinning (SJES). The obtained inorganic-organic hybrid fibers are unidirectionally aligned, have a smooth, well-defined surface, and exhibit the optical properties of the embedded PbSe fQDs. Chapter 7 concludes by summarizing the journey from the initial colloidal synthesis of 2D PbX NCs over their in-depth spectroscopic characterization to the integration of PbSe fQDs into easy-to-handle macroscopic composite materials, as presented in Chapters 3 to 8. Finally, Chapter 10 highlights and discusses possible future research questions.

Preface

This dissertation is a cumulative thesis comprising six individual articles published in peer-reviewed scientific journals. I am the first author of five of these articles and shared first author of one study. A comprehensive list of all co-authors and their respective contributions can be found in Chapter B at the end of this thesis. The scientific research I have carried out myself was conducted between November 2021 and September 2025 as a doctoral student under the guidance of Jun. Prof. Jannika Lauth at the following institutions: The Institute of Physical and Theoretical Chemistry of the Eberhard Karls University of Tübingen, the Institute of Physical and Electrochemistry at the Leibniz University Hannover, and the Laboratory of Nano and Quantum Engineering in Hannover. During this time, I co-authored one additional article and have presented my research in eight talks (seven contributed and one invited) at different international conferences (see Chapter A for a list of all scholarly contributions).

Contents

Abbreviations

0D	zero-dimensional
1D	one-dimensional
2D	two-dimensional
Ac	acoustic (phonons)
ATR-FTIR	attenuated total reflection FOURIER transform infrared spectroscopy
BS	beam splitter
CB	conduction band
CCD	charge-coupled device (sensor)
CM	carrier multiplication
CW	continuous wave
DOS	density of states
EMA	effective mass approximation
Eq.	equation
FFT	fast FOURIER transform
fQD	flat quantum dot
fwhm	full width at half maximum
GIWAXS	grazing-incidence wide-angle X-ray scattering
HMBC	heteronuclear multiple bond correlation
HR-HAADF-STEM	high-resolution high-angle annular dark-field scanning transmission electron microscopy
HRTEM	high-resolution transmission electron microscopy
HSAB	hard and soft acids and bases
HWP	half wave plate
LO	longitudinal optical (phonons)
LOESS	locally estimated scatterplot smoothing
long.	longitudinal
LT	lifetime
MCS	multichannel scaling
ML/1ML	monolayer
mo.	months
MUA	11-mercaptoundecanoic acid

NA	numerical aperture
NC	nanocrystal
NIR	near-infrared
NMR	nuclear magnetic resonance
NPL	nanoplatelet
NR	nanorod
NS	nanosheet
NW	nanowire
ODE	1-octadecene
PDF	powder diffraction file
PL	photoluminescence
PLQY	photoluminescence quantum yield
PMMA	poly(methyl methacrylate)
PMT	photomultiplier tube
POL	polarizer
PXRD	powder X-ray diffraction
QD	quantum dot
QW	quantum well
rcf	relative centrifugal force
ref.	reference
resp.	respectively
RT	room temperature
SAED	selected area electron diffraction
SAXS	small-angle X-ray scattering
SEM	scanning electron microscopy
SI	supporting information
SJES	stable jet electrospinning
STM	scanning tunneling microscopy
STS	scanning tunneling spectroscopy
SWIR	short-wave-infrared
TB	tight-binding
TBAI	tetrabutylammonium iodide
TCE	tetrachloroethylene
TEM	transmission electron microscopy

TOP	tri-*n*-octylphosphine
TOPO	tri-*n*-octylphosphine oxide
trans.	transversal
UHV	ultra-high vacuum
UV	ultraviolet
VB	valence band
vis	visible
XPS	X-ray photoelectron spectroscopy
ZIF	zeolitic imidazolate framework
ZPL	zero phonon line

1 Motivation

Both nanocrystals and infrared radiation are not directly visible to the human eye. Yet we already encounter both of them in everyday life through established applications, and they are set to play a vital role in future technologies.[1–3]

Semiconductor nanocrystals (NCs) are crystallites so small that their properties are governed by their size and accompanying quantum effects. Their most noticeable characteristic is their size-dependent change in color, caused by *quantum confinement*. Colloidal chemistry enables for the precise control and relatively scalable production of NCs and has paved the way for their first commercial applications. For instance, the unique photophysics of NCs have been put to practical use in consumer electronic displays to provide high color purity and a wider color gamut than contemporary technologies.[4] In recognition of the successes and future potential of nanotechnology with NCs, the discovery and synthesis of semiconductor NCs was awarded with the NOBLE Prize in Chemistry to BAWENDI, BRUS and YEKIMOV in 2023.

Infrared light is central to transmitting the ever-increasing amounts of information in modern society *via* optical fibers as well as for detecting diseases *via* tissue imaging.[1,5] Further, harnessing the otherwise unused near-infrared part of the sun's spectrum can increase the efficiency of solar cells, which is crucial for tackling the challenges posed by the climate crisis.[1]

The field of colloidal infrared nanocrystals combines aspects of both research areas, under the main goal of developing materials with spectrally tunable optical properties at infrared wavelengths.[1–3,5] These nanomaterials ought to be producable in large quantities and easily processed in solution, allowing for the flexible integration and fabrication of devices for the aforementioned applications. A promising material class in this regard are *colloidal lead chalcogenide PbX (X = S, Se, Te) nanocrystals*.[2,3] Their bright emission can be colloidally tailored for the transimission windows of optical fibers at near- and short-wave-infrared wavelengths (NIR: 700 –1400 nm, SWIR: 1400 – 3000 nm). In these tele-communication windows, the attenuation in silica fibers is negligible, enabling information carried by photons to be transmitted with minimal loss.[5] In a classical fiber network, the transmitted signals must be periodically reamplified for the information to reach a distant receiver, this may be achieved using

NIR-emissive NCs.[5] Thinking further, emerging quantum photonic technologies require on-demand single-photon sources to encode information into the quantum state of photons, for *e.g.* encrypted communication.[6] For quantum information science, *two-dimensional (2D) PbX NCs* with an ultrathin thickness dimension are particularly promising. They exhibit unique optical properties – such as narrow (especially at low temperaturres), efficient and blinking-free NIR emission with a high degree of linear polarization – which differentiates them from their spherical counterparts (see Chapter 6).[7] All of these properties are prerequisites for an efficient single-photon source and can be tailored by colloidal chemistry. Despite this technological interest, NIR-emitting 2D PbX NCs are underexplored compared to well-established visible-emitting 2D NC systems, such as CdSe nanoplatelets[8] or 2D lead halide perovskites.[9] The first part of this work therefore focuses on the initial stage of material development. Chapter 4 presents the first synthesis of colloidal 2D PbTe NCs with tunable NIR emission, while Chapters 3 and 5 are centered around the post-synthetic modification of 2D PbX NCs to achieve increased quantum yields and solubility in water, respectively.[10–12] Chapter 6 and 7 build on these chemistry-focused studies and are centered around the fascinating photophysics of 2D PbX NCs and their spectroscopic characterization.[7,13] Chapter 8 goes a step further, presenting the stable jet electrospinning of 2D PbSe NCs with poly(methyl methacrylate) to obtain NIR-emissive nanocomposite fibers.

2 Fundamentals

2.1 Physics of Semiconductor Nanocrystals

Semiconductors are a class of materials with an intermediate electrical conductivity higher than that of insulators, but lower than that of metals.[14,15] The properties of semiconductors are largely determined by the behavior of electrons and holes, collectively referred to as *charge carriers*. A *hole* is a fictional particle with positive charge that can occupy all energy states that are not occupied by electrons, effectively representing the absence of an electron.[15]

Electrons in macroscopic semiconductors (and other solids) can be described as quasi-free particles moving within a periodic potential created by the positively charged nuclei. This potential results in a discretization of the allowed energy levels compared to the continuous parabolic energy of free electrons. The resulting allowed energy states in a solid are called *bands*.[14,16] In a bulk semiconductor these electronic bands are very closely spaced energetically, forming continuums called the valence band and the conduction band, which are separated by the band gap (Figure 2.1).

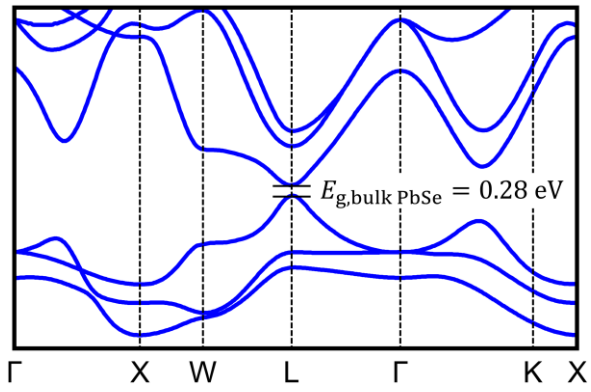

Figure 2.1. Exemplary band structure of bulk PbSe with valence band maximum and conduction band minimum at the L-point of the BRILLOUIN zone and a direct band gap of 0.28 eV.[17] (redrawn band structure based on Ref. [18,19])

The *valence band* (VB) is the energetically highest occupied band, while the *conduction band* (CB) is the energetically lowest unoccupied band. Within the separating *band gap* are no energetic states that could be occupied by charge carriers; the electronic *density of states* (DOS), defined as the number of electronic states per unit energy and per unit volume, is zero.[20] While the distinction between

insulators and semiconductors is somewhat ambiguous, the majority of relevant semiconductors exhibit a band gap of less than 2 eV (*e.g.* bulk Si 1.1 eV at 300 K).[15] The energy of the band gap can be overcome by *e.g.* thermal energy (if the gap is small enough) or by the absorption of light, which excites an electron from the VB to the CB and leaves behind a hole in the VB. The oppositely charged excited electron and created hole are attracted to each other by an electrostatic force and can form a hydrogen-like neutral quasiparticle called an *exciton*.[14,21] For nanoscaled semiconductors, the binding energy of electrons and holes is increased, which results in pronounced excitonic effects, such as sharp absorption peaks at energies that are resonant for the formation of excitons (see Subchapter 2.1.2 and 2.1.4 for a more detailed discussion).

In semiconductor nanocrystals (NCs), only a finite number of atoms contribute to the electronic bands, causing the continuous VB and CB to evolve into discrete, more atom-like energy levels, and the band gap to widen with decreasing NC size. This phenomenon is called the *quantum size effect* and gives rise to the fascinating size-dependent properties in NCs.[20]

The upcoming subchapters will introduce basic concepts encountered when researching semiconductor NCs and further establish terminology used in the subsequent chapters.

2.1.1 Quantum Size Effect

A simplified model explaining quantum confinement is the *particle in a box*. One can imagine a cuboid box with length a, width b, and height c, where the potential energy V is zero inside the box and infinite outside the box (Figure 2.2a). The wave function of an electron inside the box can then be described by the time-independent SCHRÖDINGER equation,

$$\frac{\hbar^2}{2m_\mathrm{e}}\nabla^2\varphi(\boldsymbol{r}) + [E - V(\boldsymbol{r})]\varphi(\boldsymbol{r}) = 0 \qquad \text{(Eq. 2.1)}$$

under the boundary conditions,

$$V(x,y,z) = \begin{cases} 0, |x| < \frac{a}{2} \wedge |y| < \frac{b}{2} \wedge |z| < \frac{c}{2} \\ \infty, \text{otherwise} \end{cases} \qquad \text{(Eq. 2.2)}$$

with the reduced PLANCK constant $\hbar$, the mass of the electron m_e, the Nabla operator ∇, the wavefunction $\varphi(r)$, the energy E, and the potential energy $V(r)$.[16]

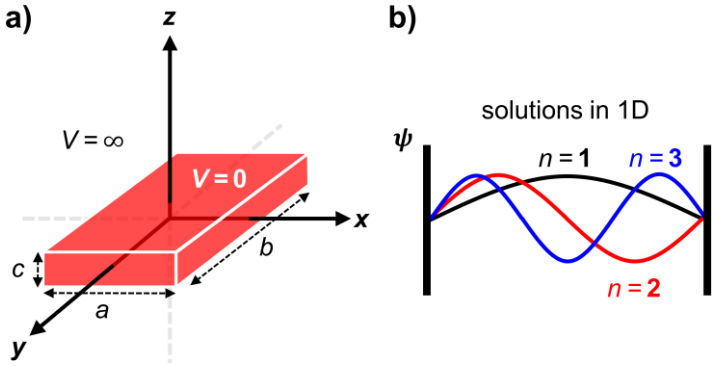

Figure 2.2. (a) Conceptual drawing of the particle-in-a-3D-box model. For a quasi-2D structure, such as a large nanosheet, the lateral dimensions a and b are effectively infinite, with the thickness c being the dimension that induces the quantum confinement. (b) Simplified representation of the standing wave solutions for n = 1, 2, 3 in one dimension. (own representation based on Ref. [16])

Solving this equation gives wavefunctions corresponding to standing waves with nodes at the potential barriers of the box and discrete energies (Figure 2.2b)

$$E_{n_x,n_y,n_z} = \frac{\hbar^2\pi^2}{2m_e}\left(\frac{{n_x}^2}{a^2} + \frac{{n_y}^2}{b^2} + \frac{{n_z}^2}{c^2}\right), \qquad n_x, n_y, n_z = 1, 2, 3, \ldots \qquad \text{(Eq. 2.3)}$$

with the quantum numbers n_x, n_y, and n_z.[16] The obtained energy levels represent the discrete energy values that an electron is allowed to have. The lowest energy level with $n_x = n_y = n_z = 1$, corresponds to the electronic ground state; the higher energy levels, *e.g.* with $n_x = 2$, $n_y = n_z = 1$, are excited states, with increasing separation due to the n^2 dependence. The inverse relationship between the energy and the dimensions of the imaginary box is the reason why the quantum size effect is observed in semiconductor NCs: smaller values of a, b and c result in energetically higher allowed energy levels, *i.e.* a larger band gap, as well as a greater separation between adjacent energy levels.[16]

Size quantization is most striking, and even visible to the naked eye, when a semiconductor exhibits a band gap energy in the visible range. For example, CdSe nanoplatelets (NPLs) show fluorescence from bright green (510 nm) over yellow (584 nm) to intense red (625 nm), depending on their thickness when illuminated with UV light.[22] In the simplified particle-in-a-box model, the NPLs' confinement inducing thickness corresponds to the smallest dimension of the box, *e.g.* the height c. The two-dimensional (2D) lead chalcogenide NCs studied in this thesis exhibit narrower band gaps, beyond visible wavelengths, so that the human eye is blind for the observation of the effects of quantum confinement and a spectrometer is needed.[7,10–13] Nonetheless, the basic concept of size quantization introduced in this subchapter applies in the same way.

To more accurately describe the electronic states in real semiconductor NCs, the electron, the hole, and their interaction must be separately included in the system's HAMILTONIAN.[16] Following this more complex approach, an analytical approximation of the band gap $E_{\mathrm{g,NC}}$ of a NC with radius r is given by the BRUS equation,[23,24]

$$E_{\mathrm{g,NC}} \approx E_{\mathrm{g,bulk}} + \frac{\hbar^2\pi^2}{2r^2}\left(\frac{1}{m_{\mathrm{e}}^*} + \frac{1}{m_{\mathrm{m}}^*}\right) - \frac{1.8e^2}{\varepsilon r} + \text{smaller terms} \qquad \text{(Eq. 2.4)}$$

with the bulk band gap of the respective semiconductor $E_{\mathrm{g,bulk}}$, the effective mass of the electron (hole) m_{e}^* (m_{h}^*), the elementary charge e, and the permittivity of the semiconductor ε. For large radii r, $E_{\mathrm{g,NC}}$ asymptotically approaches $E_{\mathrm{g,bulk}}$ and the quantum confinement effectively vanishes. Conversely, for very small r, the $1/r^2$ term becomes dominant and the band gap increases with decreasing (nano-)crystal size, *i.e.* the quantum size effect occurs.[24]

For 2D nanomaterials, the interaction between eletron and hole cannot be described by the simple $-1.8e^2/\varepsilon r$ expression, instead the materials thickness must be explicitly accounted for. This is done by the RYTOVA-KELDYSH pontential, which is analytically approximated by the STRUVE-NEUMANN potential V^{HN} for $r \gg d$ and $\varepsilon \gg \varepsilon_{1,2}$:[25]

$$V^{\mathrm{HN}}(r) = -\frac{e^2}{4\pi\varepsilon}\frac{\pi}{d}\left[H_0\left(\frac{\varepsilon_1+\varepsilon_2}{\varepsilon}\frac{r}{d}\right) - N_0\left(\frac{\varepsilon_1+\varepsilon_2}{\varepsilon}\frac{r}{d}\right)\right] \qquad \text{(Eq. 2.5)}$$

with the nanomaterials thickness d, the semiconductors permittivity ε, the permittivities of the environment ε_1 and ε_2, the in-plane distance between electron and hole r, and the STRUVE- and NEUMANN functions H_0 and N_0. Accordingly, the interaction potential between electrons and holes in low-dimensional semiconductors depends not only on the thickness (and lateral dimensions) of the material, but also on the surrounding dielectric; this is discussed in Subchapter 2.1.3.

2.1.2 Excitons

The third term of the BRUS equation ($-1.8e^2/\varepsilon r$) represents the mutual attractive force between the oppositely charged electron and hole, the COULOMB interaction.[24] An electrostatically attracted electron-hole pair can form a bound state similar to a hydrogen atom, referred to as an exciton.[14,21] Excitons can be created when a photon with an energy equal to or above the band gap energy is absorbed by a semiconductor, creating an electron in the CB and a hole in VB at the same spatial position. An exciton is stable when the attractive COULOMB potential cannot be overcome by the energy of thermally excited phonons. In other words, the *exciton binding energy* E_b must be higher than $k_\mathrm{B}T$ (~26 meV at room temperature), with k_B denoting the BOLTZMANN constant.[21] In experiments, E_b corresponds to the difference between the ground excitonic state, *i.e.* the optical band gap, and the fundamental (electronic) bandgap.[26] Thus, experimentally measuring the exciton binding energy is non-trivial and requires resolving both signatures of the exciton (*e.g.* by optical spectroscopy) and the electronic band gap (*e.g.* by scanning tunneling spectroscopy (STS)). This will be shown in Chapter 7.[13,27]

The second key parameter characterizing excitons is the *exciton BOHR radius* a_B. In analogy to the hydrogen atom, the BOHR model can be applied to excitons, which gives

$$a_\mathrm{B} = a_\mathrm{H}\frac{m_\mathrm{e}\varepsilon_\mathrm{r}}{\mu} \qquad \text{(Eq. 2.6)}$$

as the radius of the electron-hole-orbit, with the radius of the hydrogen atom a_H, the mass of the electron m_e, the relative permittivity of the semiconductor ε_r, and the reduced mass of the electron and the hole μ.[14,21] Table 2.1 lists the bulk band gaps $E_{g,bulk}$ and exciton BOHR radii a_B of lead chalcogenides investigated in this thesis and cadmium chalcogenides for reference.

Table 2.1. Bulk band gaps $E_{g,bulk}$ (at T = 300 K) and exciton BOHR radii a_B of lead and cadmium chalcogenides.

material	$E_{g,bulk}$ (eV)	a_B (nm)
PbS	**0.42** [17,28]	**20** [29] (23.5 (transversal), 17.4 (longitudinal))[28]
PbSe	**0.28** [17,28]	**46** [29] (66 (trans.), 34.7 (long.))[28]
PbTe	**0.31** [17,28]	~83, (**152** (trans.), **12.9** (long.)) [28]
CdS	2.48 [17]	~2.4 [30]
CdSe	1.74 [17]	5.4 [21]
CdTe	1.48 [17]	6.7 [21]

The exciton BOHR radius can serve as a rough estimate at which crystal size major effects of quantum confinement are to be expected.[31] One can be distinguish between no ($x, y, z/a_B \gg 1$), weak ($x, y, z/a_B \leq 1$), and/or strong to extreme quantum confinement ($x, y, z/a_B \ll 1$),[29] depending on the dimensions x, y and z of a given material. For non-spherical NCs, the confinement can accordingly vary in different directions; *e.g.* there may be no confinement in two directions and strong confinement in one direction, as is the case for extended nanosheets (NSs). For instance, the aforementioned green-, yellow-, or red-emitting CdSe NPLs exhibit lateral sizes of roughly 50 x 8 nm² and a thickness ranging from 4.5 to 8.5 monolayers (ML).[22] Comparing these dimensions to $a_{B,CdSe}$ of 5.4 nm (see Table 2.1), it becomes evident that the exciton is drastically confined by the thickness, whereas the length and width only induce a weak confinement as long as $a_{B,CdSe}$ is not approached or undercut. Notably, in the latter case, the additional confinement induced by a reduced width, results in significant changes of the materials' optoelectronic properties, *e.g.* RODÀ *et al.* recently reported increased biexciton binding energies in laterally confined CdSe NPLs.[32] Lead chalcogenides exhibit significantly larger exciton BOHR radii of 20 nm and higher (see Table 2.1),

meaning that an exciton in a PbX (X = S, Se, Te) NPL or flat quantum dot (fQD) is already quantum confined in all three dimensions at comaparatively larger dimensions, with particularly extreme confinement in the thickness dimension.

In semiconductors mainly free (or delocalized) excitons, called WANNIER-MOTT excitons, are formed, which exhibit a radius exceeding multiple lattice constants of the material and can move freely within the crystal.[14,21] WANNIER-MOTT excitons exhibit lower exciton binding energies compared to tightly bound FRENKEL excitons, which are common in insulators or molecular semiconductors (Figure 2.3).[21,27]

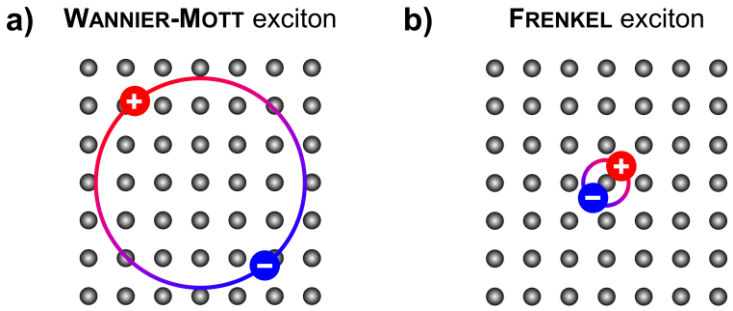

Figure 2.3. Schematic representation of a free WANNIER-MOTT exciton (a) and a strongly bound FRENKEL exciton (b). (own representation based on Ref. [21])

However, for low-dimensional (*e.g.* 2D) materials, WANNIER-MOTT excitons with high binding energies have been reported.[13,14,27] Excitons in 2D materials are highly confined by the ultrathin thickness dimension and are less screened from the dielectric environment (see Chapter 2.1.3), which results in a larger band gap compared to their 3D counterparts as well as an increase in exciton binding energy ΔE_b, due to a stronger electron-hole interaction.[33] The latter can be expressed as,[32,34]

$$\Delta E_\mathrm{b} = \left(\frac{\mu}{m_\mathrm{e}\varepsilon^2}\right)\left(\frac{2}{\alpha - 1}\right)^2 \cdot 13.6\ \mathrm{eV} \qquad \text{(Eq. 2.7)}$$

with the reduced exciton mass μ, the mass of the electron m_e, the relative permittivity ε, and the hydrogen binding energy E_H of 13.6 eV. The geometry factor α accounts for the dimensionality of the material (α = 3 for bulk and α = 2

for a 2D semiconductors), this means, when only considering this factor, ΔE_b is estimated to be four times higher in 2D materials than in 3D systems.[32] As such, excitons in both classical (*e.g.* transition metal dichalcogenides) and "non-classical" (*e.g.* lead chalcogenides) 2D nanomaterials are stable at room temperature and the materials' optical properties are dominated by excitons, making 2D materials interesting for fundamental research as well as future optoelectronic applications.[27] For example, the increased overlap between the electron and hole wave functions in tightly bound excitons results in fast radiative lifetimes that can efficiently compete with non-radiative recombination, which is important for fabricating efficient light-emitting devices.[21]

2.1.3 Dielectric Confinement

The strength of the COULOMB interaction between the electron and hole depends on the dielectric surrounding of the exciton. In a bulk semiconductor, the permittivity ε is rather high (*e.g.* $\varepsilon_{\text{bulk PbSe}}$ = 21 to 22.9 for the low to high frequency limit)[17] and "constant" throughout the material; *i.e.* the electron-hole interaction is weakened by its surroundings. However, in a colloidal NC the situation is drastically different; the dielectric constant of the surrounding medium (commonly an organic solvent (see Chapter 2.2)) is ~five to ten times lower compared to the bulk semiconductor, and the interface represents a discontinuity of the permittivity.[35] This introduces a size and dielectric constant depended *dielectric confinement effect* in addition to the quantum confinement effect discussed before. The reduced dielectric screening in colloidal solution (and in deposited films thereof) pushes the charge carriers toward the center of the NC, so that the exciton binding energy E_b is stronger than in a bulk semiconductor. The dielectric confinement is represented by the third term of the BRUS equation and decreases the band gap E_g of a NC with a $1/\varepsilon r$ dependence. This means that for small crystal sizes the dielectric confinement is outweighed by the quantum confinement increasing E_g ($1/r^2$ dependence), *i.e.* dielectric confinement is more impactful for larger NCs.[23,35] The 2D PbX NCs investigated in this thesis are all within the strong to extreme quantum confined regime, therefore dielectric confinement will rarely be discussed in the following chapters.

2.1.4 Absorption and Photoluminescence

The previous subchapters implicitly introduced the concept of light absorption as a way to overcome the band gap of a semiconductor and eventually generate excitons. In essence, the term *absorption* refers to the excitation of an electron from an occupied lower-energy band to an available higher-energy band by the interaction with a photon.[21] For such an interband transition to occur, the energy of the photon must be equal to or higher than the energy difference between the two bands, *i.e.* the band gap E_g (BOHR frequency condition)[36] and the higher-energy state must be empty, so that the spin selection rules are not violated by the transition (PAULI exclusion principle).[21] The absorption of photons with energies exceeding E_g results in the formation of so-called hot electrons and holes, which can cool to the band edge by losing their excess energy *via* exciton-phonon interactions.[37,38]

Absorbance spectra of semiconductor NCs typically show a pronounced peak or shoulder, or a series of distinguishable features, corresponding to different optical transitions (Figure 2.4).

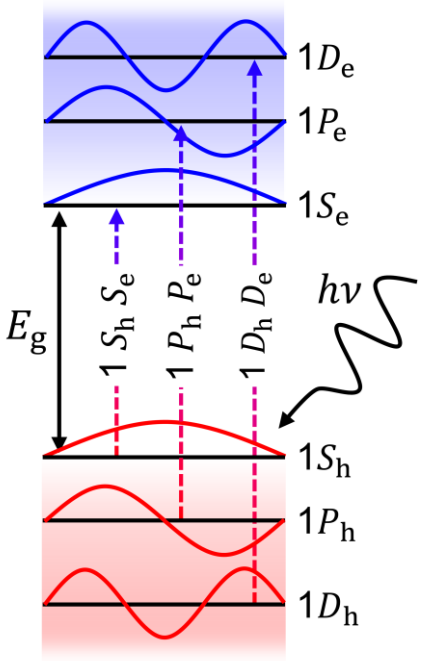

Figure 2.4. Allowed excitonic transitions in a semiconductor NC. (own representation based on Ref. [19])

The expression of these different features depends on the material, the size of the NCs and the quality (monodispersity) of the sample. The lowest-energy absorption feature corresponds to the ground state exciton (the first excited state) and is commonly denoted as the $1S_h1S_e$ transition (Figure 2.5).[26,39,40] This model/nomenclature describes each charge carrier by an envelope function, *e.g.* $1S_h1S_e$ means that hole ($_h$) and electron ($_e$) and are both in the first (1) *S*-like (*S*) envelope function.[39] Subsequent, higher-energy absorption features may then be ascribed to *e.g.* the $1P_h1P_e$ or the $1S_{h,e}1P_{e,h}$ transitions (this notation reappears in the context of scanning tunneling spectroscopy spectra in Chapter 7).[13,39,40] In the following chapters the *y*-axes of absorbance spectra will predominately be labeled with "*absorbance*" rather than "absorption"; the former includes scattering and reflection.[41]

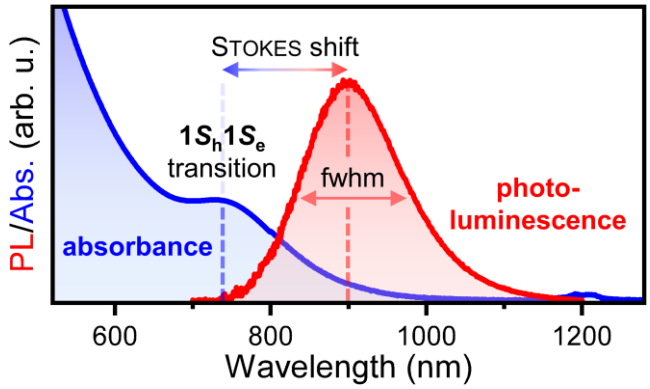

Figure 2.5. Exemplary absorbance and photoluminescence spectrum of colloidal 2D PbSe nanoplatelets illustrating the basic terms used in the subsequent chapters.

Excitons eventually decay through non-radiative or radiative recombination.[14,21] Non-radiative recombination can occur *via* phonon-mediated relaxation, whereby the released energy is dissipated as heat within the crystal lattice rather than being emitted as light. When the energy is released as a cascade of phonons (phonon ladder), the individual energy values are much smaller than those associated with overcoming the band gap by emitting a photon, so that non-radiative recombination occurs faster.[14] This means that in materials with strong exciton-phonon coupling, fast non-radiative recombination outcompedes radiative recombination, which poses a challenge for using such materials in *e.g.* lighting applications.[42] Phonon-mediated non-radiative recombination is often defect-center controlled and occurs *via* electronic *trap states* that may lie within the band gap of the material (Figure 2.6).[14] In nanocrystals, mid-gap trap states are common

and caused by the ubiquitous presence of undercoordinated atoms on the NC surface.[43] Consequently, the probability of non-radiative recombination in NCs can be reduced by suitable surface engineering, as will be demonstrated in Chapter 3.[11]

A second important non-radiative recombination process is AUGER recombination, which occurs *via* energy transfer to other charge carriers (Figure 2.6). In this process, an excited electron returns to the valence band by trasmitting its excess energy to a nearby excited electron, which in turn is excited to a higher state. From there, it can return to the band edge by sequential phonon scattering.[14] AUGER recombination is particularly relevant when high charge carrier densities are reached. For example, AUGER recombination is the dominant non-radiative decay process for biexcitons or higher-order multiexcitons.[44,45] Similarly, trions (composed of two electrons and one hole or *vice versa*) can recombine non-radiatively by transferring their energy to the third charge carrier.[46] Notably, biexciton AUGER recombination rates are reduced in 2D PbS NSs[46] or CdSe NPLs[47], which makes them particularly interesting for use in lasers or solar cells, where multiple excitons are generated.

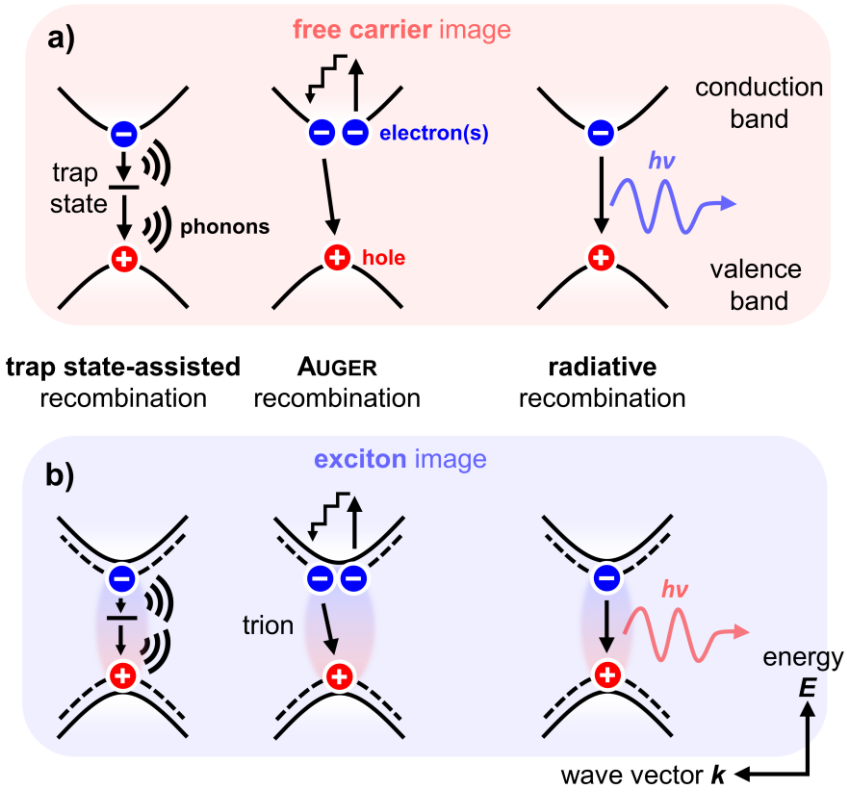

Figure 2.6. Non-radiative and radiative recombination of free charge carriers (a) and excitons (b). (own representation based on Ref. [48])

Radiative recombination in many ways can be considered the opposite of absorption: An exciton recombines by spontaneous emission of a photon (see Figure 2.5 and Figure 2.6). This process is called *photoluminescence* (PL) and occurs with a delay after the photoexcitation that corresponds to the radiative lifetime τ_r of the transition.[14,21] For a two-level system the rate equation is given by

$$\left(\frac{\mathrm{d}N}{\mathrm{d}t}\right)_{\text{radiative}} = -A \cdot N \qquad \text{(Eq. 2.8)}$$

$$N(t) = N(0)\mathrm{e}^{-At} = N(0)\mathrm{e}^{-t/\tau_\mathrm{r}} \qquad \text{(Eq. 2.9)}$$

with the higher level population $N(t)$ ($N(0)$) at time t ($t = 0$), the EINSTEIN coefficient A, and the radiative lifetime $\tau_\mathrm{r} = A^{-1}$.[21] When an emitter exhibits multiple radiative recombination pathways (*e.g.* band edge emission and emission from a bright defect state)[49] or when a mixture of different emitters is measured, the decay is multiexponential:[50]

$$F(t,\lambda) = I(\lambda)\sum a_i(\lambda)\mathrm{e}^{-t/\tau_i} \qquad \text{(Eq. 2.10)}$$

with the total amplitude $I(\lambda)$, the amplitude fractions of each component $a_i(\lambda)$, and the individual lifetimes of the decay components τ_i. For example, PbS QDs exhibit biexponential PL lifetimes (LTs), with a fast contribution from a pinned-charge defect state and a longer-lived band edge emission.[49] The relative ratio of these contributions depends on the QD size and the temperature, with the pinned state (*i.e.* independent of QD size) dominating at room temperature for highly confined QDs. Similarly, excitons in PbSe fQDs and PbTe NPLs decay biexponentially, as discussed in Chapter 3 and 4.[10,11]

Non-radiative and radiative recombination are competing processes. As such, the *photoluminescence quantum yield* Φ_PL (PLQY) is an important metric for assessing the quality of emitters. It is defined as the number of emitted photons N_em divided by the number of absorbed photons N_abs:[51]

$$\Phi_\mathrm{PL} = N_\mathrm{em}/N_\mathrm{abs} \qquad \text{(Eq. 2.11)}$$

The PLQY of colloidal NCs is determined using a basic steady-state PL spectrometer, either by relative or absolute measurements. Relative PLQY determination requires a suitable reference with a known PLQY (commonly an organic dye), to which the absorption-factor-weighted integral-PL intensity of the sample is compared.[52] Absolute PLQY measurements can be performed without a reference sample using an ULBRICHT/integrating sphere, which uniformly scatters and collects all light emitted, scattered and transmitted by the sample. The latter technique was used for the PLQY measurements of 2D PbX NCs in this thesis, since reliable NIR standards are scarce. For absolute measurements, the PLQY is calculated as[52]

$$\Phi_{\mathrm{PL}} = \frac{q_{\mathrm{p}}^{\mathrm{PL}}}{q_{\mathrm{p}}^{\mathrm{abs}}} = \frac{\int_{\lambda_{\mathrm{em}_1}}^{\lambda_{\mathrm{em}_2}} \frac{(I_{\mathrm{x}}(\lambda_{\mathrm{em}}) - I_{\mathrm{b}}(\lambda_{\mathrm{em}}))}{s(\lambda_{\mathrm{em}})} \lambda_{\mathrm{em}} \mathrm{d}\lambda_{\mathrm{em}}}{\int_{\lambda_{\mathrm{exc}}-\Delta\lambda}^{\lambda_{\mathrm{exc}}+\Delta\lambda} \frac{(I_b(\lambda_{\mathrm{exc}}) - I_x(\lambda_{\mathrm{exc}}))}{s(\lambda_{\mathrm{exc}})} \lambda_{\mathrm{exc}} \mathrm{d}\lambda_{\mathrm{exc}}} \qquad \text{(Eq. 2.12)}$$

with the emitted photon flux $q_{\mathrm{p}}^{\mathrm{PL}}$, given by the integral of the blank $I_{\mathrm{b}}(\lambda_{\mathrm{em}})$-corrected emission $I_{\mathrm{x}}(\lambda_{\mathrm{em}})$ spectrum. The absorbed photon flux $q_{\mathrm{p}}^{\mathrm{abs}}$ is the difference between the transmitted excitation light of blank $I_b(\lambda_{\mathrm{exc}})$ and sample $I_x(\lambda_{\mathrm{exc}})$ over the excitation bandwidth $\Delta\lambda_{\mathrm{exc}}$.[52] $s(\lambda_{\mathrm{em}})$ and $s(\lambda_{\mathrm{exc}})$ are the spectral responsivities of the spectrometer at the respective wavelengths.

A second quality parameter for emissive NCs is the *full width at half maximum* (fwhm) of their PL (Figure 2.5). For visible emitters, this parameter can be simply pictured as the color purity of the emitted light. The PL spectra of individual NCs exhibit a LORENTZIAN profile and the linewidth of the PL is composed of the nanocrystal's emission (or its multiple emissive states), which is homogenously broadened by coupling to *e.g.* acoustic or optical phonons (see Chapter 6).[7,49,53] For an ensemble of NCs, the PL spectrum is *inhomogeneously broadened* compared to the linewidth of an individual emitting NC; it consists of a convolution of all the the PL spectra of the homogenously broadened single NCs and exhibits a GAUSSIAN profile. Inhomogeneous broadening is mainly caused by the polydispersity of real NC samples, since the PL wavelength varies slightly between differently sized NCs.[49,53] Therefore, it can be excluded from spectral analysis by moving from ensemble to single particle measurements, while the influence of homogenous broadening can be suppressed by performing low

temperature measurements, in which the phonon population is decreased.[53–55] This concept is reflected in the cryogenic PL measurements on single PbS NPLs presented in Chapter 6 as well as the low-temperature PL spectra of PbSe fQDs in Chapter 7.[7,13]

Lastly, the STOKES shift – the difference in energy between the absorption feature of the ground state and the PL maximum – is mentioned when discussing different emitters (Figure 2.5).[56] In NCs, the STOKES shift is intrinsically linked to their excitonic fine structure. In absorbance spectra, the observed ground state feature corresponds to the lowest energy-allowed transition. However, this bright exciton state is not necessarily the lowest energy state. Dark exciton states may lie energetically below it, which are not visible in absorption spectra due to the selection rules for the respective transition(s). Excited electrons can relax to such dark exciton states and radiatively recombine from there, resulting in PL (with an increased PL LT) at a lower energy compared to the first absorption feature, *i.e.* a STOKES shift.[56] Besides this fundamental origin, the STOKES shift in colloidal NC samples can originate from an energy transfer toward smaller band gap NCs in a polydisperse ensemble. This was shown by VOZNYY *et al.* for colloidal PbS NCs and means that electrons in these inhomogeneous mixtures may predominantly recombine in the largest NCs with the narrowest band gaps (this concept reappears in Chapter 8 in the context of stacked PbSe fQDs in polymer fibers).[56] This causes the PL maximum to be shifted further away from the ground state absorbance feature. In this sense, the STOKES shift can, similarly to the fwhm, be interpreted as a measure for the polydispersity of a NC sample.

2.1.5 Dimensionality: From Spherical to 2D Nanocrystals

Starting from the discussion of the BRUS equation in Subchapter 2.1.1 and further evaluation, the band gap and the optical properties of semiconductor NCs have been discussed as a function of their radius *r*, *i.e.* their size. However, not only the quantum-confined size, but also the shape of the NCs can be controlled and used to tune their degree of quantum confinement. This concept is central to the 2D PbX NCs discussed in this thesis. The upcoming chapter on the chemistry of colloidal nanocrystals will discuss how shape control can be achieved synthetically. The main point to note about the dimensionality of NCs is that the degree of quantum

confinement may differ in different directions, which results in shape-dependent optical and electronic properties (Figure 2.7).[31]

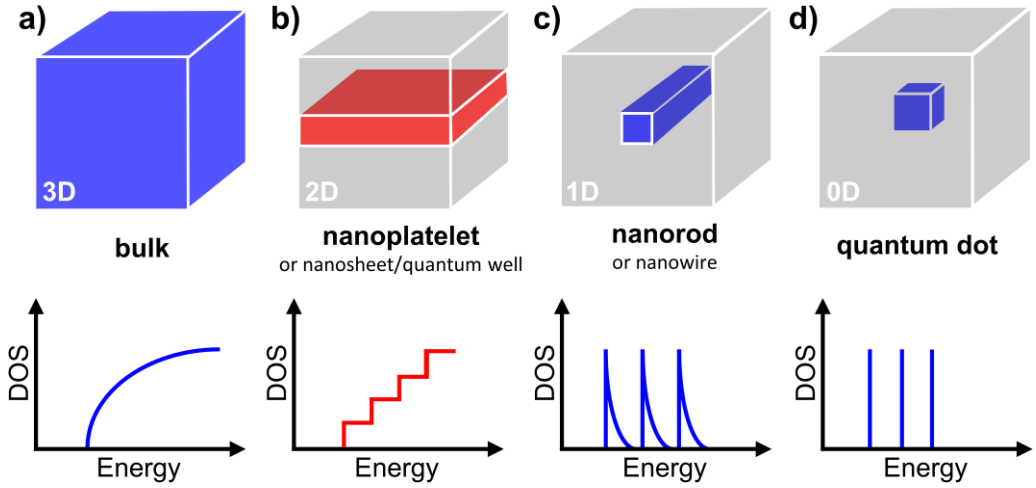

Figure 2.7. Shape-dependent density of states of a semiconductor with gradually decreasing dimensionality. (own representation based on Ref. [19,21])

Nanocrystals that are quantum confinement in all three dimensions ($r/a_B < 1$) are called *quantum dots* and are commonly referred to as zero-dimensional (0D). The DOS of (an ideal) quantum dot consists of narrow peaks (delta functions) corresponding to discrete allowed energy states (Figure 2.7d). This results in sharp absorption at these energies and reduced absorption at all other. The optical transition strength for these few transitions is very high because the overall integrated absorption is conserved, but now focused on a countable number of narrow energy intervals.[29]

When a spherical NC is elongated in one direction it becomes a *nanorod* (NR) and eventually a *nanowire* (NW). In these one-dimensional (1D) structures, with diameter d and length l, an exciton is quantum confinement in two dimensions ($d/a_B < 1,\ l/a_B > 1$).[19] For example, this results in linearly polarized emission from 1D CdSe NRs, which is tunable by their length/aspect ratio.[57]

Two-dimensional materials are confined in the thickness direction z ($z/a_B < 1,\ x,y/a_B > 1$), depending on their lateral dimensions x and y they are called either *nanoplatelets* or *nanosheets*.[19] The DOS of an idealized 2D material with infinite lateral dimensions is a step-like function, with the exciton being able to freely move in the lateral dimensions.

Real nanocrystals have finite dimensions and varying aspect ratios, so they do not necessarily fit strictly into one of these somewhat rigid definitions – an exciton in a 2D nanoplatelet might still experience a varying degree of quantum confinement in the in-plane directions or a short nanorod may weakly confine an exciton along its length.[19] At first glance, the previously mentioned example of 2D CdSe NPLs seems relatively clear: the thickness (between 4.5 and 8.5 ML) is well below the exciton BOHR radius, while the lateral dimensions are typically significantly larger. Nonetheless, examples of laterally confined CdSe NPLs with widths approaching a_B have been reported,[32,58] and STS studies have revealed lateral confinement and a 1D-like DOS in CdSe NPLs with finite length and width, which precludes the free in-plane electron motion that would be expected in an ideal 2D nanomaterial.[59] In the referred-to STS (and tight-binding) study, PERIC *et al.* demonstrated nanowire-like DOS with sharp VAN HOVE singularities for CdSe NPLs with infinite length and 6 nm width, which converges into the step-like function expected for a truly 2D material for increasing widths.[59]

For 2D PbX NCs the boundary is just as ambiguous. PbS NPLs synthesized in this thesis exhibit a lateral size of ~20 x 7 nm², for PbSe fQDs the size is ~4 x 3 nm², and PbTe NPLs show values of ~7 x 5 nm², all with a thickness ranging from a ML to a few atomic layers.[7,10,11,13,60,61] Comparing these dimensions to the exciton Bohr radii of lead chalcogenides (listed in Table 2.1), it gets apparent that the exciton is spatially confined in all three dimensions ($x, y, z/a_B < 1$), albeit with particularly severe quantum confinement in the thickness direction ($z/a_B \ll 1$). Throughout this thesis, the colloidal 2D lead chalcogenides discussed will largely be referred to as PbS NPLs, PbSe NPLs/fQDs and PbTe NPLs, or more generally as 2D PbX NCs. The change in nomenclature for 2D PbSe from NPLs to fQDs is discussed further in Chapter 7, where measurements of the DOS reveal that “flat quantum dot” is a more suitable term than “nanoplatelets” for the structures.[13] In addition to the increased quantum confinement in one dimension, the 2D geometry of PbX NPLs/fQDs gives rise to unique optical properties different from their spherical counterparts, which will be discussed for each lead chalcogenide in the Subchapters 2.3.1 to 2.3.3. One such example is the sub-meV line width in the linearly polarized low-temperature PL of 2D PbS NPLs presented in Chapter 6.[7]

2.2 *Chemistry of Colloidal Nanocrystals*

The 2D lead chalcogenide nanocrystals at the center of this thesis are colloidally dispersed and are synthesized using wet chemical methods. A *colloid* is a system consisting of a "dispersed phase [which is] distributed uniformly [and] in a finely divided state [with]in a dispersion medium".[62] A familiar example of an everyday colloid is milk, which consists of fat droplets (liquid discontinuous phase) dispersed in water (liquid continuous phase). In the case of colloidal NCs, the dispersed phase is a solid (the semiconductor itself and its stabilizing ligands), and the dispersion medium can be either an organic or aqueous solvent (Figure 2.8).

Colloidal NCs are synthesized by decomposing organometallic precursors (*e.g.* selenourea[60,63]) and/or inorganic salts (*e.g.* lead oleate[64], lead halides[65] or cadmium myristate[8]), which contain the elements that make up the NC and are referred to as its *precursors* (see Subchapter 2.2.1).[66] Similar to how the fat droplets in milk are stabilized by fatty acids, colloidal NCs are typically stabilized by amphiphilic surfactants or ligands (Figure 2.8).[67] These ligands can be added to the synthesis or be used directly as the dispersion medium/the reaction solvent. The importance of ligands for synthesising NCs, and for understanding and using their unique properties, is discussed further in Subchapter 2.2.2.

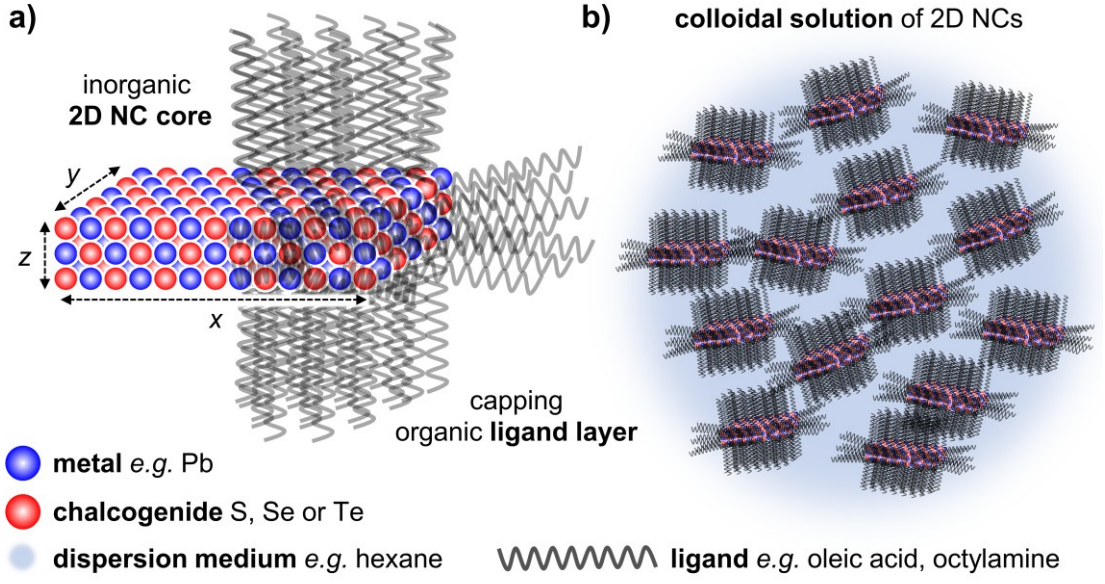

Figure 2.8. (a) Simplified schematic representation of a single 2D PbX NC capped by organic ligands and (b) a colloidal solution of 2D NCs.

The fundamental idea for producing high quality NCs, *i.e.* those with a narrow size distribution, is to separate the nucleation of stable NC nuclei from their growth toward the final NCs (LaMer model).[68] The nucleation and growth rates depend on the various reaction parameters, such as the temperature, the precursor reactivity, amount/concentration, and addition method, as well as the ligand(s) and solvent(s) used, and many other factors.[66] This high degree of complexity opens up a wide range of possibilities and makes colloidal synthesis a versatile method for producing NCs with drastically different compositions, sizes, and shapes.

The following subchapters will provide a brief overview of common NC synthesis methods, discuss the role of surface ligands, and then narrow the scope from spherical NCs to 2D NCs, and from syntheses at elevated temperature to the low-temperature synthetic methods employed for the 2D PbX NCs in this thesis.

2.2.1 Colloidal Synthesis

A common technique for the colloidal synthesis of semiconductor NCs is the *hot injection method*. Here, nucleation and growth are separated by rapidly injecting a (cold) precursor solution into a heated coordinating solvent (mixture). When the precursors are injected, the temperature in the reaction vessel drops and a supersaturated solution is formed. The precursors then begin to decompose and monomers start to accumulate. As the monomer concentration rises, the nucleation threshold is quickly reached resulting in a short *nucleation burst*, which drastically reduces the supersaturation and causes the nucleation rate to drop close to zero. From that point onward, the formed nuclei grow up to a certain size and shape which are determined by the reaction conditions. Following this strategy, all NC nuclei ideally begin growing simultaneously and under the same growth conditions, resulting in NCs with a narrow size distribution and uniform properties.[66,68,69] In reality, the nucleation burst is not a single event, but rather occurs over a certain period during which nucleation an growth happen simultaneously, so that minimizing this time frame and its relative length compared to the growth process is key to obtaining NCs of uniform size.[70] A well-known example of the hot injection method is the synthesis of nearly monodisperse CdSe NCs by Murray *et al.*[71] In short, dimethylcadmium and tri-*n*-octylphosphine selenide are dissolved in tri-*n*-octylphosphine (TOP), mixed in a syringe, and

rapidly added to a heated flask of tri-*n*-octylphosphine oxide (TOPO) (solvent and surfactant). This results in TOP/TOPO-capped CdSe NCs of increasing size, ranging from 15 to 115 Å, depending on their growth time. Examples of syntheses of 2D NCs will be discussed in the following Subchapters 2.2.3 and 2.3.

A second synthetic approach is the so-called *heat-up method*.[72] Here, the precursors, ligands and solvents are combined at room temperature and collectively heated up. This method can yield NCs with narrow size distributions when nucleation and growth occur at different temperatures. The heat-up method is particularly appealing for large-scale syntheses of NCs.[72]

A key parameter characterizing the formation of colloidal NCs is the critical radius of NC nuclei given by:[73]

$$r_{\mathrm{crit}} = \frac{2\gamma v}{k_{\mathrm{B}} T \ln S} \qquad \text{(Eq. 2.13)}$$

with the surface energy γ, the molar volume v, the BOLTZMANN constant k_{B}, the temperature T and the supersaturation of the solution S. When a formed nucleus reaches the critical radius, the probabilities of redissolution and growth are equal, *i.e.* for $r_{\mathrm{nuclei}} < r_{\mathrm{crit}}$ nuclei redissolve to monomers while for $r_{\mathrm{nuclei}} > r_{\mathrm{crit}}$ nuclei survive and grow into final NCs.[66,73] Equation 2.13 expresses that r_{crit} is inversely proportional to T and $\ln S$, which means that at higher temperatures and supersaturations, the nucleation burst occurs at an earlier stage. In addition, the dependence of r_{crit} on the supersaturation/monomer concentration also influences the subsequent growth phase. The growth of NCs can be divided into two distinct steps: (1) the diffusion of monomers to a formed nucleus and (2) the reaction of monomers at the nucleus surface. Depending on which of these two processes is the rate-limiting step (*i.e.* the slower of the two), the growth mode is called either *diffusion-controlled* or *reaction-controlled*.[70] When the diffusion rate limits the growth and the supersaturation is high ($S \gg 1$ and r_{crit} is small), the reaction is in the *size focusing* regime: All NCs grow, with the smaller ones growing faster than the large NCs, resulting in a gradual narrowing of the size distribution. Conversely, under reaction-controlled conditions (r_{crit} is large), smaller NCs dissolve and larger ones grow at their expense.[70] This process is known as *OSTWALD ripening* and will be relevant for the discussion of monolayer-defined PbSe fQDs in Chapter 7.[13]

2.2.2 Ligands and the Surface of Nanocrystals

In a bulk material, the majority of atoms are located in its interior and are chemically bound to their neighboring atoms according to the material's chemical composition, their oxidation state and the crystal structure. In contrast, NCs have a large surface-to-volume ratio, with a significant fraction of their atoms being surface atoms with broken bonds – *i.e.* empty orbitals or lone-pair electrons – commonly referred to as *dangling bonds*.[43,74,75] As a consequence, the chemistry and physics of NCs are largely determined by their surface. In the foregoing chapters, the ligands/surfactants covering the surface of NCs have already been alluded to several times and their importance cannot be overstated. Ligands dictate fundamental aspects of the NCs, such as their colloidal stability and dispersability (see Chapter 4 and 5).[10] Ligands influence the optical properties, for example PL position and intensity, PLQY and average PL lifetimes (see Chapter 3).[11,43,76–78] They affect the electronic states within the NC core[79,80] and are crucial for many device applications, *e.g.* by making NC films either conductive or insulating.[81,82] Ligands also alter the magnetic[83] and catalytic[84] properties of NCs. Finally, ligands are a tool to control the shape of NCs during synthesis.[75,85,86] This exemplary list is far from exhaustive, but it clearly shows that understanding and controlling the inorganic-organic interface of NCs and their ligands is central to nanochemistry.[74,75]

Ligands dynamically bind to the surface of NCs.[75] A common stabilizing system used in NC syntheses is the combination of oleic acid and a primary amine, often octyl- or oleylamine.[10,60,61,67] Both compounds contain a simple functional head group, consisting of heteroatoms, and a long, non-polar hydrocarbon tail (Figure 2.9). This motif is typical of most classical NC ligands.

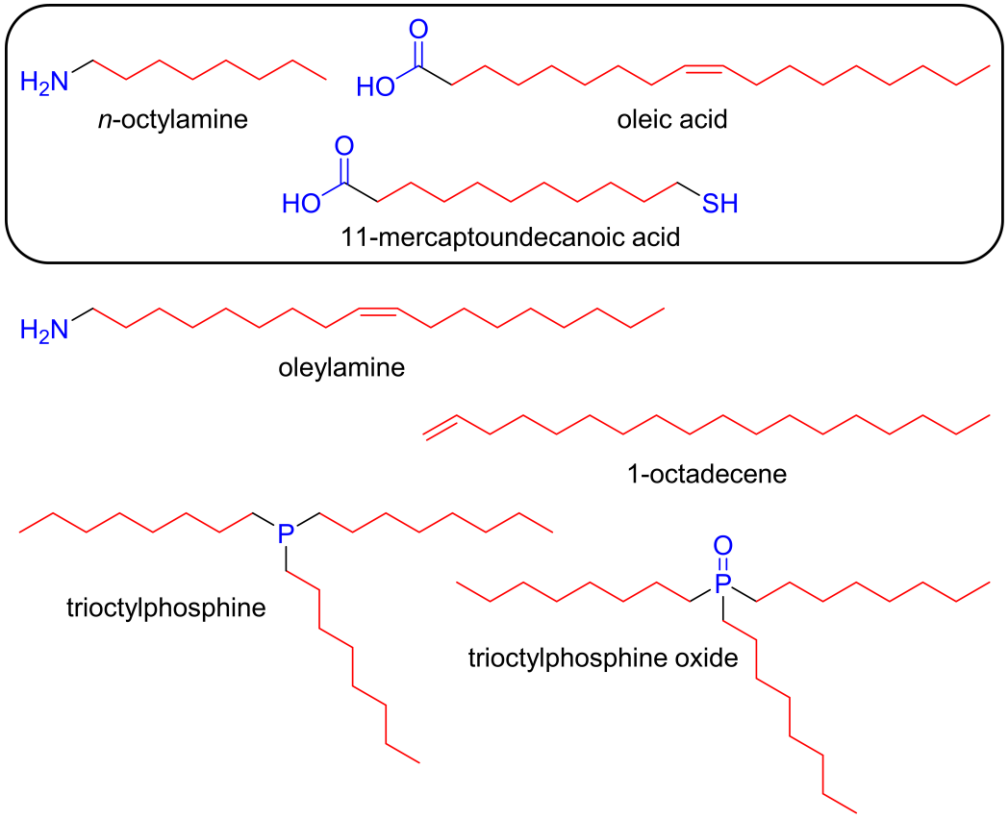

Figure 2.9. Organic ligands used for the 2D PbX NCs in this thesis (circled) shown alongside other exemplary classical NC ligands.

The headgroup anchors to the NC surface by forming a covalent or dative (coordinative) bond, and the aliphatic tail group points toward the solution and away from the NC.[74,75] This lipophilic ligand shell arrangement provides solubility in non-polar organic solvents (*e.g.* hexane) and the steric demand of the hydrocarbon tails represents a steric barrier preventing agglomeration of the NCs. Adding an antisolvent of opposite polarity reduces the efficiency of steric stabilization, causing the NCs to flocculate and to precipitate from the colloidal solution.[71] This phenomenon is often exploited to purify as-synthesized NCs from unreacted precursors or to transfer NCs from one solvent to another. The destabilized organic colloidal NC solution is then centrifuged, which results in partial or full precipitation of the NCs. Subsequently, the supernatant is discarded and the NCs are redispersed in a solvent of choice (*e.g.* from hexane to toluene). The flocculation of NCs is size and shape dependent. For well-defined and established NC systems, careful selective precipitation can be used to *e.g.* separate spherical QDs from 2D NPLs.[87]

Apart from the effective oleic acid and amine ligand system, a huge variety of ligands of different complexity has been used to tailor NCs for different functionalities and applications.[74,75] This diversity of compounds can be broken down using the covalent bond classification method, categorizing ligands based on their interaction with the NC surface into three groups (Figure 2.10):[88–90]

a. X-type ligands are anionic one-electron donors that form covalent bonds with under-coordinated surface sites that can provide one electron.
   e.g. halides X^-, carboxylates RCO_2^- or thiolates RS^-
b. L-type ligands are neutral LEWIS bases that donate two electrons to an empty orbital of a surface metal atom, forming a dative bond.
   e.g. primary amines RNH_2, tertiary phosphines (oxides) $R_3P(O)$
c. Z-type ligands are neutral, two-electron acceptors (LEWIS acids) that form dative bonds with the lone-pair electrons of electron-rich LEWIS basic surface sites (*e.g.* chalcogenide surface atoms).
   e.g. metal carboxylates $M(RCO_2)_n$, metal halides MX_n

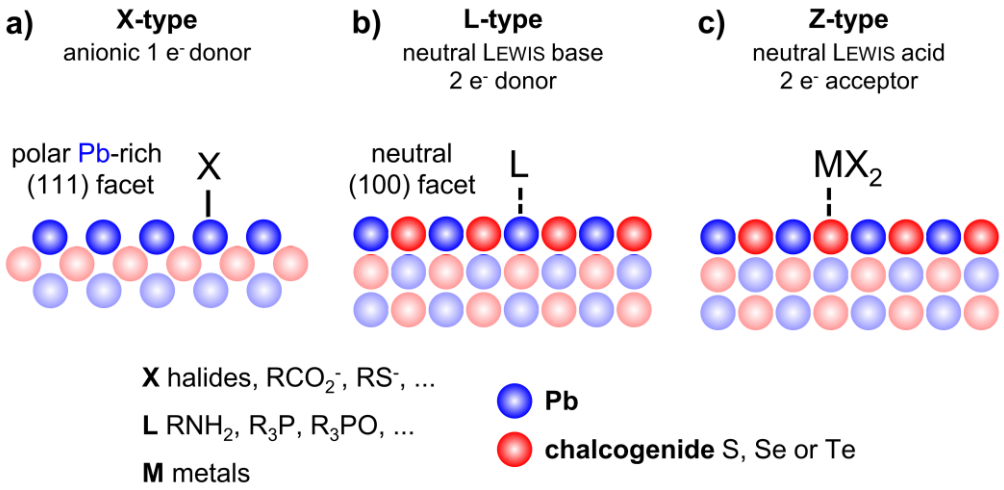

Figure 2.10. Ligand binding types on a model polar (111) and neutral (100) lead chalcogenide surface. (own representation based on Ref. [88,91–93])

Specific NC properties, such as a high PLQY[11,43] or solubility in polar solvents,[94] are often achieved by replacing the native ligands bound to an as-synthesized NC surface with different ones after the synthesis. These ligand exchange reactions occur *via* a dissociative mechanism, whereby a bound ligand detaches from the surface and is replaced by another ligand from solution.[74] Ligand exchange is

favored when the incoming ligands are in large excess and have a higher affinity to the NC surface compared to the leaving ligands. The affinity of ligands for a NC can be reasonably assessed by applying the *hard-soft acid-base* (HSAB) theory.[95] Here, strong bonds are formed between hard-hard and soft-soft combinations of LEWIS acid-base pairs, while mismatched pairings lead to weak interactions. This theory will be revisited in the context of the surface passivation method of PbSe NPLs presented in Chapter 3.[11]

Understanding the different types of ligands and ligand exchange reactions, one can better understand the aforementioned concept of applying surface treatments to address surface-related electronic trap states that form within the band gap of NCs (see Subchapter 2.1.4 and Chapter 3).[11] From a surface chemistry point of view, dangling bonds in as-synthesized NCs may be caused by at least one of two factors: (1) the absence of suitable ligands to address the respective surface sites (*e.g.* X- and L-type ligands used during synthesis cannot address negative LEWIS basic chalcogenide surface atoms), or (2) surface sites that cannot be saturated due to steric hindrance limiting the surface coverage of the NCs. In both cases, introducing a Z-type ligand can solve the issue. For instance, a metal halide MX_n can form a dative bond with negative chalcogenide surface sites *via* empty metal orbitals (1), and is less sterically demanding than most native ligands, which results in an overall more complete surface coverage (2).[11]

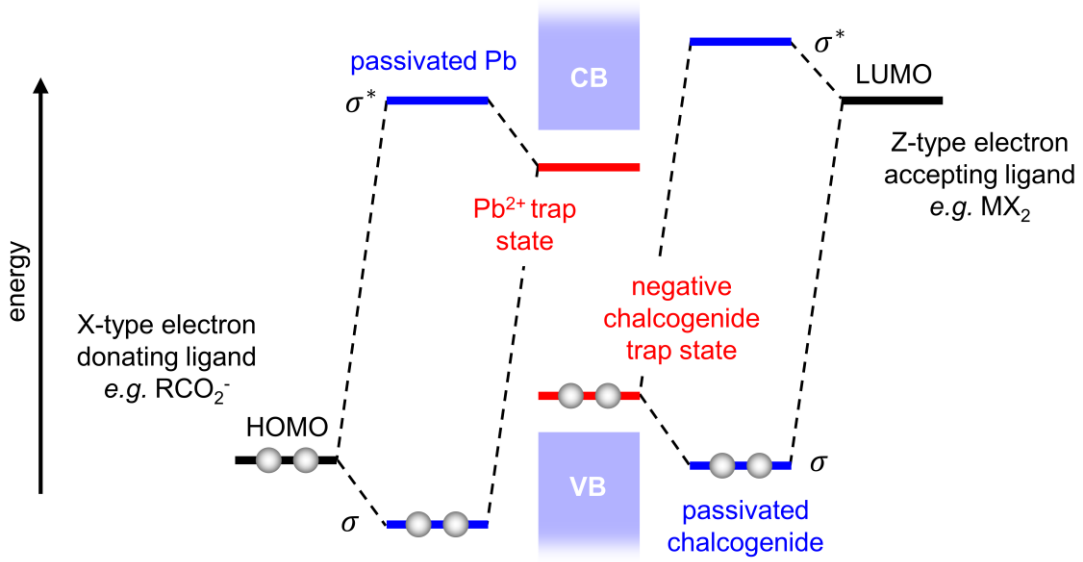

Figure 2.11. Molecular orbital diagram for the passivation of trap states in a PbX NC using X- and Z-type ligands. (own representation based on Ref. [74])

In a simplified picture of molecular orbital theory, this step can be understood as the hybridization of the occupied negative chalcogenide trap state (HOMO, which may lie slightly above the valence band) and the higher-energy LUMO of the MX_n ligand, forming a bonding σ and anti-bonding σ* molecular orbital (Figure 2.11). The formed σ and σ* orbitals then lie below and above the valence and conduction band edges, respectively, which means that the trap state is pushed outside the band gap as a result of the ligand binding.[74] This is reflected in an overall higher PLQY of surface treated NC samples. For example, KIRKWOOD *et al.* have used a $CdCl_2$ treatment to increase the PLQY of CdSe (0.3 to 12 %), CdS (8 to 20 %), InP (0.7 to 11 %) and In(Zn)P QDs (0.4 to 18 %).[11,43,61] In Chapter 3 a similar procedure for 2D PbSe NPLs is presented.[11] In addition to an increase (or change) in PLQY, ligand exchange in NCs can result in shifts of the absorption and PL features of the materials. For example, using metal halides to replace carboxylates such as oleic acid results in a *bathochromic shift* of the absorption and PL (*i.e.* a shift to higher wavelengths/smaller energies). This can be rationalized by considering the electronegativity of the ligands. Halides are more electronegative than carboxylates, which reduces the electron density within the NCs and the degree of quantum confinement in the structures.[11,96] Furthermore, replacing ligands can affect the shape/linewidth of PL signals as well as the measured average PL lifetimes. When a NC exhibits multiple radiative recombination pathways the ensemble PL signal is composed of two or more GAUSSIAN contributions. For example, suppressing a defect emission pathway by pushing the trap state that causes it outside the band gap decreases the contribution/area of one of the GAUSSIANS, resulting an overall narrower (lower fwhm) and more symmetric PL signal.[61] Similarly, the average biexponential PL lifetime in such cases increases after surface passivation, as the contribution of faster trap state emission is reduced (lower amplitude fraction).[10,11]

The steric stabilization of NCs by amphiphilic ligands was briefly explained above for the example of oleic acid and an amine. A steric barrier formed by long-chain organic compounds prevents agglomeration of NCs due to VAN DER WAALS forces and ensures solubility in non-polar solvents.[71] The second fundamentally different approach to stabilizing NCs is electrostatic static stabilization using inorganic ions. The TALAPIN group and coworkers pioneered using molecular metal chalcogenides, such as $Sn_2S_6^{4-}$, as well as metal-free inorganic ligands, *e.g.* (hydro)chalcogenides

HS^{2-}/S^{2-}, which stabilize NCs in polar solvents.[81,82,97,98] This approach is particularly interesting for producing conductive NC films for electronic applications.[99] Regardless, solubility in polar solvents can also be achieved with sterically stabilized NCs. The native ligands can be exchanged for bifunctional surfactants, with one headgroup that has a high affinity to the NCs and a second hydrophilic headgroup that can provide solubility in aqueous media. A common choice are mercaptocarboxylic acids, with the thiol/sulfur side adhering to the NC surface and the carboxylate headgroup directed toward solution, which ensures the solubitlity.[100–103] This idea was adopted for the water transfer of 2D PbX NCs presented in Chapter 5.

2.2.3 Symmetry Breaking: Growth Mechanisms of 2D Nanocrystals

Synthesizing 2D NCs from materials without inherent anisotropy yields NCs that are not in their thermodynamic equilibrium shape.[104] For example, cubic PbSe preferably grows in 3D due to its isotropic surface energy, whereas MoS_2 naturally grows in 2D due to its layered-structure. For the former materials, a driving force is required to break the symmetry and initiate and sustain the anisotropic growth. Depending on the approach, the material, and the exact synthetic parameters, there have been different growth mechanisms proposed and conducted. Some of these mechanisms rely heavily on ligand interactions, while others can explain and predict the formation of 2D NCs independently from ligand interactions. The published concepts can be grouped into three categories: oriented attachment of spherical NCs or NC intermediates, an intrinsic growth instability in isotropic materials, and template pathways, or combinations of these mechanisms. This subchapter provides an overview of growth mechanisms of 2D NCs, focusing on lead chalcogenides (cubic rock-salt structure) and cadmium chalcogenides (zinc-blende structure (cubic) or wurtzite (hexagonal)).

Oriented attachment refers to the facet-specific agglomeration of NCs with aligned crystalline orientations, which results in the formation of larger super-structures (here nanosheets, Figure 2.12).[105]

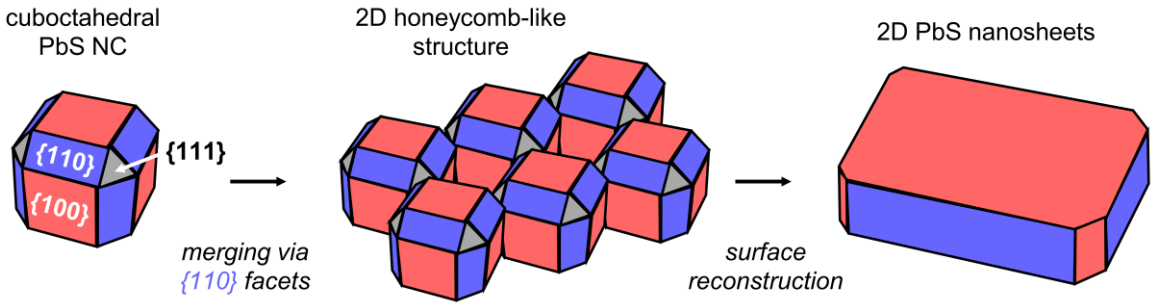

Figure 2.12. Schematic representation of the oriented attachment of PbS NCs into 2D PbS NSs, as reported by SCHLIEHE *et al.*[106] Cuboctahedral PbS NCs fuse *via* their reactive {110} facets forming a honeycomb structure, which then undergoes surface rearrangement to form single-crystal NSs. (own representation based on Ref. [106])

For example, SCHLIEHE *et al.* reported the oriented attachment of nearly spherical PbS nanoparticles (d = 2.8) into thin single-crystal nanosheets with hundreds of nanometers in lateral size.[106] The PbS NCs used exhibit a cuboctahedral shape with 12 energetically unfavorable {110} facets. In the presence of lead-complexing chloride-containing solvents, these facets stabilize by merging into 2D honeycomb-like structures, which subsequently undergo surface reconstruction to form 2D NSs. The decisive driving force behind the formation of a 2D structure over a 3D honeycomb network are ordered oleic acid ligands on the 6 {100} facets of the NCs. The formation of single-crystal 2D NSs allows the oleic acid layer to assemble in a densely packed and highly ordered phase on the {100} basal planes of the NSs. This means that the 2D growth, initiated by the minimization of high-energy surfaces, is driven by the release of adsorption enthalpy from the ligands, as well as by the stabilization from the VAN DER WAALS forces between the hydrocarbon tails of oleic acid.[106] Following this work, CHEN *et al.* investigated the feasibility of a similar mechanism for the formation of zinc-blende structured 2D CdSe NCs.[107] The authors used purified CdSe QDs (d = 1.8 nm) as seeds for 5.5 ML CdSe NPLs (6 ML Cd and 5 ML Se) with lateral dimensions of ~45 x 8 nm^2. Based on absorbance and transmission electron microscopy (TEM) measurement, they demonstrate a particle attachment mechanism with two distinct early steps: 1. "single-dot intermediates" and 2. "2D embryos" (Figure 2.13). Single-dot intermediates form in the presence of long-chain cadmium fatty acids through intraparticle ripening, transforming isotropic 1.8 nm CdSe NCs into 2D NCs (2.0 x 2.0 1.5 nm^3) with stable {100} and reactive {110} facets. 2D embryos are then formed by the oriented

attachment of two single-dot intermediates *via* the {110} facets. From there on the symmetry is broken and single-dot intermediates further attach to a growing 2D embryo *via* a {110} facet while the other facets of the formed 2D NC reconstruct into stable {100} facets.[107]

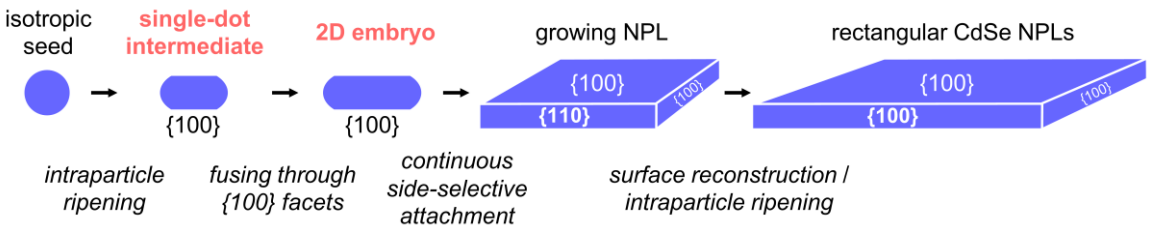

Figure 2.13. Two-step symmetry-breaking mechanism for the formation of zinc-blende CdSe NPLs by CHEN *et al.* The first symmetry-breaking originates from intraparticle ripening toward single-dot intermediates. The two lateral directions are then differentiated by the formation of {100} and {110} facets (with different reactivity) during the side-selective attachment to the growing NPLs (2nd symmetry breaking). (own representation based on Ref. [107])

Both examples highlight that oriented attachment is a complex process in which ligands (here oleic acid and cadmium carboxylates, resp.) play a major role, as their binding energy and density is facet specific.[105]

In their early work on the formation of colloidal 2D zinc-blende CdSe NPLs, ITHURRIA *et al.* described the continuous transition of spherical CdSe NCs that laterally extend toward 2D NPLs.[108] The authors demonstrated that CdSe NPL formation starts with small ~2 nm NCs, which gradually convert into CdSe NPLs with a thickness that is fixed by the diameter of the initially formed NCs. Through TEM characterization, they excluded oriented attachement or similar 2D self-assembly mechanisms of the NCs as possible growth mechanisms. Furthermore, by conducting seeded-growth experiments starting from laterally smaller CdSe NPLs, it was shown that this continuous growth occurs through the continuous reaction of the Cd and Se precursors at the edges of the NPLs. Later, the NORRIS group and coworkers developed a model for 2D growth based on an *intrinsic growth instability* in isotropic materials, which notably rationalizes the findings by ITHURRIA *et al.* by considering fundamental growth kinetics (Figure 2.14).[109,110]

This concept can describe and predict the formation of zinc-blende CdSe NPLs (as well as CdS, CdTe, and FeS_2 NPLs) without considering different ligands or ligand templating.

The authors found that CdSe NPLs can form in completely isotropic environments, require only one type of cadmium carboxylate and that they can form in melts of the precursors, where growth is not limited by the diffusion of the reactants. From there an island-nucleation-limited growth model is derived to explain the anisotropic shape of the NPLs. Accordingly, NC growth requires the nucleation of a new "island" on one its facets. Once this island reaches a critical size, it becomes stable and thermodynamics drive the growth into a complete added layer on that facet. The nucleation barrier for such a new island is significantly lower on narrow facets with a size smaller than the critical island size. This means that growth on small side facets is faster than on the large planar surfaces of a forming increasingly two-dimensional NPL.[109] Notably this model assumes fast diffusion of precursors to the growing island, whereas diffusion is a non-negligible factor in classical colloidal NC syntheses.[73]

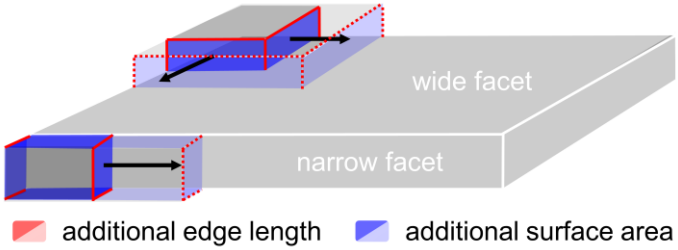

Figure 2.14. Comparison between growth of a new layer on a wide and a narrow facet of a NC. On wide facets, the nucleation barrier for a new island is given by the critical island size. Once this barrier has been overcome, the new island preferably nucleates in one of the corners, and spanning the entire facet requires additional edge energy (shown in red). In contrast, an island on a narrow facet with a thickness below the critical island size has a reduced nucleation barrier and can grow to cover the entire facet without additional edge energy, resulting in island-nucleation-limited 2D growth toward NPLs. (own representation based on Ref. [109])

The intrinsic growth instability model successfully explains the small range of accessible NPL thicknesses for zincblende CdSe; as soon as the narrower facet exhibits a width equal to or above the critical island size for a bulk surface, the

kinetic instability as the driving force for 2D growth disappears. Similarly, the formation of 2D cubic PbX NCs in this thesis could be caused by an intrinsic instability in growth kinetics.

Template pathways are based on breaking the crystal symmetry by growing NCs within bilayers of organic molecules (often amines), which guide crystallization toward a 2D shape (Figure 2.15). These templates are sometimes referred to as double lamellar structures, bilayer mesophases, planar galleries, or soft colloidal templates, with the basic mechanism being the same in all cases: 2D growth is enforced and driven by an external template that self assembles in solution.[85,111–116]

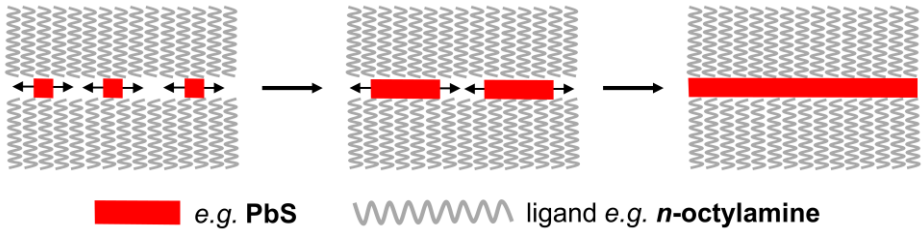

Figure 2.15. Growth of PbS NSs within a double lamellar *n*-octylamine template. (own representation based on Ref. [85])

An apparent similarity among syntheses that follow a template pathway are the comparatively low reaction temperatures. For instance, the above-mentioned oriented attachment synthesis of 2D CdSe NCs by CHEN *et al.* is performed at 250°C, whereas templated syntheses are carried out only slightly above room temperature. At these low temperatures the molecular motion is reduced and the bilayer templates can form and are more rigid than at elevated temperatures. LIU *et al.* reported a lamellar assembly pathway for the formation of 2D CdSe quantum belts *via* intermediate magic-sized nanoclusters $(CdSe)_{13}$ (*magic-size clusters* are crystallites with a discrete and countable number of atoms, with particularly stable structure[117]).[112] Using X-ray diffraction, the authors found reflections corresponding to a lamellar template assembly when dissolving cadmium acetate in *n*-octylamine at 68 °C. The alternating $Cd(OAc)_2$(*n*-octylamine)$_x$ layer structure consists of $Cd(OAc)_2$ galleries, with the amines coordinated to their outer planes *via* the amine head group. The interlayer

d-spacing between the $Cd(OAc)_2$ galleries (2.61 nm) is determined by the chain length, the tilt angle and the interpenetration fraction of the aliphatic hydrocarbon chain of the amine.[112,117] Adding selenourea at 20 – 25°C results in the formation of $(CdSe)_{13}$ clusters, which then fuse into flat quantum belts (at 64 – 85°C) that exhibit a 2D shape and dimensions predetermined by the template. MORRISON *et al.* revealed a similar soft template mechanism for the growth of 1 nm thick PbS quantum platelets in *n*-octylamine at 40°C.[85] For a mixture of $Pb(OAc)_2{\cdot}3H_2O$ and *n*-octylamine, the authors measured a periodicity of 2.78 nm in low-angle X-ray diffraction experiments, concluding on the formation of a lamellar mesophase with pseudoplanar reaction galleries containing Pb^{2+}. By combination with absorbance measurements, a template-growth pathway of three steps is proposed: 1. Nucleation occurs at a random position within the template; 2. Lateral growth within the template; and 3. Overlap of quantum platelets at large lateral sizes within the template leads to electronic coupling between platelets.[85] In the same publication, MORRISON *et al.* revisited the previously discussed PbS NS synthesis by SCHLIEHE *et al.*,[106] which follows an oriented attachment mechanism. MORRISON *et al.* found that the oleates used can (in priniciple) form mesophase bilayers similar to those of amines and bring up the idea that lamellar templates could serve as 2D galleries for the oriented attachment of the PbS NCs. Furthermore, they conclude that a template mechanism should always be considered when synthesizing NC with a 2D shape are synthesized, given their findings and the numerous reports on the subject.[85,111–116] The 2D PbX NCs discussed in this thesis are synthesized at low temperatures in mixtures of oleic acid and *n*-octylamine.[61] It is therefore conceivable that symmetry breaking in these syntheses could also occur *via* a template pathway similar to those described above.

The following chapter focuses solely on lead sulfide, selenide and telluride NCs and provides basic material properties that are relevant to the results presented in the subsequent chapters.

2.3 2D Lead Chalcogenide Nanocrystals

Lead chalcogenides are inorganic compounds made of lead (group IV, [Xe]$4f^{14}5d^{10}6s^26p^2$) and an element from the chalcogenide group (group VI, *e.g.* Se: [Ar]$3d^{10}4s^24p^4$). Their general formula is PbX (X = S, Se, Te), with lead in oxidations state +II and the chalcogenide in state -II. PbS, PbSe and PbTe all crystallize in the cubic rock salt (or NaCl) structure (space group $Fm\bar{3}m$, Figure 2.16).[17] Here, one of the ions forms a face-centered cubic lattice and the counterions occupy the octahedral holes. In this arrangement, all ions are octahedrally coordinated, surrounded by six of the respective counterions. Hence, the lattices are characterized by a single lattice constant a, which corresponds to twice the distance between Pb^{2+} and X^{2-}: 5.936 Å for PbS, 6.124 Å for PbSe and 6.462 Å for PbTe (all at ~300 K).[17]

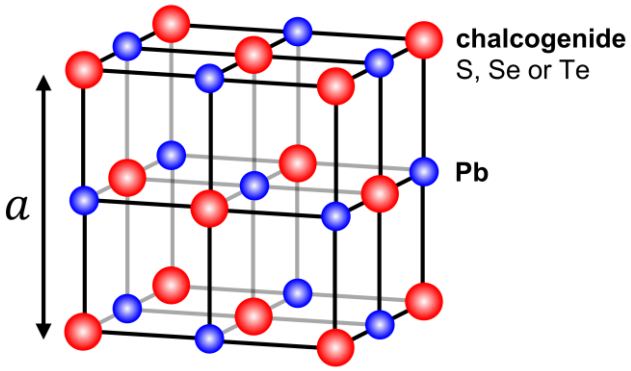

Figure 2.16. Cubic rock salt structure of lead chalcogenides. (own representation based on Ref. [118])

Besides the NaCl structure, lead chalcogenides can crystallize in an orthorhombic structure, obtainable through a polymorphic transition at high pressures.[17] Notably, this structure was found by KHAN *et al.* for colloidal PbS NPLs, however, as the authors themselves stated, this is not expected generally and rather uncommon.[119,120] Furthermore, PbTe can undergo a structural phase transition to a rhombohedral structure at cryogenic temperatures.[17]

All three compounds in their cubic crystal structure exhibit a direct narrow band gap (PbS: 0.42 eV; PbSe: 0.28 eV; PbTe: 0.31 eV – all at RT)[17,28] with the maximum (minimum) of valence (conduction) band located at the L point of the BRILLOUIN zone.[17] Furthermore, lead chalcogenides exhibit large exciton Bohr radii, which

increase down the row of chalcogenides (see Table 2.1). The effective masses of electron and hole are low and very similar, which means that quantum confinement is "shared" approximately equally between the two charge carriers.[2,29] This is rather uncommon and renders lead chalcogenides prime candidates for studying extreme confinement (see Chapter 7).[13,29]

2.3.1 Lead Sulfide Nanocrystals

Early wet chemical syntheses of PbS NCs were conducted in the mid to late 1980s using aqueous solutions of *e.g.* lead nitrate and sodium sulfide in acetonitrile in the presence of ethylene glycol.[121,122] These aqueous routes largely did not yield emissive PbS NCs (with later exceptions by *e.g.* LIFSHITZ *et al.*[123] and BAKUEVA *et al.*[124]). Nonetheless, size-dependent changes in the absorption of the crystallites were investigated as early examples of quantum confinement.[2,121] The first synthesis of PbS NCs in a hot coordinating organic solvent (hot injection method) was reported by HINES *et al.* in 2003.[125] The authors used *in situ*-generated lead oleate and bis(trimethylsilyl)sulfide in a mixture of oleic acid, ODE and TOP, yielding NIR luminescent PbS NCs with tunable lowest-energy exciton transition between 800 and 1800 nm. Subsequently, the optical properites of PbS QDs were thoroughly studied.[2] ELLINGSON *et al.* reported ultra-efficient multiple exciton generation in PbS (and PbSe) QDs, which is interesting for improving solar cell efficiency.[126]

Narrowing the scope to 2D PbS NCs, *i.e.* nanosheets, quantum platelets, or nanoplatelets, one of the earliest reports is the previously thoroughly discussed oriented attachment synthesis by SCHLIEHE *et al.* (see Subchapter 2.2.3), which yielded 2D PbS NSs that had a minium thickness of 2.2 nm and hundreds of nanometers wide. These NSs exhibit unstructured absorption that is bathochromically shifted compared to the absorption of the NC building blocks (centered at 675 nm). The authors further measured weak PL of NS stacks around 720 nm, which is hypsochromically shifted compared to the NC emission at 790 nm, due to the reduced thickness compared to the diameter of the initial NCs. Subsequently, BIELEWICZ *et al.*[127–129] and BHANDARI *et al.*[130] further investigated oriented attachment toward PbS NSs and found different reaction parameters to fine-tune the thickness of the NSs. These included changes in the oleic acid concentration, the use of different chloro- or other substituted alkanes, reaction

temperature, and precursor ratios. BIELEWICZ *et al.* largely focused on electrical transport measurements in field-effect transistors using individual PbS NS and nanostripes, finding that holes are the majority charge carriers in the fabricated devices and demonstrating *e.g.* high on/off ratios of over 3400 at room temperature.[127,128] Meanwhile, BHANDARI *et al.* reported tunable, albeit weak, PL depending on the thickness of the NSs.[130] Concurrently, direct 2D PbS syntheses were developed with the focus on reducing the thickness of the strucutres to a few atomic layers. One such example is the low-temperature, amine-solvent synthesis of PbS quantum platelets by MORRISION *et al.* (see Subchapter 2.2.3).[85] In addition, KHAN *et al.* synthesized 2D PbS NCs (2 x 200 x 50 nm^3) using the single-source precursor lead hexadecyl xanthate in trioctylamine, and demonstrated their highly stable dieletric properties.[131] Using a different single-source precursor, lead thiocyanate, AKKERMAN *et al.* reported the synthesis of 1.2 nm thick orthorhombic PbS NSs. These NSs did not exhibit any photoluminescence, but were used to fabricate photoconductor devices with high responsivity (0.1 A W^{-1}) and detectivity (1.3 x 10^9 Jones).[132] Later work by KHAN *et al.* shifted the focus to the NIR emission of PbS NPLs.[119] In short, the authors decomposed lead octadecylxanthate in trioctylamine at 80 °C, which underwent a CHUGAEV elimination reaction to yield orthorhombic 2D PbS NPLs. For NPLs with a thickness of 1.8 nm and lateral sizes ranging from 48 x 3.5 to 83 x 21 nm^2 (depending on the reaction time), PL in the range of 735 to 748 nm was measured, though no quantum yield was reported. Shortly after, ANTU *et al.* published a synthesis of few-atom-thick PbS nanoribbons with 5.7% PLQY around ~1300 nm which increases sixfold by 30 day treatment with TOP.[133] Our group first reported a synthesis of laterally small and ultrathin 2D PbS NPLs with sizable PLQY in 2021.[61] This synthesis uses lead oleate and thiourea in a mixture of octylamine and oleic acid at 35°C. It yielded as-synthesized PbS NPLs (1 – 2 x 10 x 7 nm^3) with a QY of 1.4 % centered around 720 nm, which is increased to 19.4 % by post-synthetic surface treatment with $CdCl_2$. Baring minor adjustments, this is the synthetic method that was used for the PbS NPLs throughout this thesis (see Chapter 5 and 6).[7]

The tremendous progress and diversification in the syntheses of 2D PbS nanostructures has naturally led to investigation of their photophysics. AERTS *et al.* reported highly efficient carrier multiplication (CM) of up to 90 % in PbS NSs, *i.e.* most excess photon energy above a certain threshold results in additional electron-

hole pairs.[46] Furthermore, LAUTH *et al.* determined high charge carrier mobilities of 550 – 1000 $cm^2V^{-1}s^{-1}$ for 4 to 16 nm-thick PbS NSs by using THz spectroscopy, which are interesting for thin film optoelectronic applications.[134] MOAYED *et al.* investigated RASHBA-type spin-orbit coupling in PbS NSs, intruiging for possible future spintronic devices.[135] Very recently, TANG *et al.* further reported infrared amplified spontaneous emission from 2D PbS NPLs at a low pump threshold of 76 μJcm^{-2}.[136] Another unique optical property of 2D PbS NPLs is their narrow linearly polarized emission at low temperatures, which will be presented and thouroughly discussed in Chapter 6.[7]

2.3.2 Lead Selenide Nanocrystals

Early syntheses of PbSe NCs were limited to approaches in glass matrices.[2] For instance, LIPOVSKII *et al.* synthesized 2 – 15 nm large PbSe QDs in phosphate glass in 1997.[137] Unlike for PbS NCs, there is no such variety of aqueous synthetic routes available for PbSe NCs (see previous subchapter).[2] Regardless, PbSe NCs were the first lead chalcogenide synthesized *via* the hot injection method by MURRAY *et al.* in early 2001.[138] The authors used lead oleate in diphenylether and TOPSe to obtain NCs with 3.5 to 15 nm in diameter. Shortly after, the first in-depth optical study of PbSe NCs was provided by WEHRENBERG *et al.*[139] and DU *et al.*[140] WEHRENBERG *et al.* presented optical spectra showing well-defined excitonic absorption of PbSe NCs with the lowest energy exciton transition tunable from roughly 1240 to 2480 nm. They also observed band-edge PL in the range of 1200 to 2000 nm, with a small STOKES shift of 22 meV as well as a high PLQY of 85 % at ~1440 nm (determined relatively) and a microsecond lifetime.[139] In the following year, SCHALLER *et al.* used PbSe NCs to fabricate PbSe NC/sol-gel composites and demonstrated optical gain and amplified spontaneous emission at telecommunication wavelengths centered at 1555 nm.[141] Subsequently, PIETRYGA *et al.* synthesized larger PbSe NCs that represent the first colloidal QDs with PL in the mid-infrared, ranging from 2000 to 4100 nm, with PLQYs from 25 to 0.5 % decreasing for positions further in the mid-infrared.[142] As with PbS NCs, ELLINGSON *et al.* reported a high multiple exciton generation efficiency of 300 % for 3.9 nm diameter PbSe QDs at photon energies four times higher than the band gap of the NCs.[126] Similar to PbS, these examples only offer a tiny glimpse into the

rich literature on the photophysics of PbSe NCs.[1,2] The focus in the following will be shifed to 2D PbSe NCs, which have been much less extensively studied.

The first two examples of colloidal 2D PbSe by LEE *et al.*[143] and KOH *et al.*[144] are both based on the oriented attachment of spherical PbSe NCs. LEE *et al.* used ~4 nm PbSe NCs as building blocks to grow PbSe NSs with a thickness of 4.3 nm by oriented attachement *via* the reactive (110) facets in the presence of an excess of oleic acid. The authors further hypothesize that an excess of lead acetate precursor blocks the (100) facets and prevents further growth on these sides.[143] In contrast, KOH *et al.* utilized halide passivation to promote 2D attachment and to tune the thickness of the resulting PbSe NSs (2.2 nm, 4.1 nm and 6.2 nm).[144] Accordingly, the presence of chloride and bromide during the synthesis of the PbSe QD building blocks results in oriented attachement toward NPLs. In contrast, iodide alone does not yield 2D shapes but can produce thicker NPLs when used in combination with one of the other halides. When lead chloride or bromide is used, the (111) and (110) facets of the initial NCs are largely passivated by $PbCl_2$ or $PbBr_2$, respectively. These surface sites can form Pb-Cl-Pb or Pb-Br-Pb bridges that connect and align the NCs along the (100) direction, resulting in the formation of the final NPLs. This works well for Cl^- (and Br^-) as the Pb-Cl (Pb-Br) bond length is similar to the Pb-Se bond, so that chloride (bromide) can occupy selenium positions, whereas iodide cannot. Meanwhile, thickness control using iodide is achieved because it can "reactivate" the amine-passivated (100) facets, allowing a vertical attachment. The obtained PbSe NSs exhibited featureless absorption, with an undefined onset that is shifted to higher wavelengths with increasing NS thickness, as well as weak PL with PLQYs of 0.04 % (for a thickness of 4.1 nm), which likewise shifts with the NSs' thickness.[144] Subsequent approaches toward 2D PbSe by GALLE *et al.* and SALZMANN *et al.* are based on cation exchange from CdSe NPLs.[145–147] In short, cation exchange refers to exploiting a well-established material, *i.e.* CdSe, as an anion host lattice while in a second step replacing the cations with a foreign element, under retention of the NCs' shape (Figure 2.17).

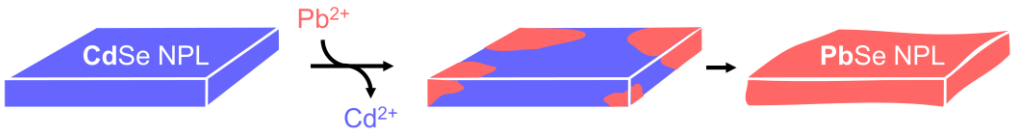

Figure 2.17. Simplified representation of Pb^{2+}-for-Cd^{2+} cation exchange from well-defined CdSe NPLs toward PbSe NPLs with a similar shape. (own representation based on Ref. [147])

Using CdSe NPLs with thicknesses ranging from 3.5 to 6.5 ML, GALLE *et al.* produced PbSe NPLs with four different thicknesses that retained their lateral shape reasonably well. These PbSe NPLs exhibit sizeable, albeit broad and asymmetric, PL features in the range of 1332 to 1545 nm with a PLQY that decreases from 15.3 to 5.1 % for position further in the NIR. The reported PL lifetimes range from 0.7 to 2.7 µs, with no trend observable within the range of NPL thicknesses.[145] In a second publication, the cation exchange procedure was modified to simultaneously exchange the oleate binding to the CdSe NPLs with ammonium iodide. From there a spray-coated photodetector was fabricated, which exhibited fast rise (5 ms) and fall times (10 ms in the visible and 15 ms in the NIR).[146] In 2022, our group reported on the first direct synthesis of colloidal 2D PbSe NPLs (as in no cation exchange or oriented attachment).[60,61] Following the same approach as for the PbS NPL synthesis, lead oleate and selenourea are combined for reaction in a mixture of oleic acid, octylamine and hexane at 0°C. Altering the amount of octylamine used and the reaction temperature enables the control over the lateral size of the PbSe NPLs within the range of ~3.5 x 3 nm^2 to 6.4 x 5.6 nm^2. Higher amounts of octylamine and higher temperatures yield larger lateral NPL sizes. Depending on this lateral size, these NPLs exhibit excitonic absorption in the range of 800 – 1000 nm and PL between 900 and 1450 nm. Post-synthetic $CdCl_2$ treatment of as-synthesized NPLs increases the PLQY from *e.g.* 17.4% to 37.4% (for PL at 980 nm) by saturation of undercoordinated surface sites.[60] This synthesis was further iterated on for the PbSe NPLs synthesized over the course this thesis. Chapter 3 presents and investigates an optimized surface passivation method.[11]

2.3.3 Lead Telluride Nanocrystals

Similar to PbSe, the initial syntheses of PbTe QDs were carried out in glass matrices.[148] The first hot injection syntheses of PbTe NCs were reported almost simultaneously and independently by URBAN *et al.* and MURPHY *et al.* in 2006.[28,149] In the former publication, lead oleate was generated *in situ* in squalene (from lead acetate and oleic acid) was subsequently combined for reaction with TOPTe at 155 – 180°C to prepare PbTe NCs with diameters of 4 – 10 nm, controllable by the oleic acid/lead acetate ratio.[149] MURPHY *et al.* likewise employed *in situ* generated lead oleate in ODE (from lead oxide and oleic acid) and TOPTe at temperatures between 80 – 130°C. The authors obtained 2.6 to 18 nm PbTe NCs, controlling the size *via* the Pb/Te ratio (larger volumes of TOPTe result in smaller NCs), the growth temperature, and the oleic acid/lead ratio. The synthesized PbTe NCs show a first exciton transition between 1009 and 2054 nm and slightly STOKES shifted narrow PL (65 meV shift and 130 meV fwhm for 2.9 nm NCs) with a PLQY in the range of 41 – 52%. Notably, both reports find a size-dependent trasition from spherical/cuboctahedral to cubic PbTe NCs and further highlight the high air and water sensitivity of PbTe NCs. In addition, MURPHY *et al.* demonstrate efficient multiple exciton generation with a QY of 250%, similar to the reports for PbS and PbSe. Furthermore, URBAN *et al.* and MURPHY *et al.* emphasize a few unique fundamental properties of PbTe, that are different from PbS and PbSe: (1) The large average exciton BOHR radius of PbTe (compare Table 2.1), and the low electron ($0.22m_0$) and hole ($0.24m_0$) masses, even amongst lead chalcogenides mean that PbTe is (one of) the semiconductor(s) in which quantum confinement has the biggest influence on its properties. (2) The exciton BOHR radius in PbTe is anisotropic, with $a_{B,PbTe,transversal}$ = 152 nm and $a_{B,PbTe,longitudinal}$ = 12.9 nm.[28] This renders PbTe particularly intriguing for shape engineering.[28,29,149] (3) PbTe is a well-studied material within the thermoelectric community, with a bulk figure of merit *ZT* of 0.4 – 0.45 at 300 K, which is even higher in lower-dimensional structures.[149–151] Despite these interesting and unusual properties of PbTe, no colloidal synthetic methods for producing 2D PbTe had been developed prior to the work presented in Chapter 4 of this thesis, possible reasons for this are discussed in Subchapter 4.2.

2.4 References

(1) Sargent, E. H. Infrared Quantum Dots. *Adv. Mater.* **2005**, *17* (5), 515–522.

(2) Rogach, A. L.; Eychmüller, A.; Hickey, S. G.; Kershaw, S. V. Infrared-Emitting Colloidal Nanocrystals: Synthesis, Assembly, Spectroscopy, and Applications. *Small* **2007**, *3* (4), 536–557.

(3) Lu, H.; Carroll, G. M.; Neale, N. R.; Beard, M. C. Infrared Quantum Dots: Progress, Challenges, and Opportunities. *ACS Nano* **2019**, *13* (2), 939–953.

(4) Houtepen, A. J.; Sargent, E. H.; Infante, I.; Owen, J. S.; Green, P. B.; Schaller, R. D.; Bals, S.; Zeiske, S.; Stöferle, T.; Hens, Z. Colloidal Quantum Dots for Optoelectronics. *Nat. Rev. Methods Primers* **2025**, *5* (1), 1–29.

(5) Harrison, M. T.; Kershaw, S. V.; Burt, M. G.; Rogach, A. L.; Kornowski, A.; Eychmüller, A.; Weller, H. Colloidal Nanocrystals for Telecommunications. Complete Coverage of the Low-Loss Fiber Windows by Mercury Telluride Quantum Dot. *Pure Appl. Chem.* **2000**, *72* (1-2), 295–307.

(6) Kagan, C. R.; Bassett, L. C.; Murray, C. B.; Thompson, S. M. Colloidal Quantum Dots as Platforms for Quantum Information Science. *Chem. Rev.* **2021**, *121* (5), 3186–3233.

(7) Li, P.; Biesterfeld, L.; Klepzig, L. F.; Yang, J.; Ngo, H. T.; Addad, A.; Rakow, T. N.; Guan, R.; Rugeramigabo, E. P.; Zaluzhnyy, I.; Schreiber, F.; Biadala, L.; Lauth, J.; Zopf, M. Sub-millielectronvolt Line Widths in Polarized Low-Temperature Photoluminescence of 2D PbS Nanoplatelets. *Nano Lett.* **2024**, *24* (51), 16293–16300.

(8) Ithurria, S.; Dubertret, B. Quasi 2D Colloidal CdSe Platelets with Thicknesses Controlled at the Atomic Level. *J. Am. Chem. Soc.* **2008**, *130* (49), 16504–16505.

(9) Sichert, J. A.; Tong, Y.; Mutz, N.; Vollmer, M.; Fischer, S.; Milowska, K. Z.; García Cortadella, R.; Nickel, B.; Cardenas-Daw, C.; Stolarczyk, J. K.; Urban, A. S.; Feldmann, J. Quantum Size Effect in Organometal Halide Perovskite Nanoplatelets. *Nano Lett.* **2015**, *15* (10), 6521–6527.

(10) Biesterfeld, L.; Vochezer, M. T.; Kögel, M.; Zaluzhnyy, I. A.; Rosebrock, M.; Klepzig, L. F.; Leis, W.; Seitz, M.; Meyer, J. C.; Lauth, J. Solving the Synthetic Riddle of Colloidal Two-Dimensional PbTe Nanoplatelets with Tunable Near-Infrared Emission. *Chem. Mater.* **2024**, *36* (15), 7197–7206.

(11) Biesterfeld, L.; Klepzig, L. F.; Niebur, A.; Rosebrock, M.; Lauth, J. Toward Bright Colloidal Near-Infrared Emitters: Surface Passivation of 2D PbSe Nanoplatelets by Metal Halides. *J. Phys. Chem. C* **2022**, *126* (45), 19277–19285.

(12) Biesterfeld, L.; Vochezer, M.; Rudolph, D.; Lauth, J. Aqueous Phase Near-Infrared Emitters: Water Transfer of Colloidal 2D PbS, PbSe and PbTe Nanoplatelets. *Nanoscale* **2025**, *17*, 24006–24016.

(13) Biesterfeld, L.; Ngo, H. T.; Addad, A.; Rudolph, D. A.; Leis, W.; Seitz, M.; Ji, G.; Grandidier, B.; Delerue, C.; Lauth, J.; Biadala, L. Monolayer-Defined Flat Colloidal PbSe Quantum Dots in Extreme Confinement. *Nano Lett.* **2025**, *25* (31), 12019–12024.

(14) Böer, K. W.; Pohl, U. W. *Semiconductor Physics*. Springer, **2018**.

(15) Ashcroft, N. W.; Mermin, N. D. *Festkörperphysik*. 3. verbesserte Auflage, Oldenbourg, **2007**.

(16) Borrelli, N. F. Photonic Applications of Semiconductor-Doped Glasses. In *Semiconductor Nanocrystals*: *From Basic Principles to Applications*. Ėfros, A. L., Lockwood, D. J., Tsybeskov, L., Eds., Nanostructure Science and Technology, Springer, **2003**, 1–51.

(17) Madelung, O. *Semiconductors*: *Data Handbook*, 3rd ed., Springer, **2004**.

(18) Allan, G.; Delerue, C. Confinement Effects in PbSe Quantum Wells and Nanocrystals. *Phys. Rev. B* **2004**, *70* (24), 245321.

(19) Koole, R.; Groeneveld, E.; Vanmaekelbergh, D.; Meijerink, A.; de Mello Donega, C. Size and Shape Effects on Semiconductor Nanoparticles. In *Nanoparticles*: *Workhorses of Nanoscience*. 2nd ed., de Mello Donegá, C., Ed., Springer, **2024**, 19–63.

(20) Norris, D. J.; Vlasov, Y. A. Quantum Dot Photonic Crystals. In *Semiconductor Nanocrystals*: *From Basic Principles to Applications*. Ėfros, A. L., Lockwood, D. J., Tsybeskov, L., Eds., Nanostructure Science and Technology, Springer, **2003**, 239–260.

(21) Fox, M. *Optical Properties of Solids*. 2nd ed., Oxford University Press, **2010**.

(22) Christodoulou, S.; Climente, J. I.; Planelles, J.; Brescia, R.; Prato, M.; Martín-García, B.; Khan, A. H.; Moreels, I. Chloride-Induced Thickness Control in CdSe Nanoplatelets. *Nano Lett.* **2018**, *18* (10), 6248–6254.

(23) Brus, L. E. Electron–Electron and Electron-Hole Interactions in Small Semiconductor Crystallites: The Size Dependence of the Lowest Excited Electronic State. *J. Chem. Phys.* **1984**, *80* (9), 4403–4409.

(24) Brus, L. Electronic Wave Functions in Semiconductor Clusters: Experiment and Theory. *J. Phys. Chem.* **1986**, *90* (12), 2555–2560.

(25) García Flórez, F.; Siebbeles, L. D. A.; Stoof, H. T. C. Effects of Material Thickness and Surrounding Dielectric Medium on Coulomb Interactions and Two-Dimensional Excitons. *Phys. Rev. B* **2020**, *102* (12), 125303.

(26) Shornikova, E. V.; Yakovlev, D. R.; Gippius, N. A.; Qiang, G.; Dubertret, B.; Khan, A. H.; Di Giacomo, A.; Moreels, I.; Bayer, M. Exciton Binding Energy in CdSe Nanoplatelets Measured by One- and Two-Photon Absorption. *Nano Lett.* **2021**, *21* (24), 10525–10531.

(27) Hansen, K. R.; Colton, J. S.; Whittaker-Brooks, L. Measuring the Exciton Binding Energy: Learning from a Decade of Measurements on Halide Perovskites and Transition Metal Dichalcogenides. *Adv. Opt. Mater.* **2024**, *12* (3), 2301659.

(28) Murphy, J. E.; Beard, M. C.; Norman, A. G.; Ahrenkiel, S. P.; Johnson, J. C.; Yu, P.; Mićić, O. I.; Ellingson, R. J.; Nozik, A. J. PbTe Colloidal Nanocrystals: Synthesis, Characterization, and Multiple Exciton Generation. *J. Am. Chem. Soc.* **2006**, *128* (10), 3241–3247.

(29) Wise, F. W. Lead Salt Quantum Dots: The Limit of Strong Quantum Confinement. *Acc. Chem. Res.* **2000**, *33* (11), 773–780.

(30) Zhang, J. Z. Interfacial Charge Carrier Dynamics of Colloidal Semiconductor Nanoparticles. *J. Phys. Chem. B* **2000**, *104* (31), 7239–7253.

(31) Rabouw, F. T.; de Mello Donega, C. Excited-State Dynamics in Colloidal Semiconductor Nanocrystals. *Top. Curr. Chem.* **2016**, *374* (5), 58.

(32) Rodà, C.; Macias-Pinilla, D. F.; Di Giacomo, A.; Planelles, J.; Climente, J. I.; Moreels, I. Enhancement of the Biexciton Binding Energy in Laterally Confined CdSe Nanoplatelets. *Nano Lett.* **2025**, *25* (35), 13251–13257.

(33) Chernikov, A.; Berkelbach, T. C.; Hill, H. M.; Rigosi, A.; Li, Y.; Aslan, O. B.; Reichman, D. R.; Hybertsen, M. S.; Heinz, T. F. Exciton Binding Energy and Nonhydrogenic Rydberg Series in Monolayer WS_2. *Phys. Rev. Lett.* **2014**, *113* (7), 76802.

(34) He, X. F. Excitons in Anisotropic Solids: The Model of Fractional-Dimensional Space. *Phys. Rev. B Condens. Matter.* **1991**, *43* (3), 2063–2069.

(35) Efros, A. L.; Brus, L. E. Nanocrystal Quantum Dots: From Discovery to Modern Development. *ACS Nano* **2021**, *15* (4), 6192–6210.

(36) Atkins, P. W.; Paula, J. de. *Atkins' Physical Chemistry*. 8th ed., Oxford University Press, **2006**.

(37) Spoor, F. C. M.; Kunneman, L. T.; Evers, W. H.; Renaud, N.; Grozema, F. C.; Houtepen, A. J.; Siebbeles, L. D. A. Hole Cooling Is Much Faster than Electron Cooling in PbSe Quantum Dots. *ACS Nano* **2016**, *10* (1), 695–703.

(38) Kambhampati, P. Hot Exciton Relaxation Dynamics in Semiconductor Quantum Dots: Radiationless Transitions on the Nanoscale. *J. Phys. Chem. C* **2011**, *115* (45), 22089–22109.

(39) Norris, D. J.; Bawendi, M. G. Measurement and Assignment of the Size-Dependent Optical Spectrum in CdSe Quantum Dots. *Phys. Rev. B* **1996**, *53* (24), 16338–16346.

(40) Trinh, M. T.; Houtepen, A. J.; Schins, J. M.; Piris, J.; Siebbeles, L. D. A. Nature of the Second Optical Transition in PbSe Nanocrystals. *Nano Lett.* **2008**, *8* (7), 2112–2117.

(41) Bertie, J. E. Glossary of Terms used in Vibrational Spectroscopy. In *Handbook of Vibrational Spectroscopy*. Chalmers, J. M., Ed., Wiley, **2002**.

(42) Peng, S.; Wei, Q.; Wang, B.; Zhang, Z.; Yang, H.; Pang, G.; Wang, K.; Xing, G.; Sun, X. W.; Tang, Z. Suppressing Strong Exciton-Phonon Coupling in Blue Perovskite Nanoplatelet Solids by Binary Systems. *Angew. Chem. Int. Ed.* **2020**, *59* (49), 22156–22162.

(43) Kirkwood, N.; Monchen, J. O. V.; Crisp, R. W.; Grimaldi, G.; Bergstein, H. A. C.; Du Fossé, I.; van der Stam, W.; Infante, I.; Houtepen, A. J. Finding and Fixing Traps in II-VI and III-V Colloidal Quantum Dots: The Importance of Z-Type Ligand Passivation. *J. Am. Chem. Soc.* **2018**, *140* (46), 15712–15723.

(44) Klimov, V. I.; Mikhailovsky, A. A.; Xu, S.; Malko, A.; Hollingsworth, J. A.; Leatherdale, C. A.; Eisler, H.; Bawendi, M. G. Optical Gain and Stimulated Emission in Nanocrystal Quantum Dots. *Science* **2000**, *290* (5490), 314–317.

(45) Li, Q.; Lian, T. Area- and Thickness-Dependent Biexciton Auger Recombination in Colloidal CdSe Nanoplatelets: Breaking the "Universal Volume Scaling Law". *Nano Lett.* **2017**, *17* (5), 3152–3158.

(46) Aerts, M.; Bielewicz, T.; Klinke, C.; Grozema, F. C.; Houtepen, A. J.; Schins, J. M.; Siebbeles, L. D. A. Highly Efficient Carrier Multiplication in PbS Nanosheets. *Nat. Commun.* **2014**, *5*, 3789.

(47) Kunneman, L. T.; Tessier, M. D.; Heuclin, H.; Dubertret, B.; Aulin, Y. V.; Grozema, F. C.; Schins, J. M.; Siebbeles, L. D. A. Bimolecular Auger Recombination of Electron–Hole Pairs in Two-Dimensional CdSe and CdSe/CdZnS Core/Shell Nanoplatelets. *J. Phys. Chem. Lett.* **2013**, *4* (21), 3574–3578.

(48) Ahmed, T.; Zha, J.; Lin, K. K.; Kuo, H.-C.; Tan, C.; Lien, D.-H. Bright and Efficient Light-Emitting Devices Based on 2D Transition Metal Dichalcogenides. *Adv. Mater.* **2023**, *35* (31), e2208054.

(49) Caram, J. R.; Bertram, S. N.; Utzat, H.; Hess, W. R.; Carr, J. A.; Bischof, T. S.; Beyler, A. P.; Wilson, M. W. B.; Bawendi, M. G. PbS Nanocrystal Emission Is Governed by Multiple Emissive States. *Nano Lett.* **2016**, *16* (10), 6070–6077.

(50) Sillen, A.; Engelborghs, Y. The Correct Use of "Average" Fluorescence Parameters. *Photochem. Photobiol.* **1998**, *67* (5), 475–486.

(51) Grabolle, M.; Spieles, M.; Lesnyak, V.; Gaponik, N.; Eychmüller, A.; Resch-Genger, U. Determination of the Fluorescence Quantum Yield of Quantum Dots: Suitable Procedures and Achievable Uncertainties. *Anal. Chem.* **2009**, *81* (15), 6285–6294.

(52) Würth, C.; Geissler, D.; Behnke, T.; Kaiser, M.; Resch-Genger, U. Critical Review of the Determination of Photoluminescence Quantum Yields of Luminescent Reporters. *Anal. Bioanal. Chem.* **2015**, *407* (1), 59–78.

(53) van der Bok, J. C.; Dekker, D. M.; Peerlings, M. L. J.; Salzmann, B. B. V.; Meijerink, A. Luminescence Line Broadening of CdSe Nanoplatelets and Quantum Dots for Application in w-LEDs. *J. Phys. Chem. C* **2020**, *124* (22), 12153–12160.

(54) Hu, Z.; Kim, Y.; Krishnamurthy, S.; Avdeev, I. D.; Nestoklon, M. O.; Singh, A.; Malko, A. V.; Goupalov, S. V.; Hollingsworth, J. A.; Htoon, H. Intrinsic Exciton Photophysics of PbS Quantum Dots Revealed by Low-Temperature Single Nanocrystal Spectroscopy. *Nano Lett.* **2019**, *19* (12), 8519–8525.

(55) Lin, K.; Jasrasaria, D.; Yoo, J. J.; Bawendi, M.; Utzat, H.; Rabani, E. Theory of Photoluminescence Spectral Line Shapes of Semiconductor Nanocrystals. *J. Phys. Chem. Lett.* **2023**, *14* (32), 7241–7248.

(56) Voznyy, O.; Levina, L.; Fan, F.; Walters, G.; Fan, J. Z.; Kiani, A.; Ip, A. H.; Thon, S. M.; Proppe, A. H.; Liu, M.; Sargent, E. H. Origins of Stokes Shift in PbS Nanocrystals. *Nano Lett.* **2017**, *17* (12), 7191–7195.

(57) Hu, J.; Li, L.; Yang, W.; Manna, L.; Wang, L.; Alivisatos, A. P. Linearly Polarized Emission from Colloidal Semiconductor Quantum Rods. *Science* **2001**, *292* (5524), 2060–2063.

(58) Di Giacomo, A.; Rodà, C.; Khan, A. H.; Moreels, I. Colloidal Synthesis of Laterally Confined Blue-Emitting 3.5 Monolayer CdSe Nanoplatelets. *Chem. Mater.* **2020**, *32* (21), 9260–9267.

(59) Peric, N.; Lambert, Y.; Singh, S.; Khan, A. H.; Franchina Vergel, N. A.; Deresmes, D.; Berthe, M.; Hens, Z.; Moreels, I.; Delerue, C.; Grandidier, B.; Biadala, L. Van Hove Singularities and Trap States in Two-Dimensional CdSe Nanoplatelets. *Nano Lett.* **2021**, *21* (4), 1702–1708.

(60) Klepzig, L. F.; Biesterfeld, L.; Romain, M.; Niebur, A.; Schlosser, A.; Hübner, J.; Lauth, J. Colloidal 2D PbSe Nanoplatelets with Efficient Emission Reaching the Telecom O-, E- and S-Band. *Nanoscale Adv.* **2022**, *4*, 590–599.

(61) Manteiga Vázquez, F.; Yu, Q.; Klepzig, L. F.; Siebbeles, L. D. A.; Crisp, R. W.; Lauth, J. Probing Excitons in Ultrathin PbS Nanoplatelets with Enhanced Near-Infrared Emission. *J. Phys. Chem. Lett.* **2021**, *12* (1), 680–685.

(62) Everett, D. H. *Basic Principles of Colloid Science*. Royal Society of Chemistry, **1988**.

(63) Campos, M. P.; Hendricks, M. P.; Beecher, A. N.; Walravens, W.; Swain, R. A.; Cleveland, G. T.; Hens, Z.; Sfeir, M. Y.; Owen, J. S. A Library of Selenourea Precursors to PbSe Nanocrystals with Size Distributions near the Homogeneous Limit. *J. Am. Chem. Soc.* **2017**, *139* (6), 2296–2305.

(64) Hendricks, M. P.; Campos, M. P.; Cleveland, G. T.; Jen-La Plante, I.; Owen, J. S. A Tunable Library of Substituted Thiourea Precursors to Metal Sulfide Nanocrystals. *Science* **2015**, *348* (6240), 1226–1230.

(65) Protesescu, L.; Yakunin, S.; Bodnarchuk, M. I.; Krieg, F.; Caputo, R.; Hendon, C. H.; Yang, R. X.; Walsh, A.; Kovalenko, M. V. Nanocrystals of Cesium Lead Halide Perovskites ($CsPbX_3$, X = Cl, Br, and I): Novel Optoelectronic Materials Showing Bright Emission with Wide Color Gamut. *Nano Lett.* **2015**, *15* (6), 3692–3696.

(66) De Mello Donegá, C. Synthesis and Properties of Colloidal Heteronanocrystals. *Chem. Soc. Rev.* **2011**, *40* (3), 1512–1546.

(67) Almeida, G.; Goldoni, L.; Akkerman, Q.; Dang, Z.; Khan, A. H.; Marras, S.; Moreels, I.; Manna, L. Role of Acid-Base Equilibria in the Size, Shape, and Phase Control of Cesium Lead Bromide Nanocrystals. *ACS Nano* **2018**, *12* (2), 1704–1711.

(68) LaMer, V. K.; Dinegar, R. H. Theory, Production and Mechanism of Formation of Monodispersed Hydrosols. *J. Am. Chem. Soc.* **1950**, *72* (11), 4847–4854.

(69) Murray, C. B.; Kagan, C. R.; Bawendi, M. G. Synthesis and Characterization of Monodisperse Nanocrystals and Close-Packed Nanocrystal Assemblies. *Annu. Rev. Mater. Sci.* **2000**, *30* (1), 545–610.

(70) Kwon, S. G.; Hyeon, T. Formation Mechanisms of Uniform Nanocrystals via Hot-Injection and Heat-Up Methods. *Small* **2011**, *7* (19), 2685–2702.

(71) Murray, C. B.; Norris, D. J.; Bawendi, M. G. Synthesis and Characterization of Nearly Monodisperse CdE (E = Sulfur, Selenium, Tellurium) Semiconductor Nanocrystallites. *J. Am. Chem. Soc.* **1993**, *115* (19), 8706–8715.

(72) Park, J.; Joo, J.; Kwon, S. G.; Jang, Y.; Hyeon, T. Synthesis of Monodisperse Spherical Nanocrystals. *Angew. Chem. Int. Ed.* **2007**, *46* (25), 4630–4660.

(73) Thanh, N. T. K.; Maclean, N.; Mahiddine, S. Mechanisms of Nucleation and Growth of Nanoparticles in Solution. *Chem. Rev.* **2014**, *114* (15), 7610–7630.

(74) Boles, M. A.; Ling, D.; Hyeon, T.; Talapin, D. V. The Surface Science of Nanocrystals. *Nat. Mater.* **2016**, *15* (2), 141–153.

(75) Yin, Y.; Alivisatos, A. P. Colloidal Nanocrystal Synthesis and the Organic-Inorganic Interface. *Nature* **2005**, *437* (7059), 664–670.

(76) Singh, S.; Tomar, R.; Brinck, S. ten; Roo, J. de; Geiregat, P.; Martins, J. C.; Infante, I.; Hens, Z. Colloidal CdSe Nanoplatelets, A Model for Surface Chemistry/Optoelectronic Property Relations in Semiconductor Nanocrystals. *J. Am. Chem. Soc.* **2018**, *140* (41), 13292–13300.

(77) Hassinen, A.; Moreels, I.; Nolf, K. de; Smet, P. F.; Martins, J. C.; Hens, Z. Short-Chain Alcohols Strip X-Type Ligands and Quench the Luminescence of PbSe and CdSe Quantum Dots, Acetonitrile does not. *J. Am. Chem. Soc.* **2012**, *134* (51), 20705–20712.

(78) Dufour, M.; Qu, J.; Greboval, C.; Méthivier, C.; Lhuillier, E.; Ithurria, S. Halide Ligands To Release Strain in Cadmium Chalcogenide Nanoplatelets and Achieve High Brightness. *ACS Nano* **2019**, *13* (5), 5326–5334.

(79) Kroupa, D. M.; Vörös, M.; Brawand, N. P.; McNichols, B. W.; Miller, E. M.; Gu, J.; Nozik, A. J.; Sellinger, A.; Galli, G.; Beard, M. C. Tuning Colloidal Quantum Dot Band Edge Positions through Solution-Phase Surface Chemistry Modification. *Nat. Commun.* **2017**, *8* (1), 15257.

(80) Brown, P. R.; Kim, D.; Lunt, R. R.; Zhao, N.; Bawendi, M. G.; Grossman, J. C.; Bulović, V. Energy Level Modification in Lead Sulfide Quantum Dot Thin Films through Ligand Exchange. *ACS Nano* **2014**, *8* (6), 5863–5872.

(81) Kovalenko, M. V.; Bodnarchuk, M. I.; Zaumseil, J.; Lee, J.-S.; Talapin, D. V. Expanding the Chemical Versatility of Colloidal Nanocrystals Capped with Molecular Metal Chalcogenide Ligands. *J. Am. Chem. Soc.* **2010**, *132* (29), 10085–10092.

(82) Kovalenko, M. V.; Scheele, M.; Talapin, D. V. Colloidal Nanocrystals with Molecular Metal Chalcogenide Surface Ligands. *Science* **2009**, *324* (5933), 1417–1420.

(83) Duan, H.; Kuang, M.; Wang, X.; Wang, Y. A.; Mao, H.; Nie, S. Reexamining the Effects of Particle Size and Surface Chemistry on the Magnetic Properties of Iron Oxide Nanocrystals: New Insights into Spin Disorder and Proton Relaxivity. *J. Phys. Chem. C* **2008**, *112* (22), 8127–8131.

(84) Kwon, S. G.; Krylova, G.; Sumer, A.; Schwartz, M. M.; Bunel, E. E.; Marshall, C. L.; Chattopadhyay, S.; Lee, B.; Jellinek, J.; Shevchenko, E. V. Capping Ligands as Selectivity Switchers in Hydrogenation Reactions. *Nano Lett.* **2012**, *12* (10), 5382–5388.

(85) Morrison, P. J.; Loomis, R. A.; Buhro, W. E. Synthesis and Growth Mechanism of Lead Sulfide Quantum Platelets in Lamellar Mesophase Templates. *Chem. Mater.* **2014**, *26* (17), 5012–5019.

(86) Peng, X.; Manna, L.; Yang, W.; Wickham, J.; Scher, E.; Kadavanich, A.; Alivisatos, A. P. Shape Control of CdSe Nanocrystals. *Nature* **2000**, *404* (6773), 59–61.

(87) Tessier, M. D.; Biadala, L.; Bouet, C.; Ithurria, S.; Abecassis, B.; Dubertret, B. Phonon Line Emission Revealed by Self-Assembly of Colloidal Nanoplatelets. *ACS Nano* **2013**, *7* (4), 3332–3340.

(88) Anderson, N. C.; Hendricks, M. P.; Choi, J. J.; Owen, J. S. Ligand Exchange and the Stoichiometry of Metal Chalcogenide Nanocrystals: Spectroscopic Observation of Facile Metal-Carboxylate Displacement and Binding. *J. Am. Chem. Soc.* **2013**, *135* (49), 18536–18548.

(89) Green, M. A New Approach to the Formal Classification of Covalent Compounds of the Elements. *J. Organomet. Chem.* **1995**, *500* (1-2), 127–148.

(90) Owen, J. The Coordination Chemistry of Nanocrystal Surfaces. *Science* **2015**, *347*, 615–616.

(91) Dones Lassalle, C. Y.; Dempsey, J. L. Optoelectronic Properties of PbS Nanocrystals Preserved through L-Type Ligand Surface Reactivity. *Chem. Mater.* **2024**, *36* (19), 9480–9492.

(92) Uppala, V. V. S.; Dones Lassalle, C. Y.; Kelm, J. E.; Camp, A. M.; ter Horst, M. A.; Esker, A. R.; Dempsey, J. L.; Madsen, L. A. Ligand Exchange and Binding at the Surface of PbS Quantum Dots Quantified Using Multimodal Magnetic Resonance. *ACS Nano* **2025**, *19* (30), 27246–27258.

(93) Imperiale, C. J.; Yarur Villanueva, F.; Nikbin, E.; Howe, J. Y.; Wilson, M. W. B. Direct Synthesis of Ultrasmall PbS Nanocrystals Passivated with a Metal-Halide-Perovskite-like Monolayer. *Chem. Mater.* **2024**, *36* (9), 4121–4134.

(94) Lin, Q.; Yun, H. J.; Liu, W.; Song, H.-J.; Makarov, N. S.; Isaienko, O.; Nakotte, T.; Chen, G.; Luo, H.; Klimov, V. I.; Pietryga, J. M. Phase-Transfer Ligand Exchange of Lead Chalcogenide Quantum Dots for Direct Deposition of Thick, Highly Conductive Films. *J. Am. Chem. Soc.* **2017**, *139* (19), 6644–6653.

(95) Pearson, R. G. Absolute Electronegativity and Hardness: Application to Inorganic Chemistry. *Inorg. Chem.* **1988**, *27* (4), 734–740.

(96) Bederak, D.; Balazs, D. M.; Sukharevska, N. V.; Shulga, A. G.; Abdu-Aguye, M.; Dirin, D. N.; Kovalenko, M. V.; Loi, M. A. Comparing Halide Ligands in PbS Colloidal Quantum Dots for Field-Effect Transistors and Solar Cells. *ACS Appl. Nano Mater.* **2018**, *1* (12), 6882–6889.

(97) Lee, J.-S.; Kovalenko, M. V.; Huang, J.; Chung, D. S.; Talapin, D. V. Band-Like Transport, High Electron Mobility and High Photoconductivity in All-Inorganic Nanocrystal Arrays. *Nat. Nanotechnol.* **2011**, *6* (6), 348–352.

(98) Nag, A.; Kovalenko, M. V.; Lee, J.-S.; Liu, W.; Spokoyny, B.; Talapin, D. V. Metal-free Inorganic Ligands for Colloidal Nanocrystals: S^{2-}, HS^{-}, Se^{2-}, HSe^{-}, Te^{2-}, HTe^{-}, TeS_3^{2-}, OH^{-}, and NH^{2-} as Surface Ligands. *J. Am. Chem. Soc.* **2011**, *133* (27), 10612–10620.

(99) Talapin, D. V.; Lee, J.-S.; Kovalenko, M. V.; Shevchenko, E. V. Prospects of Colloidal Nanocrystals for Electronic and Optoelectronic Applications. *Chem. Rev.* **2010**, *110* (1), 389–458.

(100) Wuister, S. F.; Swart, I.; van Driel, F.; Hickey, S. G.; de Mello Donegá, C. Highly Luminescent Water-Soluble CdTe Quantum Dots. *Nano Lett.* **2003**, *3* (4), 503–507.

(101) Tamang, S.; Beaune, G.; Texier, I.; Reiss, P. Aqueous Phase Transfer of InP/ZnS Nanocrystals Conserving Fluorescence and High Colloidal Stability. *ACS Nano* **2011**, *5* (12), 9392–9402.

(102) Kodanek, T.; Banbela, H. M.; Naskar, S.; Adel, P.; Bigall, N. C.; Dorfs, D. Phase Transfer of 1- and 2-Dimensional Cd-based Nanocrystals. *Nanoscale* **2015**, *7* (45), 19300–19309.

(103) Bagaria, H. G.; Ada, E. T.; Shamsuzzoha, M.; Nikles, D. E.; Johnson, D. T. Understanding Mercapto Ligand Exchange on the Surface of FePt Nanoparticles. *Langmuir* **2006**, *22* (18), 7732–7737.

(104) Nasilowski, M.; Mahler, B.; Lhuillier, E.; Ithurria, S.; Dubertret, B. Two-Dimensional Colloidal Nanocrystals. *Chem. Rev.* **2016**, *116* (18), 10934–10982.

(105) Salzmann, B. B. V.; van der Sluijs, M. M.; Soligno, G.; Vanmaekelbergh, D. Oriented Attachment: From Natural Crystal Growth to a Materials Engineering Tool. *Acc. Chem. Res.* **2021**, *54* (4), 787–797.

(106) Schliehe, C.; Juarez, B. H.; Pelletier, M.; Jander, S.; Greshnykh, D.; Nagel, M.; Meyer, A.; Foerster, S.; Kornowski, A.; Klinke, C.; Weller, H. Ultrathin PbS Sheets by Two-Dimensional Oriented Attachment. *Science* **2010**, *329* (5991), 550–553.

(107) Chen, Y.; Chen, D.; Li, Z.; Peng, X. Symmetry-Breaking for Formation of Rectangular CdSe Two-Dimensional Nanocrystals in Zinc-Blende Structure. *J. Am. Chem. Soc.* **2017**, *139* (29), 10009–10019.

(108) Ithurria, S.; Bousquet, G.; Dubertret, B. Continuous Transition from 3D to 1D Confinement Observed During the Formation of CdSe Nanoplatelets. *J. Am. Chem. Soc.* **2011**, *133* (9), 3070–3077.

(109) Riedinger, A.; Ott, F. D.; Mule, A.; Mazzotti, S.; Knüsel, P. N.; Kress, S. J. P.; Prins, F.; Erwin, S. C.; Norris, D. J. An Intrinsic Growth Instability in Isotropic Materials Leads to Quasi-Two-Dimensional Nanoplatelets. *Nat. Mater.* **2017**, *16* (7), 743–748.

(110) Ott, F. D.; Riedinger, A.; Ochsenbein, D. R.; Knüsel, P. N.; Erwin, S. C.; Mazzotti, M.; Norris, D. J. Ripening of Semiconductor Nanoplatelets. *Nano Lett.* **2017**, *17* (11), 6870–6877.

(111) Wang, F.; Wang, Y.; Liu, Y.-H.; Morrison, P. J.; Loomis, R. A.; Buhro, W. E. Two-Dimensional Semiconductor Nanocrystals: Properties, Templated Formation, and Magic-Size Nanocluster Intermediates. *Acc. Chem. Res.* **2015**, *48* (1), 13–21.

(112) Liu, Y.-H.; Wang, F.; Wang, Y.; Gibbons, P. C.; Buhro, W. E. Lamellar Assembly of Cadmium Selenide Nanoclusters into Quantum Belts. *J. Am. Chem. Soc.* **2011**, *133* (42), 17005–17013.

(113) Son, J. S.; Wen, X.-D.; Joo, J.; Chae, J.; Baek, S.-I.; Park, K.; Kim, J. H.; An, K.; Yu, J. H.; Kwon, S. G.; Choi, S.-H.; Wang, Z.; Kim, Y.-W.; Kuk, Y.; Hoffmann, R.; Hyeon, T. Large-Scale Soft Colloidal Template Synthesis of 1.4 nm Thick CdSe Nanosheets. *Angew. Chem. Int. Ed.* **2009**, *48* (37), 6861–6864.

(114) Wang, Y.; Liu, Y.-H.; Zhang, Y.; Kowalski, P. J.; Rohrs, H. W.; Buhro, W. E. Preparation of Primary Amine Derivatives of the Magic-Size Nanocluster $(CdSe)_{13}$. *Inorg. Chem.* **2013**, *52* (6), 2933–2938.

(115) Yener, D. O.; Sindel, J.; Randall, C. A.; Adair, J. H. Synthesis of Nanosized Silver Platelets in Octylamine-Water Bilayer Systems. *Langmuir* **2002**, *18* (22), 8692–8699.

(116) Son, J. S.; Park, K.; Kwon, S. G.; Yang, J.; Choi, M. K.; Kim, J.; Yu, J. H.; Joo, J.; Hyeon, T. Dimension-controlled Synthesis of CdS Nanocrystals: From 0D Quantum Dots to 2D Nanoplates. *Small* **2012**, *8* (15), 2394–2402.

(117) Nagamine, G.; Santen, J.; Crimmann, J. G.; Mule, A. S.; Pun, A. B.; Norris, D. J. Spectroscopy of Single CdSe Magic-Sized Nanocrystals. *Nano Lett.* **2025**, *25* (33), 12539–12546.

(118) Binnewies, M.; Jäckel, M.; Willner H.; Rayner-Canham, G. *Allgemeine und Anorganische Chemie*, 2. Auflage, Spektrum Akademischer Verlag, **2011**.

(119) Khan, A. H.; Brescia, R.; Polovitsyn, A.; Angeloni, I.; Martín-García, B.; Moreels, I. Near-Infrared Emitting Colloidal PbS Nanoplatelets: Lateral Size Control and Optical Spectroscopy. *Chem. Mater.* **2017**, *29* (7), 2883–2889.

(120) Macias-Pinilla, D. F.; Echeverría-Arrondo, C.; Gualdrón Reyes, A. F.; Agouram, S.; Muñoz-Sanjosé, V.; Planelles, J.; Mora-Seró, I.; Climente, J. I. Morphology and Band Structure of Orthorhombic PbS Nanoplatelets: An Indirect Band Gap Material. *Chem. Mater.* **2021**, *33* (1), 420–429.

(121) Nenadovic, M. T.; Rajh, T.; Micic, O. I. Size Quantization in Small Semiconductor Particles. *J. Phys. Chem.* **1985**, *89* (3), 397–399.

(122) Rossetti, R.; Hull, R.; Gibson, J. M.; Brus, L. E. Hybrid Electronic Properties between the Molecular and Solid State Limits: Lead Sulfide and Silver Halide Crystallites. *J. Chem. Phys.* **1985**, *83* (3), 1406–1410.

(123) Lifshitz, E.; Sirota, M.; Porteanu, H. Continuous and Time-Resolved Photoluminescence Study of Lead Sulfide Nanocrystals, Ebmedded in Polymer Film. *J. Cryst. Growth* **1999**, *196* (1), 126–134.

(124) Bakueva, L.; Gorelikov, I.; Musikhin, S.; Zhao, X. S.; Sargent, E. H.; Kumacheva, E. PbS Quantum Dots with Stable Efficient Luminescence in the Near-IR Spectral Range. *Adv. Mater.* **2004**, *16* (11), 926–929.

(125) Hines, M. A.; Scholes, G. D. Colloidal PbS Nanocrystals with Size-Tunable Near-Infrared Emission: Observation of Post-Synthesis Self-Narrowing of the Particle Size Distribution. *Adv. Mater.* **2003**, *15* (21), 1844–1849.

(126) Ellingson, R. J.; Beard, M. C.; Johnson, J. C.; Yu, P.; Micic, O. I.; Nozik, A. J.; Shabaev, A.; Efros, A. L. Highly Efficient Multiple Exciton Generation in Colloidal PbSe and PbS Quantum Dots. *Nano Lett.* **2005**, *5* (5), 865–871.

(127) Bielewicz, T.; Dogan, S.; Klinke, C. Tailoring the Height of Ultrathin PbS Nanosheets and their Application as Field-Effect Transistors. *Small* **2015**, *11* (7), 826–833.

(128) Bielewicz, T.; Ramin Moayed, M. M.; Lebedeva, V.; Strelow, C.; Rieckmann, A.; Klinke, C. From Dots to Stripes to Sheets: Shape Control of Lead Sulfide Nanostructures. *Chem. Mater.* **2015**, *27* (24), 8248–8254.

(129) Bielewicz, T.; Klein, E.; Klinke, C. New Ways to Synthesize Lead Sulfide Nanosheets-Substituted Alkanes Direct the Growth of 2D Nanostructures. *Nanotechnology* **2016**, *27* (35), 355602.

(130) Bhandari, G. B.; Subedi, K.; He, Y.; Jiang, Z.; Leopold, M.; Reilly, N.; Lu, H. P.; Zayak, A. T.; Sun, L. Thickness-Controlled Synthesis of Colloidal PbS Nanosheets and Their Thickness-Dependent Energy Gaps. *Chem. Mater.* **2014**, *26* (19), 5433–5436.

(131) Khan, A. H.; Pal, S.; Dalui, A.; Pradhan, J.; Sarma, D. D.; Acharya, S. Solution-Processed Free-Standing Ultrathin Two-Dimensional PbS Nanocrystals with Efficient and Highly Stable Dielectric Properties. *Chem. Mater.* **2017**, *29* (3), 1175–1182.

(132) Akkerman, Q. A.; Martín-García, B.; Buha, J.; Almeida, G.; Toso, S.; Marras, S.; Bonaccorso, F.; Petralanda, U.; Infante, I.; Manna, L. Ultrathin Orthorhombic PbS Nanosheets. *Chem. Mater.* **2019**, *31* (19), 8145–8153.

(133) Antu, A. D.; Jiang, Z.; Premathilka, S. M.; Tang, Y.; Hu, J.; Roy, A.; Sun, L. Bright Colloidal PbS Nanoribbons. *Chem. Mater.* **2018**, *30* (11), 3697–3703.

(134) Lauth, J.; Failla, M.; Klein, E.; Klinke, C.; Kinge, S.; Siebbeles, L. D. A. Photoexcitation of PbS Nanosheets Leads to Highly Mobile Charge Carriers and Stable Excitons. *Nanoscale* **2019**, *11* (44), 21569–21576.

(135) Ramin Moayed, M. M.; Bielewicz, T.; Zöllner, M. S.; Herrmann, C.; Klinke, C. Towards Colloidal Spintronics Through Rashba Spin-Orbit Interaction in Lead Sulphide Nanosheets. *Nat. Commun.* **2017**, *8*, 15721.

(136) Tang, Y.; Aryal, S.; Fox, J. R.; Wang, J.; Schaller, R. D.; Sun, L. Infrared Amplified Spontaneous Emission from Two-Dimensional PbS Nanoplatelets. *Nano Lett.* **2025**, *25* (34), 12921–12929.

(137) Lipovskii, A.; Kolobkova, E.; Petrikov, V.; Kang, I.; Olkhovets, A.; Krauss, T.; Thomas, M.; Silcox, J.; Wise, F.; Shen, Q.; Kycia, S. Synthesis and Characterization of PbSe Quantum Dots in Phosphate Glass. *Appl. Phys. Lett.* **1997**, *71* (23), 3406–3408.

(138) Murray, C. B.; Sun, S.; Gaschler, W.; Doyle, H.; Betley, T. A.; Kagan, C. R. Colloidal Synthesis of Nanocrystals and Nanocrystal Superlattices. *IBM J. Res. Dev.* **2001**, *45* (1), 47–56.

(139) Wehrenberg, B. L.; Wang, C.; Guyot-Sionnest, P. Interband and Intraband Optical Studies of PbSe Colloidal Quantum Dots. *J. Phys. Chem. B* **2002**, *106* (41), 10634–10640.

(140) Du, H.; Chen, C.; Krishnan, R.; Krauss, T. D.; Harbold, J. M.; Wise, F. W.; Thomas, M. G.; Silcox, J. Optical Properties of Colloidal PbSe Nanocrystals. *Nano Lett.* **2002**, *2* (11), 1321–1324.

(141) Schaller, R. D.; Petruska, M. A.; Klimov, V. I. Tunable Near-Infrared Optical Gain and Amplified Spontaneous Emission Using PbSe Nanocrystals. *J. Phys. Chem. B* **2003**, *107* (50), 13765–13768.

(142) Pietryga, J. M.; Schaller, R. D.; Werder, D.; Stewart, M. H.; Klimov, V. I.; Hollingsworth, J. A. Pushing the Band Gap Envelope: Mid-Infrared Emitting Colloidal PbSe Quantum Dots. *J. Am. Chem. Soc.* **2004**, *126* (38), 11752–11753.

(143) Lee, S.; Lee, D. T.; Ko, J.-H.; Kim, W.-J.; Joo, J.; Jeong, S.; McGuire, J. A.; Kim, Y.-H.; Lee, D. C. Slow Colloidal Growth of PbSe Nanocrystals for Facile Morphology and Size Control. *RSC Adv.* **2014**, *4* (19), 9842.

(144) Koh, W.-K.; Dandu, N. K.; Fidler, A. F.; Klimov, V. I.; Pietryga, J. M.; Kilina, S. V. Thickness-Controlled Quasi-Two-Dimensional Colloidal PbSe Nanoplatelets. *J. Am. Chem. Soc.* **2017**, *139* (6), 2152–2155.

(145) Galle, T.; Samadi Khoshkhoo, M.; Martin-Garcia, B.; Meerbach, C.; Sayevich, V.; Koitzsch, A.; Lesnyak, V.; Eychmüller, A. Colloidal PbSe Nanoplatelets of Varied Thickness with Tunable Optical Properties. *Chem. Mater.* **2019**, *31* (10), 3803–3811.

(146) Galle, T.; Spittel, D.; Weiß, N.; Shamraienko, V.; Decker, H.; Georgi, M.; Hübner, R.; Metzkow, N.; Steinbach, C.; Schwarz, D.; Lesnyak, V.; Eychmüller, A. Simultaneous Ligand and Cation Exchange of Colloidal CdSe Nanoplatelets toward PbSe Nanoplatelets for Application in Photodetectors. *J. Phys. Chem. Lett.* **2021**, *12* (21), 5214–5220.

(147) Salzmann, B. B. V.; Wit, J. de; Li, C.; Arenas-Esteban, D.; Bals, S.; Meijerink, A.; Vanmaekelbergh, D. Two-Dimensional CdSe-PbSe Heterostructures and PbSe Nanoplatelets: Formation, Atomic Structure, and Optical Properties. *J. Phys. Chem. C* **2022**, *126* (3), 1513–1522.

(148) Reynoso, V.; Paula, A. M. de; Cuevas, R. F.; Medeiros Neto, J. A.; Alves, O. L.; Cesar, C. L.; Barbosa, L. C. PbTe Quantum Dot Doped Glasses with Absorption Edge in the 1.5 μm Wavelength Region. *Electron. Lett.* **1995**, *31* (12), 1013–1015.

(149) Urban, J. J.; Talapin, D. V.; Shevchenko, E. V.; Murray, C. B. Self-Assembly of PbTe Quantum Dots into Nanocrystal Superlattices and Glassy Films. *J. Am. Chem. Soc.* **2006**, *128* (10), 3248–3255.

(150) Dresselhaus, M. S.; Chen, G.; Tang, M. Y.; Yang, R. G.; Lee, H.; Wang, D. Z.; Ren, Z. F.; Fleurial, J.-P.; Gogna, P. New Directions for Low-Dimensional Thermoelectric Materials. *Adv. Mater.* **2007**, *19* (8), 1043–1053.

(151) Harman, T. C.; Spears, D. L.; Manfra, M. J. High Thermoelectric Figures of Merit in PbTe Quantum Wells. *J. Electron. Mater.* **1996**, *25* (7), 1121–1127.

3 Toward Bright Colloidal Near-Infrared Emitters: Surface Passivation of 2D PbSe Nanoplatelets by Metal Halides

This chapter is centered around the development of a surface passivation method for colloidal 2D PbSe NPLs to enhance their photoluminescence quantum yield. The highest values of *e.g.* 61% at 989 nm were achieved by using PbI_2, which can act as both X- and Z-type ligand to saturate undercoordinated surface atoms.

The results presented here have been published in *J. Phys. Chem. C* **2022**, *126* (45), 19277–19285. For details about the author contributions see Chapter B.

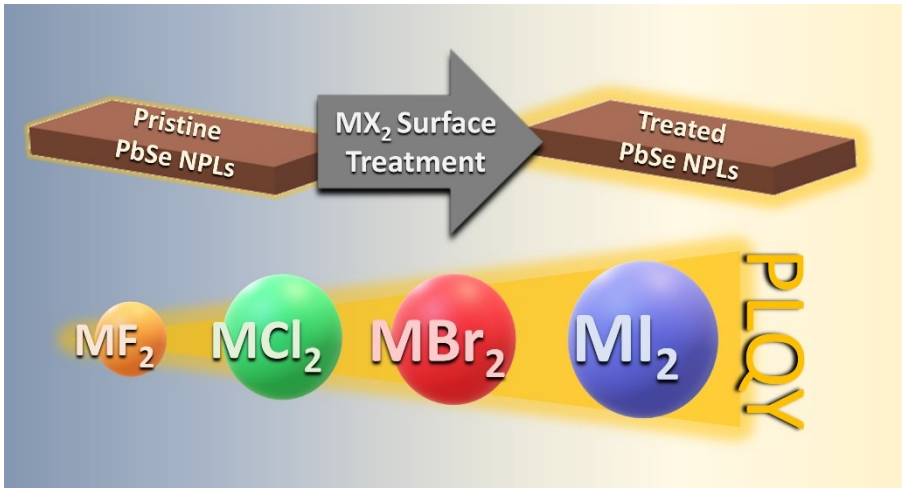

Leon Biesterfeld,[a,b,c] *Lars F. Klepzig,*[b,c] *André Niebur,*[b,c] *Marina Rosebrock,*[b,c] *and Jannika Lauth* [*a,b,c]

[a] Institute of Physical and Theoretical Chemistry, Universität Tübingen, D-72076 Tübingen, Germany.

[b] Cluster of Excellence PhoenixD (Photonics, Optics, and Engineering – Innovation Across Disciplines), D-30167 Hannover, Germany.

[c] Institute of Physical Chemistry and Electrochemistry, Leibniz Universität Hannover, D-30167 Hannover, Germany.

* Corresponding author

3.1 Abstract

Colloidal 2D PbSe nanoplatelets (NPLs) are promising near- and short wave-infrared emitters for optoelectronic applications at telecommunication wavelengths. However, their photoluminescence quantum yield (PLQY) is limited by the ubiquitous presence of surface-related trap states. Here, we apply a treatment of colloidal PbSe NPLs with different metal halides (MX_2, M = Zn, Cd, Pb; X = F, Cl, Br, I) to improve their emission brightness. A surface passivation of the NPLs by PbI_2 leads to the best results with a strongly increased PLQY (27% for PbSe NPLs emitting at 0.98 eV (1265 nm) and up to 61% for PbSe NPLs emitting at 1.25 eV (989 nm)). Simultaneously, the full width at half-maximum of the NPL photoluminescence decreased by 10% after the treatment. X-ray photoelectron spectroscopy and complementary surface treatment of PbSe NPLs with organic halides reveal the combined passivating role of both X-type binding halides X^- and Z-type binding metal halides MX_2 in enhancing the optical properties of the PbSe NPLs. Our results emphasize the potential of 2D PbSe NPLs for efficient emission tailored for the application in fiber optics.

3.2 Introduction

A commonality of all colloidal nanomaterials is their high surface-to-volume ratio, making surface chemistry a major task in nanochemistry.[1,2] In the nanoregime, the materials' surface is critical for numerous properties including the colloidal stability or photoluminescence (PL)[3] of the structures and can give rise to new properties such as size-[4] and facet[5]-dependent catalytic activity. Consequently, the relationship between the surface chemistry and the optical properties of semiconductor nanocrystals (NCs), nanosheets (NSs), and nanoplatelets (NPLs) has been thoroughly investigated for a number of different model systems.[2,6–8] A common finding is the photoluminescence quantum yield (PLQY) to be sensitively responsive to the addition or removal of surfactant molecules.[6,9,10] This can be understood by considering undercoordinated surface atoms as one limiting factor for the PLQY of colloidal nanomaterials. These surface traps enable nonradiative recombination pathways of excited charge carriers.[11–13] Insufficient surface passivation of as-synthesized NCs or NPLs is commonly caused by the steric hindrance between long-chained organic ligands used for synthesis and preventing a full surface covering of the nanostructures.[14] Therefore, a suitable (postsynthetic)

ligand engineering is required to optimize the optoelectronic properties of colloidal nanomaterials.[2] Surface treatment of nanostructures with both organic and/or inorganic ligands has proven to be a powerful tool in addressing surface defects for example by the saturation of dangling bonds.[15–18] Typically, the employed ligands are categorized by the covalent bond model introduced by GREEN[19] to classify covalent transition-metal compounds, which ANDERSON *et al.*[10] have adapted to suit the description of nanocrystal surfaces. Briefly, L-type ligands act as neutral LEWIS bases donating two electrons to an unoccupied orbital on the surface, X-type ligands are one-electron donors (such as halides) forming covalent bonds to singly occupied surface orbitals, and Z-type ligands act as LEWIS acids that accept two electrons from occupied orbitals on the surface.[6,20]

Ultrathin 2D lead chalcogenide NSs and NPLs have recently become a substantial line of research since their tunable absorption and photoluminescence properties are suitable to cover the technologically relevant near-infrared (NIR, 1.65–0.89 eV (750–1400 nm)) and short-wave-infrared (SWIR, 0.89–0.41 eV (1400–3000 nm)) regions of the electro-magnetic spectrum, *e.g.*, where glass fiber optics exhibit negligible attenuation.[21–27] The optical properties of NSs and NPLs are mainly determined by their strongly confined thickness dimension, giving rise to interesting properties and photophysics different from spherical NCs, albeit at the cost of a higher synthetic complexity.[28] While PbSe NPLs are less comprehensively studied, because they have only recently become synthetically accessible, PbS NSs have been thoroughly investigated. For example, PbS NSs show remarkably efficient charge carrier multiplication (CM efficiencies of 0.9–0.55 for PbS NSs with a thickness range of 4–7 nm)[29] and high charge carrier mobility (550–1000 $cm^2V^{-1}s^{-1}$ for PbS NSs with a thickness of 4–16 nm),[30] indicating the high potential of 2D lead chalcogenides for optical applications such as solar cells,[31] photodetectors,[32] and field effect transistors.[33]

However, accessing NPLs with highly efficient PL in the NIR is a synthetic challenge. For example, NIR-emitting PbSe NPLs have been synthesized by oriented attachment of PbSe NCs[23] and by cation exchange of CdSe NPLs.[22,32] Additionally, more elaborate NIR-active systems such as CdSe-PbSe heterostructures[34] and HgX NCs on HgX NPLs (X = Se or Te)[35] have been realized *via* cation exchange from Cd-based NPLs. However, only few direct syntheses have yielded PbSe NPLs up to now.[23,36] A recent example from our group is the direct

synthesis of colloidal PbSe NPLs from lead oleate and selenourea at 0°C, reaching a PLQY of 37.4% at 1.27 eV (980 nm).[36]

Here, we investigate the influence of different metal halide compounds on the optical properties of 2D PbSe NPLs. The PbSe NPLs applied exhibit a thickness of 0.8 ± 0.1 nm, and their PL maximum is tunable between 1.43–0.83 eV (860–1510 nm) *via* mainly controlling the lateral size of the NPLs.[36] We chose two sets of synthetic parameters, which result in the formation of PbSe NPLs that exhibit a PL maximum near the two ends of the tunable energy range at 1.36 eV (912 nm) and 0.98 eV (1265 nm). Previous work on the surface treatment and passivation has been focused on NCs[9,37–39] and Cd-based NPLs with PL mainly in the visible region.[15,40] This work expands the metal halide surface treatment passivation to 2D PbSe NPLs with PL at technologically relevant NIR wavelengths.

3.3 Experimental Section

3.3.1 Chemicals

Cadmium bromide ($CdBr_2$, 99.99%), cadmium chloride ($CdCl_2$, 99.99%), cadmium iodide (CdI_2, 99%), lead bromide ($PbBr_2$, 99.99%), lead chloride ($PbCl_2$, 99.99%), octylamine (99%), triethylamine (≥ 99.5%), trifluoroacetic anhydride (≥ 99%), and zinc iodide (ZnI_2, ≥ 98%) were purchased from SIGMA-ALDRICH/MERCK. Cadmium fluoride (CdF_2, 99.99%), analytical grade hexane (99.99%), lead iodide (PbI_2, 99.99%), lead oxide (99.99%), selenourea (99.97%), tetrabutylammonium iodide (TBAI, 98%), zinc bromide ($ZnBr_2$, 98%), and zinc chloride monohydrate ($ZnCl_2 \cdot H_2O$, 99.99%) were purchased from ALFA AESAR. Oleic acid (90%) and trifluoroacetic acid (99%) were purchased from ABCR. Tetrachloroethylene (99.9%) was purchased from MERCK-MILLIPORE. Octylamine and oleic acid were dried by freeze-pump-thawing three times prior to use and stored inside a N_2-filled glovebox. All other reagents were used as received without any further purification steps.

3.3.2 Lead Oleate Precursor Synthesis

The lead oleate precursor was synthesized according to a method of HENDRICKS *et al.*[41] First, PbO (20.0 g, 89.6 mmol) was stirred in acetonitrile (40.0 mL) for 10 min at 0°C. Trifluoroacetic acid (1.4 mL, 18.2 mmol) and trifluoroacetic anhydride (12.4 mL, 89.6 mmol) were added, and after an

additional 15 min at 0°C the solution was allowed to heat to room temperature, yielding a clear solution. In a separate flask oleic acid (90%, 50.8 g, 162 mmol), isopropanol (360 mL), and triethylamine (28.1 mL, 202 mmol) were mixed. Briefly, the two solutions were combined, immediately yielding lead oleate as a white precipitate, which was recrystallized from isopropanol at 80°C. The lead oleate solution was stored in a freezer at -20°C for 16 h, filtered, generously washed with methanol, and dried under vacuum. The dried lead oleate was stored under inert gas conditions at -25°C.

3.3.3 Selenourea Precursor Preparation

The selenourea precursor was prepared by dissolving selenourea (193 mg, 1.57 mmol) in a mixture of octylamine (2.025 mL, 12.2 mmol), oleic acid (0.225 mL, 0.71 mmol), and hexane (0.75 mL, 5.7 mmol) at 35°C for 24 h under inert gas conditions.

3.3.4 PbSe NPL Synthesis

The PbSe NPLs synthesis is adapted from a method described by KLEPZIG *et al.*[36] that is originally based on a PbS NPLs synthesis by MANTEIGA VÁZQUEZ *et al.*[26] The two adjustments compared to the procedure by KLEPZIG *et al.* are a scale-up by a factor of 10 and the introduction of a thorough purification step. The scale-up results in a higher consistency and reproducibility of the pristine PbSe NPLs. The purification step serves to remove residues of unreacted precursors and to allow for an efficient and comparable surface treatment.

All steps, including purification and surface treatment, were performed under inert gas conditions. For a typical synthesis, lead oleate (1.83 g, 2.7 mmol) was dissolved in a mixture of octylamine (2.0 mL, 12 mmol), oleic acid (4.0 mL, 12.5 mmol), and hexane (18.0 mL, 137 mmol) at 35°C and subsequently cooled to 0°C using an ice bath. The selenourea precursor solution (2.5 mL) was injected rapidly, causing a color change from colorless to dark brown, indicating the formation of the PbSe NPLs. After 10 min at 0°C the reaction was quenched by the addition of ethanol (18.5 mL).

3.3.5 Purification of Pristine PbSe NPLs

The pristine PbSe NPLs were purified by centrifugation of the quenched reaction mixture at 2500 rcf for 10 min. The supernatant was discarded, and the precipitant was redispersed in hexane (10 mL). This procedure was repeated two more times with a hexane-to-ethanol ratio of 2:1, before storing the purified pristine PbSe NPLs at -25°C inside a nitrogen-filled glovebox (the dispersed pristine PbSe NPLs are stable for several weeks).

3.3.6 Surface Treatment of Pristine PbSe NPLs

For the surface treatment of the PbSe NPLs, 0.1 M solutions of the metal halides were prepared in octylamine and oleic acid with a molar ratio of 9:1.[42] Typically, the PbSe NPLs solution (0.5 mL) was diluted with hexane (0.75 mL) before the respective metal halide solution (1.0 mL) was rapidly injected and stirred for 40 min at 35°C. The treated PbSe NPLs were stored at -25°C inside a nitrogen-filled glovebox.

3.3.7 Vis-NIR Absorption and PL Spectroscopy

The samples for optical spectroscopy were prepared by diluting the PbSe NPLs in tetrachloroethylene (2.5 mL) in a quartz cuvette with a light path length of 1 cm (optical density below 0.2 at 500 nm). Optical Vis–NIR absorbance spectra were acquired using a CARY 5000 spectrophotometer from AGILENT TECHNOLOGIES. Steady-state PL spectra were obtained using an EDINBURGH FLS 1000 UV-Vis-NIR PL spectrometer. PL spectra were collected by exciting the NPLs at 500 nm with a xenon lamp using an InGaAs PMT for signal detection. The PLQYs were determined with the same device utilizing an integrating sphere, measuring the scattering at 500 nm and the PL in the NIR region of both the pure solvent and the PbSe NPLs sample, considering the sensitivity difference of both detectors.[43] The multichannel scaling (MCS) PL lifetime data were acquired utilizing a picosecond pulsed diode laser with a pulse width of 110 ps at 445.1 nm obtained from EDINBURGH INSTRUMENTS.

3.3.8 Transmission Electron Microscopy

TEM images were collected using a FEI TECNAI G2 F20 transmission electron microscope with a field emission gun operating at 200 kV. For TEM analysis the colloidal PbSe NPLs solutions were drop-casted onto a carbon-coated copper grid (300 mesh) acquired from QUANTIFOIL and cleaned by a method from LI *et al.* utilizing a combination of ethanol and activated carbon.[44]

3.3.9 X-ray Photoelectron Spectroscopy

XPS data were acquired using a PHI 5000 VERSAPROBE III from ULVAC-PHI. The spectra were obtained utilizing an aluminum X-ray source (Al K_α = 1476.6 eV) operated at 48.3 W with a beam diameter of 100 µm. Survey spectra were measured with a pass energy of 224 eV; high-resolution spectra were collected with a pass energy of 27 eV. Charging effects were accounted for by setting the C1s peak of sp^3 carbon to 284.4 eV. The NPL samples were prepared by drop-casting the colloidal solution onto a silicon wafer and drying under vacuum overnight to remove the organic solvents.

3.3.10 Attenuated Total Reflection-Fourier Transform IR Spectroscopy

The ATR-FTIR spectrum of pristine PbSe NPLs was acquired using a CARY 360 FTIR spectrometer from AGILENT TECHNOLOGIES. The sample was prepared by drop-casting the colloidal solution onto an ATR crystal. The measurement data were acquired under ambient conditions.

3.3.11 Powder X-ray Diffraction

PXRD patterns were collected in BRAGG-BRENTANO geometry with a BRUKER D8 Advance equipped with a Cu $K_{\alpha 1}$ source operating at 40 kV and 30 mA. The NPLs samples were prepared by drop-casting the colloidal solution onto a single crystal silicon sample holder.

3.4 Results and Discussion

3.4.1 Surface Treatment of PbSe NPLs with Different Metal Halides MX_2

Figure 3.1a-c shows PL spectra of pristine PbSe NPLs treated with different metal halides MX_2 (M = Zn, Cd, Pb; X = F, Cl, Br, I).

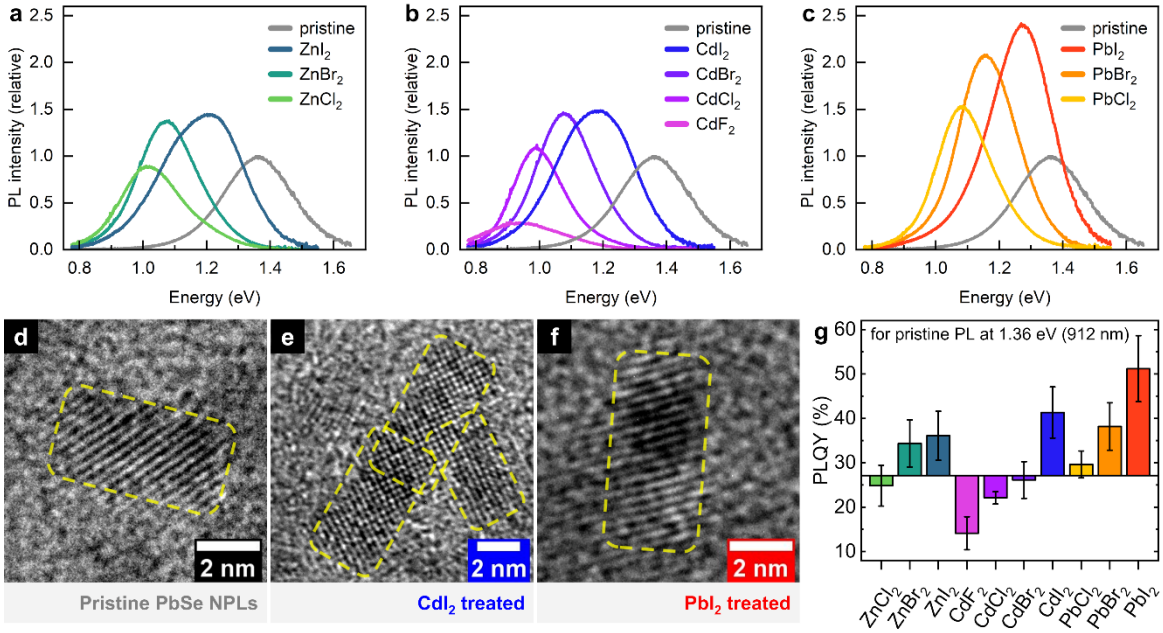

Figure 3.1. Metal halide surface treatment of pristine PbSe NPLs with PL at 1.36 eV (912 nm) and a PLQY of 27% used as benchmark structures. (a–c) PL spectra of pristine and MX_2 treated PbSe NPLs. Smaller and more electronegative halides X are associated with an increased bathochromic shift and a lower PL intensity of the NPLs after the surface passivation. The treatment with PbI_2 results in the highest PL intensities and average PLQY of 51% compared to the pristine PbSe NPLs. (d–f) TEM images of pristine, CdI_2 treated, and PbI_2 treated PbSe NPLs. (g) PLQYs for surface treated PbSe NPLs shown in (a–c). The effect of metal halide treatment is depicted by the colored bars with respect to the pristine PbSe NPLs. PbI2 treatment results in the highest PLQY.

The as-synthesized PbSe NPLs are capped with oleate (X-type) and octylamine (L-type) ligands (see Figure S3.1 for ATR-FTIR spectroscopy), exhibit a cubic rock-salt crystal structure (see Figure S3.2a for powder X-ray diffraction), and exhibit a PL maximum at 1.36 eV (912 nm). The metal halide surface treatment in all cases is accompanied by a bathochromic shift of the PL maximum, with its extent

strongly depending on the halide introduced (see Figure 3.1). The smallest bathochromic shift occurs for metal iodide treatments and increases gradually when using metal bromides, chlorides, and fluorides, which results in the largest shifts. This trend is in line with work performed by BEDERAK *et al.* for thin films of colloidal PbS NCs, who attribute the increasing bathochromic shift of the NCs PL to a ligand-dependent loss of quantum confinement in the NCs.[17] This gets apparent when considering the electronegativity of the halides. Halides with higher electronegativity reduce the electron density within the NPLs and hence decrease their quantum confinement. Note that the bathochromic shift of 368 meV (338 nm) for the $CdCl_2$ surface treatment in this work is larger compared to results previously shown by KLEPZIG *et al.* (78 meV (65 nm); see Figure S3.3).[36] We ascribe this difference to the elevated temperature present during the treatment step (35°C compared to 0°C), which causes a higher replacement rate of oleate by chloride on the NPL surface. The larger share of chloride on the NPL surface, in turn, results in a more strongly decreased quantum confinement as with oleate ligands and hence causes a larger bathochromic shift of the PL maximum. This can be further understood by considering the temperature dependence of the acid-base equilibrium between octylamine and oleic acid with elevated temperatures shifting the equilibrium away from the oleate and promoting a binding of chloride to the NPL surface.[42]

Because of solubility difficulties, CdF_2 was the only fluoride used for surface treatment (see Figure 3.1b). However, we expect the trend observed with CdF_2 to be similar for ZnF_2 and PbF_2.[17]

Figure 3.1d–f shows transmission electron microscopy (TEM) images of pristine, CdI_2 treated, and PbI_2 treated PbSe NPLs with PL at 1.36 eV (910 nm), 1.25 eV (989 nm), and 1.31 eV (942 nm), respectively (associated size distributions are shown in Figure S3.4). Pristine PbSe NPLs exhibit a length and width of $(4.9 \pm 0.9) \times (2.7 \pm 0.5)$ nm², which corresponds to an aspect ratio of 1:1.8. Upon their surface treatment the NPLs tend to show slight size growth ($(5.1 \pm 1.3) \times (3.0 \pm 0.6)$ nm² for PbI_2 treatment) and the aspect ratio decrease (1:1.6 for PbI_2 treatment). We ascribe the size increase to the newly introduced layer of inorganic metal halide ligands. To preclude a further growth of the PbSe NPLs upon addition of PbX_2, the PbSe NPLs were precipitated and purified three times from unreacted precursors prior to their surface treatment. Additionally, in

the case of CdX_2, the formation of a CdSe shell is not expected at a low treatment temperature of 35°C. However, we attribute the decreased aspect ratio to self-reconstruction processes of the PbSe NPLs during the surface treatment, which are facilitated by the higher temperature compared to the 0°C used for pristine PbSe NPLs.[13,45] PbSe NPLs exhibit a thickness of 0.8 ± 0.1 nm, as has been determined by KLEPZIG *et al. via* TEM.[36] Correlating the energy of the first excitonic transition to the lateral size of the NPLs reveals their additional confinement due to their 2D structure compared to spherical PbSe NCs (see Figure S3.5). However, it should be noted that the NPLs exhibit strong confinement in all three dimensions due to the large exciton BOHR radius of PbSe (46 nm).[46]

Figure 3.1g shows the PLQY of metal halide treated PbSe NPLs compared to the PLQY of pristine PbSe NPLs. The error bars represent fluctuations on the PLQY of several PbSe NPL batches prepared with the same synthetic parameters. Similar to the relative PL intensity compared to the pristine PbSe NPLs and PL position, we observe a strong influence of the metal halide treatment on the PLQY of the PbSe NPLs. Generally, PLQY values increase from metal fluoride to metal iodide treated NPLs, with CdF_2 roughly halving the initial PLQY value of the NPLs and PbI_2 doubling the PLQY of pristine NPLs. We assume this stems from partial X-type ligation of halide anions to surface Pb^{2+} cations based on the concept of hard and soft acids and bases (HSAB). Accordingly, the soft Pb^{2+} cation preferably interacts with the soft iodide, resulting in the highest degree of surface passivation and associated average PLQY of 51%. However, the HSAB principle fails to explain the difference between different metal iodides MI_2 and suggests that X-type binding of iodide to undercoordinated Pb surface sites is not the only process active for the PLQY increase. Metal halides can also act as Z-type ligands binding to undercoordinated selenium surface sites *via* the metal cation.[10,15] Notably, results for the PbX_2 treatment generally result in the highest PLQYs for the respective halide and are in good agreement with work by PURCELL-MILTON *et al.*[47] The authors find CdX_2 to lead to the highest PLQYs for a surface treatment of CdSe quantum dots (QDs) and state the importance of using a metal halide with a metal cation already present on the surface for surface treatment.

To address the question of the metal halide ligand binding to the PbSe NPL surface, we perform X-ray photoelectron spectroscopic (XPS) measurements for pristine and metal halide treated PbSe NPLs. Additionally, we conducted surface

treatment with organic halides. Because of steric hindrance, the organic halides act as X-type ligands *via* the halide anions, as opposed to the metal halides with their Lewis acidic character, which can bind to the NPLs by Z-type ligation.

3.4.2 Study of the Metal Halide Ligand Binding Type

Figure 3.2a,b shows XPS data of the Pb-4f and Se-3d core levels of pristine as well as $CdCl_2$, CdI_2, and PbI_2 treated PbSe NPLs. The data are used to determine the binding energies of the different atomic species present in the NPLs.

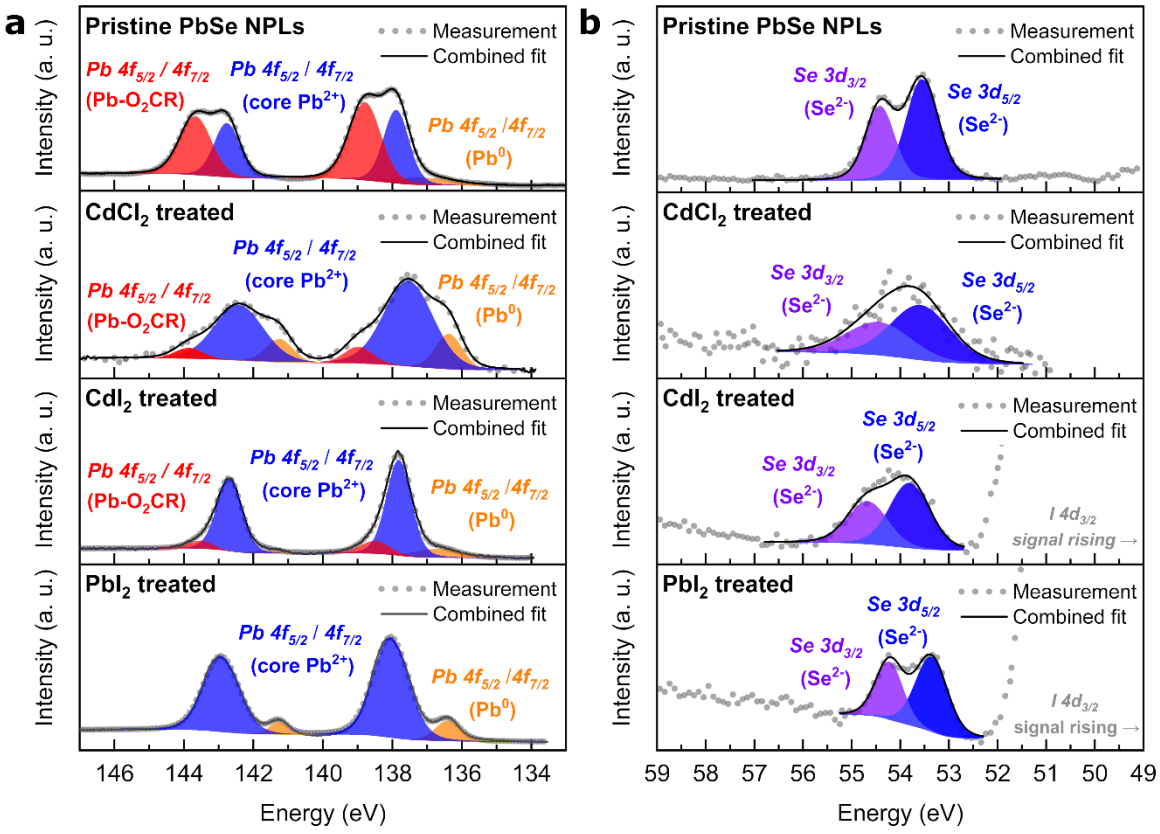

Figure 3.2. XPS spectra of the Pb-4f (a) and Se-3d (b) core levels of pristine as well as $CdCl_2$, CdI_2, and PbI_2 treated PbSe NPLs. (a) The Pb-O_2CR signal (red) becomes gradually less pronounced in MX_2 treated NPLs and indicates a successful replacement of oleates by halides on the NPLs surface. (b) The less intensive Se signals are broadened for the CdX_2 treatment compared to the pristine and PbI_2 treated PbSe NPLs and indicate a change in the chemical environment of the selenium ascribed to Z-type binding.

All components are fitted by a symmetric VOIGT function (convolution of LORENTZIAN and GAUSSIAN distribution). The spin-orbit doublet between 135 and 145 eV is attributed to Pb^{2+}, contains the $4f_{7/2}$ and $4f_{5/2}$ signals, and is fitted by three components in total (see Figure 3.2a). The lowest energy component at 136.7 ± 0.4 and 141.4 ± 0.2 eV (orange) is ascribed to metallic Pb, which can be formed by X-ray photolysis during the XPS measurement of Pb in the presence of halides.[48] Consequently, we evaluate this signal with caution and focus on the higher energetic components at 137.8 ± 0.2 and 142.7 ± 0.2 eV (blue) as well as 138.6 ± 0.1 and 143.5 ± 0.1 eV (red). The binding energies of these components are in excellent agreement with values reported by PETERS *et al.* and SYKORA *et al.* for PbSe NCs and are therefore assigned as follows.[49,50] The medium binding energy peak at 137.8 ± 0.2 and 142.7 ± 0.2 eV (blue) is attributed to core Pb^{2+} bound to Se^{2-}. The high-energy peak at 138.6 ± 0.1 and 143.5 ± 0.1 eV (red) is assigned to Pb^{2+} bound to oleate (Pb-O_2CR).[49,50] Accordingly, we find the Pb-O_2CR component (red) to be far less pronounced in the metal halide treated NPLs compared to the pristine NPLs, which shows the X-type ligand exchange of oleates by halides upon the surface treatment. Additionally, the expression of the Pb-O_2CR component gradually decreases from the $CdCl_2$ treatment over the CdI_2 treatment to the PbI_2 treatment and indicates an increasing X-type ligand replacement of oleates bound to Pb^{2+} by halides in this experimental series. While oleates cannot sufficiently passivate the NPLs surface due to steric repulsion between the long-chained organic ligands, halides can cover a higher proportion of the surface. A higher share of halides replacing the oleates thus causes an efficient passivation of the NPL surface. This is also reflected in and strongly supported by the PLQY measurements of the treated PbSe NPLs (PbI_2 > CdI_2 > $CdCl_2$; see Figure 3.1f).

The spin-orbit doublet between 52 and 56 eV is attributed to Se^{2-} and contains a $3d_{5/2}$ and $3d_{3/2}$ signal (see Figure 3.2b). The two features of the doublet are located at 53.6 ± 0.2 eV (Se $3d_{5/2}$) and 54.4 ± 0.2 eV (Se $3d_{3/2}$). On the basis of previously reported values, the signals are assigned to Se^{2-} bound to Pb^{2+}.[49–51] Generally, the Se^{2-} signals are broader for $CdCl_2$ and CdI_2 surface treatment compared to the pristine and PbI_2 treated NPLs. We assume this broadening is caused by a change in the chemical environment of Se^{2-} due to a Z- type binding of $CdCl_2$ and CdI_2 to Se^{2-}. A Z-type binding of PbI_2 to Se^{2-} does not result in broader features of the selenium doublet because Pb^{2+} is the inherent cation bound to Se^{2-} in any case,

regardless of the surface treatment applied. To further investigate whether a Z-type ligation is needed to achieve enhanced optical properties in PbSe NPLs, a surface treatment of pristine PbSe NPLs with tetrabutylammonium halides (*e.g.*, TBAI) is performed. An exemplary absorbance and PL spectrum for TBAI treated PbSe NPLs is shown in Figure S3.6. We find that unlike in the passivation with metal halides, a surface treatment of PbSe NPLs with organic halides leads to a deterioration of the optical properties of pristine NPLs and to a drastic bathochromic shift of their PL maximum (from 1.36 eV (912 nm) to 0.95 eV (1305 nm); see Figure S3.6). This indicates that a treatment with X-type binding exclusively is not sufficient to passivate the NPLs surface, and Z-type ligation is required, too. Notably, this is in line with previous reports for CdSe NCs showing that (L-promoted) Z-type ligand removal is accompanied by a PL decrease.[10,52,53]

Combining the XPS data (see Figure 3.2) and the optical spectroscopy results (see Figure 3.1 and Figure S3.6), we conclude that both X-type ligation of X^- to Pb^{2+} and Z-type ligation of MX_2 to Se^{2-} are responsible and needed to obtain an efficient photoluminescence enhancement in PbSe NPLs.

3.4.3 Optical Properties of PbI_2 Treated PbSe NPLs

Figure 3.3a,b shows the absorption and photoluminescence spectra of larger ((6.0 ± 0.9) × (4.0 ± 0.4) nm^2) and smaller ((4.9 ± 0.9) × (2.7 ± 0.5) nm^2) pristine and PbI_2 treated PbSe NPLs (see Figure S3.2b,c and Figure S3.4 for TEM images and size histograms) in comparison. The larger NPLs exhibit excitonic absorbance at 1.28 eV (967 nm) with an associated PL maximum at 0.98 eV (1265 nm; see Figure 3.3a). The optical features do not shift upon PbI_2 surface treatment. We assume the lack of a bathochromic shift of the optical features is caused by a comparatively lower influence of the iodide on the confinement in larger NPLs compared to smaller ones. Figure 3.3b shows the smaller NPLs: here, the pristine NPLs exhibit excitonic absorbance at 1.49 eV (832 nm) with an associated PL maximum at 1.30 eV (953 nm). The optical features of the small PbI_2 treated NPLs are shifted to lower energies with absorbance at 1.41 eV (879 nm) and PL at 1.25 eV (989 nm) (see Figure S3.7 for the determination of the absorbance maxima).

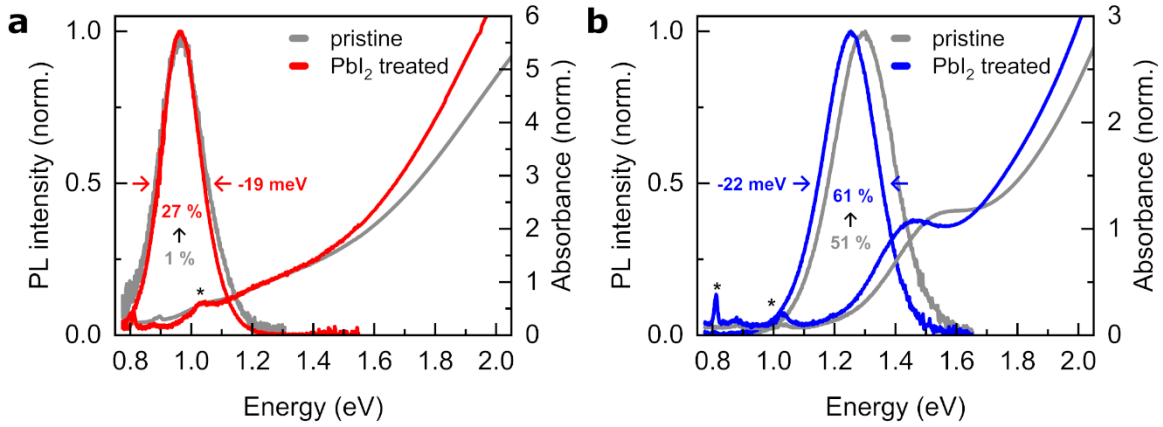

Figure 3.3. Optical properties of pristine and PbI_2 treated PbSe NPLs emitting at (a) 0.98 eV (1265 nm) with no bathochromic shift upon PbI_2 treatment and (b) 1.30 eV (953 nm) and 1.25 eV (989 nm). A treatment with PbI_2 results in a narrowed PL, sharpened absorbance features, and increased PLQYs. *The signals at 0.81 and 1.03 eV are caused by the solvents and are present in all measurements.

The respective positions correspond to STOKES shifts of 300 meV for larger NPLs, 190 meV for smaller pristine NPLs, and 160 meV for smaller PbI_2 treated NPLs. In PbS NCs the STOKES shift is directly proportional to the extent of the quantum confinement.[54–56] Here, we find the PbSe NPLs' STOKES shifts are smaller compared to those of small PbSe NCs (560 meV, $d = 1.1$ nm)[57] and PbS NCs (525 meV, $d = 1$ nm),[58] as the NPLs are strongly confined in their thickness dimension mainly. For the smaller pristine NPLs, we observe a decreased STOKES shift after the PbI_2 surface treatment (190 to 160 meV), which is in line with the bathochromic shift of absorbance and PL due to a decreased quantum confinement in the NPLs caused by the electronegativity of the iodide introduced to the surface.[17] We assume the increased STOKES shift for the larger NPLs (300 meV) is caused by a higher lateral polydispersity ((6.0 ± 0.9) × (4.0 ± 0.4) nm²), which has previously been associated with a larger STOKES shift in polydisperse PbS NC ensembles.[59] The PLQY of the large PbSe NPLs (see Figure 3.3a) increases from 1% to 27% upon PbI_2 surface treatment. Note that larger PbSe NPLs emitting at 0.98 eV (1265 nm) reach their maximum PLQY after being stirred under surface treatment conditions for 72 h, while the smaller PbI_2 treated PbSe NPLs emitting at 1.30 eV (953 nm) reach their maximum PLQY value after 40 min under treatment conditions (after 40 min the larger PbSe NPLs exhibit a PLQY of 18% (Figure S3.8)). We ascribe the time difference for surface passivation to a higher

share of surface-bound ligands compared to edge- or ledge-bound ligands in larger NPLs, which have shown to have higher binding strength.[6] For smaller NPLs, the relative PLQY increase is less drastic (51% to 61%) after surface treatment, and we additionally observe a stronger pronounced excitonic absorbance after the surface treatment (Figure 3.3b). The obtained PLQY values are in line with the effect of NCs and NPLs with a larger band gap exhibiting a lower PLQY, which is explained by the "energy gap law".[60] Accordingly, a transition between two electronic states shows an exponential dependence on the energy difference, meaning that decay rate k_{gap} increases as the energy gap ΔE decreases.

$$k_{\mathrm{gap}} = k_{\mathrm{gap}}^{0} e^{-\alpha \Delta E} \qquad \text{(Eq. 3.1)}$$

with k_{gap}^{0} and α being arbitrary constants. This universal correlation has been previously observed in PbS and PbSe NPLs.[36,60]

Besides the PLQY increase, the PbI_2 surface treatment causes a decrease in full width at half-maximum (fwhm) of the PL by 10% (see Figure 3.3a, 173 to 154 meV, and Figure 3.3b, 235 to 213 meV).

Figure 3.4 shows the multichannel scaling (MCS) lifetime (LT) measurements of metal halide treated PbSe NPLs.

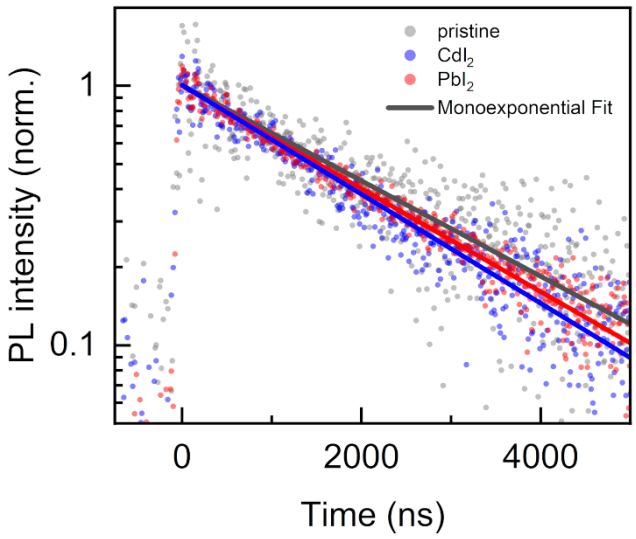

Figure 3.4. MCS PL lifetime measurements of pristine, CdI_2 treated, and PbI_2 treated PbSe NPLs, taken at each PL maximum (see Table 3.1). All PL LT were fitted by a monoexponential decay and show slightly shorter lifetimes after the treatment and an accompanying bathochromic shift of the PL.

The measurements are collected at each PL maximum and fitted monoexponentially as summarized in Table 3.1.

Table 3.1. Summary of the optical properties of the MCS photoluminescence Lifetime measurements shown in Figure 3.4.

sample	PL position	PLQY	lifetime τ
pristine	1.39 eV (890 nm)	39%	2.36 ± 0.06 µs
CdI_2 treated	1.24 eV (1000 nm)	18%	1.99 ± 0.03 µs
PbI_2 treated	1.30 eV (955 nm)	64%	2.19 ± 0.02 µs

The PL lifetimes of PbSe NPLs are in the microseconds range, slightly longer than reported lifetimes for PbSe NCs (~100–1000 ns) and similar to literature reports on PbSe NPL PL lifetimes.[22,50,61,62] In contrast to results in our previous work on the synthesis of PbSe NPLs, we find a monoexponential decay of the PbSe NPL photoluminescence lifetime, which has been observed before for PbSe NCs.[22,36,63,64] We ascribe this trend to the already increased PLQY values of our pristine PbSe NPLs (15% at 1.26 eV (985 nm) previously and 39% at 1.39 eV (890 nm) in this work) caused by slight synthesis adjustments including upscaling of the reaction and multiple precipitation steps (see the Experimental Section). Because of these adjustments, the PL spectra of the obtained PbSe NPLs can be fitted by a single GAUSSIAN, rather than the sum of two GAUSSIANS, ascribed to two emissive states,[36] and the PL lifetime decays monoexponentially within our measurement window. The MCS photoluminescence lifetime analysis shows that the PL lifetime of PbSe NPLs remains similar even after the metal halide treatment. The slight decrease of the PL lifetime from 2.36 µs over 2.19 and 1.99 µs for the PbI_2 and CdI_2 treated NPLs, respectively, can be explained by the bathochromic shift and the energy gap law contribution in NPLs with a smaller band gap described above. We assume the increase of the PLQY in metal halide treated PbSe NPLs is caused by a reduced contribution of nonradiative recombination processes in the surface treated samples. We note that the MCS method for determining PL lifetimes has a rather broad time resolution of ~10 ns, which lacks temporal covering of the fast (non-radiative) recombination processes. Ultrafast spectroscopic studies on PbSe NPLs are therefore currently underway.

3.5 Conclusion

We have studied the surface treatment of colloidal pristine 2D PbSe NPLs with different metal halides MX_2. Treating the PbSe NPLs with PbI_2 results in a strongly enhanced photoluminescence quantum yield from 1% to 27% for a PL at 0.98 nm (1265 nm) and 51% to 61% at 1.25 eV (989 nm), which renders PbSe NPLs highly efficient NIR emitters. XPS analysis shows that the enhancement of the PLQY can be ascribed to both X-type ligation of halides to Pb^{2+} and Z-type ligation of MX_2 to Se^{2-} on the NPLs' surface. Our results underline the great potential of 2D PbSe NPLs for optoelectronic applications in the fiber-optics-relevant tele-communication window.

3.6 References

(1) Yin, Y.; Alivisatos, A. P. Colloidal Nanocrystal Synthesis and the Organic-Inorganic Interface. *Nature* **2005**, *437* (7059), 664–670.

(2) Boles, M. A.; Ling, D.; Hyeon, T.; Talapin, D. V. The Surface Science of Nanocrystals. *Nat. Mater.* **2016**, *15* (2), 141–153.

(3) Murray, C. B.; Kagan, C. R.; Bawendi, M. G. Synthesis and Characterization of Monodisperse Nanocrystals and Close-Packed Nanocrystal Assemblies. *Annu. Rev. Mater. Sci.* **2000**, *30* (1), 545–610.

(4) Bell, A. T. The Impact of Nanoscience on Heterogeneous Catalysis. *Science* **2003**, *299* (5613), 1688–1691.

(5) Kim, S.; Noh, J.; Choi, H.; Ha, H.; Song, J. H.; Shim, H. C.; Jang, J.; Beard, M. C.; Jeong, S. One-Step Deposition of Photovoltaic Layers Using Iodide Terminated PbS Quantum Dots. *J. Phys. Chem. Lett.* **2014**, *5* (22), 4002–4007.

(6) Singh, S.; Tomar, R.; ten Brinck, S.; De Roo, J.; Geiregat, P.; Martins, J. C.; Infante, I.; Hens, Z. Colloidal CdSe Nanoplatelets, A Model for Surface Chemistry/Optoelectronic Property Relations in Semiconductor Nanocrystals. *J. Am. Chem. Soc.* **2018**, *140* (41), 13292–13300.

(7) Bai, Y.; Hao, M.; Ding, S.; Chen, P.; Wang, L. Surface Chemistry Engineering of Perovskite Quantum Dots: Strategies, Applications, and Perspectives. *Adv. Mater.* **2022**, *34* (4), 2105958.

(8) Hartley, C. L.; Kessler, M. L.; Dempsey, J. L. Molecular-Level Insight into Semiconductor Nanocrystal Surfaces. *J. Am. Chem. Soc.* **2021**, *143* (3), 1251–1266.

(9) Hassinen, A.; Moreels, I.; De Nolf, K.; Smet, P. F.; Martins, J. C.; Hens, Z. Short-Chain Alcohols Strip X-type Ligands and Quench the Luminescence of PbSe and CdSe Quantum Dots, Acetonitrile Does Not. *J. Am. Chem. Soc.* **2012**, *134* (51), 20705–20712.

(10) Anderson, N. C.; Hendricks, M. P.; Choi, J. J.; Owen, J. S. Ligand Exchange and the Stoichiometry of Metal Chalcogenide Nanocrystals: Spectroscopic Observation of Facile Metal-Carboxylate Displacement and Binding. *J. Am. Chem. Soc.* **2013**, *135* (49), 18536–18548.

(11) Houtepen, A. J.; Hens, Z.; Owen, J. S.; Infante, I. On the Origin of Surface Traps in Colloidal II-VI Semiconductor Nanocrystals. *Chem. Mater.* **2017**, *29* (2), 752–761.

(12) Kirkwood, N.; Monchen, J. O. V.; Crisp, R. W.; Grimaldi, G.; Bergstein, H. A. C.; Du Fossé, I.; van der Stam, W.; Infante, I.; Houtepen, A. J. Finding and Fixing Traps in II-VI and III-V Colloidal Quantum Dots: The Importance of Z-Type Ligand Passivation. *J. Am. Chem. Soc.* **2018**, *140* (46), 15712–15723.

(13) Sun, B.; Vafaie, M.; Levina, L.; Wei, M.; Dong, Y.; Gao, Y.; Kung, H. T.; Biondi, M.; Proppe, A. H.; Chen, B.; *et al.* Ligand-Assisted Reconstruction of Colloidal Quantum Dots Decreases Trap State Density. *Nano Lett.* **2020**, *20* (5), 3694–3702.

(14) Taylor, D. A.; Teku, J. A.; Cho, S.; Chae, W.-S.; Jeong, S.-J.; Lee, J.-S. Importance of Surface Functionalization and Purification for Narrow FWHM and Bright Green-Emitting InP Core-Multishell Quantum Dots via a Two-Step Growth Process. *Chem. Mater.* **2021**, *33* (12), 4399–4407.

(15) Dufour, M.; Qu, J.; Greboval, C.; Méthivier, C.; Lhuillier, E.; Ithurria, S. Halide Ligands To Release Strain in Cadmium Chalcogenide Nanoplatelets and Achieve High Brightness. *ACS Nano* **2019**, *13* (5), 5326–5334.

(16) Bae, W. K.; Joo, J.; Padilha, L. A.; Won, J.; Lee, D. C.; Lin, Q.; Koh, W.-K.; Luo, H.; Klimov, V. I.; Pietryga, J. M. Highly Effective Surface Passivation of PbSe Quantum Dots through Reaction with Molecular Chlorine. *J. Am. Chem. Soc.* **2012**, *134* (49), 20160–20168.

(17) Bederak, D.; Balazs, D. M.; Sukharevska, N. V.; Shulga, A. G.; Abdu-Aguye, M.; Dirin, D. N.; Kovalenko, M. V.; Loi, M. A. Comparing Halide Ligands in PbS Colloidal Quantum Dots for Field-Effect Transistors and Solar Cells. *ACS Appl. Nano Mater.* **2018**, **1** (12), 6882–6889.

(18) Ghosh, S.; Manna, L. The Many "Facets" of Halide Ions in the Chemistry of Colloidal Inorganic Nanocrystals. *Chem. Rev.* **2018**, *118* (16), 7804–7864.

(19) Green, M. A New Approach to the Formal Classification of Covalent Compounds of the Elements. *J. Organomet. Chem.* **1995**, *500* (1–2), 127–148.

(20) Zhou, Y.; Wang, F.; Buhro, W. E. Large Exciton Energy Shifts by Reversible Surface Exchange in 2D II-VI Nanocrystals. *J. Am. Chem. Soc.* **2015**, *137* (48), 15198–15208.

(21) Schliehe, C.; Juarez, B. H.; Pelletier, M.; Jander, S.; Greshnykh, D.; Nagel, M.; Meyer, A.; Foerster, S.; Kornowski, A.; Klinke, C.; *et al.* Ultrathin PbS Sheets By Two-Dimensional Oriented Attachment. *Science* **2010**, *329* (5991), 550–553.

(22) Galle, T.; Samadi Khoshkhoo, M.; Martin-Garcia, B.; Meerbach, C.; Sayevich, V.; Koitzsch, A.; Lesnyak, V.; Eychmüller, A. Colloidal PbSe Nanoplatelets of Varied Thickness with Tunable Optical Properties. *Chem. Mater.* **2019**, *31* (10), 3803–3811.

(23) Koh, W.-K.; Dandu, N. K.; Fidler, A. F.; Klimov, V. I.; Pietryga, J. M.; Kilina, S. V. Thickness-Controlled Quasi-Two-Dimensional Colloidal PbSe Nanoplatelets. *J. Am. Chem. Soc.* **2017**, *139* (6), 2152–2155.

(24) Ding, M.; Fan, D.; Wang, W.; Luo, Y.; Peng, G.-D. In *Handbook of Optical Fibers*; Peng, G.-D., Ed.; Springer: **2020**; pp 1099–1137.

(25) Zhou, Y.; Celikin, M.; Camellini, A.; Sirigu, G.; Tong, X.; Jin, L.; Basu, K.; Barba, D.; Ma, D.; Sun, S.; *et al.* Ultrasmall Nanoplatelets: The Ultimate Tuning of Optoelectronic Properties. *Adv. Energy Mater.* **2017**, *7* (17), 1602728.

(26) Manteiga Vázquez, F.; Yu, Q.; Klepzig, L. F.; Siebbeles, L. D. A.; Crisp, R. W.; Lauth, J. Probing Excitons in Ultrathin PbS Nanoplatelets with Enhanced Near-Infrared Emission. *J. Phys. Chem. Lett.* **2021**, *12* (1), 680–685.

(27) D'Amico, A.; Di Natale, C.; Lo Castro, F.; Iarossi, S.; Catini, A.; Martinelle, E. In *Unexploded Ordnance Detection and Mitigation*; Byrnes, J. S., Ed.; Springer: **2008**; p 22.

(28) Nasilowski, M.; Mahler, B.; Lhuillier, E.; Ithurria, S.; Dubertret, B. Two-Dimensional Colloidal Nanocrystals. *Chem. Rev.* **2016**, *116* (18), 10934–10982.

(29) Aerts, M.; Bielewicz, T.; Klinke, C.; Grozema, F. C.; Houtepen, A. J.; Schins, J. M.; Siebbeles, L. D. A. Highly Efficient Carrier Multiplication in PbS Nanosheets. *Nat. Commun.* **2014**, *5*, 3789.

(30) Lauth, J.; Failla, M.; Klein, E.; Klinke, C.; Kinge, S.; Siebbeles, L. D. A. Photoexcitation of PbS Nanosheets Leads to Highly Mobile Charge Carriers and Stable Excitons. *Nanoscale* **2019**, *11* (44), 21569–21576.

(31) Dogan, S.; Bielewicz, T.; Lebedeva, V.; Klinke, C. Photovoltaic Effect in Individual Asymmetrically Contacted Lead Sulfide Nanosheets. *Nanoscale* **2015**, *7* (11), 4875–4883.

(32) Galle, T.; Spittel, D.; Weiß, N.; Shamraienko, V.; Decker, H.; Georgi, M.; Hübner, R.; Metzkow, N.; Steinbach, C.; Schwarz, D.; *et al.* Simultaneous Ligand and Cation Exchange of Colloidal CdSe Nanoplatelets toward PbSe Nanoplatelets for Application in Photodetectors. *J. Phys. Chem. Lett.* **2021**, *12* (21), 5214–5220.

(33) Dogan, S.; Bielewicz, T.; Cai, Y.; Klinke, C. Field–Effect Transistors made of Individual Colloidal PbS Nanosheets. *Appl. Phys. Lett.* **2012**, *101* (7), 73102.

(34) Salzmann, B. B. V.; Wit, J. de; Li, C.; Arenas-Esteban, D.; Bals, S.; Meijerink, A.; Vanmaekelbergh, D. Two-Dimensional CdSe-PbSe Heterostructures and PbSe Nanoplatelets: Formation, Atomic Structure, and Optical Properties. *J. Phys. Chem. C* **2022**, *126* (3), 1513–1522.

(35) Tenney, S. M.; Vilchez, V.; Sonnleitner, M. L.; Huang, C.; Friedman, H. C.; Shin, A. J.; Atallah, T. L.; Deshmukh, A. P.; Ithurria, S.; Caram, J. R. Mercury Chalcogenide Nanoplatelet-Quantum Dot Heterostructures as a New Class of Continuously Tunable Bright Shortwave Infrared Emitters. *J. Phys. Chem. Lett.* **2020**, *11* (9), 3473–3480.

(36) Klepzig, L. F.; Biesterfeld, L.; Romain, M.; Niebur, A.; Schlosser, A.; Hübner, J.; Lauth, J. Colloidal 2D PbSe Nanoplatelets with Efficient Emission Reaching the Telecom O-, E- and S-Band. *Nanoscale Adv.* **2022**, *4*, 590–599.

(37) Hartley, C. L.; Kessler, M. L.; Dones Lassalle, C. Y.; Camp, A. M.; Dempsey, J. L. Effects of Ligand Shell Composition on Surface Reduction in PbS Quantum Dots. *Chem. Mater.* **2021**, *33* (22), 8612–8622.

(38) Sluydts, M.; De Nolf, K.; Van Speybroeck, V.; Cottenier, S.; Hens, Z. Ligand Addition Energies and the Stoichiometry of Colloidal Nanocrystals. *ACS Nano* **2016**, *10* (1), 1462–1474.

(39) Greaney, M. J.; Couderc, E.; Zhao, J.; Nail, B. A.; Mecklenburg, M.; Thornbury, W.; Osterloh, F. E.; Bradforth, S. E.; Brutchey, R. L. Controlling the Trap State Landscape of Colloidal CdSe Nanocrystals with Cadmium Halide Ligands. *Chem. Mater.* **2015**, *27* (3), 744–756.

(40) Zhang, Z.; Thung, Y. T.; Wang, L.; Chen, X.; Ding, L.; Fan, W.; Sun, H. Surface Depletion Effects in Bromide-Ligated Colloidal Cadmium Selenide Nanoplatelets: Toward Efficient Emission at High Temperature. *J. Phys. Chem. Lett.* **2021**, *12* (37), 9086–9093.

(41) Hendricks, M. P.; Campos, M. P.; Cleveland, G. T.; Jen-La Plante, I.; Owen, J. S. A Tunable Library of Substituted Thiourea Precursors to Metal Sulfide Nanocrystals. *Science* **2015**, *348* (6240), 1226–1230.

(42) Almeida, G.; Goldoni, L.; Akkerman, Q.; Dang, Z.; Khan, A. H.; Marras, S.; Moreels, I.; Manna, L. Role of Acid-Base Equilibria in the Size, Shape, and Phase Control of Cesium Lead Bromide Nanocrystals. *ACS Nano* **2018**, *12* (2), 1704–1711.

(43) Würth, C.; Geissler, D.; Behnke, T.; Kaiser, M.; Resch-Genger, U. Critical Review of the Determination of Photoluminescence Quantum Yields of Luminescent Reporters. *Anal. Bioanal. Chem.* **2015**, *407* (1), 59–78.

(44) Li, C.; Tardajos, A. P.; Wang, DA.; Choukroun, D.; van Daele, K.; Breugelmans, T.; Bals, S. A Simple Method to Clean Ligand Contamination on TEM Grids. *Ultramicroscopy* **2021**, *221*, 113195.

(45) Fang, C.; van Huis, M. A.; Vanmaekelbergh, D.; Zandbergen, H. W. Energetics of Polar and Nonpolar Facets of PbSe Nanocrystals from Theory and Experiment. *ACS Nano* **2010**, *4* (1), 211–218.

(46) Brus, L. Electronic Wave Functions in Semiconductor Clusters: Experiment and Theory. *J. Phys. Chem.* **1986**, *90* (12), 2555–2560.

(47) Purcell-Milton, F.; Chiffoleau, M.; Gun'ko, Y. K. Investigation of Quantum Dot-Metal Halide Interactions and Their Effects on Optical Properties. *J. Phys. Chem. C* **2018**, *122*, 25075–25084.

(48) McGettrick, J. D.; Hooper, K.; Pockett, A.; Baker, J.; Troughton, J.; Carnie, M.; Watson, T. Sources of Pb(0) Artefacts during XPS Analysis of Lead Halide Perovskites. *Mater. Lett.* **2019**, *251*, 98–101.

(49) Peters, J. L.; van der Bok, J. C.; Hofmann, J. P.; Vanmaekelbergh, D. Hybrid Oleate-Iodide Ligand Shell for Air-Stable PbSe Nanocrystals and Superstructures. *Chem. Mater.* **2019**, *31* (15), 5808–5815.

(50) Sykora, M.; Koposov, A. Y.; McGuire, J. A.; Schulze, R. K.; Tretiak, O.; Pietryga, J. M.; Klimov, V. I. Effect of Air Exposure on Surface Properties, Electronic Structure, and Carrier Relaxation in PbSe Nanocrystals. *ACS Nano* **2010**, *4* (4), 2021–2034.

(51) Weser, U.; Sokolowski, G.; Pilz, W. Reaction of Selenite with Biochemically Active Thiols: An X-Ray Photoelectron Spectroscopic Study. *J. Electron Spectrosc. Relat. Phenom.* **1977**, *10* (4), 429–439.

(52) Saniepay, M.; Mi, C.; Liu, Z.; Abel, E. P.; Beaulac, R. Insights into the Structural Complexity of Colloidal CdSe Nanocrystal Surfaces: Correlating the Efficiency of Nonradiative Excited-State Processes to Specific Defects. *J. Am. Chem. Soc.* **2018**, *140* (5), 1725–1736.

(53) Drijvers, E.; De Roo, J.; Martins, J. C.; Infante, I.; Hens, Z. Ligand Displacement Exposes Binding Site Heterogeneity on CdSe Nanocrystal Surfaces. *Chem. Mater.* **2018**, *30* (3), 1178–1186.

(54) Caram, J. R.; Bertram, S. N.; Utzat, H.; Hess, W. R.; Carr, J. A.; Bischof, T. S.; Beyler, A. P.; Wilson, M. W. B.; Bawendi, M. G. PbS Nanocrystal Emission Is Governed by Multiple Emissive States. *Nano Lett.* **2016**, *16* (10), 6070–6077.

(55) Fernée, M. J.; Thomsen, E.; Jensen, P.; Rubinsztein-Dunlop, H. Highly Efficient Luminescence from a Hybrid State Found in Strongly Quantum Confined PbS Nanocrystals. *Nanotechnology* **2006**, *17* (4), 956–962.

(56) Ushakova, E. V.; Litvin, A. P.; Parfenov, P. S.; Fedorov, A. V.; Artemyev, M.; Prudnikau, A. V.; Rukhlenko, I. D.; Baranov, A. V. Anomalous Size-Dependent Decay of Low-Energy Luminescence from PbS Quantum Dots in Colloidal Solution. *ACS Nano* **2012**, *6* (10), 8913–8921.

(57) Ma, W.; Swisher, S. L.; Ewers, T.; Engel, J.; Ferry, V. E.; Atwater, H. A.; Alivisatos, A. P. Photovoltaic Performance of Ultrasmall PbSe Quantum Dots. *ACS Nano* **2011**, *5* (10), 8140–8147.

(58) Warner, J. H.; Thomsen, E.; Watt, A. R.; Heckenberg, N. R.; Rubinsztein-Dunlop, H. Time-Resolved Photoluminescence Spectroscopy of Ligand-Capped PbS Nanocrystals. *Nanotechnology* **2005**, *16* (2), 175–179.

(59) Voznyy, O.; Levina, L.; Fan, F.; Walters, G.; Fan, J. Z.; Kiani, A.; Ip, A. H.; Thon, S. M.; Proppe, A. H.; Liu, M.; *et al.* Origins of Stokes Shift in PbS Nanocrystals. *Nano Lett.* **2017**, *17* (12), 7191–7195.

(60) Semonin, O. E.; Johnson, J. C.; Luther, J. M.; Midgett, A. G.; Nozik, A. J.; Beard, M. C. Absolute Photoluminescence Quantum Yields of IR-26 Dye, PbS, and PbSe Quantum Dots. *J. Phys. Chem. Lett.* **2010**, *1* (16), 2445–2450.

(61) An, J. M.; Franceschetti, A.; Zunger, A. The Excitonic Exchange Splitting and Radiative Lifetime in PbSe Quantum Dots. *Nano Lett.* **2007**, *7* (7), 2129–2135.

(62) Kigel, A.; Brumer, M.; Maikov, G. I.; Sashchiuk, A.; Lifshitz, E. Thermally Activated Photoluminescence in Lead Selenide Colloidal Quantum Dots. *Small* **2009**, *5* (14), 1675–1681.

(63) Skurlov, I.; Sokolova, A.; Galle, T.; Cherevkov, S.; Ushakova, E.; Baranov, A.; Lesnyak, V.; Fedorov, A.; Litvin, A. Temperature-Dependent Photoluminescent Properties of PbSe Nanoplatelets. *Nanomaterials* **2020**, *10* (12), 2570.

(64) Kigel, A.; Brumer, M.; Maikov, G.; Sashchiuk, A.; Lifshitz, E. The Ground-State Exciton Lifetime of PbSe Nanocrystal Quantum Dots. *Superlattices Microstruct.* **2009**, *46* (1–2), 272–276.

3.7 Supporting Information

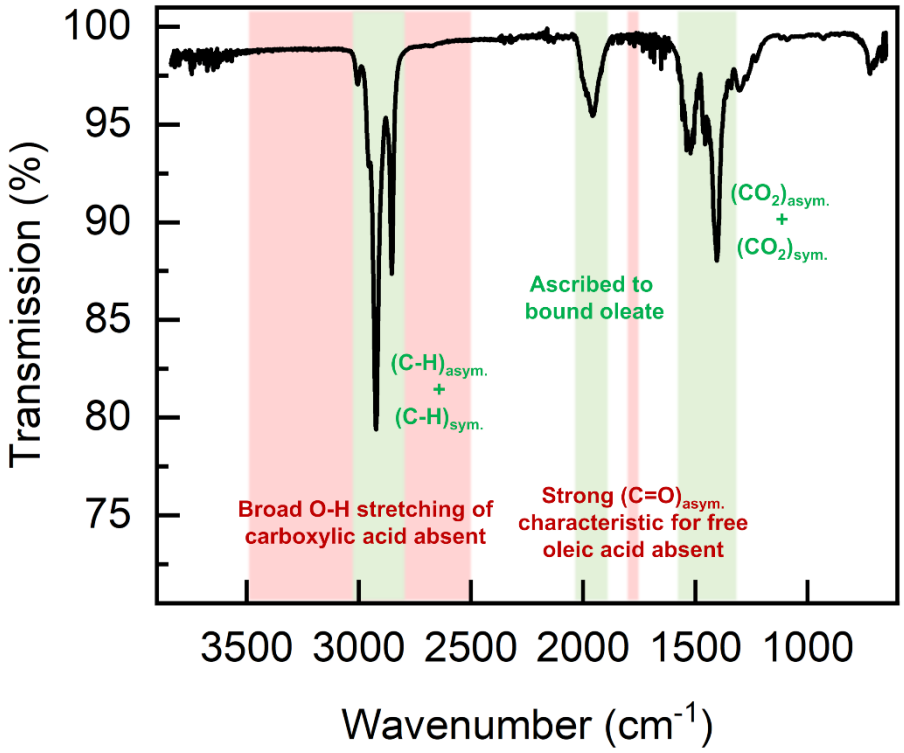

Figure S3.1. ATR-FTIR spectrum of pristine PbSe NPLs. The absence of a broad O-H stretching vibration centered around 3000 cm^{-1} and a strong $(C=O)_{asym.}$ stretching vibration at 1710 cm^{-1} (red) that are characteristic for pure oleic acid indicate that oleic acid is bound to the NPLs surface as oleate (X-type binding).[1] Due to the overlap of oleate and octylamine bands distinguishing both species in the IR spectrum is difficult. However, we expect octylamine to be present on the NPLs' surface as an L-type ligand, because of its crucial role in tuning the size of the PbSe NPLs.[2]

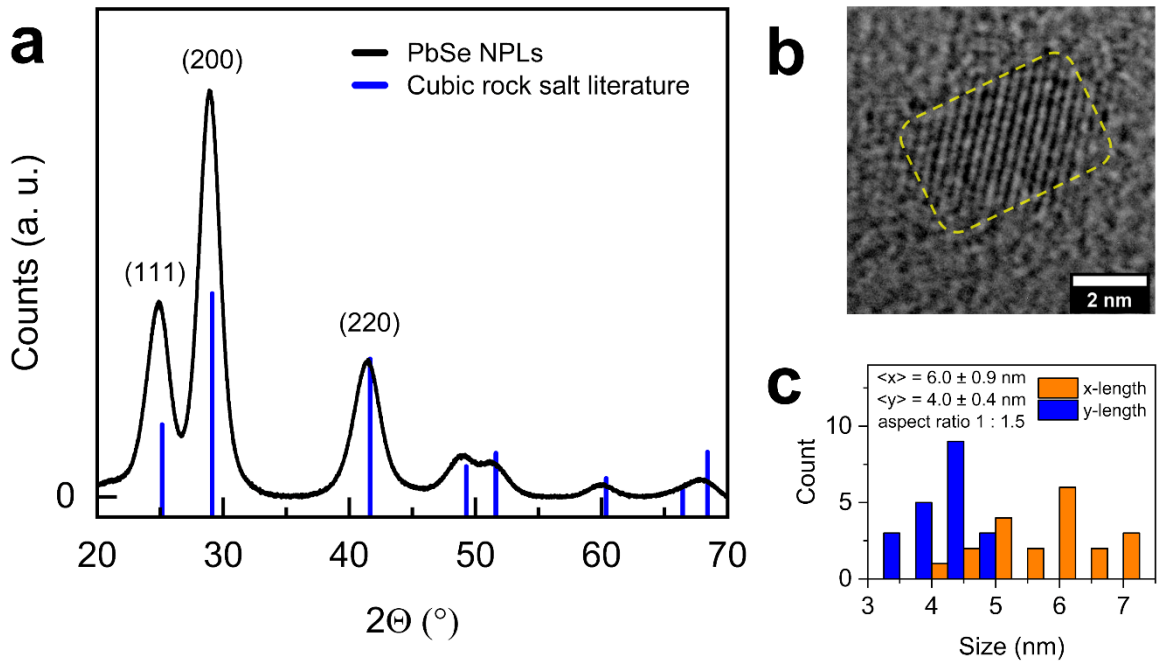

Figure S3.2. (a) Powder X-ray diffraction (PXRD) of pristine PbSe NPLs emitting at 0.95 eV (1311 nm) and exhibiting a cubic rock salt crystal structure (PDF card 01-077-0245). (b) TEM image of the PbSe NPLs used for the PXRD. (c) Size histogram of the PbSe NPLs measured in (a) and shown in (b).

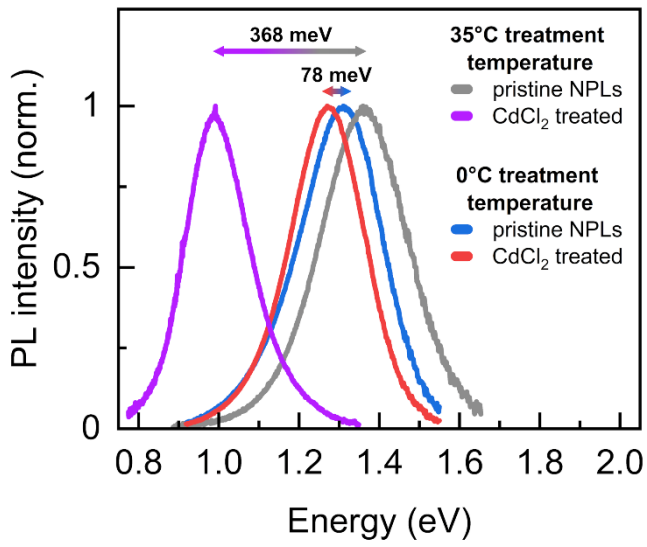

Figure S3.3. PL spectra of pristine and $CdCl_2$ treated PbSe NPLs synthesized at 35°C (shown in Figure 3.1b of the main manuscript) and 0°C treatment temperature (KLEPZIG *et al.*[2]). The increased bathochromic shift for a surface treatment at 35°C (368 meV (338 nm)) is ascribed to a higher replacement rate of oleate by chloride on the NPL surface at the elevated temperature and a resulting decreased quantum confinement caused by the electronegativity of chloride.

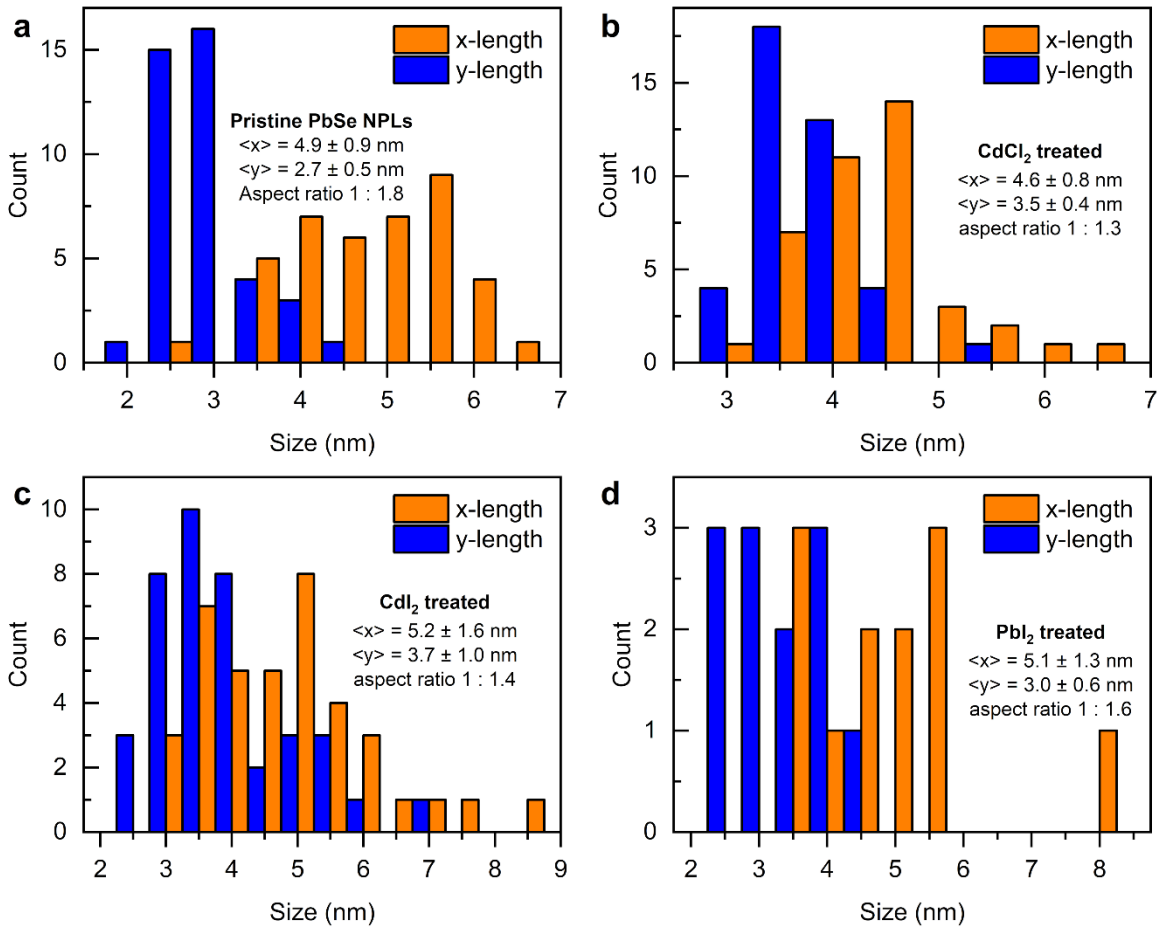

Figure S3.4. Size histograms of the pristine and metal halide treated PbSe NPLs shown in the TEM images in Figure 3.1. The same samples are used for the XPS measurements shown in Figure 3.2.

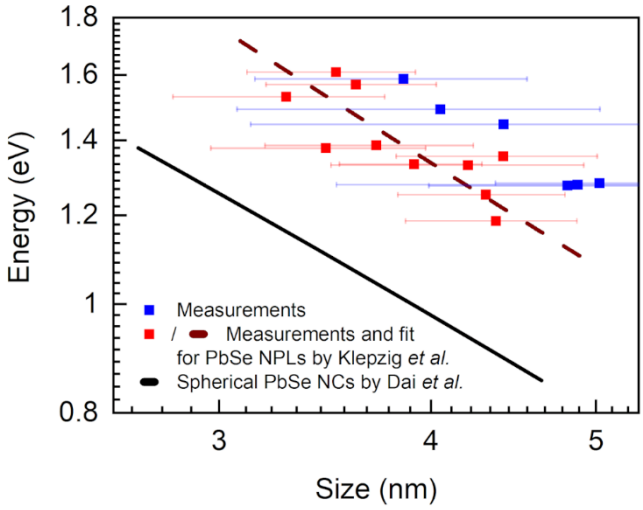

Figure S3.5. Correlation between the first excitonic transition and lateral size of the NPLs averaged over their *x*- and *y*-length as determined by TEM images. The red squares and the brown line represent data and an empirical fit for PbSe NPLs published by KLEPZIG *et al.*,[2] while the black line is a fit for PbSe NCs published by DAI *et al.*[3] Synthesized PbSe NPLs in this work (blue squares) exhibit significantly stronger confinement compared to spherical NCs due to their 2D structure and slightly higher energy values compared to results by KLEPZIG *et al.* The minor increase may be related to the increased aspect ratios (1:1.3 to 1.8 compared 1:1.1 to 1.2 in this work) effecting the lateral confinement in the NPLs.

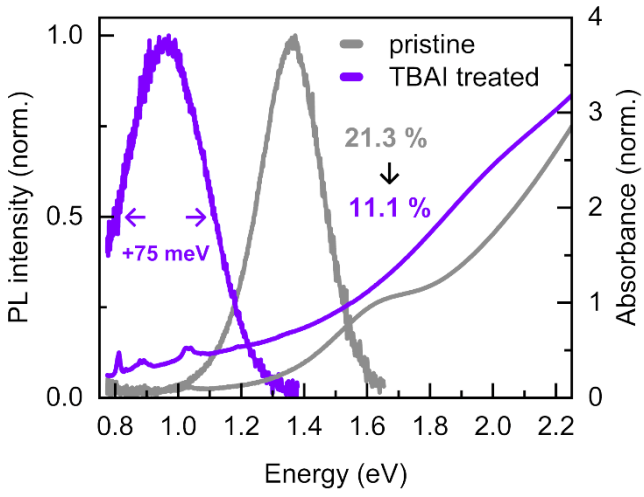

Figure S3.6. Optical properties of pristine and TBAI treated PbSe NPLs. The TBAI treatment causes a bathochromic shift of the PL by 410 meV (from 1.36 eV (912 nm) to 0.95 eV (1305 nm)), a broadening of the PL and a decrease in PLQY from 21.3 % to 11.1 % after the treatment. This supports our assumption that X-type ligation alone is not sufficient to achieve enhanced optical properties.

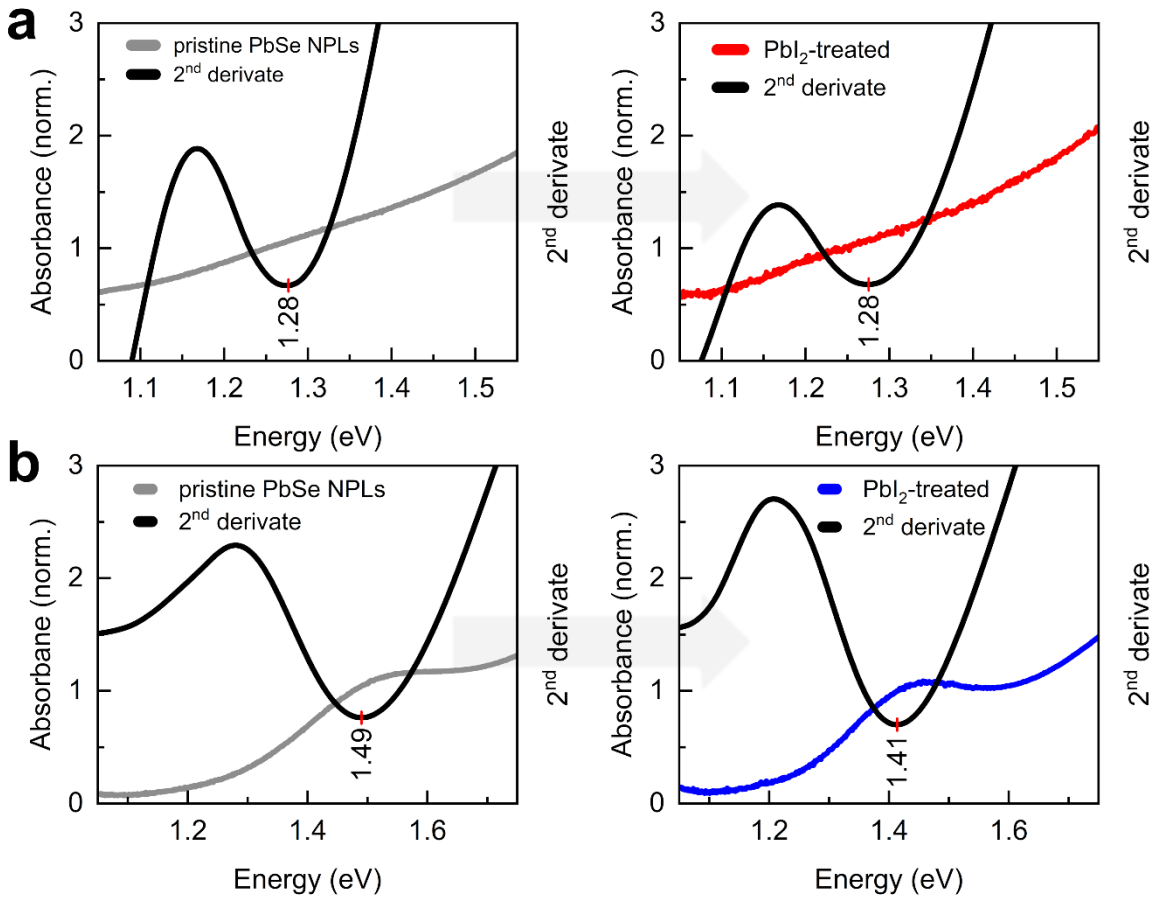

Figure S3.7. Determination of the absorbance maxima of the PbI_2 treated PbSe NPLs shown in Figure 3.3. The absorbance maxima were determined *via* the local minimum of the 2nd derivate. Before calculating the 2nd derivate, the raw data was smoothed with a LOESS (locally estimated scatterplot smoothing) plot.

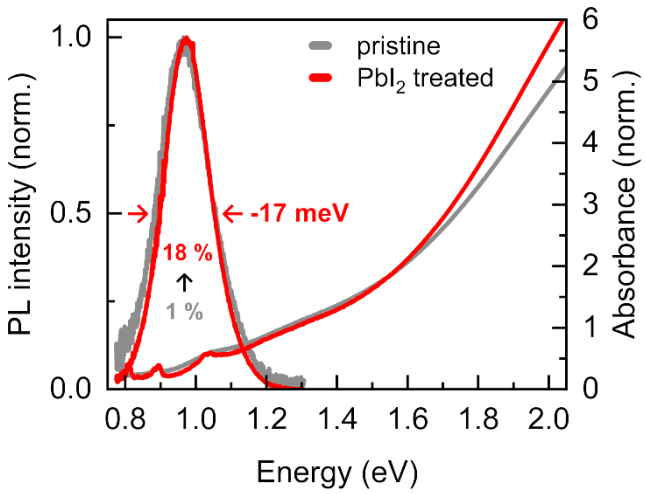

Figure S3.8. Optical properties of large pristine and PbI_2 treated PbSe NPLs emitting at 0.97 eV (1272 nm) after a surface treatment time of 40 min and corresponding to the data shown in Figure 3.3a.

3.7.1 References

(1) Zhang, L.; He, R.; Gu, H.-C. Oleic Acid Coating on the Monodisperse Magnetite Nanoparticles. *Appl. Surf. Sci.* **2006**, *253*, 2611–2617.

(2) Klepzig, L. F.; Biesterfeld, L.; Romain, M.; Niebur, A.; Schlosser, A.; Hübner, J.; Lauth, J. Colloidal 2D PbSe Nanoplatelets with Efficient Emission Reaching the Telecom O-, E- and S- Band. *Nanoscale Adv.* **2022**, *4*, 590-599.

(3) Dai, Q.; Wang, Y.; Li, X.; Zhang, Y.; Pellegrino, D. J.; Zhao, M.; Zou, B.; Seo, J.; Wang, Y.; Yu, W. W. Size-Dependent Composition and Molar Extinction Coefficient of PbSe Semiconductor Nanocrystals. *ACS Nano* **2009**, *3* (6), 1518–1524.

4 Solving the Synthetic Riddle of Colloidal Two-Dimensional PbTe Nanoplatelets with Tunable Near-Infrared Emission

The following chapter covers the development of the first direct synthesis of colloidal 2D PbTe NPLs by using a highly reactive aminophosphine precursor. The PbTe NPLs exhibit tunable NIR PL (910–1460 nm) with QYs up to 15% and represent the previsouly missing final piece in the group of colloidal 2D PbX NCs.

The results presented here have been published in *Chem. Mater.* **2024**, *36* (15), 7197–7206. For details about the author contributions see Chapter B.

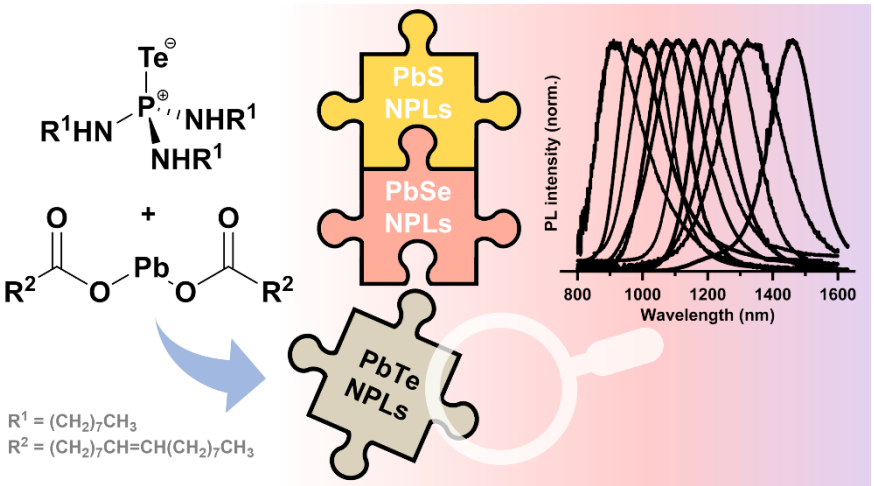

Leon Biesterfeld,[a,b,c] Mattis T. Vochezer,[a] Marco Kögel,[d] Ivan A. Zaluzhnyy,[e] Marina Rosebrock,[b,c] Lars F. Klepzig,[b,c] Wolfgang Leis,[f] Michael Seitz,[f] Jannik C. Meyer,[d,e] and Jannika Lauth [a,b,c]

[a] Institute of Physical and Theoretical Chemistry, Eberhard Karls University of Tübingen, D-72076 Tübingen, Germany.

[b] Cluster of Excellence PhoenixD (Photonics, Optics, and Engineering – Innovation Across Disciplines), D-30167 Hannover, Germany.

[c] Institute of Physical Chemistry and Electrochemistry, Leibniz Universität Hannover, D-30167 Hannover, Germany.

[d] Natural and Medical Sciences Institute, Eberhard Karls University of Tübingen, D-72770 Reutlingen, Germany.

[e] Institute of Applied Physics, Eberhard Karls University of Tübingen, D-72076 Tübingen, Germany.

[f] Institute of Inorganic Chemistry, Eberhard Karls University of Tübingen, D-72076 Tübingen, Germany.

* Corresponding author

Reprinted (adapted) with permission from *Chem. Mater.* 2024, 36 (15), 7197–7206.

4.1 Abstract

Near-infrared emitting colloidal two-dimensional (2D) PbX (X = S, Se) nanoplatelets (NPLs) have emerged as interesting materials with strong size quantization in the thickness dimension. They act as model systems for efficient charge carrier multiplication and hold potential as intriguing candidates for fiber-based photonic quantum applications. However, synthetic access to the third family member, 2D PbTe, remains elusive due to challenging precursor chemistry. Here, we report a direct synthesis for 2D PbTe NPLs with tunable photoluminescence [PL, 910–1460 nm (1.36–0.85 eV), PL quantum yields 1–15%], based on aminophosphine precursor chemistry. *Ex situ* transamination of tris(dimethylamino)phosphine telluride with octylamine is confirmed by ^{31}P nuclear magnetic resonance and yields a reactive tellurium precursor for the formation of 2D PbTe NPLs at temperatures as low as 0°C. The PL position of the PbTe NPLs is tunable by controlling the Pb/Te ratio in the reaction. Grazing-incidence wide-angle X-ray scattering confirms the 2D geometry of the NPLs and the formation of superlattices. The importance of a postsynthetic passivation of PbTe NPLs by PbI_2 to ensure colloidal stability of the otherwise oxygen-sensitive samples is supported by X-ray photoelectron spectroscopy. Our results expand and complete the row of lead chalcogenide-based 2D NPLs, opening up new ways for further pushing the optical properties of 2D NPLs into the infrared and toward technologically relevant wavelengths.

4.2 Introduction

In pursuit of small band gap colloidal semiconductors to cover absorption and emission beyond visible wavelengths, two-dimensional (2D) lead chalcogenide nanosheets (NSs) and nanoplatelets (NPLs) have attracted considerable attention as candidates for solution processable optoelectronics.[1–5] The materials exhibit tunable optical properties, determined primarily by their quantum-confined thickness, which span near-infrared wavelengths [NIR, 750–1400 nm (1.65–0.89 eV)] and reach up to the short-wavelength infrared [1400–3000 nm (0.89–0.41 eV)].[6–10] Access to these spectral windows is desirable for fiber optic applications, as glass fibers exhibit negligible optical attenuation in this range.[11] The strong vertical confinement in the 2D geometry of NSs and NPLs gives rise to interesting photophysics, for example, efficient charge carrier multiplication (up to

90% for 4 nm thick PbS NSs, which means that almost all excess photon energy is converted into additional electron-hole pairs),[12] thickness dependent RASHBA-type spin-orbit coupling,[13] and highly mobile charge carriers (550–1000 $cm^2V^{-1}s^{-1}$ for PbS NSs with a thickness of 4–16 nm).[14] Consequently, colloidal 2D lead chalcogenides are intriguing as active materials in solar cells,[3] photodetectors,[2] and field effect transistors[15] and have received increasing attention in the realm of single photon emission, which is highly desirable for fiber-based photonic quantum technologies operating at telecommunication wavelengths.[16,17] Noteworthy, PbTe in particular has additionally been thoroughly investigated as an intermediate-temperature thermoelectric material (bulk figure of merit *ZT* of 0.4–0.45 at 300 K) and PbTe quantum wells grown *via* molecular beam epitaxy have shown $Z_{2D}T > 1.2$ due to the high density of states in the 2D geometry.[18,19] However, the colloidal synthesis of 2D lead chalcogenide NSs and NPLs is challenging since anisotropic crystal growth has to be realized for materials with an isotropic crystal structure [rock salt for PbX (X = S, Se, Te)].[1,20–22] While there are several ways to synthesize PbS NPLs[10,23] and NSs,[1,4,20,24] the selenium, and especially tellurium, analogues are far less accessible compared to PbS. Syntheses of 2D PbS and PbSe NPLs are commonly conducted in amine solvents (*e.g.*, *n*-octylamine) at comparatively low reaction temperatures (0–40°C). With these methods, the organometallic precursors can nucleate within soft lamellar amine bilayer templates supporting the 2D growth toward NPLs.[20] Following this approach, the limited synthetic access to PbSe and PbTe NPLs is presumably partially caused by a limited variety of precursors, which are sufficiently reactive at low temperatures, combined with a typically low stability of the final NPL product under ambient conditions. In addition to autoclave syntheses of PbTe NSs (with a thickness between 20 and 80 nm) by ZHU *et al.*[25] and PbSe/PbTe micropeonies composed of NPLs by JIN et al.,[26] CHATTERJEE and BISWAS[27] have synthesized $Pb_mBi_{2n}Te_{3n+m}$ NSs with a thickness of a few nanometers *via* a solution-based method. However, to the best of our knowledge, to date, no direct colloidal synthesis of ultrathin and optically active 2D PbTe NPLs has been reported.

Concerning the precursor chemistry, thiourea and selenourea as well as their substituted derivates have been thoroughly studied in the context of nanocrystal syntheses and have been successfully used, among other chalcogen sources, for the direct low-temperature synthesis of PbS and PbSe NPLs, respectively.[6,20,28,29]

MORRISON *et al.* obtained 1 nm thick PbS quantum platelets using thiourea as a sulfur source at 40°C and established the lamellar mesophase template mechanism for the formation of the platelets.[20] Similarly, our group has recently applied selenourea to directly synthesize PbSe NPLs at 0°C with efficient NIR emission [PL quantum yields (PLQY) up to 61% for PL at 989 nm (1.25 eV) and 27% for PL at 1265 nm (0.98 eV)].[6,9] However, reports on tellurourea and its derivates are scarce since it is prone to detelluration and is light as well as moisture sensitive and hardly soluble in low-polarity organic solvents due to elaborate aromatic carbene ligands being required to stabilize the C=Te bond.[30] Consequently, a different precursor chemistry is needed for the synthesis of PbTe NPLs. A common telluride source is trioctylphosphine telluride (TOP-Te), which has been used by IZQUIERDO *et al.* to synthesize NIR emitting HgTe NPLs [PLQY of 10% at 880 nm (1.41 eV) with 40 nm (57 meV) fwhm *via* cation exchange from CdTe NPLs].[31] However, TOP-Te lacks reactivity at the low temperatures required to synthesize 2D PbTe NPLs *via* a soft template mechanism.[32–34] SUN *et al.* have used tris(dimethylamino)phosphine telluride as a more reactive alternative to well-established TOP-Te sources for the synthesis of CdTe NPLs, $(CdTe)_{13}$ nanoclusters and CdTe nanowires and concluded that transaminated derivates are the actual reactive tellurium source in primary amine solvents.[32]

Here, we adapt aminophosphine precursor chemistry to present a straightforward synthesis for colloidal 2D PbTe NPLs with tunable near-infrared PL [910–1460 nm (1.36–0.85 eV), PLQY 1–14%] by using lead oleate and transaminated tris(dimethylamino)phosphine telluride at low reaction temperatures of 0°C. The colloidal stability of the as-synthesized PbTe NPLs is increased by quenching the reaction and passivating the NPLs surface with lead iodide in one step.

4.3 Experimental Section

4.3.1 Chemicals

Acetonitrile (≥ 99.5%), chloroform-d ($CDCl_3$, 99.8 atom % D), isopropanol (≥ 99.5%), lead(II) oxide (≥ 99.99%), methanol (≥ 99.8%), *n*-octylamine (99%), tellurium powder (30 mesh, 99.99%), tetrachloroethylene (TCE, ≥ 99%), triethylamine (≥ 99%), trifluoroacetic acid (99%), trifluoracetic anhydride (≥ 99%), and tris(dimethylamino)phosphine [$P(N(CH_3)_2)_3$, 97%] were purchased from SIGMA-ALDRICH/MERCK. *n*-Hexane (97%) was purchased from ACROS ORGANICS. Lead(II) iodide (99.99%) was purchased from ALFA AESAR. Oleic acid (90%) was purchased from ABCR. *n*-Octylamine and oleic acid were degassed by the freeze-pump-thaw method three times prior to being stored and used inside a nitrogen-filled glovebox. All other reagents were directly used as received from the listed suppliers.

4.3.2 Preparation of the Lead Oleate Precursor

Lead oleate was synthesized following an established procedure by HENDRICKS *et al.*[28] Accordingly, lead(II) oxide (10 g, 44.8 mmol) was dispersed in acetonitrile (20 mL) at 0°C; trifluoroacetic anhydride (6.2 mL, 44.8 mmol) and trifluoroacetic acid (0.7 mL, 9.1 mmol) were added, and after 15 min at 0°C, the clear solution was allowed to heat to room temperature. In a separate flask, oleic acid (90%, 25.4 g, 81 mmol), triethylamine (14.1 mL, 101 mmol), and isopropanol (180 mL) were mixed. Upon combining the two solutions, lead oleate was immediately obtained as a white precipitate. After recrystallization from isopropanol and generous washing with methanol, the lead oleate was dried under reduced pressure and stored under inert gas conditions (N_2) at -25°C. A stock solution (0.5 M) of lead oleate (2.31 g, 3.00 mmol) in *n*-octylamine (6.0 mL) was prepared and stored inside a nitrogen-filled glovebox and used for multiple PbTe NPL syntheses (within up to one month).

4.3.3 Preparation of the Aminophosphine Telluride Precursor

The aminophosphine telluride precursor preparation was adapted from SUN *et al.*[32] with the major difference that an *ex situ* transamination of tris(dimethylamino)phosphine with *n*-octylamine was performed prior to the PbTe NPL synthesis. A precursor stock solution (0.5 M) was prepared by heating a

stirred mixture of tellurium powder (255 mg, 2.00 mmol), tris(dimethylamino)-phosphine (2 mL, 11.0 mmol), and *n*-octylamine (2 mL, 12.1 mmol) to 100°C for 3 h under inert gas conditions. Subsequently, the ocher colored solution was filtered using a polytetrafluoroethylene syringe filter (pore size 0.2 µm), allowed to cool to room temperature, and used for multiple PbTe NPL syntheses (within up to 2 weeks).

4.3.4 Preparation of Lead Iodide Surface Passivation

A lead iodide stock solution (0.1 M) for quenching and passivating crude PbTe NPLs was prepared by dissolving lead iodide (461 mg, 1.00 mmol) in *n*-octylamine (7.87 mL, 47.5 mmol) and oleic acid (2.13 mL, 6.75 mmol) at 35°C for 1 h under stirring inside a nitrogen-filled glovebox.

4.3.5 PbTe NPL Synthesis

In a 5 mL round-bottom flask, 0.4 mL of the lead oleate precursor solution described above was diluted in hexane (3.6 mL) and cooled to 0°C under stirring. Subsequently, 0.2 mL of the aminophosphine telluride precursor solution was rapidly injected, causing the colorless solution to turn light brown. After a reaction time of 30 min, the increasingly dark mixture was quenched by injecting 2 mL of the lead iodide solution and diluted with hexane (6 mL). The passivated PbTe NPLs were stored at -25°C inside a nitrogen-filled glovebox and used for further experiments without precipitation.

4.3.6 NIR and UV-Vis-NIR Absorbance Spectroscopy

All samples for optical spectroscopy were prepared by diluting the colloidal PbTe NPLs in TCE (2.5 mL) in a quartz cuvette [quartz glass high-performance QS 200–2500 nm (6.20–0.5 eV) by HELLMA] with a path length of 1 cm [optical density below 0.2 at 500 nm (2.48 eV)]. NIR PL spectra were acquired by using an EDINBURGH FLS 1000 UV (ultraviolet)-vis (visible)-NIR PL spectrometer and a PTI QUANTAMASTER QM4 spectrofluorometer. The EDINBURGH FLS 1000 UV-vis-NIR spectrometer is equipped with a 450 W ozone-free xenon arc lamp for excitation. PL was monitored using a liquid-nitrogen-cooled InGaAs NIR photomultiplier tube 1650 detector from EDINBURGH. The PTI QUANTAMASTER QM4 spectrofluorometer is equipped with a 75 W steady-state xenon short arc lamp for excitation. PL was monitored by using a liquid-nitrogen-cooled PTI P1.7R detector

module (HAMAMATSU PMT R5509-72). To avoid higher order excitation light, a RG780 long pass filter glass plate (thickness = 3 mm) was used in the emission path. Spectral selection was achieved by single grating monochromators (excitation: 1200 grooves/mm, 300 nm blaze; NIR emission: 600 grooves/mm, 1200 nm blaze). PL spectra were collected by exciting PbTe NPLs at 500 nm (2.48 eV). Absolute PLQYs were determined with the FLS1000 spectrometer using an integrating sphere. For this, scattering at 500 nm (2.48 eV) and PL in the NIR region of both, the pure solvent and the NPLs, were separately measured, considering the sensitivity difference of both detectors with a correction factor. Multichannel scaling (MCS) PL lifetime analysis was performed with the FLS 1000 spectrometer equipped with a picosecond pulsed diode laser [pulse width of 110 ps at 445.1 nm (2.79 eV)] from EDINBURGH INSTRUMENTS.

Vis-NIR absorbance spectra were collected by using a CARY 5000 spectrophotometer from AGILENT TECHNOLOGIES.

4.3.7 High-Resolution Transmission Electron Microscopy

High resolution transmission electron microscopy (HRTEM) images were obtained using a JEOL ARM 200F equipped with a CETCOR aberration corrector operating at 80 kV. Samples for TEM analysis were prepared by drop casting the colloidal PbTe NPL solution onto graphene-coated QUANTIFOIL grids acquired from GRAPHENEA. The dry samples were washed with hexane.

4.3.8 Powder X-ray Diffraction

Powder X-ray diffraction (PXRD) patterns were measured in BRAGG-BRETANO geometry with a BRUKER D8 ADVANCE equipped with a Cu $K_{\alpha 1}$ source operating at 40 kV and 30 mA. For measuring diffractograms, colloidal PbTe NPL solutions were prepared by drop casting onto single crystal silicon sample holders.

4.3.9 Grazing-Incidence Wide-Angle X-ray Scattering

Grazing-incidence wide-angle X-ray scattering (GIWAXS) data were obtained at the P03 beamline of the PETRA III synchrotron facility at an incidence angle of 0.4° with an X-ray photon energy of 11.875 keV. The diffraction data were recorded with a LAMBDA 9 M detector placed 205 mm behind the sample. The samples were prepared by drop casting the colloidal PbTe NPL solution onto silicon wafers (5 mm × 5 mm, p-type doped with boron, ⟨100⟩ surface, purchased from PLANO).

4.3.10 Nuclear Magnetic Resonance Spectroscopy

Nuclear magnetic resonance (NMR) measurements were conducted with a BRUKER AVANCE III HDX 400 instrument with a frequency of 400 MHz. Samples were prepared by filtering each specimen through a polytetrafluoroethylene syringe filter (pore size 0.2 µm) and diluting in dry chloroform in an NMR tube inside a nitrogen-filled glovebox. Spectra were analyzed using BRUKER TOPSPIN 4.2.0 software. The residual solvent peak of chloroform-d (7.26 ppm) was used as an internal reference for the ^{1}H spectra. The ^{31}P spectra were measured with proton decoupling and indirectly referenced to the ^{1}H NMR frequency of the same sample using the "xiref"-function of BRUKER TOPSPIN 4.2.0.

4.3.11 X-ray Photoelectron Spectroscopy

X-ray photoelectron spectroscopy (XPS) data were collected using a PHI 5000 VERSAPROBE III instrument from ULVAC-PHI. The spectra were obtained with an aluminum X-ray source (Al K_α = 1486.6 eV) operating at 24.4 W with a beam diameter of 100 µm. Survey spectra were measured with a pass energy of 224 eV; high-resolution spectra were acquired with a pass energy of 27 eV. Charging effects were accounted for by setting the C 1s peak of sp^3 carbon to 284.4 eV. The samples for XPS analysis were prepared by drop casting the colloidal PbTe NPL solution onto a silicon wafer from PLANO and drying under a vacuum overnight.

4.4 Results and Discussion

4.4.1 Tunable Optical Properties of PbTe NPLs

Figure 4.1a–c includes HRTEM images of PbTe NPLs with three different lateral size distributions (corresponding size histograms are depicted in Figure S 4.1; typical TEM images used for determining the size are shown in Figure S 4.2). The majority of NPLs resemble a rectangular shape with rounded edges with occasionally more irregular shapes as well. Their crystal phase is determined by selected area electron diffraction (SAED, see Figure 4.1d) and PXRD (see Figure 4.1e). The SAED pattern is composed of the characteristic diffraction peaks of the cubic PbTe phase (space group $Fm\bar{3}m$) with the corresponding lattice spacings of 3.23 Å (200), 2.30 Å (220), and 1.50 Å (331) (PDF card 01-072-6645). Complementary to SAED, PXRD underpins the cubic rock salt structure of PbTe for the whole NPL ensemble. Additional information on the size and 2D shape of

PbTe NPLs is obtained by GIWAXS measurements of drop-casted solutions on silicon substrates (see Figure 4.1f). Clearly visible diffraction peaks suggest that the NPLs form a superlattice. The significant difference in the spacing between the diffraction peaks in the vertical and horizontal directions indicates that the superlattice has substantially different lattice parameter values in these two directions. Such a difference can be explained by the highly anisotropic shape of the NPLs. A possible superlattice structure is shown in Figure 4.1g (see Figure S 4.3 for complementary X-ray reflectivity data). The small interparticle distance of 0.5 nm suggests that the ordered NPLs (in this measurement) consist of a single (001) atomic layer of PbTe separated by iodide ligands (Pb-I bond length of ~0.32 nm).[35]

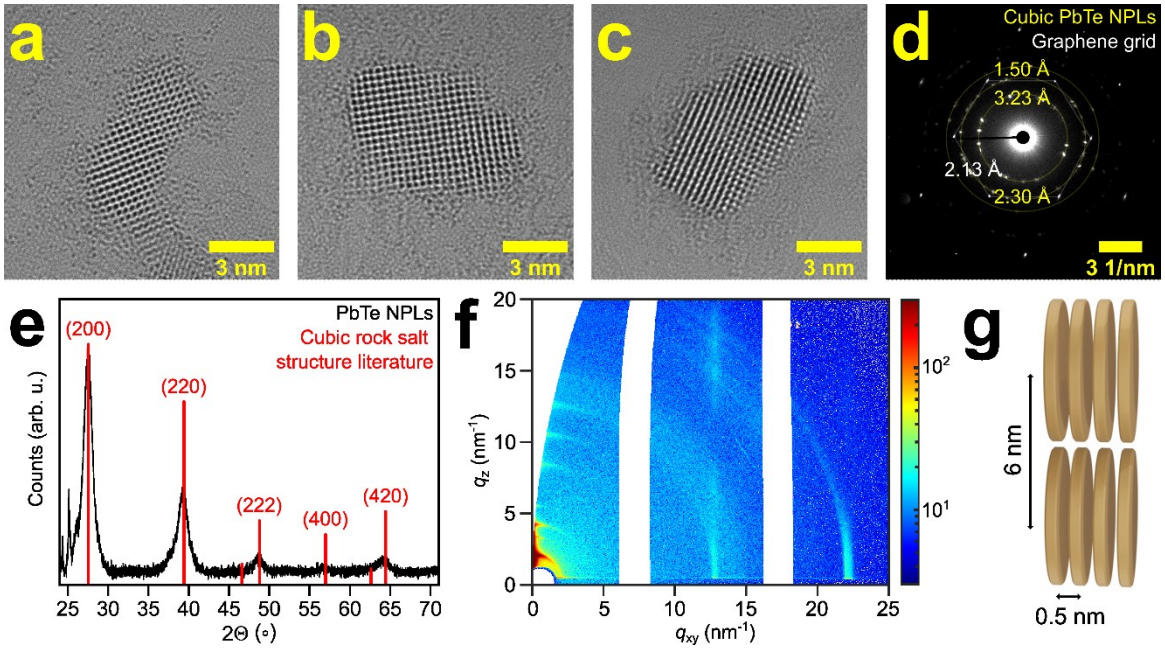

Figure 4.1. (a–c) HR-TEM images of PbTe NPLs exhibiting a slightly rectangular shape. (d) SAED of the PbTe NPL sample shown in (a) reveals their cubic rock salt crystal structure. (e) PXRD of a macroscopic PbTe NPL ensemble exhibits the cubic rock salt structure. (f) GIWAXS diffraction pattern of drop-casted PbTe NPLs on a silicon substrate (white areas correspond to detector gaps). The diffraction peaks in the vertical direction correspond to stacking in real space with a period of ~6 nm. The diffraction peaks in the horizontal direction indicate a periodicity of ~0.5 nm. (g) Possible scheme for a superlattice formed by PbTe NPLs with corresponding length scales.

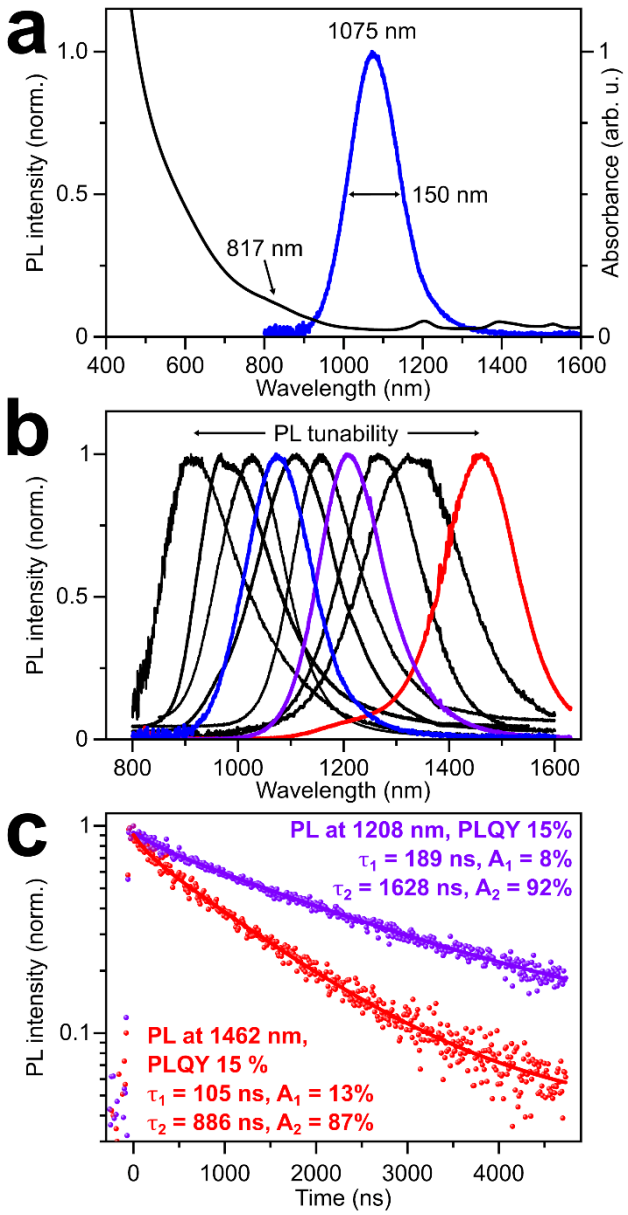

Figure 4.2. (a) Vis-NIR absorbance, (b) NIR PL spectra, and (c) MCS lifetimes of colloidal 2D PbTe NPLs. (a) Exemplary PbTe NPLs exhibit a length and width of (6.9 ± 0.75) × (4.9 ± 0.9) nm², excitonic absorbance at 817 nm (1.52 eV), PL at 1075 nm (1.15 eV) with a fwhm of 160 meV (150 nm), and a PLQY of 11%. (b) The PL of PbTe NPLs is tunable between 910 and 1460 nm (1.36–0.85 eV) by adjusting the NPLs size *via* the reaction conditions. (c) MCS lifetimes of PbTe NPLs with PL at 1208 (1.03 eV) and 1462 nm (0.85 eV). The biexponential decay is dominated by a long lifetime contribution ($\tau_{2,1208nm}$ = 1628 ns and $\tau_{2,1462nm}$ = 886 ns) for both PbSe NPL samples and attributed to band edge PL.

Figure 4.2a shows the absorbance and PL spectra of PbTe NPLs exhibiting a weakly pronounced feature at 817 nm (1.52 eV) and associated PL at 1075 nm (1.15 eV) with a fwhm of 160 meV (150 nm) and a PLQY of 11%. Besides the highly confined thickness of the NPLs (see Figure S 4.4), the large exciton BOHR radius of PbTe ($a_{B,transversal}$ = 152 nm, $a_{B,longitudinal}$ = 12.9 nm)[36] results in additional confinement in their lateral dimension (*i.e.*, strong confinement in all three dimensions, where $r/a_B \ll 1$).[37] Changes in the thickness and lateral size of the PbTe NPLs consequently lead to a continuous shift of the PL position and are synthetically achieved by altering the Pb/Te ratio used for synthesis. With a higher lead excess during synthesis, larger PbTe NPLs with PL shifted further into the NIR are obtained (see Figure S 4.5). Figure 4.2b illustrates the tunability of the PL maximum of PbTe NPLs in the range of 910–1460 nm (1.36–0.85 eV). The wide wavelength (energy) range combined with the absence of discrete steps (as has been observed for, *e.g.*, CdSe NPLs),[38,39] point toward a combined role of thickness and lateral size of the NPLs in shifting the PL maxima. PbTe NPLs shown in Figure 4.1a–c with average lengths of 7.1 ± 0.9, 7.7 ± 1.0, and 8.7 ± 2.2 nm, respectively, exhibit corresponding PL at 1217 nm (1.02 eV), 1293 nm (0.96 eV), and 1459 nm (0.85 eV) (see Figure S 4.1 and Figure S 4.5). NPL widths do not strictly follow this trend (see Figure S 4.1), underpinning that the confined thickness dimension predominately determines the PL position, while the lateral dimension plays a smaller role (it has to be noted that the determined NPL widths exhibit higher relative error margins due to the varying NPL shape). The fwhm of the PL signals shown in Figure 4.2b varies between 282 meV (190 nm) for PL at 910 nm (1.36 eV) and 100 meV (173 nm) for PL further in the NIR at 1460 nm (0.85 eV). Not all PL signals strictly follow this trend, which we attribute to an inhomogeneous broadening of the PL signals caused by the size distribution of the NPLs. Compared to fwhm values of directly synthesized colloidal 2D PbSe NPLs [214 meV (164 nm) for PL at 976 nm (1.27 eV) and 184 meV (269 nm) for PL at 1362 nm (0.91 eV)],[6] the PbTe NPLs shown here exhibit broader PL at shorter wavelengths but significantly narrower PL at longer wavelengths approaching the low-loss third telecommunication window around 1550 nm (0.80 eV).[11] Within the PL tunability range, the PLQY of PbTe NPLs gradually rises from 1% near 900 nm (1.38 eV) up to 15% for PL maxima above 1265 nm (0.98 eV) (Figure S 4.6). This trend of a generally increasing PLQY toward longer NIR wavelengths is different

from previous descriptions for PbS and PbSe NCs and NPLs, where larger radii or lateral sizes are associated with a reduced PLQY.[6,9,40] Here, a decreasing PLQY in smaller band gap NCs and NPLs is explained by the *energy gap law*, which expresses the exponential relationship of the transition rate and energy difference between two states: nonradiative recombination rates are increased in larger NCs and NPLs, where dark trap states are located closer to the band edge.[40] While trap states in PbX NPLs are expected to be caused mainly by undercoordinated edge or ledge atoms at the surface (of which larger NPLs contain a lower fraction compared with smaller NPLs), the energy gap law counteracts this positive influence on the PLQY for PbS and PbSe NPLs. In contrast, for PbTe, the lower fraction of edge or ledge atoms in larger NPLs seems to outweigh the negative effect of the energy gap law on the PLQY. This reversed influence in PbTe NPLs could be, *e.g.*, caused by dark trap states located further away from the conduction band edge energetically compared to PbS and PbSe NPLs and an associated a reduced effect of accelerated recombination to dark states in larger NPLs.

MCS PL lifetimes of PbTe NPLs (see Figure 4.2) are fitted biexponentially with a minor short lifetime contribution and a dominating long lifetime contribution. For PbTe NPLs emitting at 1208 nm (1.03 eV) and 1462 nm (0.85 eV), time constants of $\tau_{1,1208nm}$ = 189 ns (8%) and $\tau_{2,1208nm}$ = 1628 ns (92%) as well as $\tau_{1,1462nm}$ = 105 ns (13%) and $\tau_{2,1462nm}$ = 886 ns (87%) are determined (R^2 = 0.99 and R^2 = 0.99). In accordance with previous work on PbX (X = S, Se) NCs and NPLs, we attribute these two lifetime contributions to two different radiative recombination pathways. We assign the shorter lifetime contribution to the *energy gap law* and associated defect emission, while the dominant longer lifetimes are ascribed to band edge emission.[9,41,42] The biexponential nature and the depicted lifetimes are in good agreement with values reported by LIN *et al.* for spherical PbTe QDs capped with oleylamine in TCE [τ_1 = 96 ns (34%) and τ_2 = 1490 ns (66%)],[43] as well as our previous work on colloidal PbSe NPLs passivated with $CdCl_2$ [τ_{1PL} = 168 ns (15%) and τ_{2PL} = 1320 ns (85%) for PL at 980 nm (1.27 eV)].[6] The smaller contribution of the shorter lifetime in PbI_2-passivated PbTe NPLs (8 and 13%, respectively) [and the $CdCl_2$-passivated PbSe NPLs (15%)] compared to the 34:66 ratio for oleylamine-capped PbTe QDs, indicate that the fast recombination can be suppressed by a more complete surface passivation, *i.e.*, it is related to defect emission. Furthermore, GALLE *et al.* determined slightly longer PL lifetimes of

0.7–2.7 µs for PbSe NPLs synthesized *via* cation exchange from CdSe (depending on the thickness of the initial CdSe NPLs),[6,8] and BABAEV *et al.* reported PL lifetimes of ~2 µs for PbSe/PbS core/shell NPLs obtained *via* cation exchange from CdSe/CdS core/shell NPLs.[44] It should be noted that KHAN *et al.* found significantly shorter PL lifetimes in the range of 8.4–59 ns for colloidal 2D PbS NPLs with PL ranging from 735 to 748 nm, although such short lifetimes have not been reported for selenium (and tellurium) analogues.[23] Generally, room temperature PL lifetimes of lead chalcogenide NPLs are significantly longer in comparison to those of CdSe NPLs (faster than 10 ns).[38,39] Theoretical calculations for spherical PbSe and CdSe NCs have ascribed long PL lifetimes in PbSe NCs to a reduced oscillator strength of the lowest energy bright exciton states caused by intervalley coupling among the four equivalent L points in the BRILLOUIN zone.[45] Given that PbTe exhibits the same crystal structure (cubic rock salt) as well as a similar band gap and structure as PbSe,[46] we assume the same holds for the comparatively long PL lifetimes in 2D PbTe NPLs.

4.4.2 Synthesis of PbTe NPLs

Lead oleate and lead acetate (which is converted to lead oleate *in situ*) are commonly used as lead sources for the synthesis of 2D PbS and PbSe NPLs.[6,20] Lead oleate was also chosen as a Pb precursor in this work for PbTe NPLs, as it is readily soluble in amines at low temperatures. Our initial efforts for finding a suitable tellurium precursor are based on work by SUN *et al.*, who used tris(dimethylamino)phosphine telluride for the synthesis of CdTe NPLs, $(CdTe)_{13}$ nanoclusters, and CdTe nanowires at temperatures as low as 70°C in case of the nanoclusters.[32] For this, tellurium granules were dissolved in tris(dimethylamino)-phosphine at a molar ratio of 1:5.5 at 100°C for 3 h and yielded a yellow solution. However, when cooling down to room temperature, white crystals of $TeP(N(CH_3)_2)_3$ precipitated from the solution, hindering the use in a low-temperature synthetic approach. When circumventing precipitation by injecting a yellow $TeP(N(CH_3)_2)_3$ solution at elevated temperatures prior to precipitation, no reaction with $Pb(oleate)_2$ at 0°C occurred. This observation can be rationalized by the findings of SUN *et al.*, who inferred that transaminated $TeP(N(CH_3)_2)_3$ derivates are the active tellurium precursor in their syntheses. The transamination of aminophosphines with amines, usually oleyl- or octylamine, is well-known.[47,48] For

instance, TESSIER *et al.* reported on the role of tris(oleylamino)phosphine during the synthesis of InP quantum dots in oleylamine as an explanation for similar results regardless of the initial use of tris(dimethylamino)phosphine or tris(diethylamino)phosphine.[49]

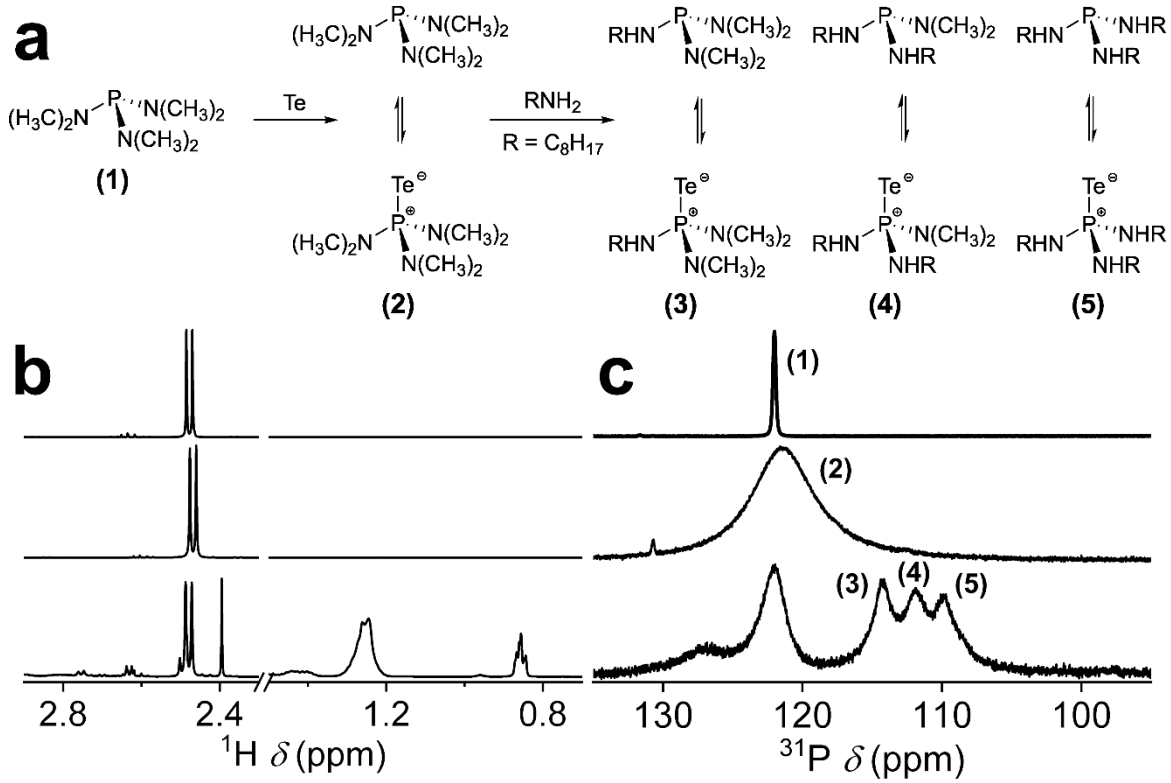

Figure 4.3. (a) Scheme of the combined telluration and transamination reaction of tris(dimethylamino)phosphine [$P(N(CH_3)_2)_3$] with tellurium and *n*-octylamine. (b) ^{1}H- and (c) ^{31}P{^{1}H}-NMR spectra of pure tris(dimethylamino)phosphine [$P(N(CH_3)_2)_3$ (1)], tris(dimethylamino)phosphine telluride [$TeP(N(CH_3)_2)_3$ / $(P(N(CH_3)_2)_3$ (2)], and transaminated tris(dimethylamino)phosphine telluride $TeP(N(CH_3)_2)_{3-x}(NHR)_x$/$P(N(CH_3)_2)_{3-x}(NHR)_x$, R = C_8H_{17} (3–5)) in $CDCl_3$. The presence of three phosphorus resonances corresponding to the triple (5), double (4), and single (3) transaminated aminophosphine underpins the successful transamination reaction.

For the synthesis of PbTe, we apply *ex situ* transamination by dissolving tellurium in a mixture of tris(dimethylamino)phosphine and *n*-octylamine at 100°C for 3 h prior to the PbTe NPL synthesis (see Figure 4.3a). At first, we obtained the same yellow solution as in the absence of the octylamine, but over time the color of the

mixture changed from yellow to ocher, and no precipitation occurred when cooling down to room temperature. During the reaction time, intense gas formation was observed, similar to what has been described by TESSIER *et al.* (*via* a $CuSO_4$ gas trap)[49] and SUN *et al.* (*via* $^{13}C\{^1H\}$ and ^1H NMR)[32] as dimethylamine and indicating a successful transamination reaction. Figure 4.3b,c shows ^1H- and $^{31}P\{^1H\}$-NMR spectra of pure tris(dimethylamino)phosphine [$P(N(CH_3)_2)_3$ (1)], tris-(dimethylamino)phosphine telluride [$TeP(N(CH_3)_2)_3$/$P(N(CH_3)_2)_3$ (2)], and trans-aminated tris(dimethylamino)phosphine telluride [$TeP(N(CH_3)_2)_{3-x}(NHR)_x$/ $P(N(CH_3)_2)_{3-x}(NHR)_x$, R = C_8H_{17} (3–5)] in $CDCl_3$ in the range of 0.7–3.05 ppm and 95–135 ppm [0–95 ppm available in the Supporting Information (Figure S 4.7)]. The $^{31}P\{^1H\}$-NMR spectra were evaluated by comparison to literature values and with the help of heteronuclear multiple bond correlation (HMBC) NMR spectra shown in the Supporting Information (Figure S 4.8–Figure S 4.10).[32,49,50] The ^1H NMR spectrum of pure tris(dimethylamino)phosphine (1) features a single doublet resonance at 2.48 ppm with a coupling constant of 9.15 Hz corresponding to the PN*CH*$_3$ protons coupling to the phosphorus atom. The associated $^{31}P\{^1H\}$-NMR spectrum shows a single sharp resonance of $P(N(CH_3)_2)_3$ at 122 ppm. Upon telluration, (2) strong broadening of the $P(N(CH_3)_2)_3$ resonance around 122 ppm occurs, which might be attributed to the enduring reaction dynamic. The PN*CH*$_3$ resonance in ^1H NMR is barely shifted to 2.47 ppm with an increased coupling constant of 9.69 Hz. The ^1H NMR spectra of transaminated tris(dimethylamino)phosphine telluride [$TeP(N(CH_3)_2)_{3-x}(NHR)_x$/$P(N(CH_3)_2)_{3-x}$ $(NHR)_x$, R = C_8H_{17} (3–5)] exhibits the *CH*$_3$ resonance of $P(N(CH_3)_2)_3$ (at 2.48 ppm, J = 9.55 Hz) as well as several multiplets or broad signals attributed to the protons of the aliphatic carbon chain of n-octylamine or *n*-octylamino groups in different chemical environments. The corresponding $^{31}P\{^1H\}$-NMR contains three new resonances upfield shifted with respect to the tris(dimethylamino)phosphine telluride resonance at 122 ppm. The three resonances at 110, 112, and 114 ppm are assigned to the triple (5), double (4), and single (3) transaminated aminophosphine, thus confirming the successful transamination of tris(dimethylamino)phosphine telluride.[32,49] This assignment is substantiated by $^{31}P\{^1H\}$-NMR spectra of aliquots from the transamination reaction mixture at different temperatures (Figure S 4.11a). The three ^{31}P resonances arise in order from 3 to 5 when heating from 40 °C to the reaction temperature of 100 °C,

indicating a gradual substitution of the initial dimethylamino group (-NMe_2). Combined with the images of the collected aliquots (Figure S 4.11b), which show a distinct color change upon reaching 100°C, the spectra underpin the prerequisite of the *ex situ* transamination since substitution would not occur at PbTe NPL synthesis temperature of 0°C.

By utilization of the *ex situ* transaminated aminophosphine telluride for our synthesis, PbTe NPLs were obtained within a reaction time of 30 min at 0°C. To conclude a specific reaction pathway and a definitive reason for the necessity of the transamination, a comprehensive mechanistic study would be required. In analogy to SUN *et al.*, we expect a nucleophilic substitution of one oleate (in lead oleate) by the transaminated aminophosphine telluride *via* a nucleophilic attack from the telluride on the lead, followed by a nucleophilic attack of the eliminated oleate on the phosphorus, which results in the formation of PbTe and the second oleate (see

Figure S 4.12).[32] Coherently, we assume the enhanced reactivity of the transaminated aminophosphine telluride may be caused by the increased nucleophilicity of the phosphorus atom. The electron-donating character of the long alkyl chains combined with the electron-donating character of the amino nitrogen lone pairs contributes to the stabilization of a positive charge on the phosphorus atom and facilitates the release of Te^{2-} for the formation of PbTe.[32,49] In contrast to high-temperature syntheses with aminophosphine precursors in which the high-boiling amine solvents primarily determine the reactivity, the *ex situ* transamination allows to further tune the precursor reactivity *via* the organic tail group of the amine (see Figure S 4.13). The use of aminophosphine telluride precursors transaminated with linear aliphatic primary amines of increasing chain lengths for PbTe NPL synthesis results in a bathochromic shift of the PL maximum. We propose that longer alkyl chains reduce the reactivity of the tellurium precursor due to steric hindrance and consequently result in the formation of larger PbTe NPLs with PL further shifted into the NIR.

4.4.3 Passivation of PbTe NPLs

To increase the colloidal stability of the as-synthesized PbTe NPLs, postsynthetic surface passivation with lead iodide was performed. Lead iodide can act as both, X- and Z-type ligands and passivate dangling bonds of unsaturated lead or chalcogen surface sites.[9] Figure 4.4 shows XPS analysis of the Pb-4f and Te-3d core level regions of pristine and PbI_2-passivated PbTe NPLs. All components are fitted by symmetric VOIGT functions (convolution of a LORENTZIAN and GAUSSIAN distribution) with maxima corresponding to the binding energies of the different atomic species.

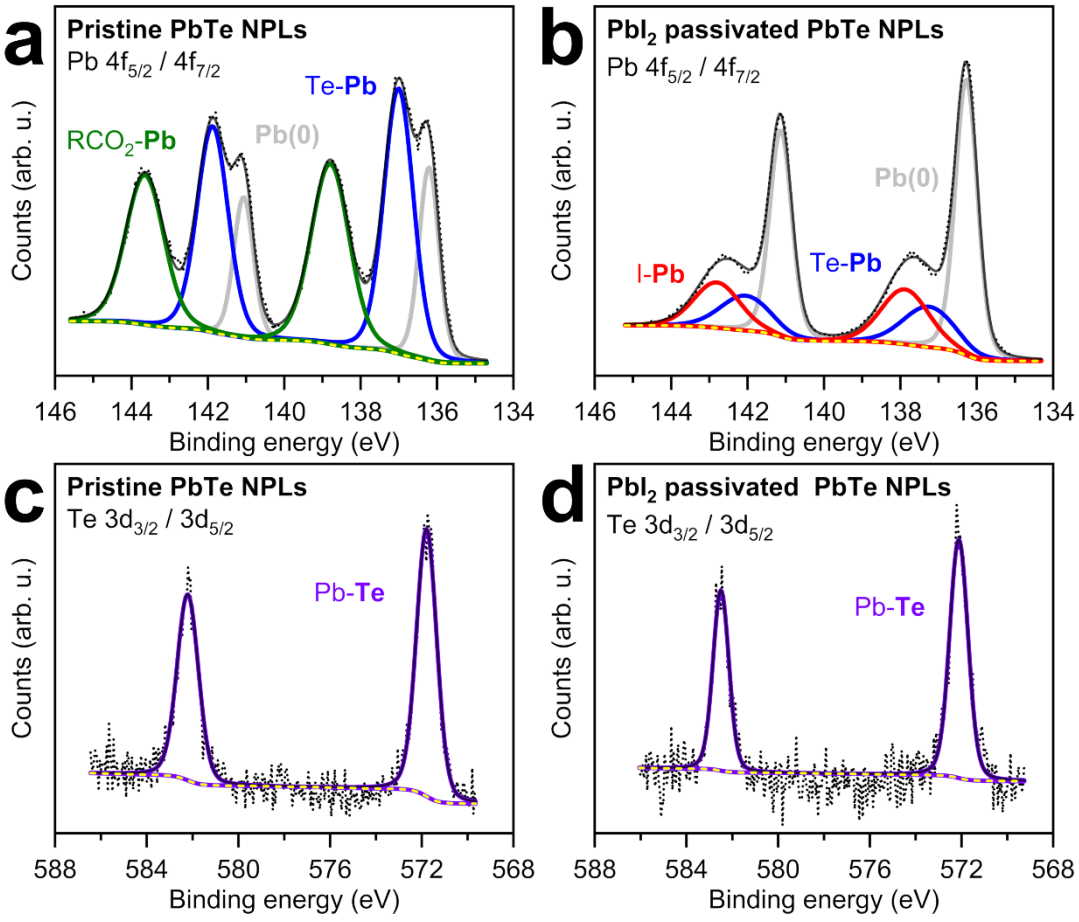

Figure 4.4. XPS analysis of the (a,b) Pb-4f and (c,d) Te-3d core levels of pristine and PbI_2-passivated PbTe NPLs. The RCO_2–Pb (R = $C_7H_{14}CH{=}CHC_8H_{17}$) component vanishes upon lead iodide treatment and is replaced by an I-Pb signal, indicating the successful X-type ligand exchange of oleate with iodide. Passivation with lead iodide results in improved colloidal stability compared with pristine PbTe NPLs and leads to preservation of optical properties during storage of PbTe NPLs (see Figure S 4.14).

The spin-orbit doublet in the range of 135–145 eV is composed of the 4f7/2 and 4f5/2 signals of lead and is fitted by four different components (Figure 4.4a,b). The lowest energy component at 136.2 and 141.1 eV for pristine PbTe NPLs and 136.3 and 141.1 eV for PbI_2-passivated PbTe NPLs is attributed to elemental lead in the oxidation state zero. The formation of metallic lead *via* photodegradation under XPS conditions has previously been reported for lead halide perovskite nanocrystals capped with oleic acid/oleylamine.[51,52] In particular, the presence of PbI_2/I^- is associated with a high degree of photodegradation, thus explaining the high intensity of the Pb(0) signal in PbI_2-passivated NPLs. The second component at 137.3 and 142.1 eV (pristine) as well as 137.0 and 141.9 eV (passivated) PbTe NPLs is ascribed to lead bound to tellurium.[53,54] The highest energy component in case of the pristine PbTe NPLs occurs at 138.8 and 143.6 eV and corresponds to lead bound to carboxylate.[55,56] Upon surface passivation with lead iodide, this signal disappears, and a new component, ascribed to lead bound to iodide, emerges at 137.9 and 142.8 eV. We conclude a successful passivation of the pristine PbTe NPL surfaces by X-type ligand exchange of oleate with iodide. The tellurium $3d_{3/2}$ and $3d_{5/2}$ spin-orbit doublet in the range of 570–584 eV in Figure 4.4c,d is fitted by a single component assigned to tellurium bound to lead.[57] The small shift of 0.3 eV for the signals of the passivated PbTe NPLs (571.8 to 572.1 eV and 582.2 to 582.5 eV) could be an indication of the change in the chemical environment upon introduction of the iodide to the NPLs surface. Figure S 4.14 shows a photograph of the pristine PbTe NPLs compared with the passivated NPLs 24 h after the synthesis. Pristine NPLs exhibited a color change from dark brown to black, and a black precipitate formed in solution, while metallic/elemental tellurium formed on the inside of the vial. On the other hand, iodide-passivated PbTe NPLs preserve their dark brown color, colloidal stability, and optical properties. We assume a double role of lead iodide in passivating the NPL surface and in forming a stable iodophosphonium salt $[IP(N(CH_3)_2)_{3-x}(NHR)_x]^+I^-$ ($R = C_8H_{17}$) as a byproduct in analogy to the proposed pathway by SUN *et al.* for the reaction of transaminated tris(dimethylamino)-phosphine with $CdCl_2$ toward CdTe nanostructures.[32] By employing PbI_2 passivation, we obtain colloidal PbTe NPL solutions that are long-term stable (multiple months), can be postprocessed for measurements under ambient conditions, and be drop casted or spin coated onto different substrates.

4.5 Conclusion

Up to now, there has been no direct wet-chemical pathway to 2D PbTe NPLs with tunable and efficient NIR photoluminescence. Here, we demonstrate a low-temperature colloidal synthesis of 2D PbTe NPLs with a cubic rock salt structure by using highly reactive aminophosphine telluride precursor chemistry. Our corresponding comprehensive NMR study shows the synthetic importance of an *ex situ* transamination reaction of tris(dimethylamino)phosphine telluride for sufficient precursor reactivity at 0°C to form 2D PbTe NPLs. Associated GIWAXS measurements confirm the 2D geometry of PbTe NPLs and the formation of superlattices from stacked NPLs. Postsynthetically PbI_2-passivated PbTe NPLs exhibit tunable NIR PL between 910 and 1460 nm (1.36–0.85 eV) (PLQY 1–15%) and narrow fwhm [100 meV (173 nm)], especially at longer wavelengths. By matching the precursor reactivity of aminophosphine telluride with lead oleate, we have now complemented synthetic access to 2D PbS and PbSe NPLs by 2D PbTe, which will help to further tune, explore, and make use of the strong excitonic effects in 2D NPLs in the NIR.

4.6 References

(1) Schliehe, C.; Juarez, B. H.; Pelletier, M.; Jander, S.; Greshnykh, D.; Nagel, M.; Meyer, A.; Foerster, S.; Kornowski, A.; Klinke, C.; Weller, H. Ultrathin PbS Sheets by Two-Dimensional Oriented Attachment. *Science* **2010**, *329*, 550–553.

(2) Galle, T.; Spittel, D.; Weiß, N.; Shamraienko, V.; Decker, H.; Georgi, M.; Hübner, R.; Metzkow, N.; Steinbach, C.; Schwarz, D.; Lesnyak, V.; Eychmüller, A. Simultaneous Ligand and Cation Exchange of Colloidal CdSe Nanoplatelets toward PbSe Nanoplatelets for Application in Photodetectors. *J. Phys. Chem. Lett.* **2021**, *12* (21), 5214–5220.

(3) Dogan, S.; Bielewicz, T.; Lebedeva, V.; Klinke, C. Photovoltaic Effect in Individual Asymmetrically Contacted Lead Sulfide Nanosheets. *Nanoscale* **2015**, *7*, 4875–4883.

(4) Akkerman, Q. A.; Martín-García, B.; Buha, J.; Almeida, G.; Toso, S.; Marras, S.; Bonaccorso, F.; Petralanda, U.; Infante, I.; Manna, L. Ultrathin Orthorhombic PbS Nanosheets. *Chem. Mater.* **2019**, *31* (19), 8145–8153.

(5) Babaev, A. A.; Skurlov, I. D.; Timkina, Y. A.; Fedorov, A. V. Colloidal 2D Lead Chalcogenide Nanocrystals: Synthetic Strategies, Optical Properties, and Applications. *Nanomaterials* **2023**, *13* (11), 1797.

(6) Klepzig, L. F.; Biesterfeld, L.; Romain, M.; Niebur, A.; Schlosser, A.; Hübner, J.; Lauth, J. Colloidal 2D PbSe Nanoplatelets with Efficient Emission Reaching the Telecom O-, E- and S-Band. *Nanoscale Adv.* **2022**, *4*, 590–599.

(7) Zhou, Y.; Celikin, M.; Camellini, A.; Sirigu, G.; Tong, X.; Jin, L.; Basu, K.; Tong, X.; Barba, D.; Ma, D.; Sun, S.; Vidal, F.; Zavelani-Rossi, M.; Wang, Z. M.; Zhao, H.; Vomiero, A.; *et al.* Ultrasmall Nanoplatelets: The Ultimate Tuning of Optoelectronic Properties. *Adv. Energy Mater.* **2017**, *7*, 1602728.

(8) Galle, T.; Samadi Khoshkhoo, M.; Martin-Garcia, B.; Meerbach, C.; Sayevich, V.; Koitzsch, A.; Lesnyak, V.; Eychmüller, A. Colloidal PbSe Nanoplatelets of Varied Thickness with Tunable Optical Properties. *Chem. Mater.* **2019**, *31* (10), 3803–3811.

(9) Biesterfeld, L.; Klepzig, L. F.; Niebur, A.; Rosebrock, M.; Lauth, J. Toward Bright Colloidal Near-Infrared Emitters: Surface Passivation of 2D PbSe Nanoplatelets by Metal Halides. *J. Phys. Chem. C* **2022**, *126* (45), 19277–19285.

(10) Manteiga Vázquez, F.; Yu, Q.; Klepzig, L. F.; Siebbeles, L. D. A.; Crisp, R. W.; Lauth, J. Probing Excitons in Ultrathin PbS Nanoplatelets with Enhanced Near-Infrared Emission. *J. Phys. Chem. Lett.* **2021**, *12* (1), 680–685.

(11) Harrison, M. T.; Kershaw, S. V.; Burt, M. G.; Rogach, A. L.; Kornowski, A.; Eychmüller, A.; Weller, H. Colloidal Nanocrystals for Telecommunications. Complete Coverage of the Low-Loss Fiber Windows by Mercury Telluride Quantum Dot. *Pure Appl. Chem.* **2000**, *72* (1–2), 295–307.

(12) Aerts, M.; Bielewicz, T.; Klinke, C.; Grozema, F. C.; Houtepen, A. J.; Schins, J. M.; Siebbeles, L. D. A. Highly Efficient Carrier Multiplication in PbS Nanosheets. *Nat. Commun.* **2014**, *5*, 3789.

(13) Ramin Moayed, M. M.; Bielewicz, T.; Zöllner, M. S.; Herrmann, C.; Klinke, C. Towards Colloidal Spintronics Through Rashba Spin-Orbit Interaction in Lead Sulphide Nanosheets. *Nat. Commun.* **2017**, *8*, 15721.

(14) Lauth, J.; Failla, M.; Klein, E.; Klinke, C.; Kinge, S.; Siebbeles, L. D. A. Photoexcitation of PbS Nanosheets Leads to Highly Mobile Charge Carriers and Stable Excitons. *Nanoscale* **2019**, *11*, 21569–21576.

(15) Dogan, S.; Bielewicz, T.; Cai, Y.; Klinke, C. Field-Effect Transistors Made of Individual Colloidal PbS Nanosheets. *Appl. Phys. Lett.* **2012**, *101*, 073102.

(16) Krishnamurthy, S.; Singh, A.; Hu, Z.; Blake, A. V.; Kim, Y.; Singh, A.; Dolgopolova, E. A.; Williams, D. J.; Piryatinski, A.; Malko, A. V.; Htoon, H.; Sykora, M.; Hollingsworth, J. A. PbS/CdS Quantum Dot Room-Temperature Single-Emitter Spectroscopy Reaches the Telecom O and S Bands via an Engineered Stability. *ACS Nano* **2021**, *15* (1), 575–587.

(17) Hanson, C. J.; Hartmann, N. F.; Singh, A.; Ma, X.; DeBenedetti, W. J. I.; Casson, J. L.; Grey, J. K.; Chabal, Y. J.; Malko, A. V.; Sykora, M.; Piryatinski, A.; Htoon, H.; Hollingsworth, J. A. Giant PbSe/CdSe/CdSe Quantum Dots: Crystal-Structure-Defined Ultrastable Near-Infrared Photoluminescence from Single Nanocrystals. *J. Am. Chem. Soc.* **2017**, *139* (32), 11081–11088.

(18) Harman, T. C.; Spears, D. L.; Manfra, M. J. High Thermoelectric Figures of Merit in PbTe Quantum Wells. *J. Electron. Mater.* **1996**, *25*, 1121–1127.

(19) Dresselhaus, M. S.; Chen, G.; Tang, M. Y.; Yang, R. G.; Lee, H.; Wang, D. Z.; Ren, Z. F.; Fleurial, J.-P.; Gogna, P. New Directions for Low-Dimensional Thermoelectric Materials. *Adv. Mater.* **2007**, *19*, 1043–1053.

(20) Morrison, P. J.; Loomis, R. A.; Buhro, W. E. Synthesis and Growth Mechanism of Lead Sulfide Quantum Platelets in Lamellar Mesophase Templates. *Chem. Mater.* **2014**, *26* (17), 5012–5019.

(21) Son, J. S.; Wen, X.-D.; Joo, J.; Chae, J.; Baek, S.-I.; Park, K.; Kim, J. H.; An, K.; Yu, J. H.; Kwon, S. G.; Choi, S.-H.; Wang, Z.; Kim, Y.-W.; Kuk, Y.; Hoffmann, R.; Hyeon, T. Large-Scale Soft Colloidal Template Synthesis of 1.4 nm Thick CdSe Nanosheets. *Angew. Chem., Int. Ed.* **2009**, *48*, 6861–6864.

(22) Liu, Y.-H.; Wang, F.; Wang, Y.; Gibbons, P. C.; Buhro, W. E. Lamellar Assembly of Cadmium Selenide Nanoclusters into Quantum Belts. *J. Am. Chem. Soc.* **2011**, *133* (42), 17005–17013.

(23) Khan, A. H.; Brescia, R.; Polovitsyn, A.; Angeloni, I.; Martín-García, B.; Moreels, I. Near-Infrared Emitting Colloidal PbS Nanoplatelets: Lateral Size Control and Optical Spectroscopy. *Chem. Mater.* **2017**, *29* (7), 2883–2889.

(24) Bielewicz, T.; Ramin Moayed, M. M.; Lebedeva, V.; Strelow, C.; Rieckmann, A.; Klinke, C. From Dots to Stripes to Sheets: Shape Control of Lead Sulfide Nanostructures. *Chem. Mater.* **2015**, *27* (24), 8248–8254.

(25) Zhu, T. J.; Chen, X.; Meng, X. Y.; Zhao, X. B.; He, J. Anisotropic Growth of Cubic PbTe Nanoparticles to Nanosheets: Controlled Synthesis and Growth Mechanisms. *Cryst. Growth Des.* **2010**, *10* (8), 3727–3731.

(26) Jin, R.; Chen, G.; Pei, J.; Sun, J.; Wang, Q. Controllable Synthesis and Thermoelectric Transport Properties of Binary-Phased PbTe/PbSe Nanocrystals. *CrystEngComm* **2012**, *14*, 4461–4466.

(27) Chatterjee, A.; Biswas, K. Solution-Based Synthesis of Layered Intergrowth Compounds of the Homologous $Pb_mBi2_nTe_{3n+m}$ Series as Nanosheets. *Angew. Chem., Int. Ed.* **2015**, *54*, 5623–5627.

(28) Hendricks, M. P.; Campos, M. P.; Cleveland, G. T.; Jen-La Plante, I.; Owen, J. S. A Tunable Library of Substituted Thiourea Precursors to Metal Sulfide Nanocrystals. *Science* **2015**, *348*, 1226–1230.

(29) Campos, M. P.; Hendricks, M. P.; Beecher, A. N.; Walravens, W.; Swain, R. A.; Cleveland, G. T.; Hens, Z.; Sfeir, M. Y.; Owen, J. S. A Library of Selenourea Precursors to PbSe Nanocrystals with Size Distributions near the Homogeneous Limit. *J. Am. Chem. Soc.* **2017**, *139* (6), 2296–2305.

(30) Ritch, J. S. Synthesis and Coordination Chemistry of Cyclic Seleno- and Telluroureas. *Phys. Sci. Rev.* **2019**, *4*, 20170128.

(31) Izquierdo, E.; Robin, A.; Keuleyan, S.; Lequeux, N.; Lhuillier, E.; Ithurria, S. Strongly Confined HgTe 2D Nanoplatelets as Narrow Near-Infrared Emitters. *J. Am. Chem. Soc.* **2016**, *138* (33), 10496–10501.

(32) Sun, H.; Wang, F.; Buhro, W. E. Tellurium Precursor for Nanocrystal Synthesis: Tris(dimethylamino)phosphine Telluride. *ACS Nano* **2018**, *12* (12), 12393–12400.

(33) Wang, Y.; Zhou, Y.; Zhang, Y.; Buhro, W. E. Magic-Size II-VI Nanoclusters as Synthons for Flat Colloidal Nanocrystals. *Inorg. Chem.* **2015**, *54* (3), 1165–1177.

(34) Zhang, J.; Jin, S.; Fry, H. C.; Peng, S.; Shevchenko, E.; Wiederrecht, G. P.; Rajh, T. Synthesis and Characterization of Wurtzite ZnTe Nanorods with Controllable Aspect Ratios. *J. Am. Chem. Soc.* **2011**, *133* (39), 15324–15327.

(35) Sinha, S.; Zhu, T.; France-Lanord, A.; Sheng, Y.; Grossman, J. C.; Porfyrakis, K.; Warner, J. H. Atomic Structure and Defect Dynamics of Monolayer Lead Iodide Nanodisks with Epitaxial Alignment on Graphene. *Nat. Commun.* **2020**, *11*, 823.

(36) Murphy, J. E.; Beard, M. C.; Norman, A. G.; Ahrenkiel, S. P.; Johnson, J. C.; Yu, P.; Mićić, O. I.; Ellingson, R. J.; Nozik, A. J. PbTe Colloidal Nanocrystals: Synthesis, Characterization, and Multiple Exciton Generation. *J. Am. Chem. Soc.* **2006**, *128* (10), 3241–3247.

(37) Wise, F. W. Lead Salt Quantum Dots: The Limit of Strong Quantum Confinement. *Acc. Chem. Res.* **2000**, *33* (11), 773–780.

(38) Ithurria, S.; Bousquet, G.; Dubertret, B. Continuous Transition from 3D to 1D Confinement Observed during the Formation of CdSe Nanoplatelets. *J. Am. Chem. Soc.* **2011**, *133* (9), 3070–3077.

(39) Christodoulou, S.; Climente, J. I.; Planelles, J.; Brescia, R.; Prato, M.; Martín-García, B.; Khan, A. H.; Moreels, I. Chloride-Induced Thickness Control in CdSe Nanoplatelets. *Nano Lett.* **2018**, *18* (10), 6248–6254.

(40) Semonin, O. E.; Johnson, J. C.; Luther, J. M.; Midgett, A. G.; Nozik, A. J.; Beard, M. C. Absolute Photoluminescence Quantum Yields of IR-26 Dye, PbS, and PbSe Quantum Dots. *J. Phys. Chem. Lett.* **2010**, *1* (16), 2445–2450.

(41) Hyun, B.-R.; Chen, H.; Rey, D. A.; Wise, F. W.; Batt, C. A. Near-Infrared Fluorescence Imaging with Water-Soluble Lead Salt Quantum Dots. *J. Phys. Chem. B* **2007**, *111* (20), 5726–5730.

(42) Caram, J. R.; Bertram, S. N.; Utzat, H.; Hess, W. R.; Carr, J. A.; Bischof, T. S.; Beyler, A. P.; Wilson, M. W. B.; Bawendi, M. G. PbS Nanocrystal Emission Is Governed by Multiple Emissive States. *Nano Lett.* **2016**, *16* (10), 6070–6077.

(43) Lin, Q.; Yun, H. J.; Liu, W.; Song, H.-J.; Makarov, N. S.; Isaienko, O.; Nakotte, T.; Chen, G.; Luo, H.; Klimov, V. I.; Pietryga, J. M. Phase-Transfer Ligand Exchange of Lead Chalcogenide Quantum Dots for Direct Deposition of Thick, Highly Conductive Films. *J. Am. Chem. Soc.* **2017**, *139* (19), 6644–6653.

(44) Babaev, A. A.; Skurlov, I. D.; Cherevkov, S. A.; Parfenov, P. S.; Baranov, M. A.; Kuzmenko, N. K.; Koroleva, A. V.; Zhizhin, E. V.; Fedorov, A. V. PbSe/PbS Core/Shell Nanoplatelets with Enhanced Stability and Photoelectric Properties. *Nanomaterials* **2023**, *13* (23), 3051.

(45) An, J. M.; Franceschetti, A.; Zunger, A. The Excitonic Exchange Splitting and Radiative Lifetime in PbSe Quantum Dots. *Nano Lett.* **2007**, *7* (7), 2129–2135.

(46) Li, X.-B.; Guo, P.; Zhang, Y.-N.; Peng, R.-F.; Zhang, H.; Liu, L.-M. High Carrier Mobility of Few-Layer PbX (X = S, Se, Te). *J. Mater. Chem. C* **2015**, *3*, 6284–6290.

(47) Gopalakrishnan, J. Aminophosphines: Their Chemistry and Role as Ligands and Synthons. *Appl. Organomet. Chem.* **2009**, *23*, 291–318.

(48) Burgada, R.; Bernard, D. *La Chimie Organique du Phosphore – Principes Généraux et Nouveaux Concepts 1re Partie*; L'Actualité Chimique: Paris, **1975**.

(49) Tessier, M. D.; De Nolf, K.; Dupont, D.; Sinnaeve, D.; De Roo, J.; Hens, Z. Aminophosphines: A Double Role in the Synthesis of Colloidal Indium Phosphide Quantum Dots. *J. Am. Chem. Soc.* **2016**, *138* (18), 5923–5929.

(50) Al-Shnani, F.; Mutyala, C. S.; Rodà , C.; Moreels, I. Fluorescence Quantum Efficiency Enhancement in Size-Controlled 3.5 Monolayer Cadmium Telluride Nanoplatelets. *Chem. Mater.* **2023**, *35* (16), 6258–6265.

(51) Wahl, J.; Haizmann, P.; Kirsch, C.; Frecot, R.; Mukharamova, N.; Assalauova, D.; Kim, Y. Y.; Zaluzhnyy, I.; Chassé, T.; Vartanyants, I. A.; Peisert, H.; Scheele, M. Mitigating the Photodegradation of All-Inorganic Mixed-Halide Perovskite Nanocrystals by Ligand Exchange. *Phys. Chem. Chem. Phys.* **2022**, *24*, 10944–10951.

(52) McGettrick, J. D.; Hooper, K.; Pockett, A.; Baker, J.; Troughton, J.; Carnie, M.; Watson, T. Sources of Pb(0) Artefacts during XPS Analysis of Lead Halide Perovskites. *Mater. Lett.* **2019**, *251*, 98–101.

(53) Tkalich, A. K.; Demin, V. N.; Zlomanov, V. P. Oxidation States of In in $Pb_{1-x}In_xTe$. *J. Solid State Chem.* **1995**, *116*, 33–36.

(54) Pederson, L. R. Two-Dimensional Chemical-State Plot for Lead Using XPS. *J. Electron Spectrosc. Relat. Phenom.* **1982**, *28*, 203–209.

(55) Sykora, M.; Koposov, A. Y.; McGuire, J. A.; Schulze, R. K.; Tretiak, O.; Pietryga, J. M.; Klimov, V. I. Effect of Air Exposure on Surface Properties, Electronic Structure, and Carrier Relaxation in PbSe Nanocrystals. *ACS Nano* **2010**, *4* (4), 2021–2034.

(56) Peters, J. L.; van der Bok, J. C.; Hofmann, J. P.; Vanmaekelbergh, D. Hybrid Oleate-Iodide Ligand Shell for Air-Stable PbSe Nanocrystals and Superstructures. *Chem. Mater.* **2019**, *31* (15), 5808–5815.

(57) Mandale, A. B.; Badrinarayanan, S. X-Ray Photoelectron Spectroscopic Studies of the Semimagnetic Semiconductor System $Pb_{1-x}Mn_xTe$. *J. Electron Spectrosc. Relat. Phenom.* **1990**, *53*, 87–95.

4.7 Supporting Information

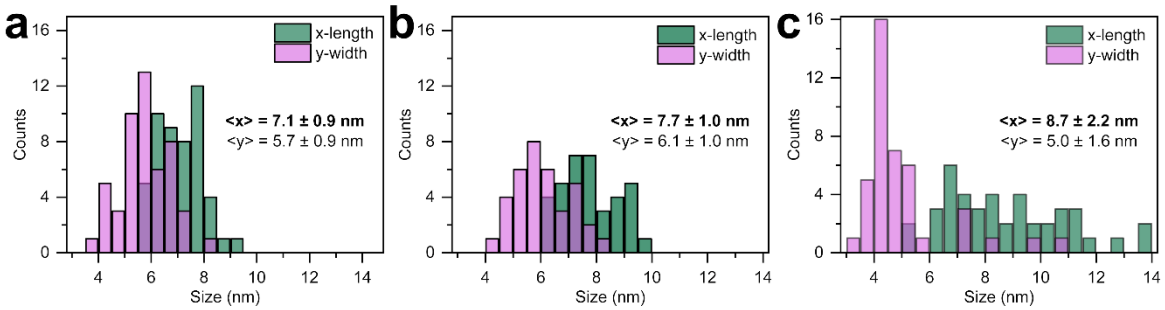

Figure S 4.1. Size histograms of the PbTe NPLs shown in the TEM images in Figure 4.1. *x*-Lengths were determined by measuring the longest dimension of the NPLs, *y*-width is the longest distance orthogonal to the *x*-length.

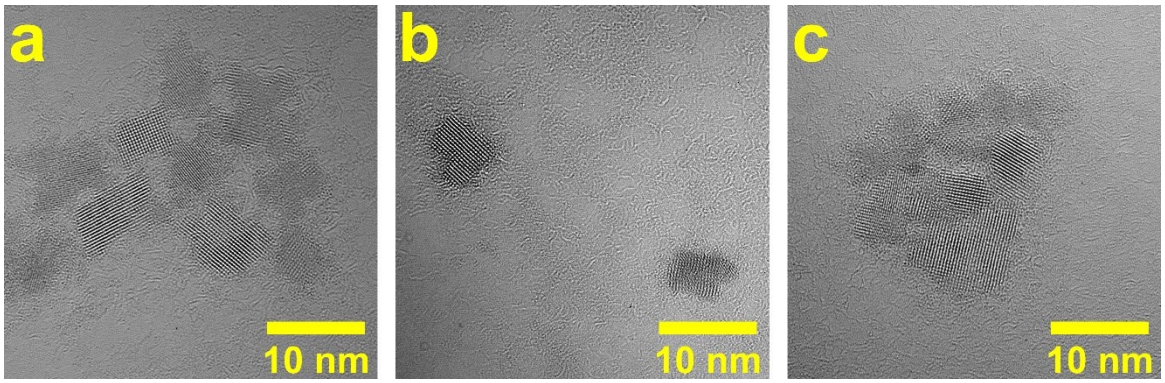

Figure S 4.2. Typical TEM images used for determining lengths and widths of PbTe NPLs shown in Figure 4.1.

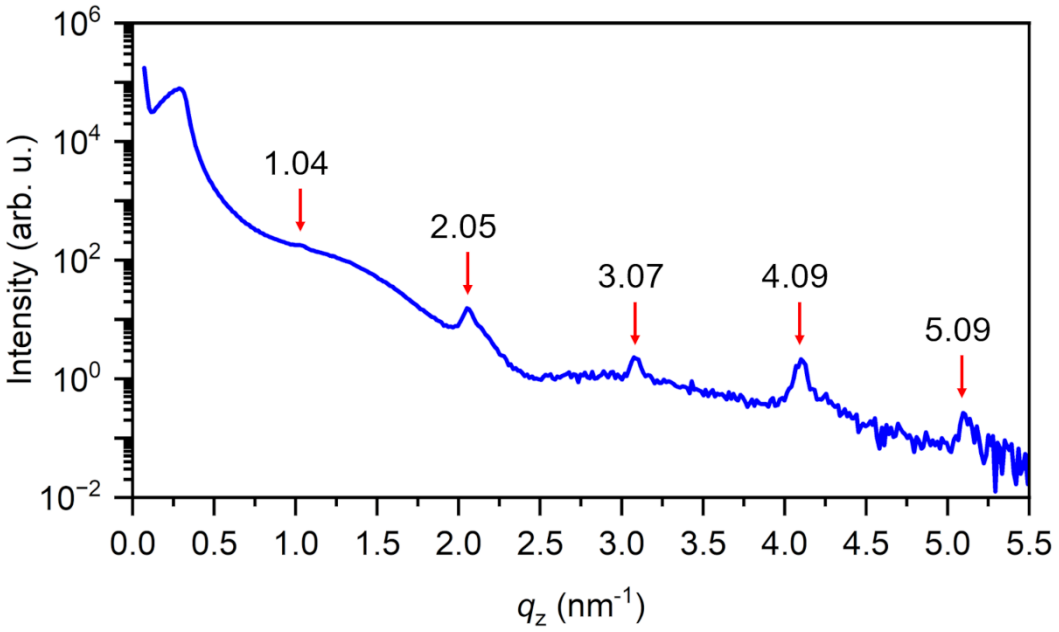

Figure S 4.3. Additional information on the vertical stacking of the PbTe NPLs superlattice was obtain by an X-ray reflectivity experiment. The scattering data were recorded using Cu $K_{\alpha 1}$ radiation with an energy of 8.064 keV on a laboratory diffractometer (3303TT, GE). Due to a weak scattering signal, data could only be recorded up to scattering vector $\Delta q_z \approx 6$ nm^{-1}. Superlattice peaks with a spacing $\Delta q_z \approx 1$ nm^{-1} are highlighted with red arrows.

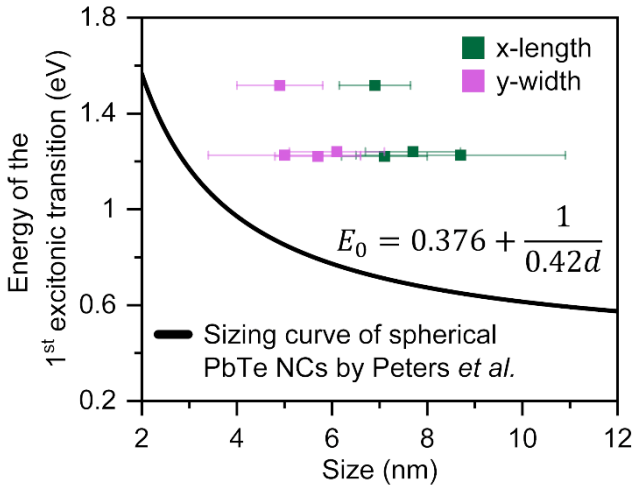

Figure S 4.4. Energy of the first excitonic transition *vs.* lateral sizes of 2D PbTe NPLs compared to a sizing curve for spherical PbTe NCs by PETERS *et al.*[1] 2D PbTe NPLs exhibit their first excitonic absorbance at higher energies compared to spherical PbTe NCs of the same diameter, emphasizing the additional vertical quantum confinement in the NPLs. It should be noted, however, that the

determined values for the energy of the first excitonic transition in 2D PbTe NPLs are error-prone due to rather weakly expressed absorbance feature (see Figure 4.2a). This is caused by the overlap of the band edge peak transition with different allowed transitions directly following the first exciton.[1,2]

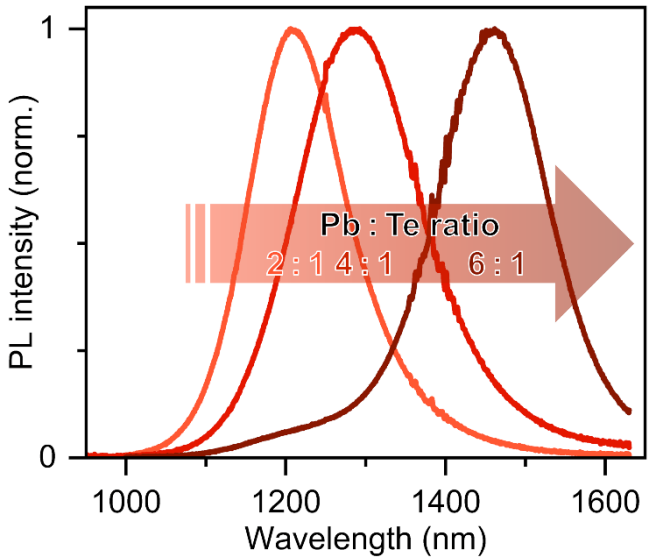

Figure S 4.5. PL spectra of PbTe NPLs synthesized with three different Pb:Te ratios of 2:1, 4:1, and 6:1. The PL position is synthetically tunable by changing the Pb:Te ratio, with a higher amount of lead precursor yielding thicker and larger NPLs. TEM images and corresponding size histograms are shown in Figure 4.1 as well as in Figure S 4.1, resp.

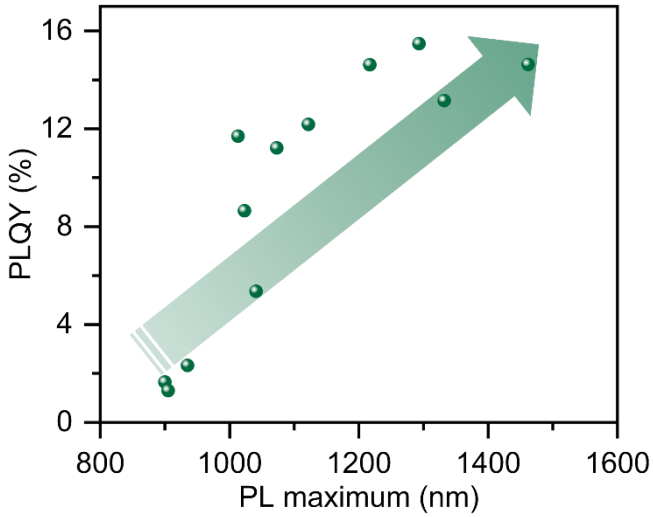

Figure S 4.6. PLQY of PbTe NPLs *vs.* the associated PL maxima. The PLQY gradually increases from 1% at 910 nm (1.36 eV) to 15% for PL above 1240 nm (1.0 eV).

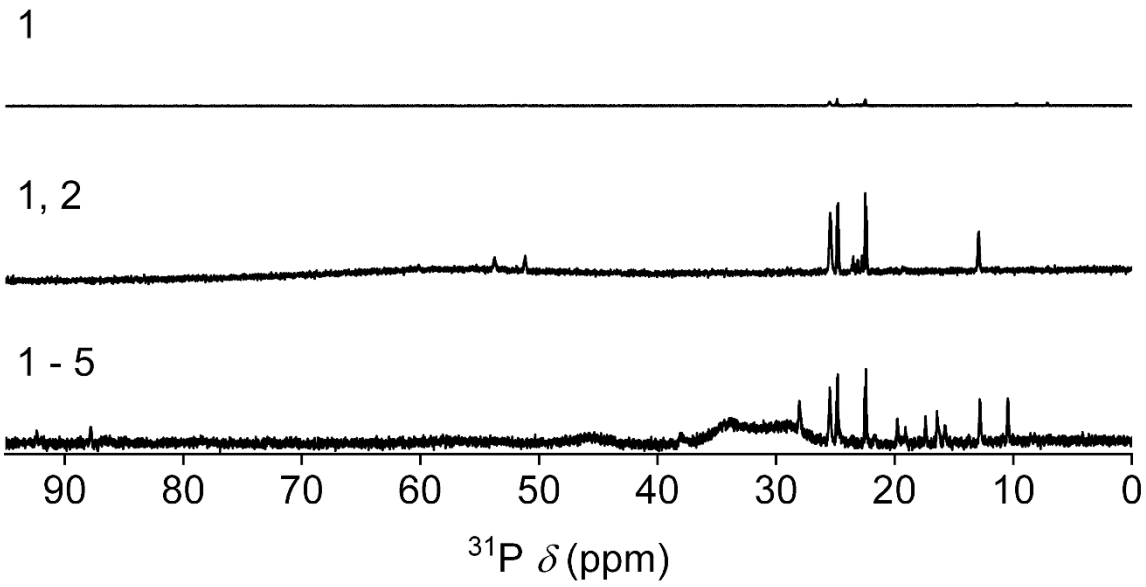

Figure S 4.7. $^{31}P\{^{1}H\}$ NMR spectrum of pure tris(dimethylamino)phosphine ($P(N(CH_3)_2)_3$ (1)), tris(dimethylamino)phosphine telluride ($TeP(N(CH_3)_2)_3$ / $P(N(CH_3)_2)_3$ (2)), and transaminated tris(dimethylamino)phosphine telluride ($TeP(N(CH_3)_2)_{3-x}(NHR)_x$ / $P(N(CH_3)_2)_{3-x}(NHR)_x$, R = C_8H_{17} (3–5)) in $CDCl_3$ in the range of 0–95 ppm corresponding to the ^{31}P NMR spectra shown in Figure 4.3.

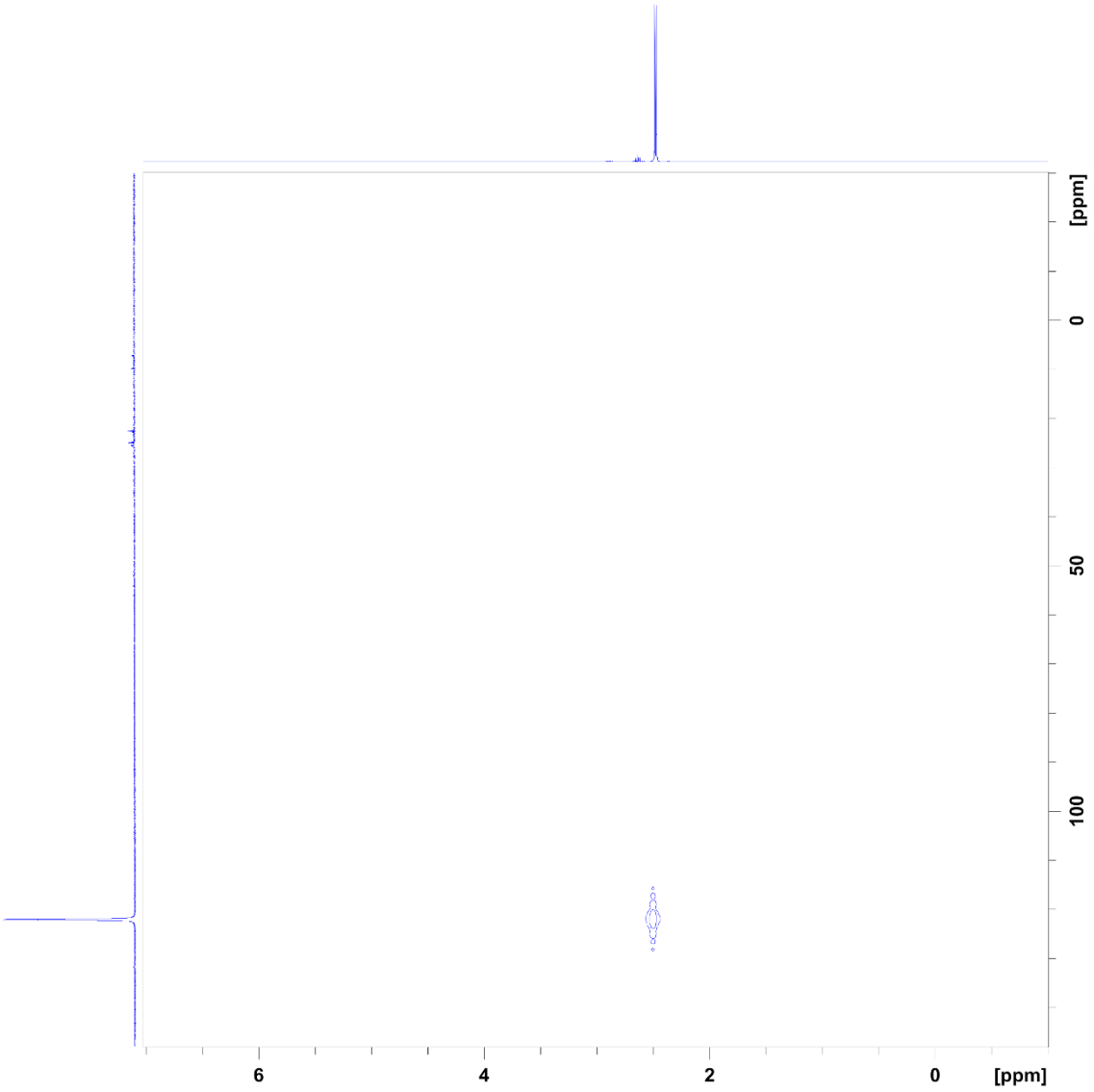

Figure S 4.8. ^{1}H-^{31}P HMBC NMR spectrum of pure tris(dimethylamino)-phosphine ($P(N(CH_3)_2)_3$ (1)) in $CDCl_3$, showing that the ^{1}H doublet resonance at 2.48 ppm is linked to the single sharp 122 ppm resonance in the ^{31}P NMR.

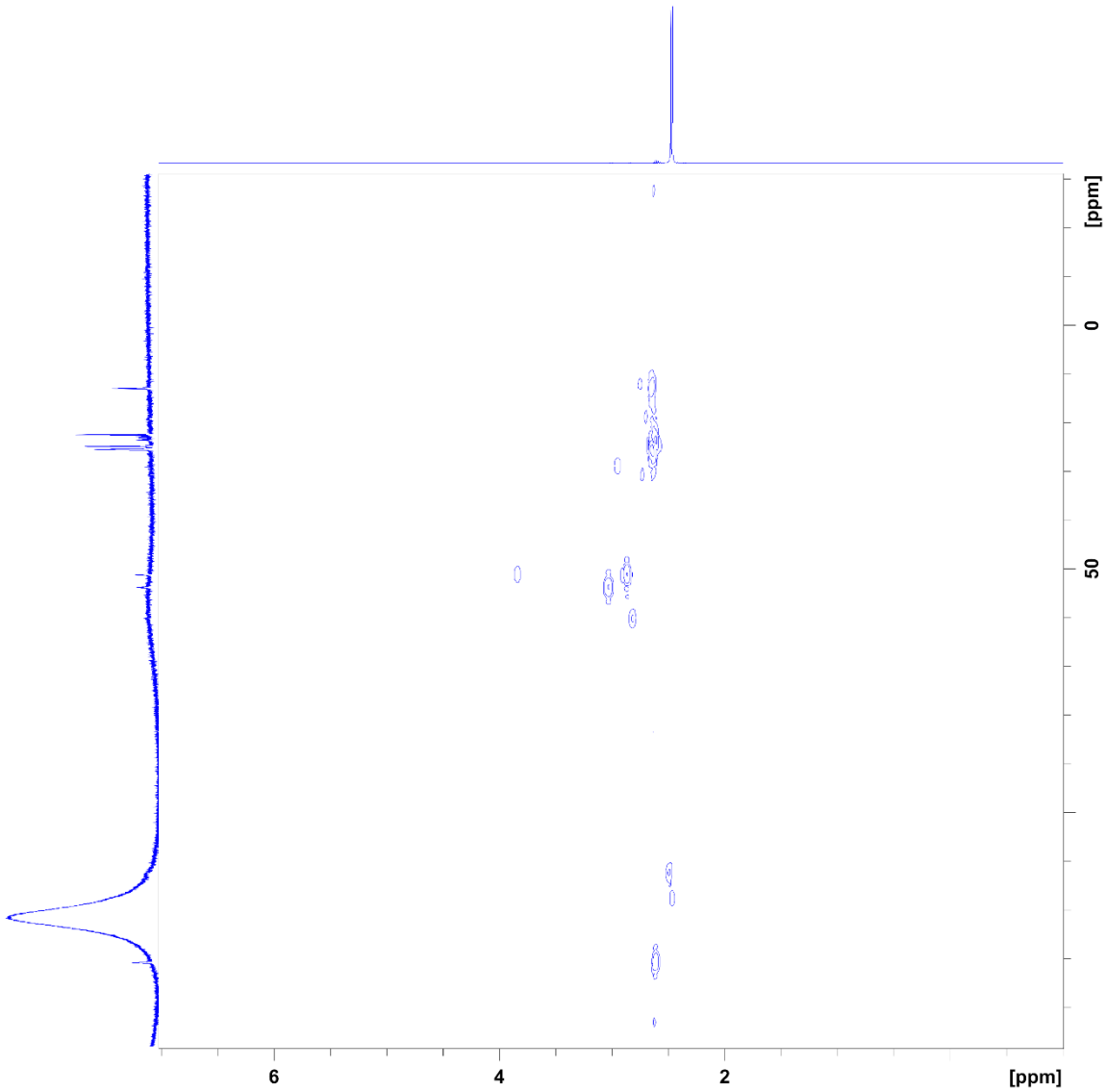

Figure S 4.9. ^{1}H-^{31}P HMBC NMR spectrum of tris(dimethylamino)phosphine telluride ($TeP(N(CH_3)_2)_3$ / $P(N(CH_3)_2)_3$ (2)) in $CDCl_3$, showing that the ^{1}H doublet resonance at 2.47 ppm is related to the broadened 122 ppm resonance in the ^{31}P NMR.

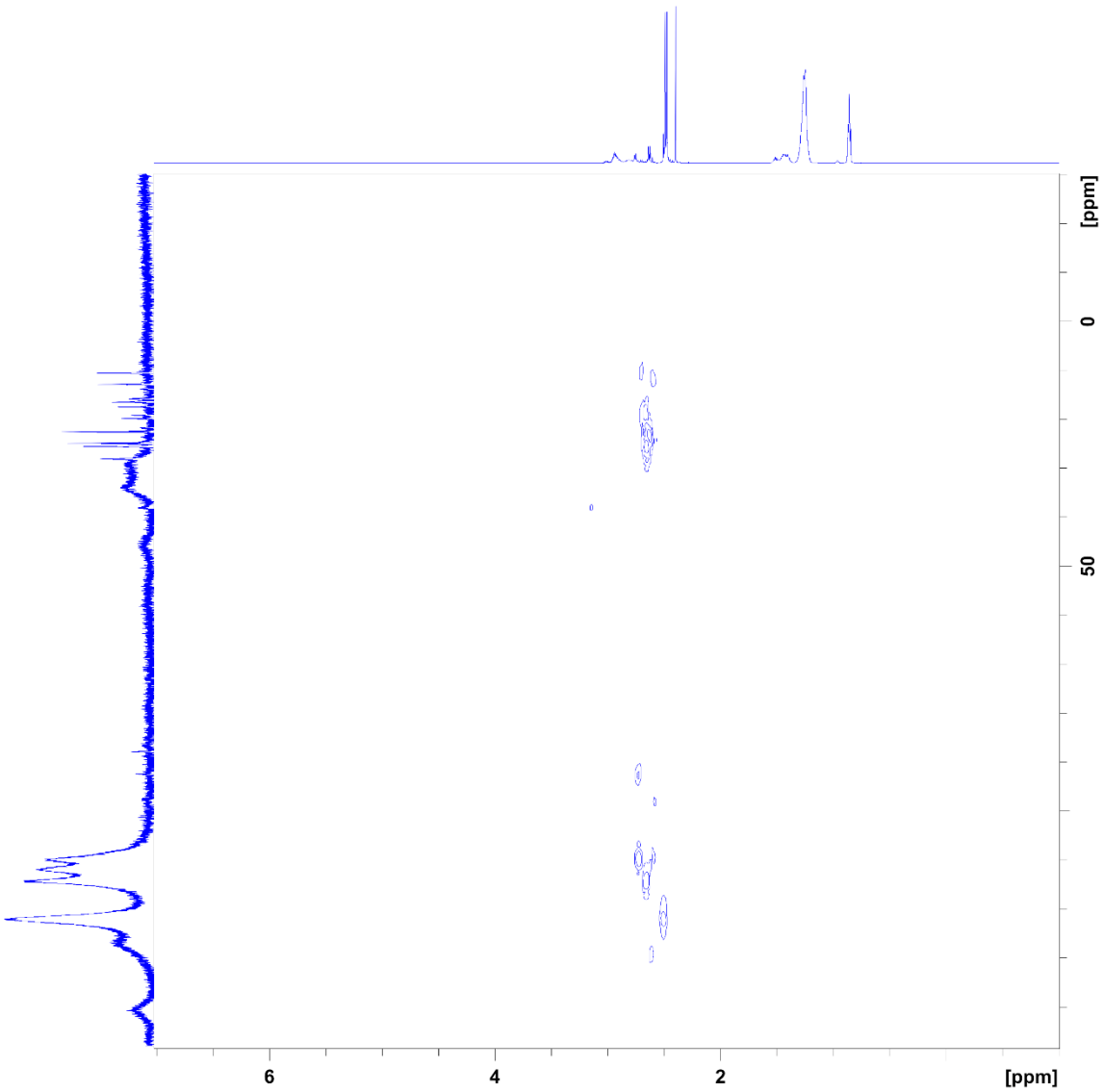

Figure S 4.10. ^{1}H-^{31}P HMBC NMR spectrum of transaminated tris(dimethylamino)phosphine telluride ($TeP(N(CH_3)_2)_{3-x}(NHR)_x$ / $P(N(CH_3)_2)_{3-x}(NHR)_x$, R = C_8H_{17} (3–5)) in $CDCl_3$, showing the link between the ^{1}H doublet resonance at 2.48 ppm and the three ^{31}P resonances at 110 ppm, 112 ppm, and 114 ppm.

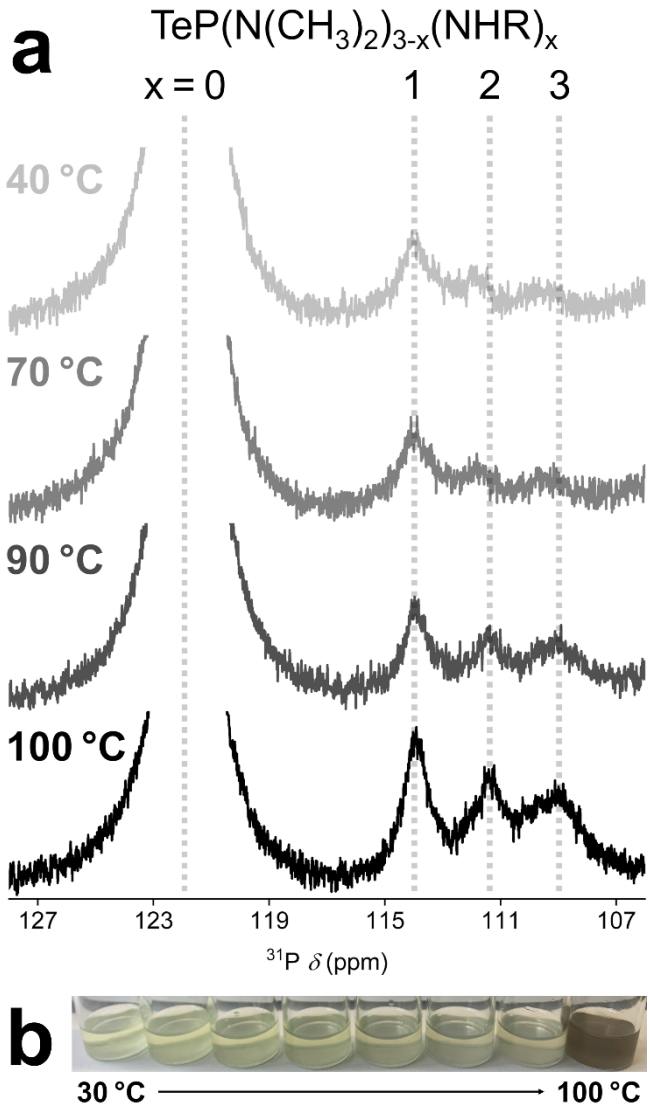

Figure S 4.11. (a) $^{31}P\{^{1}H\}$ NMR spectra of aliquots from a tris-(dimethylamino)phosphine telluride transamination reaction mixture at different temperatures (40°C, 70°C, 90°C, and 100°C). The three ^{31}P resonances corresponding to the single, double, and triple transaminated aminophosphine arise in order when heating up from 40°C to 100°C. The spectra show that partial transamination occurs already at 40°C (and 70°C), however especially the double and triple transaminated phosphine telluride are mainly formed at elevated temperatures above 90°C, emphasizing the necessity of *ex situ* transamination. (b) Images of collected aliquots from the transamination reaction, showing a distinct color change upon reaching 100°C and further underpinning the need for elevated temperatures.

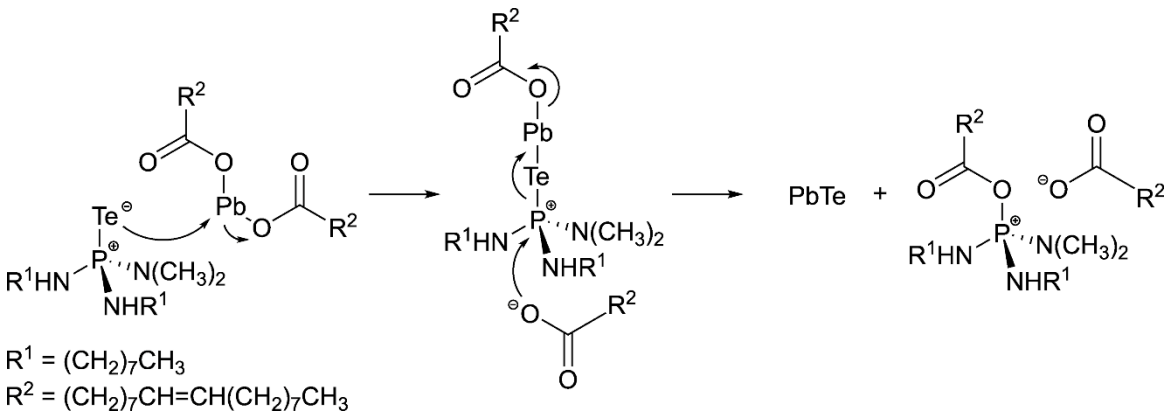

Figure S 4.12. Nucleophilic substitution reaction pathway for the formation of PbTe NPLs from lead oleate and transaminated aminophosphine telluride in analogy to the proposed reaction mechanism by SUN *et al.*[3] for the formation of CdTe.

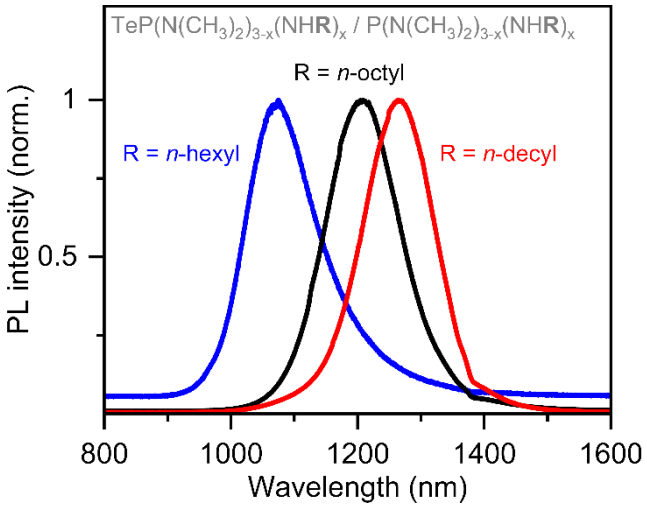

Figure S 4.13. PL spectra of PbTe NPLs synthesized using aminophosphine telluride precursors transaminated with three different linear aliphatic primary amines (*n*-hexylamine, *n*-octylamine, *n*-decylamine). Longer alkyl chains reduce the reactivity of the precursor, presumably due to steric hindrance, which results in the formation of thicker and larger NPLs with PL further shifted into the NIR.

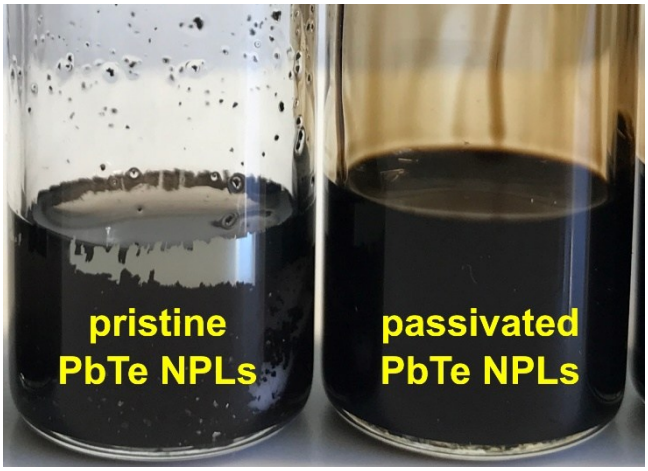

Figure S 4.14. Image of pristine and PbI_2 passivated PbTe NPLs 24 h after synthesis. While pristine PbTe NPLs rapidly change color from dark brown to black and metallic/elemental tellurium forms at the inside of the vial, PbI_2 passivated NPLs are stable and their dark brown color, colloidal stability and optical properties are retained.

4.7.1 References

(1) Peters, J. L.; Wit, J. de; Vanmaekelbergh, D. Sizing Curve, Absorption Coefficient, Surface Chemistry, and Aliphatic Chain Structure of PbTe Nanocrystals. *Chem. Mater.* **2019**, *31*, 5, 1672–1680.

(2) Murphy, J. E.; Beard, M. C.; Norman, A. G.; Ahrenkiel, S. P.; Johnson, J. C.; Yu, P.; Mićić, O. I.; Ellingson, R. J.; Nozik, A. J. PbTe Colloidal Nanocrystals: Synthesis, Characterization, and Multiple Exciton Generation. *J. Am. Chem. Soc.* **2006**, *128*, 10, 3241–3247.

(3) Sun, H.; Wang, F.; Buhro, W. E. Tellurium Precursor for Nanocrystal Synthesis: Tris(dimethylamino)phosphine Telluride. *ACS Nano* **2018**, *12*, 12, 12393–12400.

5 Aqueous Phase Near-Infrared Emitters: Water Transfer of Colloidal 2D PbS, PbSe and PbTe Nanoplatelets

The upcoming chapter reports on a water transfer protocol toward NIR-emissive aqueous 2D PbS, PbSe and PbTe NPLs. Combined X- and L-type passivation by 11-mercaptoundecanoic acid makes the NPLs soluble in water and results in well-retained optical properties, *e.g.* PL at 1023 nm with a QY of 13 % for aqueous 2D PbSe NPLs.

The results presented here have been published in *Nanoscale*, 2025, **17**, 24006–24016. For details about the author contributions see Chapter B.

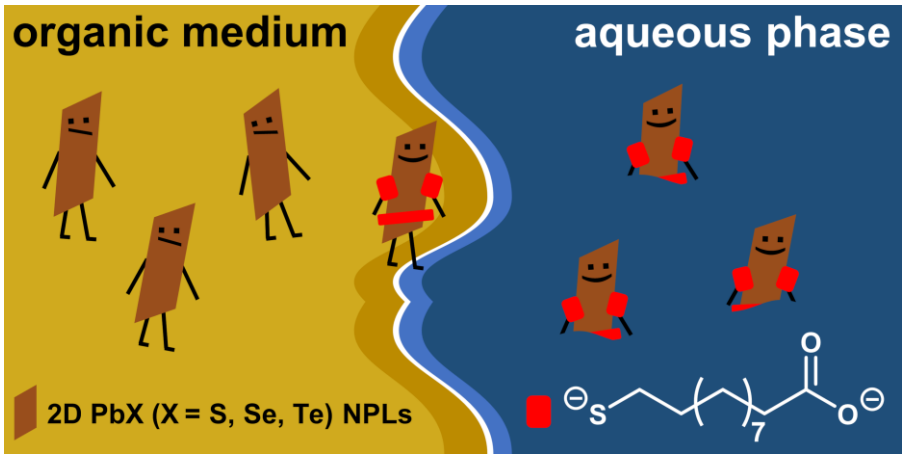

Leon Biesterfeld,[a,b,c] *Mattis T. Vochezer,*[b] *Dominik A. Rudolph,*[a,c,d] *Jannika Lauth* *[a,b,c,d]

[a] Cluster of Excellence PhoenixD (Photonics, Optics, and Engineering – Innovation Across Disciplines), Welfengarten 1A, D-30167 Hannover, Germany.
[b] Institute of Physical and Theoretical Chemistry, Eberhard Karls University of Tübingen, Auf der Morgenstelle 18, D-72076 Tübingen, Germany.
[c] Institute of Physical Chemistry and Electrochemistry, Leibniz University Hannover, Callinstr. 3A, D-30167 Hannover, Germany.
[d] Laboratory of Nano and Quantum Engineering, Leibniz University Hannover, Schneiderberg 39, D-30167 Hannover, Germany.

Reproduced from *Nanoscale*, 2025, 17, 24006–24016 with permission from the Royal Society of Chemistry.

5.1 Abstract

Colloidal two-dimensional (2D) lead chalcogenide PbX (X = S, Se, Te) nanoplatelets (NPLs) are strongly confined narrow band gap semiconductors with tuneable efficent photoluminescence (PL) in the near-infrared (NIR). They hold high potential for the use as classical and quantum emitters in fiber-based photonics that operate at telecommunication wavelengths. Up to now, the insolubility of 2D PbX NCs in water and other polar solvents has been a challenge that complicates their post-synthesic processing, *e.g.* into future functional nanocomposites. Here, we describe a phase transfer protocol from hexane to water using 11-mercaptoundecanoic acid (MUA), which yields aqueous phase 2D PbS, PbSe, and PbTe NPLs with preserved shape, crystallinity and NIR PL (*e.g.* PbS: 724 nm, PbSe: 1023 nm and PbTe: 1184 nm). Water-soluble 2D PbSe shows efficient emission (up to 13% PL quantum yield at 1023 nm), thereby retaining 65% of the initial quantum yield and making it highly interesting as an aqueous NIR light source. By using X-ray photoelectron spectroscopy (XPS) and nuclear magnetic resonance (NMR), we follow the phase transfer on a molecular level and find two binding motifs of MUA to the 2D PbX surfaces: X-type bound thiolate and L-type bound thiol. Our results shine new light on mercaptocarboxylic acid-based nanomaterial phase transfers and represent a crucial step for incorporating NIR-emissive 2D PbX into (fiber) optics.

5.2 Introduction

Colloidal 2D semiconductor nanocrystals (NCs), so-called nanoplatelets (NPLs) or flat quantum dots (fQDs), with the most prominent UV-Vis emitting example of CdX (X = S, Se, and/or Te) NPLs, are highly topical materials and exhibit fast radiative, spectrally narrow, and efficient directed photoluminescence (PL) caused by their strong anisotropic quantum confinement.[1–4] However, for near-infrared (NIR) wavelength use such as (quantum) optical communication[5,6] or IR sensing,[7,8] materials with a smaller band gap than cadmium chalcogenides are required. NIR emitting 2D CdX-associated examples include $Hg_xCd_{1-x}Se$ NPLs, HgX NC decorated HgX NPLs,[9] and CdSe-PbSe NPLs as well as PbSe NPLs,[10] all prepared *via* cation exchange from CdX NPLs.

On the other hand, direct colloidal synthesis routes for narrow band gap 2D lead chalcogenide (PbX; X = S, Se, Te) NPLs and fQDs have been developed in recent years. 2D PbX NPLs and fQDs exhibit efficient telecommunication band emission (1st, 2nd and 3rd low-loss optical fiber windows at ~850 nm, ~1300 nm and ~1550 nm, respectively)[11] at NIR to short-wave-infrared (SWIR) wavelengths (PbS: up to 19% PLQY at ~720 nm,[12,13] PbSe: up to 61% between 860–1510 nm,[14–16] PbTe: up to 15% for 910–1460 nm).[17] They are intriguing materials for example for fiber optics-based photonics. In addition, colloidal 2D PbS exhibits high carrier multiplication efficiencies (0.9–0.55 for 4–7 nm thick PbS nanosheets (NSs)),[18] narrow linearly polarized emission (down to 615 μeV with a linear degree of polarization of up to 90%),[19] efficient charge carrier mobilities (550–1000 $cm^2V^{-1}s^{-1}$ for 4–16 nm thick PbS NSs),[20] and RASHBA-type band splitting.[21] These unique properties may be leveraged for future optoelectronic or spintronic applications.

A shared aspect of the direct 2D PbX NPL syntheses is the use of low-polarity solvents and long-chain aliphatic amines, which are assumed to help template the anisotropic growth of the (isotropic) cubic rock salt crystal-structured materials.[22] As a consequence, the obtained 2D PbX flat fQDs, NPLs, or NSs, are covered by lipophilic ligands, typically L-type bound amines and X-type bound oleates,[14,23] which ensure their colloidal stability in organic environments and render them insoluble in aqueous (and other polar) solutions. While post-synthetic surface passivation with metal halides (*e.g.* $CdCl_2$ or PbI_2) has proven to be a powerful tool to enhance the colloidal stability and PL/PLQY of 2D lead chalcogenides,[14] ligand engineering with respect to the solubility of the materials has not been investigated so far, limiting their general applicability. Up to now, the restrictions imposed by post-synthetic processing of hydrophobic 2D PbX NPLs and fQDs complicate numerous encapsulation techniques toward easy to handle solid-state composite materials feasible from aqueous solution. For example, we have assembled aqueous core-crown CdSe/CdS NPLs *via* layer-by-layer deposition with polyelectrolytes[24] and have incorporated CdSe/CdS NPLs into zeolitic imidazolate frameworks (ZIF) to produce photoluminescent composite films.[25] Such hybrid materials (made from phase transferred NCs) combine the functionality of two different materials classes, *e.g.* the inertness or chemical function of a polymer or the high specific surface area of a ZIF with the unique photophysics of NPLs. On

the other hand, inorganic–organic nanocomposites possess new application-oriented functionalities such as switching of the optical properties based on external stimuli, *e.g.* humidity changes or electric and magnetic fields.[25,26] Water phase transfer of NIR-emissive NCs is also frequently discussed in the context of biomedical imaging and labelling,[27,28] albeit we note that heavy metal-containing NCs require thorough matrix incorporation (which may be facilitated from aqueous solution). In addition, aqueous ligand exchange often coincides with the replacement of long insulating ligands (*e.g.* oleic acid) by shorter chained molecules, which are beneficial for charge transport in NC-based solidstate devices such as field-effect transistors, photodetectors, and solar cells.[29–33]

A common strategy to phase transfer lipophilic emissive NCs, while retaining their PL, is the exchange of the pristine ligands with bifunctional mercaptocarboxylic acids (see Figure 5.1). The latter coordinate to the NCs' surface *via* the sulfur, while the free carboxylate headgroup provides solubility in water.[34–36] For example, TAMANG *et al.* reported the aqueous phase transfer of InP/ZnS core/shell NCs, CdSe/CdS/ZnS NCs, $CuInS_2$/ZnS NCs, and CdSe as well as CdSe/CdS nanorods using different hydrophilic thiols (*e.g.* cysteine, thioglycolic acid, and 11-mercaptoundecanoic acid).[28] The authors, and other reports, further emphasize the importance of alkaline pH conditions during ligand exchange and subsequent storage of the aqueous colloidal solution.[28,35,36] This is needed because the thiol and the carboxyl group of the mercaptocarboxylic acids must both be deprotonated, so that the thiolate can bind covalently to the surface of the NCs, while the carboxylate enables solubility in aqueous solution (MUA with a protonated carboxyl group is hardly soluble in water). Phase transferred NCs using MUA specifically have been used for imaging of human colon cancer cells (PbS QDs-MUA)[27] or as an active component in the aforementioned zeolitic imidazolate framework composites for PL-based gas sensing (aqueous core-crown CdSe/CdS NPLs).[25]

Here, we demonstrate a ligand exchange protocol using 11-mercaptoundecanoic acid to water transfer highly confined 2D lead chalcogenide NPLs and fQDs (PbS, PbSe, and PbTe), which exhibit telecommunication band emission in the NIR. The obtained water-soluble 2D PbX NPLs and fQDs bridge the gap between classical and quantum emitters and solubility requirements of common downstream processing techniques. By applying X-ray photoelectron spectroscopy (XPS) and

NMR, we disentangle X- and L-type binding motifs of thiolate and protonated thiols to the PbX NPLs' surface after the universal phase transfer. These findings add new insights to the molecular understanding of mercaptocarboxylic acid-based water transfers of nanomaterials and lead the way for the post-synthetic processing of 2D PbX NPLs into nanocomposites with technologically relevant telecommunication band emission.

5.3 Experimental

5.3.1 Chemicals

Acetonitrile (≥ 99.5 %), cadmium(II) chloride (99.99 %), chloroform (≥ 99 %, contains 0.5 – 1 % ethanol as stabilizer), ethanol (EtOH, max. 0.01 % H_2O), *iso*-propanol (≥ 99.5 %), lead(II) oxide (≥ 99.99 %), 11-mercaptoundecanoic acid (MUA, 95 %), methanol (MeOH, ≥ 99.8 %), *n*-octylamine (99 %), tellurium powder (30 mesh, 99.99 %), tetrachloroethylene (TCE, ≥ 99 %), triethylamine (≥ 99 %), trifluoroacetic acid (99 %), trifluoracetic anhydride (≥ 99 %), and tris(dimethylamino)-phosphine (97 %) were purchased from SIGMA-ALDRICH/MERCK. Lead(II) iodide (99.99 %), selenourea (99.97 %), and thiourea (99 %) were purchased from ALFA AESAR. Oleic acid (90 %) was purchased from ABCR. *n*-Hexane (97 %) was purchased from ACROS ORGANICS. Potassium hydroxide pellets were purchased from AVANTOR/VWR. Deuterium oxide (D_2O, 99.9 atom% D) was purchased from CARL ROTH. *n*-Octylamine and oleic acid were degassed using the freeze-pump-thaw technique prior to being stored and handled inside a nitrogen-filled glove box. All other reagents were used as received from the listed suppliers. Lead oleate was synthesized according to an established method by HENDRICKS *et al.*[37] All steps of the NPL syntheses and phase transfers not involving deionized water or D_2O were performed under inert gas conditions in a nitrogen-filled glove box, unless stated otherwise.

5.3.2 PbS NPL Synthesis

PbS NPLs were synthesized using a method similar to that of MANTEIGA VÁZQUEZ *et al.*[12] Seven days before the actual synthesis, a solution of thiourea (240 mg, 3.15 mmol) in octylamine (6 ml) was prepared and stirred at 35°C until use in the PbS NPL synthesis. For a typical synthesis, lead oleate (183 mg, 0.24 mmol) was dissolved in a mixture of octylamine (0.75 ml), oleic acid (0.4 ml),

and hexane (1.15 ml) at 35°C. After complete dissolution, 0.25 ml of thiourea solution was rapidly injected and the reaction was allowed to run for 16 min, during which the colorless mixture became bronze colored. The PbS NPLs were subsequently passivated by injecting 1.25 ml of a 0.1 M $CdCl_2$ solution (in octylamine and oleic acid with a molar ratio of 9:1), followed by stirring for 40 min at 35°C. For thorough purification, the NPLs were precipitated by the dropwise addition of EtOH until the colloidal solution was visibly destabilized (typically requiring 2 ml), centrifuged at 2500 rcf for 10 min. The supernatant was discarded, and the precipitate was redispersed in dry hexane (2 ml). This process was repeated three times before the purified PbS NPLs were sealed under N_2 atmosphere and stored in a refrigerator.

5.3.3 PbSe fQD Synthesis

PbSe fQDs were synthesized using a method previously described by our group.[14–16] Two days before the actual synthesis, a solution of selenourea (193 mg, 1.57 mmol) in a mixture of octylamine (2.03 ml), oleic acid (0.23 ml), and hexane (0.75 ml) was prepared and stirred at 35°C until use in the PbSe fQD synthesis. For a typical synthesis, lead oleate (1.83 mg, 2.7 mmol) was dissolved in a mixture of octylamine (2 ml), oleic acid (4 ml), and hexane (18 ml) at 35°C. After complete dissolution, the sealed mixture was cooled to 0°C using an ice bath. Shortly after, the selenourea solution (2.5 ml) was rapidly injected into the vigorously stirred lead oleate mixture. After a reaction time of 10 min, the dark brown reaction mixture was quenched by adding dry EtOH (18.5 ml). For purification, the destabilized colloidal PbSe fQD solution was processed as described above for PbS NPLs.

5.3.4 PbTe NPL Synthesis

PbTe NPLs were synthesized using a method previously described by us.[17] Before the actual synthesis, an aminophosphine telluride precursor solution was prepared by heating a stirred mixture of tellurium powder (255 mg, 2 mmol), tris(dimethylamino)phosphine (2 ml, 11 mmol), and octylamine (2 ml, 12.1 mmol) to 100°C for 3 h under a N_2 atmosphere. After cooling to room temperature, the solution was passed through a 0.2 µm polytetrafluoroethylene syringe filter and stored in a refrigerator until use. For a typical PbTe NPL synthesis, 0.4 ml of a lead oleate stock solution (lead oleate (2.31 g, 3 mmol) in octylamine (6 ml)) was diluted

in hexane (3.6 ml) and cooled down to 0°C under vigorous stirring. Shortly after, 0.2 ml of the aminophosphine telluride precursor solution was rapidly injected, causing a color change to light brown. After a reaction time of 30 min, the dark brown mixture was quenched by adding 2 ml of a 0.1 M PbI_2 solution (in octylamine and oleic acid with a molar ratio of 9:1) and diluted with hexane (6 ml). For purification, the PbTe NPL solution was processed as described above for PbS NPLs.

5.3.5 Phase Transfer

2D PbX fQDs and NPLs were phase transferred by adapting a protocol for Cd-based nanorods and NPLs described by KODANEK *et al.*[35] First, a phase transfer stock solution containing MUA (1.21 g, 5.56 mmol) and KOH (0.4 mg, 7.09 mmol) in MeOH (18.75 ml) was prepared and stirred at 35°C until complete dissolution. For a typical phase transfer, the thoroughly purified PbX solutions in hexane (0.3 ml) were further diluted with hexane (0.7 ml) and the MUA phase transfer solution (1.5 ml) was added, resulting in a cloudy biphasic system, which was shaken overnight on a laboratory shaker. Subsequently, the mixture was centrifuged (2500 rcf for 10 min), the biphasic supernatant was discarded, and the precipitated PbX NPLs were redispersed in 2 ml of alkaline water (0.1 M KOH) using a laboratory vortex mixer. To remove any excess ligands, the aqueous 2D PbX solution was thoroughly washed by adding chloroform (2 ml), shaking on a laboratory shaker (10 min), centrifugation (2500 rcf for 10 min), and removal of the organic phase. This process was repeated at least three times, or until the chloroform phase remained completely transparent after shaking, with no white subphase being formed at the chloroform-water interface. The aqueous 2D PbX solutions were stored at 8°C in a refrigerator.

5.3.6 Transmission Electron Microscopy

For TEM, colloidal 2D PbX NPL solutions were drop-cast onto carbon-coated Cu grids (300 mesh) acquired from QUANTIFOIL. TEM images were obtained using a FEI TECNAI G2 F20 transmission electron microscope equipped with a field emission gun operating at 200 kV.

5.3.7 Visible-NIR PL and Absorbance Spectroscopy

Samples for optical spectroscopy were prepared by diluting the colloidal 2D PbX solutions in TCE for lipophilic fQDs and NPLs and D_2O for phase transferred aqueous samples (optical density below 0.2 at 500 nm) in quartz cuvettes (quartz glass high performance QS 200 – 2500 nm with an optical path length of 1 cm from HELLMA). Vis-NIR PL spectra were collected using an EDINBURGH FLS1000 PL spectrometer equipped with a 450 W ozone free Xe arc lamp for excitation (450 nm for all samples). PbS NPL PL was monitored using a photon counting photomultiplier tube 980 detector from EDINBURGH INSTRUMENTS; PbSe fQD and PbTe NPL NIR PL was monitored using a liquid N_2 cooled InGaAs 1650 photomultiplier tube detector from EDINBURGH INSTRUMENTS. Absolute PLQYs were determined using an integrating sphere. For this, scattering at 450 nm and the PL of TCE/D_2O and the fQDs and NPLs were measured separately, accounting for the difference in sensitivity of both detectors with a correction factor. Visible-NIR absorbance spectra were collected using a double beam CARY 5000 spectrophotometer from AGILENT TECHNOLOGIES equipped with a tungsten halogen (visible) and deuterium arc (ultraviolet) lamp and a PbSmart NIR detector for monitoring.

5.3.8 X-ray Photoelectron Spectroscopy

Samples for XPS analysis were prepared by drop-casting the colloidal NPL solutions onto silicon wafers (<001> surface, p-doped with B) from PLANO and drying *in vacuo* overnight. XPS data were obtained on a PHI 5000 VERSAPROBE III from ULVAC-PHI using an aluminum X-ray source (Al K_α = 1486.6 eV) operating at 24.4 W with a beam diameter of 100 µm. Survey spectra were measured with a pass energy of 224 eV; high-resolution spectra were acquired with a pass energy of 27 eV. Charging effects were accounted for by setting the C 1s peak of sp^3 adventitious carbon to 284.8 eV. The background was fitted by a classic SHIRLEY background; all components were fitted by symmetric VOIGT functions.

5.3.9 Nuclear Magnetic Resonance

Samples for NMR analysis were prepared by diluting each specimen in D_2O (typically 600 µl) in an NMR tube. NMR measurements were conducted using a BRUKER AVANCE III HDX 400 instrument with a frequency of 400 MHz. Spectra

were analyzed using the BRUKER TOPSPIN 4.2.0 software. The residual solvent peak of D_2O/H_2O (4.79 ppm) was used as an internal reference for the ^1H spectra.

5.4 Results and Discussion

5.4.1 Phase Transfer of 2D PbX fQDs and NPLs

Colloidal 2D PbX (X = S, Se, Te) NPLs and fQDs were synthesized from lead oleate and thiourea, selenourea, or aminophosphine telluride, respectively, using methods described previously by our group.[12,14,15,17] Figure 5.1 illustrates the general ligand exchange procedure used for the phase transfer (see Figure S 5.1 for photographs of the phase transfer process). Two-fold deprotonated 11-mercaptoundecanoic acid (dissolved with KOH in water) is used to replace the native oleic acid (and octylamine) ligands bound to the as-synthesized fQD and NPL surface. MUA coordinates to 2D PbX mainly *via* the sulfur, with the unbound carboxylate function ensuring colloidal stability in the aqueous solution. We note that it is crucial to thoroughly precipitate and redisperse the organic pristine PbX fQDs and NPLs so that unreacted precursors or excess ligands are absent prior to adding the phase transfer solution (MUA and KOH in MeOH). This prevents the formation of large quantities of potassium oleate.

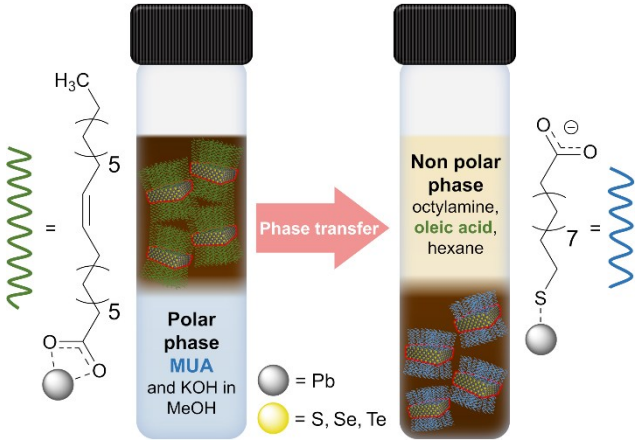

Figure 5.1. Schematic representation of the organic to aqueous phase transfer of 2D PbX fQDs and NPLs (dark brown) using 11-mercaptoundecanoic acid at alkaline pH conditions. Upon vigorous shaking of the biphasic system, the fQDs and NPLs change to the MeOH phase (light blue); consecutive purification with chloroform and redispersion in 0.1 M KOH in water yields colloidally stable aqueous 2D PbX solutions.

Figure 5.2 shows TEM images of PbS NPLs, PbSe fQDs, and PbTe NPLs before (a–c) and after (d–f) the phase transfer. The as-synthesized 2D PbS NPLs, in line with previous reports, exhibit a considerably larger lateral size of (20.2 ± 2.4) × (6.6 ± 1.7) nm² (a) compared to PbSe fQDs ((4.3 ± 0.8) × (3.2 ± 0.5) nm² (b)) and PbTe NPLs ((5.5 ± 1.5) × (3.9 ± 1.1) nm² (c)) and show the biggest aspect ratio (3.1:1), closely resembling a rectangular shape (see Figure S 5.2 for lateral size histograms of all samples shown). For organic PbS NPLs we further observe stacking of vertically aligned NPLs in the TEM images (see Figure S 5.3), consistent with previous reports. Laterally smaller and slightly more irregularly shaped PbSe fQDs and PbTe NPLs do not show stacking.

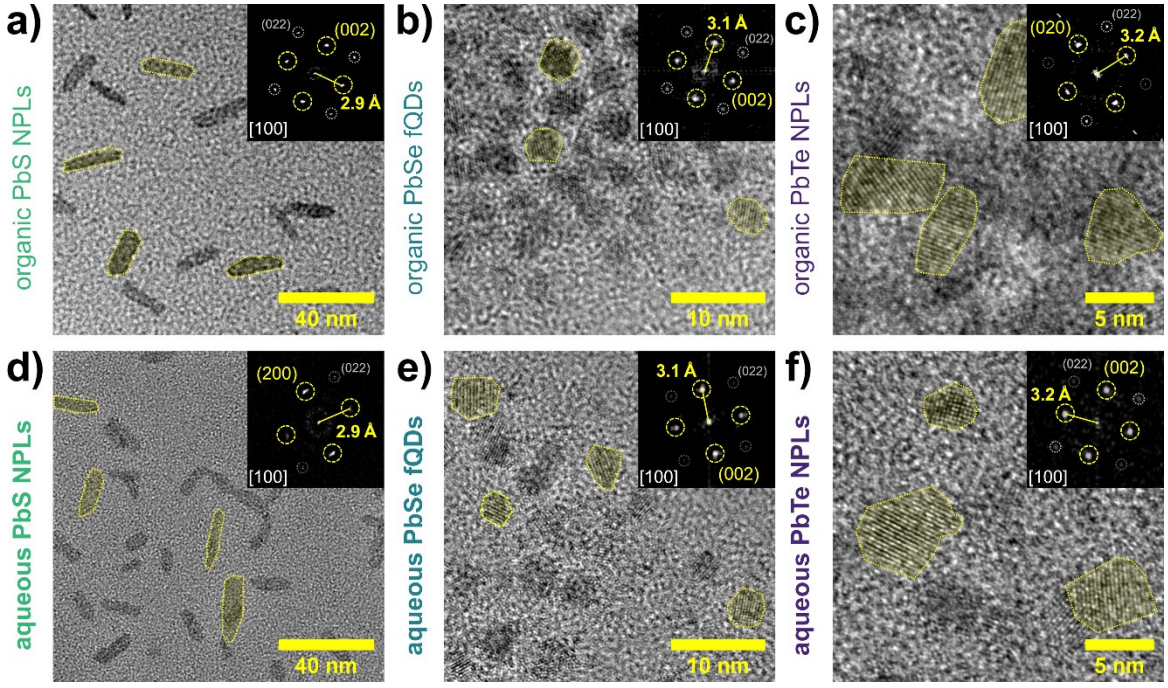

Figure 5.2. TEM images of organic PbS (a), PbSe (b), and PbTe (c) NPLs, as well as aqueous PbS (d), PbSe (e), and PbTe (f) NPLs (exemplary NPLs are highlighted for visual aid), exhibiting average lateral sizes ranging from (4.3 ± 0.8) x (3.2 ± 0.5) to (20.2 ± 2.4) x (6.6 ± 1.7) nm² with PbS NPLs generally being the largest. Notably, there is no apparent significant change in the lateral size of the NPLs after the phase transfer to water. All of the presented lead chalcogenide NPLs exhibit the cubic rock salt crystal structure, as indicated by the FFT patterns shown in the insets in each panel, which are composed of the characteristic (200) diffraction peaks (corresponding to 2.9 Å (PbS), 3.1 Å (PbSe), and 3.2 Å (PbTe)).

Recently, we have assessed the PbX fQDs and NPLs thickness directly *via* scanning tunneling microscopy[16] as well as by X-ray scattering experiments[17] and from stacking in TEM.[15,19] We find values ranging from 0.6–2 nm, which corresponds to a monolayer (1 ML) to a few atomic monolayers. After the phase transfer the average lateral sizes of 2D PbX NCs exhibit only minor changes ((19.3 ± 3.1) × (6.4 ± 1.2) nm² (d), (4.4 ± 0.8) × (3.3 ± 0.6) nm² (e), and (5.6 ± 1.0) × (3.8 ± 0.8) nm² (f)). The cubic rock salt crystalline structure (space group $Fm\bar{3}m$) remains visible from the lattice fringes in TEM (see Figure 5.2 and Figure S 5.4 for examples at higher magnification) as well as the reflexes in the FFT patterns shown in the associated insets in Figure 5.2 (characteristic (200) lattice spacings of 2.9 Å (PbS), 3.1 Å (PbSe), and 3.2 Å (PbTe); see Figure S 5.4 additionally). The minor size changes can be attributed to surface self-reconstruction of the materials and coincidental size separation due to the additional centrifugation steps during the phase transfer and subsequent purification.

5.4.2 Optical Properties of Aqueous 2D PbX fQDs and NPLs

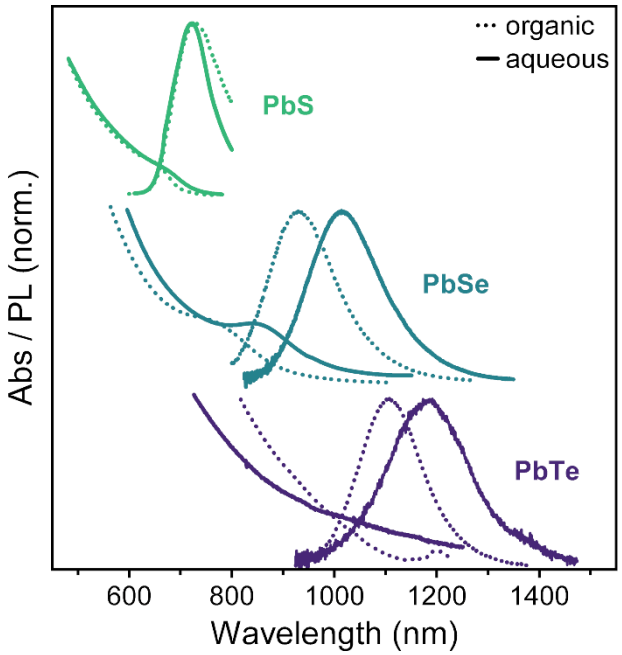

Figure 5.3. Vis-NIR absorbance and PL spectra of PbS NPLs (top), PbSe fQDs (middle) and PbTe NPLs (bottom) before (dotted) and after (straight line) phase transfer. 2D PbX NCs exhibit weekly expressed excitonic absorbance in the range from 584 and 990 nm as well as NIR PL from 724 to 1184 nm.

Table 5.1. Excitonic absorbance features (λ_{Abs}, determined by the 2nd derivative of the absorbance), PL maxima (λ_{PL}), and fwhm of the PL of organic and aqueous PbS NPLs, PbSe fQDs, and PbTe NPLs.

sample	λ_{Abs} (nm)	λ_{PL} (nm)	PL fwhm (meV)
org. PbS NPLs	584	731	264
aq. PbS NPLs	592	724	221
org PbSe fQDs	787	929	233
aq. PbSe fQDs	870	1023	212
org PbTe NPLs	990	1111	155
aq. PbTe NPLs	989	1184	167

Figure 5.3 displays normalized absorbance (Abs) and NIR PL spectra of PbX fQDs and NPLs before (organic; dotted line) and after (aqueous; solid line) the transfer to aqueous solution. The optical characteristics (absorbance features, PL maxima, and fwhm of the PL) of the samples are summarized in Table 5.1.

Before phase transfer all three 2D PbX NC samples exhibit NIR PL at positions (with associated fwhm) that are in good agreement with our previous reports and are representative of the respective material system.[12,14,17,19] PLQY values (org. PbS: 1%, org. PbSe: 23%, and org. PbTe: 4%) are similarly, albeit slightly lower for PbS and PbTe NPLs. We attribute this to the relatively harsh purification required to remove excess oleate and oleic acid before the phase transfer, which is in turn accompanied by ligand stripping, exposing surface traps. The purification step is particularly demanding for PbS and PbTe NPLs, since their syntheses require a large amount of oleic acid and they are generally more labile to chemical changes than PbSe fQDs.

After the phase transfer all three 2D PbX NCs retain sizeable telecommunication band NIR PL. The PL of PbSe fQDs and PbTe NPLs shows bathochromic shifts from 929 nm to 1023 nm and 1111 nm to 1184 nm, respectively. This observation has previously been attributed to a reduction of quantum and dielectric confinement, caused by the addition of a quasi-sulfide layer by the MUA-ligand[38] and a dielectric surrounding change due to the water transfer.[28,39] However, for the PbS NPLs we find a slight blue-shift in the absorbance (731 nm to 724 nm). It is assumed that the dielectric surrounding effects are counteracted by size narrowing/exclusion caused by the rigorous washing in the PbS NPL case. This is

also reflected in the small decrease in average lateral size, from (20.2 ± 2.4) × (6.6 ± 1.7) nm² down to (19.3 ± 3.1) × (6.4 ± 1.2) nm². In addition, PbS NPLs have the largest lateral size and PbS exhibits the smallest exciton Bohr radius ($a_{B,PbS}$ = 20 nm),[40] making it the system with the smallest confinement and minor changes in the chemical environment are expected to influence PbS NPLs less than the extremely confined PbSe fQDs ($a_{B,PbSe}$ = 46 nm)[40] and PbTe NPLs ($a_{B,PbTe}$ ≈ 82 nm).[41]

After the phase transfer, the PbX NPLs and fQDS exhibit a PLQY of 1% for PbS NPLs, 15% for PbSe fQDs and 2% for PbTe NPLs. This corresponds to retaining 65% of the initial PLQY in organic solution for PbSe fQDs (a decrease from 23% to 15%) and 50% for PbTe NPLs (from 4% down to 2%), which is in good agreement with the relative PLQY decrease observed during the phase transfer of CdSe NPLs to water (~50% loss).[24,35] These results render aqueous 2D PbSe fQDs in particular efficient NIR emitters in aqueous solution. For example, in comparison with well-established zero-dimensional PbSe QDs at these wavelengths, *e.g.* HYUN *et al.* reported "at least 10%" PLQY for aqueous PbS and PbSe QDs,[27] and LIN *et al.* measured 3.8 to 10% PLQY for ligand exchanged PbS, PbSe, and PbTe NCs in N-methyl-formamide.[31] To further improve the PLQY of (aqueous phase) 2D lead chalcogenides, shelling with *e.g.* CdS, resulting in type-I heterostructures, is under investigation currently.[6,42,43]

5.4.3 Ligand Binding to Aqueous 2D PbX fQDs and NPLs

To follow and characterize the lipophilic-to-hydrophilic ligand exchange at the molecular level, we perform X-ray photoelectron spectroscopy (XPS) measurements. Figure 5.4 shows the S2p XPS core-level spectra of organic (a–c) and aqueous (d–f) 2D PbX NCs. The signals primarily consist of the spin–orbit split S $2p_{3/2}$ and $2p_{1/2}$ doublet, with a 2:1 area ratio and a doublet separation of 1.2 eV (ref. 44) and minor overlapping non-sulfur contributions by the Se $3p_{3/2}$ and $3d_{1/2}$ doublet[45,46] (separation of 5.3 eV) in case of the PbSe fQDs (Figure 5.4b and e) and the Te 4s singlet[47] in case of aqueous PbTe NPLs (Figure 5.4f).

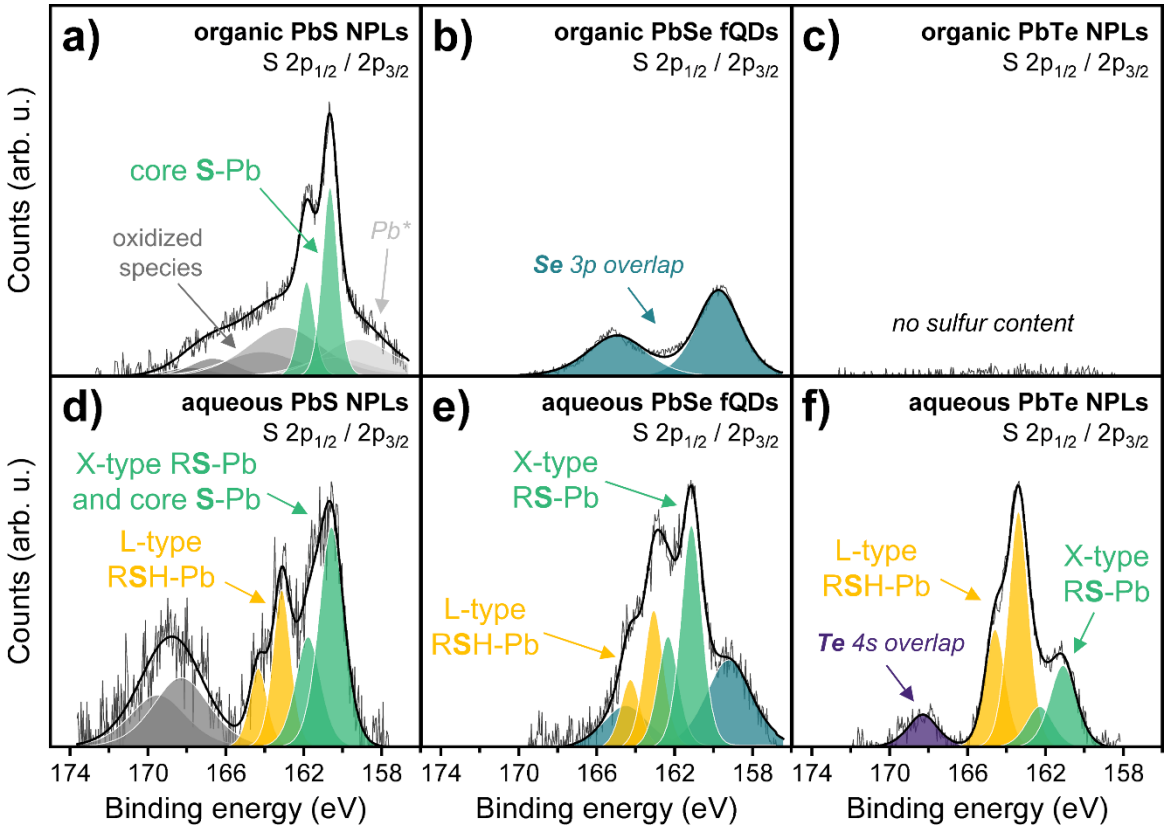

Figure 5.4. XPS analysis of the S 2p core level region prior to and after phase transfer of PbS NPLs (a, d), PbSe fQDs (b, e), and PbTe (c, f) NPLs. After the phase transferring to water by the introducing MUA as a ligand, the spectra of all three aqueous 2D PbX NCs show the appearance of RS-Pb (light green) and RSH-Pb (yellow) components, which indicates a combination of X-type bound thiolate and L-type binding of the protonated thiol to the 2D PbX NC surface.

The absence of the Te 4s singlet in organic PbTe NPLs suggests that the phase-exchanged PbTe NPLs are more stable under ambient conditions (which is crucial given the aqueous solutions are typically stored outside of the glovebox). They do not decompose by short-term exposure to air, for example during transfer into the vacuum of the XPS. In contrast, the less stable organic PbTe NPLs likely form oxide moieties, with a Te 4s signal consequently shifted to higher energies and originated outside the measured S 2p region compared to the Te-Pb binding motif.

Of the three organic 2D PbX NCs prior to phase transfer, only PbS NPLs (Figure 5.4a) exhibit significant S 2p core-level region signals. This can be explained by organic PbSe and PbTe NPLs both not containing sulfur or sulfur-containing ligands. In perfect agreement with values reported by CAO *et al.* and MALGRAS *et al.*, the narrow, high-intensity signal contribution at 160.6 and

161.8 eV (S-Pb, light green) is attributed to sulfur bound to lead within the PbS NPL core.[48,49] Additionally, minor contributions of sulfur species with higher oxidation states occur above 163.0 eV (dark grey), which are assigned to the oxidation of sulfur surface atoms due to a lack of protective ligands following the purification required prior to the phase transfer.[49] The lowest intensity components (Pb*, light grey) was previously assigned to the energy loss from Pb 4f signals.[49]

After the ligand exchange and transfer to water (d–f) S 2p signals rise for all 2D PbX NCs, as the sulfur-containing MUA ligand is introduced. The main component at 160.9 ± 0.3 and 162.1 ± 0.3 eV (RS-Pb and S-Pb, light green) is attributed to deprotonated MUA, which is bound to Pb surface sites *via* the thiolate function in an X-type manner (see Figure S 5.5 for a schematic representation of the different ligands binding types).[46,50] For PbS NPLs, these signals coincide with the S-Pb core component and are thus rather indistinguishable. Notably, the X-type binding motif, where thiolate as an anionic one-electron donor forms a covalent bond to a surface metal atom,[23] is the expected one. This motif is commonly depicted in reports on the water transfer of different NCs (also shown in Figure 5.1) with mercaptocarboxylic acids (though it is not necessarily probed).[28,35] The assignment of the second major component present for all 2D PbX NCs at 163.2 ± 0.2 and 164.4 ± 0.2 eV (yellow) is less unambiguous in literature, with three different options:

i. Free, unbound thiol (here MUA).[48]
ii. "Reverse" X-type binding of mercaptocarboxylic acid by the carboxylate with the free thiol facing the solution.[36]
iii. L-type binding of a protonated thiol as a neutral LEWIS base which donates two electrons from the sulfur to form a dative covalent bond.[23,51]

Similar to BAGARIA *et al.*, we deem the presence of considerable amounts of free, unbound MUA to be unlikely in our case, since the aqueous colloidal solutions were thoroughly precipitated to remove excess MUA (as well as any amine or oleate residues).[36] In addition, the drop-casted XPS samples were further rinsed with chloroform prior to being measured. To clarify this and to distinguish between the other two options (see Figure S 5.5), ^{1}H NMR measurements were performed and are discussed in Figure 5.5. Lastly, it is noteworthy that PbSe fQD and PbTe NPL

XPS spectra show no signs of oxidized sulfur species at higher binding energies. This result is consistent with the stability of relatively long-chained thiols towards photooxidation. It underpins that the oxidized sulfur species present in the aqueous PbS NPL sample originates from sulfur atoms in the core that are already present in organic PbS NPLs (see discussion above) and therefore are not to be expected for PbSe fQDs and PbTe NPLs.[52]

Figure 5.5 depicts ^{1}H NMR spectra of deprotonated MUA (phase transfer stock solution (a)), as well as aqueous PbS NPLs (b), PbSe fQDs (c), and PbTe NPLs (d) in D_2O, within the range of 1.45–2.85 ppm. The relevant protons and their respective chemical shifts are labeled in panel (e) and were assigned by applying work of RISTIG *et al.*[53] Two-fold unbound deprotonated MUA (as present in the phase transfer stock solution) exhibits two triplet resonances at 2.47 ppm (t, 2H, α_S-CH_2) and 2.10 ppm (t, 2H, α_{COO}-CH_2) corresponding to the protons in the α-position of the thiolate (1) and the carboxylate (2), respectively. The β-protons appear as two overlapping quintet resonances at approximately 1.53 ppm and 1.50 ppm (m, 4H, β-CH_2). The aliphatic protons, not shown in Figure 5.5a, occur as a broad singlet resonance around 1.24 ppm (s, 12H, CH_2), the thiol-proton of partial protonated MUA is expected at a similar resonance (s, 1H, SH), overlapping with the aliphatic protons. The carboxyl-proton (expected above 10 ppm (s, 1H, COOH)) is not present in any of the samples. For discussing the aqueous 2D PbX NC spectra, we focus on the α- and β-protons, all of which are downfield shifted by a similar amount compared to the free MUA for the three lead chalcogenides, which indicates a binding to the 2D PbX surface. It has to be noted that the fQD and NPL spectra do not show resonances of the unbound MUA ligand, which further confirms that the aqueous samples are indeed free of excess ligand (and ruling out free unbound thiol as the origin of the discussed XPS signals at 163.2 ± 0.2 and 164.4 ± 0.2 eV). In detail, the α-protons are shifted by +0.30 ppm to 2.74 (t, 2H, α_S-CH_2, (1)) and +0.07 ppm to 2.17 ppm (t, 2H, α_{COO}-CH_2, (2)), respectively. These shifts are consistent with those of the β-protons, which diverge in the fQD and NPL samples, resulting in two well separated quintets with shifts of +0.16 ppm to 1.69 ppm (q, 2H, β_S-CH_2, (3.1)) and +0.04 ppm to 1.54 ppm (q, 2H, β_{COO}-CH_2, (3.2)), respectively. Notably, the similar shift ratios $\Delta\delta(\alpha_S\text{-}CH_2)/\Delta\delta(\alpha_{COO}\text{-}CH_2)$ of 4.29 and $\Delta\delta(\beta_S\text{-}CH_2)/\Delta\delta(\beta_{COO}\text{-}CH_2)$ of 4.0 underpin the proton assignments.

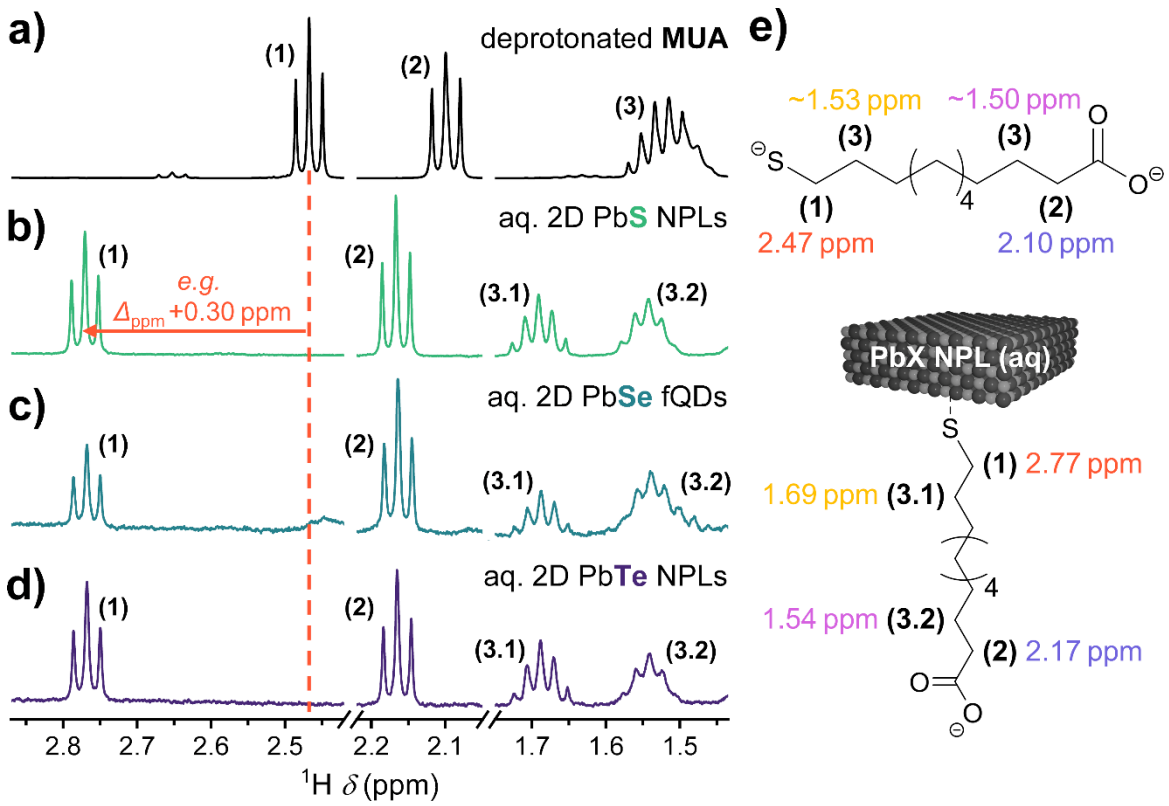

Figure 5.5. ^{1}H NMR spectra of free, deprotonated MUA (a) as well as aqueous PbS NPLs (b), PbSe fQDs (b), and PbTe NPLs (c). The downfield shift of the resonances of free MUA (assigned in panel (e)) compared to MUA in the 2D PbX samples indicates its binding to the 2D PbX surface. The larger shift of the α- and β-protons of the thiolate side ((1) and (3.1)) in comparision to the carboxylate side ((2) and (3.2)) of MUA suggests preferential binding via the sulfur.

The downfield shifting is associated with binding to the surface because the NC deshields the nuclei of the ligand.[53,54] Consequently, nuclei in closer proximity to the NC surface experience larger deshielding than those farther away. From the larger shifts of the α_S-CH_2 and β_S-CH_2 it is concluded, that MUA is bound to the fQD and NPL surface *via* the sulfur side. Together with the XPS data it is inferred that the aqueous PbX fQD and NPL surface is covered by a combination of X-type and L-type bound MUA. The NMR analysis further rules out the presence of large quantities of "reversely" X-type bound MUA. Such a configuration would result in different chemical shifts, showing two sets of resonances for the two different orientations. Notably, we do not observe significant NMR line broadening (around 1 Hz for the α_S-proton), which we attribute to solvent-ligand interactions, previously described by De Roo *et al.*[55] In brief, the authors conclude that poor

ligand solvation is the main cause for NMR line broadening in NC samples and found that water/D_2O produces the narrowest line widths in their study. We assume the same for the highly soluble deprotonated MUA ligands applied here.

The combination of X- and L-type bound MUA can address surface sites in a manner similar to the commonly used combination of X- and L-type oleate and octyl- or oleylamine in organic solution. This may be interpreted as one of the reasons for the successful and widespread use of mercaptocarboxylic acids in phase transfer processes involving compositionally and structurally very diverse NC systems.[27,28,35]

5.5 Conclusion

Up to now, there have been no phase transfer protocols for 2D PbX fQDs and NPLs with telecommunication band NIR PL in aqueous solution. Here, we adopt phase transfer protocols based on MUA to PbS NPLs, PbSe fQDs, and PbTe NPLs, yielding aqueous solutions and retaining their NIR PL. Aqueous PbSe fQDs (post-phase transfer quantum yield of 13%) are competitive with aqueous spherical PbX NCs, making them interesting for further processing into functional nanocomposites. Using XPS and NMR, we conclude on a combined role of X- and L-type binding of MUA to the fQDs and NPLs *via* the sulfur side (as thiolate and thiol). Our findings advance the understanding of efficient mercaptocarboxylic acid-based nanomaterial water transfer and will help to use the potential of 2D PbX NPLs and fQDs for the incorporation in (quantum) optical applications at technologically relevant wavelengths.

5.6 References

1 S. Ithurria, M. D. Tessier, B. Mahler, R. P. S. M. Lobo, B. Dubertret and A. L. Efros, Colloidal Nanoplatelets with Two-Dimensional Electronic Structure, *Nat. Mater.*, 2011, **10** (12), 936–941.

2 S. Ithurria and B. Dubertret, Quasi 2D Colloidal CdSe Platelets with Thicknesses Controlled at the Atomic Level, *J. Am. Chem. Soc.*, 2008, **130** (49), 16504–16505.

3 R. Scott, J. Heckmann, A. V. Prudnikau, A. Antanovich, A. Mikhailov, N. Owschimikow, M. Artemyev, J. I. Climente, U. Woggon, N. B. Grosse and A. W. Achtstein, Directed Emission of CdSe Nanoplatelets Originating from Strongly Anisotropic 2D Electronic Structure, *Nat. Nanotechnol.*, 2017, **12** (12), 1155–1160.

4 B. T. Diroll, B. Guzelturk, H. Po, C. Dabard, N. Fu, L. Makke, E. Lhuillier and S. Ithurria, 2D II-VI Semiconductor Nanoplatelets: From Material Synthesis to Optoelectronic Integration, *Chem. Rev.*, 2023, **123** (7), 3543–3624.

5 R. E. Correa, E. A. Dauler, G. Nair, S. H. Pan, D. Rosenberg, A. J. Kerman, R. J. Molnar, X. Hu, F. Marsili, V. Anant, K. K. Berggren and M. G. Bawendi, Single Photon Counting from Individual Nanocrystals in the Infrared, *Nano Lett.*, 2012, **12** (6), 2953–2958.

6 S. Krishnamurthy, A. Singh, Z. Hu, A. V. Blake, Y. Kim, A. Singh, E. A. Dolgopolova, D. J. Williams, A. Piryatinski, A. V. Malko, H. Htoon, M. Sykora and J. A. Hollingsworth, PbS/CdS Quantum Dot Room-Temperature Single-Emitter Spectroscopy Reaches the Telecom O and S Bands via an Engineered Stability, *ACS Nano*, 2021, **15** (1), 575–587.

7 G. Konstantatos, I. Howard, A. Fischer, S. Hoogland, J. Clifford, E. Klem, L. Levina and E. H. Sargent, Ultrasensitive Solution-Cast Quantum Dot Photodetectors, *Nature*, 2006, **442** (7099), 180–183.

8 V. Sukhovatkin, S. Hinds, L. Brzozowski and E. H. Sargent, Colloidal Quantum-Dot Photodetectors Exploiting Multiexciton Generation, *Science*, 2009, **324**, 1542–1544.

9 S. M. Tenney, V. Vilchez, M. L. Sonnleitner, C. Huang, H. C. Friedman, A. J. Shin, T. L. Atallah, A. P. Deshmukh, S. Ithurria and J. R. Caram, Mercury Chalcogenide Nanoplatelet-Quantum Dot Heterostructures as a New Class of Continuously Tunable Bright Shortwave Infrared Emitters, *J. Phys. Chem. Lett.*, 2020, **11** (9), 3473–3480.

10 B. B. V. Salzmann, J. de Wit, C. Li, D. Arenas-Esteban, S. Bals, A. Meijerink and D. Vanmaekelbergh, Two-Dimensional CdSe-PbSe Heterostructures and PbSe Nanoplatelets: Formation, Atomic Structure, and Optical Properties, *J. Phys. Chem. C*, 2022, **126** (3), 1513–1522.

11 M. T. Harrison, S. V. Kershaw, M. G. Burt, A. L. Rogach, A. Kornowski, A. Eychmüller and H. Weller, Colloidal Nanocrystals for Telecommunications. Complete Coverage of the Low-Loss Fiber Windows by Mercury Telluride Quantum Dot, *Pure Appl. Chem.*, 2000, **72** (1–2), 295–307.

12 F. Manteiga Vázquez, Q. Yu, L. F. Klepzig, L. D. A. Siebbeles, R. W. Crisp and J. Lauth, Probing Excitons in Ultrathin PbS Nanoplatelets with Enhanced Near-Infrared Emission, *J. Phys. Chem. Lett.*, 2021, **12** (1), 680–685.

13 A. H. Khan, R. Brescia, A. Polovitsyn, I. Angeloni, B. Martín-García and I. Moreels, Near-Infrared Emitting Colloidal PbS Nanoplatelets: Lateral Size Control and Optical Spectroscopy, *Chem. Mater.*, 2017, **29** (7), 2883–2889.

14 L. Biesterfeld, L. F. Klepzig, A. Niebur, M. Rosebrock and J. Lauth, Toward Bright Colloidal Near-Infrared Emitters: Surface Passivation of 2D PbSe Nanoplatelets by Metal Halides, *J. Phys. Chem. C*, 2022, **126** (45), 19277–19285.

15 L. F. Klepzig, L. Biesterfeld, M. Romain, A. Niebur, A. Schlosser, J. Hübner and J. Lauth, Colloidal 2D PbSe Nanoplatelets with Efficient Emission Reaching the Telecom O-, E- and S-Band, *Nanoscale Adv.*, 2022, **4**, 590-599.

16 L. Biesterfeld, H. T. Ngo, A. Addad, D. A. Rudolph, W. Leis, M. Seitz, G. Ji, B. Grandidier, C. Delerue, J. Lauth and L. Biadala, Monolayer-Defined Flat Colloidal PbSe Quantum Dots in Extreme Confinement, *Nano Lett.*, 2025, **25** (31), 12019–12024.

17 L. Biesterfeld, M. T. Vochezer, M. Kögel, I. A. Zaluzhnyy, M. Rosebrock, L. F. Klepzig, W. Leis, M. Seitz, J. C. Meyer and J. Lauth, Solving the Synthetic Riddle of Colloidal Two-Dimensional PbTe Nanoplatelets with Tunable Near-Infrared Emission, *Chem. Mater.*, 2024, **36** (15), 7197–7206.

18 M. Aerts, T. Bielewicz, C. Klinke, F. C. Grozema, A. J. Houtepen, J. M. Schins and L. D. A. Siebbeles, Highly Efficient Carrier Multiplication in PbS Nanosheets, *Nat. Commun.*, 2014, **5**, 3789.

19 P. Li, L. Biesterfeld, L. F. Klepzig, J. Yang, H. T. Ngo, A. Addad, T. N. Rakow, R. Guan, E. P. Rugeramigabo, I. Zaluzhnyy, F. Schreiber, L. Biadala, J. Lauth and M. Zopf, Sub-millielectronvolt Line Widths in Polarized Low-Temperature Photoluminescence of 2D PbS Nanoplatelets, *Nano Lett.*, 2024, **24** (51), 16293–16300.

20 J. Lauth, M. Failla, E. Klein, C. Klinke, S. Kinge and L. D. A. Siebbeles, Photoexcitation of PbS Nanosheets Leads to Highly Mobile Charge Carriers and Stable Excitons, *Nanoscale*, 2019, **11** (44), 21569–21576.

21 M. M. Ramin Moayed, T. Bielewicz, M. S. Zöllner, C. Herrmann and C. Klinke, Towards Colloidal Spintronics Through Rashba Spin-Orbit Interaction in Lead Sulphide Nanosheets, *Nat. Commun.*, 2017, **8** (1), 15721.

22 P. J. Morrison, R. A. Loomis and W. E. Buhro, Synthesis and Growth Mechanism of Lead Sulfide Quantum Platelets in Lamellar Mesophase Templates, *Chem. Mater.*, 2014, **26** (17), 5012–5019.

23 N. C. Anderson, M. P. Hendricks, J. J. Choi and J. S. Owen, Ligand Exchange and the Stoichiometry of Metal Chalcogenide Nanocrystals: Spectroscopic Observation of Facile Metal-Carboxylate Displacement and Binding, *J. Am. Chem. Soc.*, 2013, **135** (49), 18536–18548.

24 F. Li, L. F. Klepzig, N. Keppler, P. Behrens, N. C. Bigall, H. Menzel and J. Lauth, Layer-by-Layer Deposition of 2D CdSe/CdS Nanoplatelets and Polymers for Photoluminescent Composite Materials, *Langmuir*, 2022, **38** (37), 11149–11159.

25 L. F. Klepzig, N. C. Keppler, D. A. Rudolph, A. Schaate, P. Behrens and J. Lauth, Highly Transparent, Yet Photoluminescent: 2D CdSe/CdS Nanoplatelet-Zeolitic Imidazolate Framework Composites Sensitive to Gas Adsorption, *Small*, 2024, **20** (18), 2309533.

26 Z. Chai, X. Hu, F. Wang, X. Niu, J. Xie and Q. Gong, Ultrafast All-Optical Switching, *Adv. Opt. Mater.*, 2017, **5** (7), 1600665.

27 B.-R. Hyun, H. Chen, D. A. Rey, F. W. Wise and C. A. Batt, Near-Infrared Fluorescence Imaging with Water-Soluble Lead Salt Quantum Dots, *J. Phys. Chem. B*, 2007, **111** (20), 5726–5730.

28 S. Tamang, G. Beaune, I. Texier and P. Reiss, Aqueous Phase Transfer of InP/ZnS Nanocrystals Conserving Fluorescence and High Colloidal Stability, *ACS Nano*, 2011, **5** (12), 9392–9402.

29 M. Chen, H. Yu, S. V. Kershaw, H. Xu, S. Gupta, F. Hetsch, A. L. Rogach and N. Zhao, Fast, Air–Stable Infrared Photodetectors Based on Spray–Deposited Aqueous HgTe Quantum Dots, *Adv. Funct. Mater.*, 2014, **24** (1), 53–59.

30 T. Galle, D. Spittel, N. Weiß, V. Shamraienko, H. Decker, M. Georgi, R. Hübner, N. Metzkow, C. Steinbach, D. Schwarz, V. Lesnyak and A. Eychmüller, Simultaneous Ligand and Cation Exchange of Colloidal CdSe Nanoplatelets Toward PbSe Nanoplatelets for Application in Photodetectors, *J. Phys. Chem. Lett.*, 2021, **12** (21), 5214–5220.

31 Q. Lin, H. J. Yun, W. Liu, H.-J. Song, N. S. Makarov, O. Isaienko, T. Nakotte, G. Chen, H. Luo, V. I. Klimov and J. M. Pietryga, Phase-Transfer Ligand Exchange of Lead Chalcogenide Quantum Dots for Direct Deposition of Thick, Highly Conductive Films, *J. Am. Chem. Soc.*, 2017, **139** (19), 6644–6653.

32 Y. Gao, M. Aerts, C. S. S. Sandeep, E. Talgorn, T. J. Savenije, S. Kinge, L. D. A. Siebbeles and A. J. Houtepen, Photoconductivity of PbSe Quantum-Dot Solids: Dependence on Ligand Anchor Group and Length, *ACS Nano*, 2012, **6** (11), 9606–9614.

33 Y. Liu, M. Gibbs, J. Puthussery, S. Gaik, R. Ihly, H. W. Hillhouse and M. Law, Dependence of Carrier Mobility on Nanocrystal Size and Ligand Length in PbSe Nanocrystal Solids, *Nano Lett.*, 2010, **10** (5), 1960–1969.

34 S. F. Wuister, I. Swart, F. van Driel, S. G. Hickey and C. de Mello Donegá, Highly Luminescent Water-Soluble CdTe Quantum Dots, *Nano Lett.*, 2003, **3** (4), 503–507.

35 T. Kodanek, H. M. Banbela, S. Naskar, P. Adel, N. C. Bigall and D. Dorfs, Phase Transfer of 1- and 2-Dimensional Cd-Based Nanocrystals, *Nanoscale*, 2015, **7** (45), 19300–19309.

36 H. G. Bagaria, E. T. Ada, M. Shamsuzzoha, D. E. Nikles and D. T. Johnson, Understanding Mercapto Ligand Exchange on the Surface of FePt Nanoparticles, *Langmuir*, 2006, **22** (18), 7732–7737.

37 M. P. Hendricks, M. P. Campos, G. T. Cleveland, I. Jen-La Plante and J. S. Owen, A Tunable Library of Substituted Thiourea Precursors to Metal Sulfide Nanocrystals, *Science*, 2015, **348** (6240), 1226–1230.

38 B. Mahler, B. Nadal, C. Bouet, G. Patriarche and B. Dubertret, Core/Shell Colloidal Semiconductor Nanoplatelets. *J. Am. Chem. Soc.*, 2012, **134** (45), 18591–18598.

39 U. T. D. Thuy, N. Q. Liem, D. X. Thanh, M. Protière and P. Reiss, Optical Transitions in Polarized CdSe, CdSe/ZnSe, and CdSe/CdS/ZnS Quantum Dots Dispersed in Various Polar Solvents, *Appl. Phys. Lett.*, 2007, **91** (24), 241908.

40 F. W. Wise, Lead Salt Quantum Dots: The Limit of Strong Quantum Confinement, *Acc. Chem. Res.*, 2000, **33** (11), 773–780.

41 J. E. Murphy, M. C. Beard, A. G. Norman, S. P. Ahrenkiel, J. C. Johnson, P. Yu, O. I. Mićić, R. J. Ellingson and A. J. Nozik, PbTe Colloidal Nanocrystals: Synthesis, Characterization, and Multiple Exciton Generation, *J. Am. Chem. Soc.*, 2006, **128** (10), 3241–3247.

42 C. J. Hanson, N. F. Hartmann, A. Singh, X. Ma, W. J. I. DeBenedetti, J. L. Casson, J. K. Grey, Y. J. Chabal, A. V. Malko, M. Sykora, A. Piryatinski, H. Htoon and J. A. Hollingsworth, Giant PbSe/CdSe/CdSe Quantum Dots: Crystal-Structure-Defined Ultrastable Near-Infrared Photoluminescence from Single Nanocrystals, *J. Am. Chem. Soc.*, 2017, **139** (32), 11081–11088.

43 Z. Hu, Y. Kim, S. Krishnamurthy, I. D. Avdeev, M. O. Nestoklon, A. Singh, A. V. Malko, S. V. Goupalov, J. A. Hollingsworth and H. Htoon, Intrinsic Exciton Photophysics of PbS Quantum Dots Revealed by Low-Temperature Single Nanocrystal Spectroscopy, *Nano Lett.*, 2019, **19** (12), 8519–8525.

44 D. G. Castner, K. Hinds and D. W. Grainger, X-Ray Photoelectron Spectroscopy Sulfur 2p Study of Organic Thiol and Disulfide Binding Interactions with Gold Surfaces, *Langmuir*, 1996, **12** (21), 5083–5086.

45 Y. Tong, T. Jiang, A: Bendounan, F. Nicolas, S: Kubsky and V. A. Esaulov, Selenium, Benzeneselenol, and Selenophene Interaction with Cu(100), *J. Phys. Chem. C*, 2016, **120** (38), 21486–21495.

46 R. T. Graf, K. Tran, M. Rosebrock, H. Borg, J. Schlenkrich, F. Lübkemann-Warwas, F. Renz, D. Dorfs and N. C. Bigall, Self-Assembly of Semiconductor Nanoplatelets into Stacks Directly in Aqueous Solution, *Adv. Mater. Interfaces*, 2023, **10** (35), 2300408.

47 J. F. Moulder and J. Chastain, Handbook of X-Ray Photoelectron Spectroscopy: A Reference Book of Standard Spectra for Identification and Interpretation of XPS Data, *Perkin-Elmer Physical Electronics Division*, 1992.

48 Y. Cao, A. Stavrinadis, T. Lasanta, D. So and G. Konstantatos, The Role of Surface Passivation for Efficient and Photostable PbS Quantum Dot Solar Cells, *Nat. Energy*, 2016, **1** (4), 1–6.

49 V. Malgras, A. Nattestad, Y. Yamauchi, S. X. Dou and J. H. Kim, The Effect of Surface Passivation on the Structure of Sulphur-Rich PbS Colloidal Quantum Dots for Photovoltaic Application, *Nanoscale*, 2015, **7** (13), 5706–5711.

50 C. Zubrägel, C. Deuper, F. Schneider, M. Neumann, M. Grunze, A. Schertel and C. Wöll, The Presence of Two Different Sulfur Species in Self-Assembled Films of n-Alkanethiols on Au and Ag Surfaces, *Chem. Phys. Lett.*, 1995, **238** (4-6), 308–312.

51 M. L. Kessler, J. E. Kelm, H. E. Starr, E. N. Cook, J. D. Miller, N. A. Rivera, H. Hsu-Kim and J. L. Dempsey, Unraveling Changes to PbS Nanocrystal Surfaces Induced by Thiols, *Chem. Mater.*, 2022, **34** (4), 1710–1721.

52 D. A. Hutt and G. J. Leggett, Influence of Adsorbate Ordering on Rates of UV Photooxidation of Self-Assembled Monolayers, *J. Phys. Chem.*, 1996, **100** (16), 6657–6662.

53 S. Ristig, D. Kozlova, W. Meyer-Zaika and M. Epple, An Easy Synthesis of Autofluorescent Alloyed Silver-Gold Nanoparticles, *J. Mater. Chem. B.*, 2014, **2** (45), 7887–7895.

54 Z. Hens and J. C. A. Martins, Solution NMR Toolbox for Characterizing the Surface Chemistry of Colloidal Nanocrystals, *Chem. Mater.*, 2013, **25** (8), 1211–1221.

55 J. de Roo, N. Yazdani, E. Drijvers, A. Lauria, J. Maes, J. S. Owen, I. van Driessche, M. Niederberger, V. Wood, J. C. Martins, I. Infante and Z. Hens, Probing Solvent–Ligand Interactions in Colloidal Nanocrystals by the NMR Line Broadening, *Chem. Mater.*, 2018, **30** (15), 5485–5492.

5.7 Supplementary Information

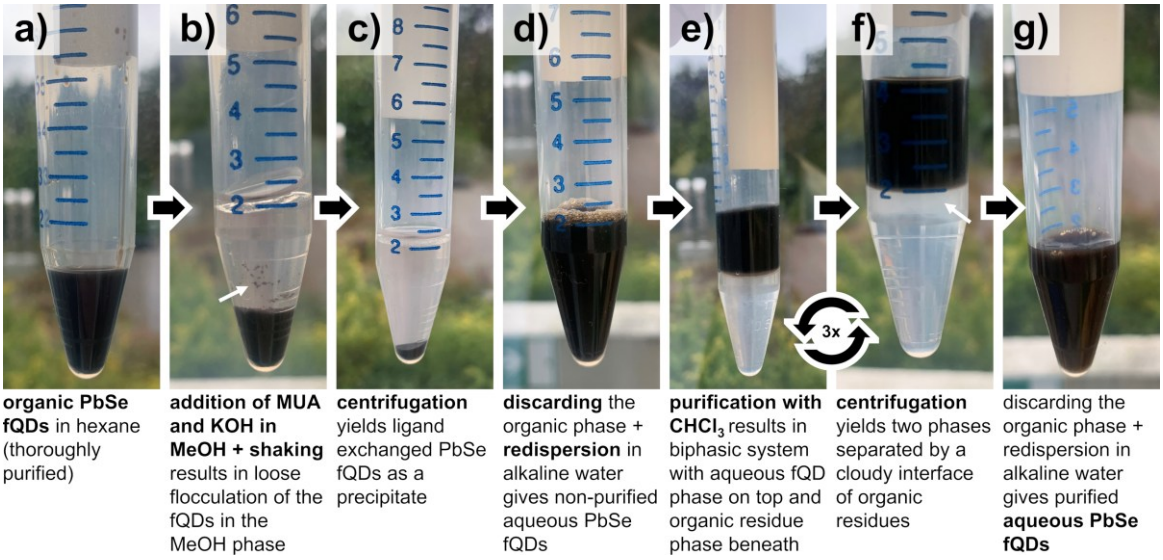

Figure S 5.1. Photo series showing the phase transfer process for the example of PbSe fQDs. (a) Thoroughly purified organic PbSe fQDs are dispersed in hexane. (b) Addition of a phase transfer solution (MUA and KOH in MeOH) results in the PbSe fQDs changing phase and loosely flocculating in the bottom MeOH phase. (c, d) Subsequent centrifugation followed by discarding of the biphasic supernatant and redispersion in water (0.1 M KOH) yields non-purified aqueous PbSe fQDs. (e–g) Purifying the aqueous PbSe fQDs with chloroform gives the final aqueous PbSe fQDs.

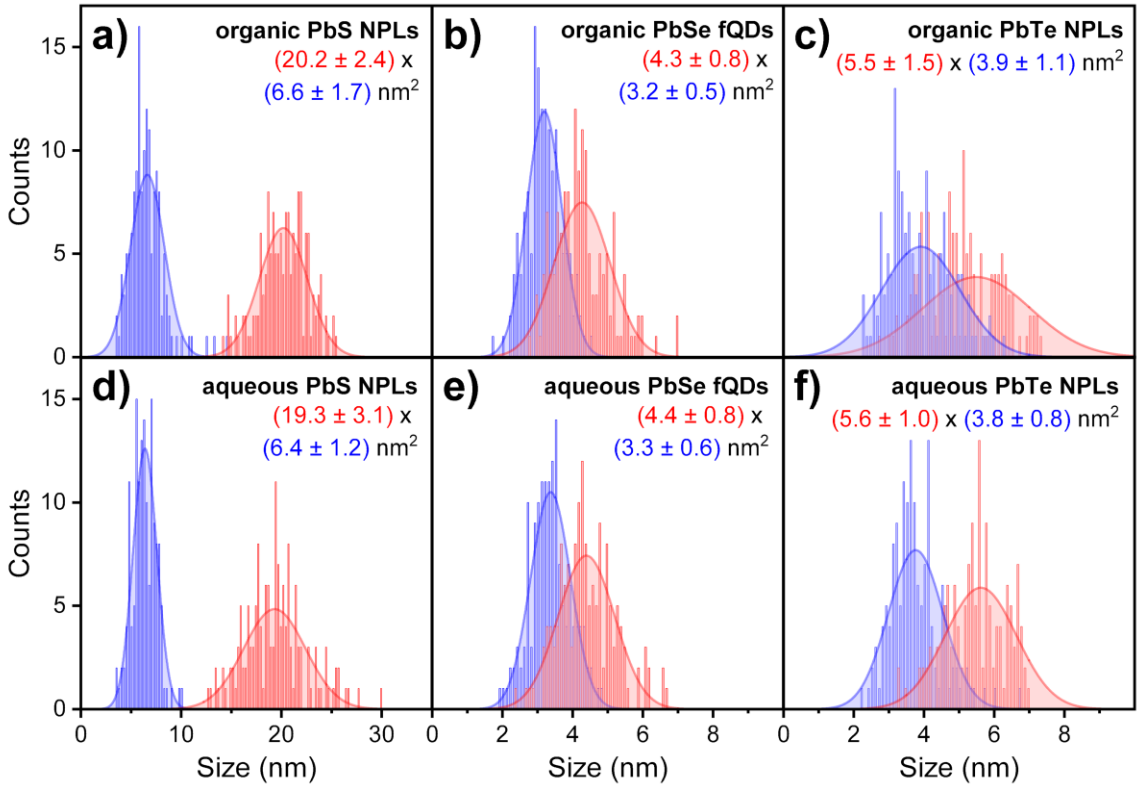

Figure S 5.2. Lateral size histograms of PbS NPLs, PbSe fQDs, and PbTe NPLs before (a–c) and after (d–f) phase transfer to water. The lateral sizes do not change significantly. *x*-Lengths (red) are the longest dimension of the fQDs and NPLs, *y*-widths (blue) were determined by measuring the largest distance perpendicular to the *x*-length. A sample size *n* of 150 NPLs was measured for each sample.

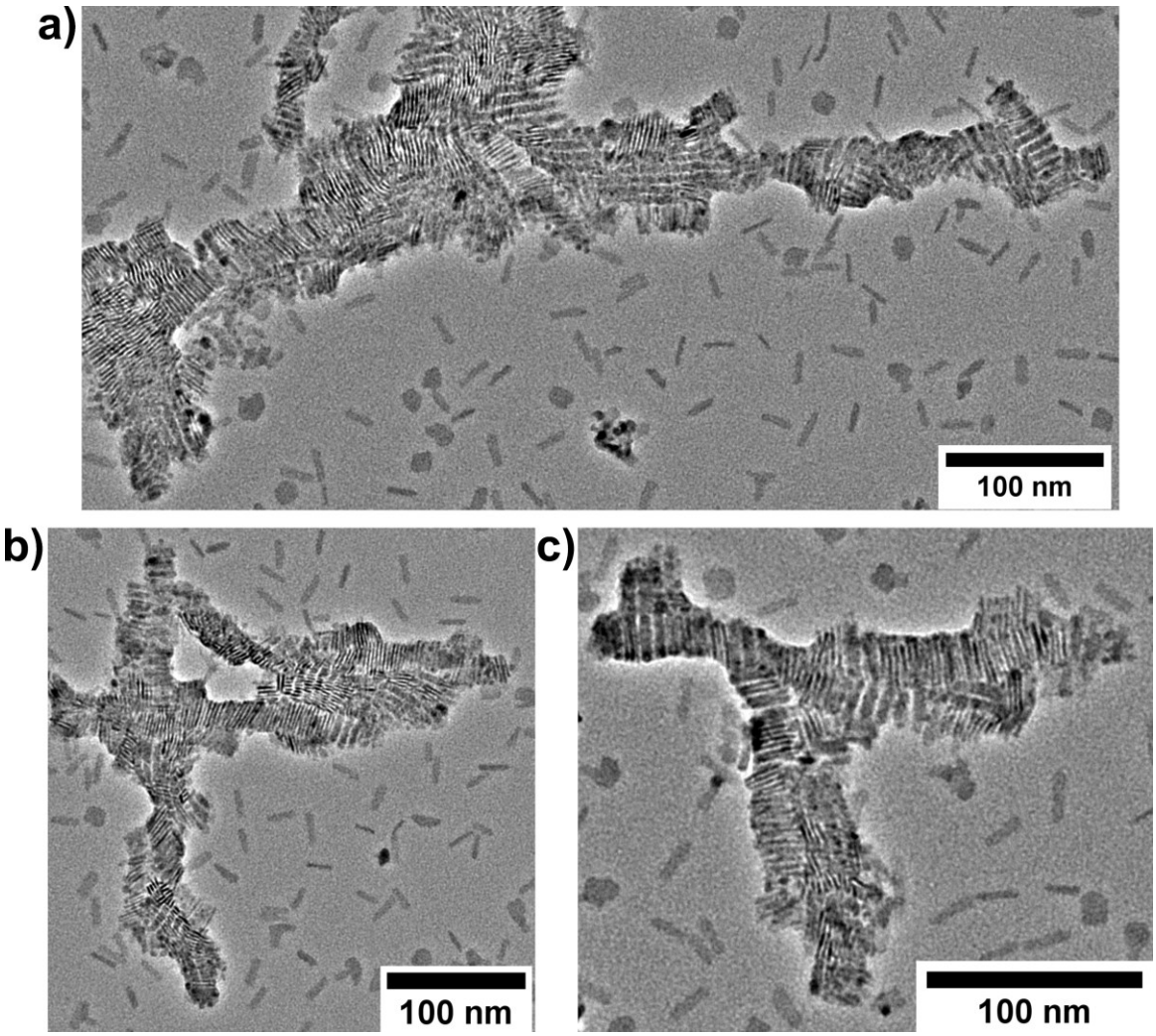

Figure S 5.3. TEM images of large stacks of vertically aligned 2D PbS NPLs (drop-casted from organic colloidal solution onto amorphous carbon-coated TEM grids). The rigorous purification before the phase transfer, accompanied by ligand stripping, promotes the formation of such stacks.

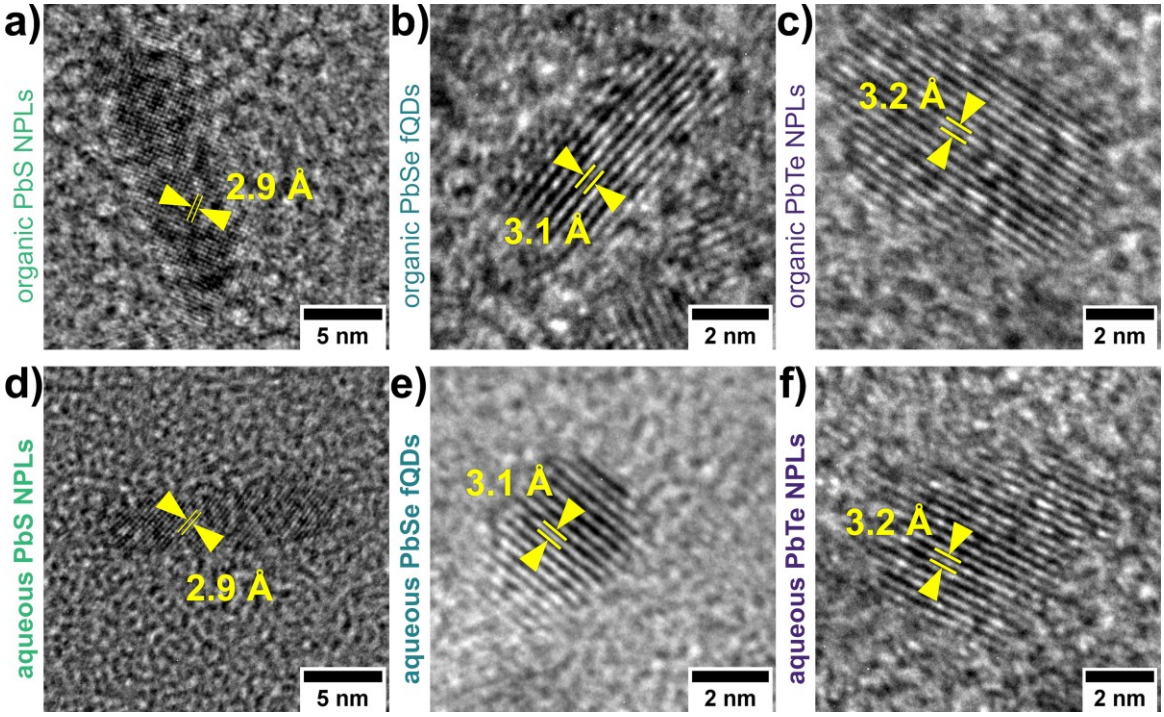

Figure S 5.4. High magnification TEM images of 2D PbX fQDs and NPLs before (a–c) and after (d–f) the aqueous phase transfer. The clearly visible lattice fringes underpin the crystallinity of the materials.

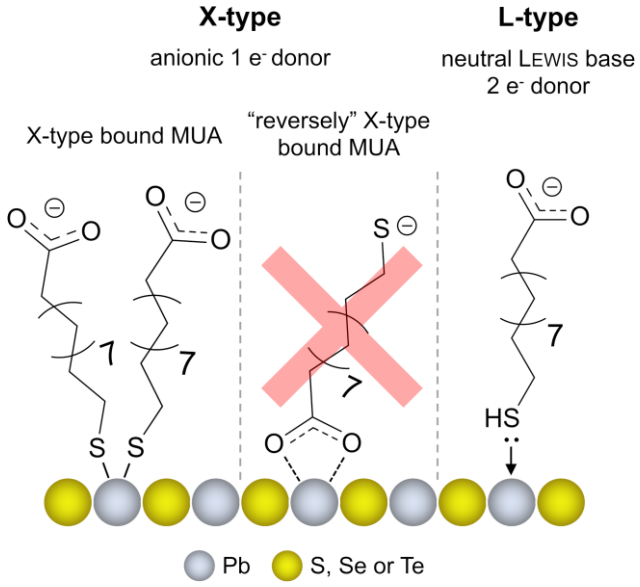

Figure S 5.5. Schematic representation of the possible binding motifs of MUA to the PbX NPL surface. By combining XPS and NMR measurements we rule out the presence of "reversely" X-type bound MUA and conclude on a combined passivation by X- and L-type bound MUA.

6 Sub-millielectronvolt Line Widths in Polarized Low-Temperature Photoluminescence of 2D PbS Nanoplatelets

This chapter focuses on the PL properties of single 2D PbS NPLs at cryogenic temperatures. At 4 K PbS NPLs exhibit blinking-free, linearly polarized PL (up to 90%), with linewidths down to 615 µeV and trions as the dominant PL source.

The results presented here have been published in *Nano Lett.* **2024**, *24* (51), 16293–16300. For details about the author contributions see Chapter B.

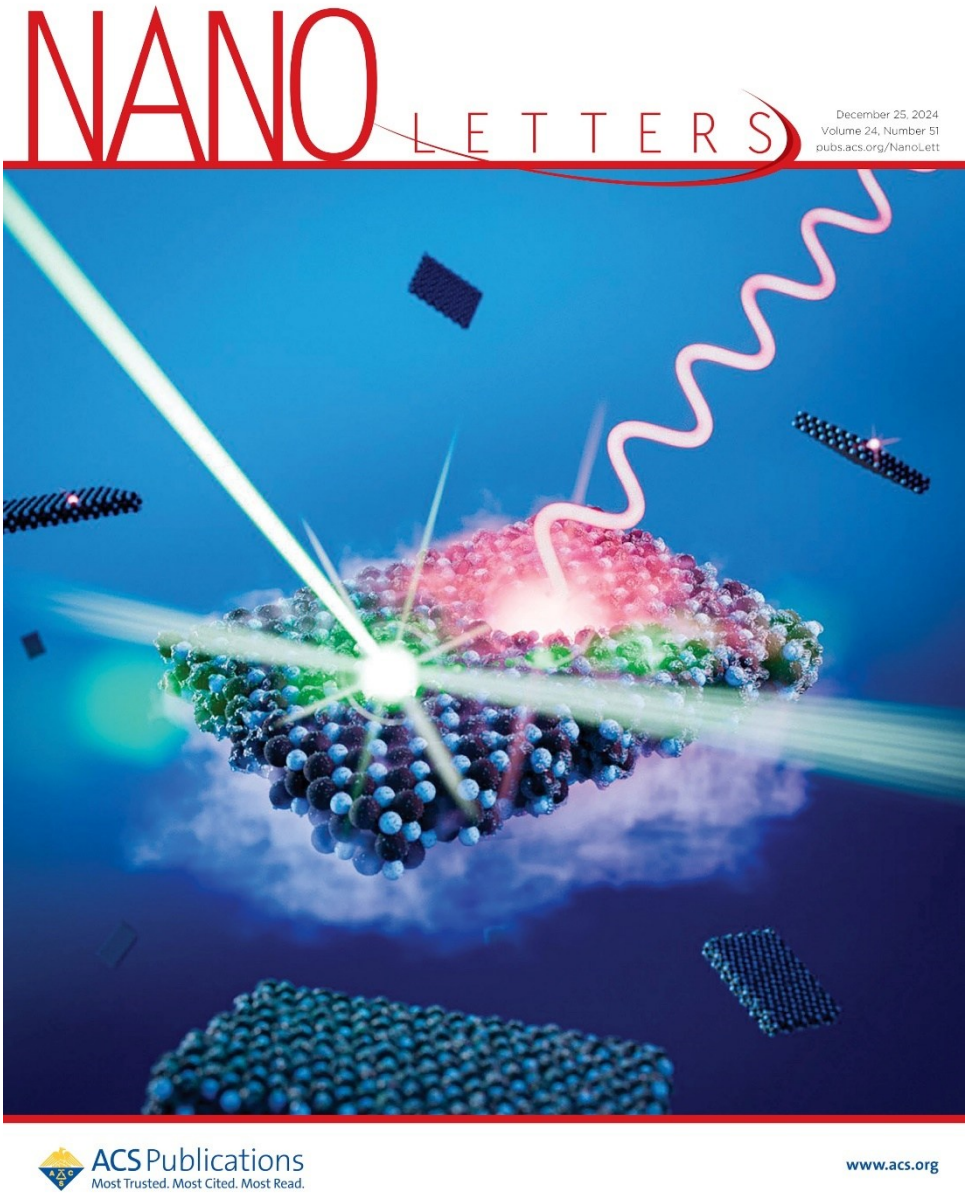

Pengji Li,[‡a] Leon Biesterfeld,[‡b,c,d] Lars F. Klepzig,[b,d] Jingzhong Yang,[a] Huu Thoai Ngo,[e] Ahmed Addad,[f] Tom N. Rakow,[a] Ruolin Guan,[a] Eddy P. Rugeramigabo,[a] Ivan Zaluzhnyy,[g] Frank Schreiber,[g] Louis Biadala,[e] Jannika Lauth,*[b,c,d,h] and Michael Zopf *[a,h]*

[a] Institute of Solid State Physics, Leibniz University Hannover, D-30167 Hannover, Germany.
[b] Cluster of Excellence PhoenixD (Photonics, Optics, and Engineering – Innovation Across Disciplines), D-30167 Hannover, Germany.
[c] Institute of Physical and Theoretical Chemistry, Eberhard Karls University of Tübingen, D-72076 Tübingen, Germany.
[d] Institute of Physical Chemistry and Electrochemistry, Leibniz Universität Hannover, D-30167 Hannover, Germany.
[e] Université de Lille, CNRS, Centrale Lille, Université Polytechnique Hauts-de-France, Junia-ISEN, UMR 8520 – IEMN, F-59000 Lille, France.
[f] Université de Lille, CNRS, INRAE, Centrale Lille, UMR 8207 – UMET – Unité Matériaux et Transformations, F-59000 Lille, France.
[g] Institute of Applied Physics, Eberhard Karls University of Tübingen, D-72076 Tübingen, Germany.
[h] Laboratory of Nano and Quantum Engineering, Leibniz University Hannover, D-30167 Hannover, Germany.
[‡] Equal contributions
* Corresponding author(s)

Reprinted with permission from *Nano Lett.* 2024, 24 (51), 16293–16300.

6.1 Abstract

Colloidal semiconductor nanocrystals are promising materials for classical and quantum light sources due to their efficient photoluminescence (PL) and versatile chemistry. While visible emitters are well-established, excellent (near-infrared) sources are still being pursued. We present the first comprehensive analysis of low-temperature PL from two-dimensional (2D) PbS nanoplatelets (NPLs). Ultrathin 2D PbS NPLs exhibit high crystallinity confirmed by scanning transmission electron microscopy, revealing MOIRÉ patterns in overlapping NPLs. At 4 K, unique PL features are observed in single PbS NPLs, including narrow zero-phonon lines with line widths down to 0.6 meV and a linear degree of polarization up to 90%. Time-resolved measurements identify trions as the dominant emission source with a 2.3 ns decay time. Sub-meV spectral diffusion and no inherent blinking over minutes are observed, as well as discrete spectral jumps without memory effects. These findings advance the understanding and underscore the potential of colloidal PbS NPLs for optical and quantum technologies.

6.2 Introduction

Colloidal semiconductor nanocrystals are being extensively studied for their use as classical and quantum light sources due to their optical properties dominated by size quantization.[1–3] Key requirements for their application include photostable PL with high quantum yields, short radiative lifetimes, low spectral broadening and diffusion, as well as scalable fabrication. At UV to visible wavelengths, cadmium chalcogenide CdX (X = S, Se, and Te) NPLs and heterostructures are known for their excellent optical properties. In particular, CdSe-based NPL systems exhibit narrow line widths below 40 meV at room temperature,[4,5] between 80% and up to unity PL quantum yield,[6–8] fast radiative decay in the nanosecond range,[4,9] and highly directional PL.[10] In recent years, colloidal lead halide perovskite nanocrystals have emerged as emitters with efficient (quantum yield over 96%),[11] narrow (12–42 nm) and rapidly decaying (1–29 ns) room-temperature PL at visible wavelengths,[12] as well as single photon emission.[13–15] However, materials with similar characteristics at (near-)infrared (NIR) wavelengths are yet highly sought for, in particular for photonic quantum communication applications.[16–18] Potential candidates include Ag-doped CdSe NPLs,[19] HgTe NPLs[20] or InAs/CdSe core-shell nanocrystals.[21] Another promising material class are lead chalcogenide

PbX (X = S, Se, Te) QDs,[22–24] NPLs[25–27] and related heterostructures:[28–30] For instance, KRISHNAMURTHY *et al.* demonstrated single spherical PbS/CdS QDs emitting in the telecom O-band (near 0.95 eV) at room-temperature, featuring photon antibunching and an average line width of 89.5 meV.[29] In a similar system and at T = 4 K, HU *et al.* reported on bleaching-free PL at around 1.0 eV and mean intrinsic PL line width of 16.4 meV, featuring asymmetric line shapes caused by the coupling of excitons to optical and acoustic phonon modes.[28] In both cases, the broad line widths (compared to their II-VI analogues, such as CdSe QDs) are a result of a 64-fold degenerated band-edge exciton in PbX QDs that splits into multiple energetically similar transitions, resulting in intrinsic PL broadening.[28,31,32] A closely related, yet unexplored system at the single particle level are photoluminescent 2D PbS NPLs. MANTEIGA VÁZQUEZ *et al.* developed a synthesis of rock salt cubic-structured PbS NPLs exhibiting a PL quantum yield of up to 19.4% for PL at 1.7 eV (720 nm) upon surface passivation with $CdCl_2$.[25] This strongly enhanced emission efficiency provides the opportunity to investigate the excitonic emission properties of 2D PbS NPLs at the individual emitter level and exploring their electronic structure, phonon interactions and spectral characteristics at cryogenic temperatures.

Our findings provide the first in-depth optical study of individual PbS NPLs at cryogenic temperatures. Highly polarized emissions at around 1.82 eV (677.6 nm) with sub-meV line widths are observed at T = 4 K, accompanied by an acoustic phonon sideband. Time-resolved and excitation power dependent measurements reveal trion states as the dominant cause of PL. The emissions exhibit exceptional spectral stability with sub-meV spectral diffusion and are blinking-free over several minutes, promoting the potential of 2D PbS NPLs for reaching near-infrared optoelectronic applications.

6.3 Results and Discussion

NIR emitting colloidal PbS NPLs passivated with $CdCl_2$ were synthesized by a method described by MANTEIGA VÁZQUEZ *et al.*[25] Figure 6.1a shows an overview TEM image of PbS NPLs resembling a rectangular shape with average lateral dimensions of (16.0 ± 1.6) × (9.2 ± 1.2) nm² and a corresponding aspect ratio of 1.7:1 (see Figure S 6.1 for an additional overview image and the corresponding size histogram).

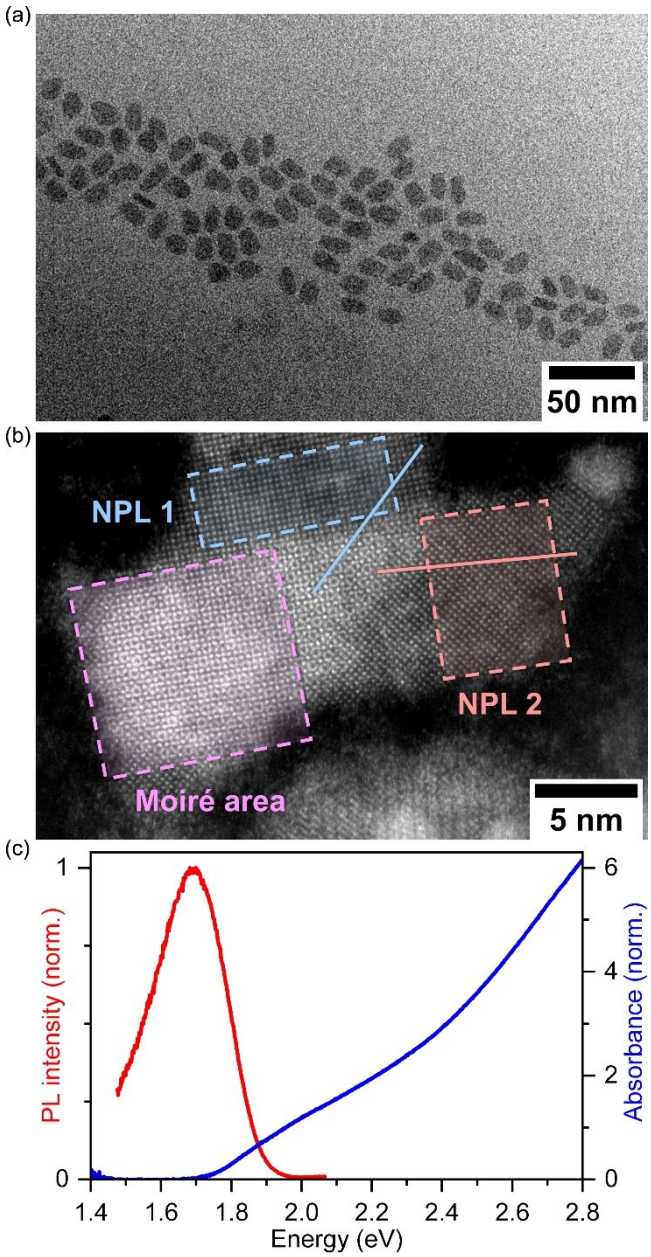

Figure 6.1. (a) Overview TEM image of rectangular PbS NPLs exhibiting average lateral dimensions of (16.0 ± 1.6) × (9.2 ± 1.2) nm². (b) HR-HAADF-STEM image of two overlapping PbS NPLs forming a MOIRÉ pattern. The formation of the interference pattern emphasizes the ultrathin 2D geometry of the PbS NPLs. (c) Ensemble room temperature absorbance and PL spectrum of PbS NPLs (in colloidal solution), exhibiting excitonic absorption at 1.96 eV and NIR PL at 1.70 eV.

Figure 6.1b depicts a HR-HAADF-STEM image of two overlapping PbS NPLs (the corresponding FFT patterns of the highlighted crystal areas are shown in Figure S 6.2a). The individual PbS NPLs are highly crystalline and exhibit the cubic

rock salt structure (space group $Fm\bar{3}m$) expected for 2D PbS nanosheets (NSs) and NPLs[25,33,34] with the characteristic lattice spacings of 2.9 Å (200) and 2.1 Å (220) (PDF card 01-078-1900). Notably, no diffraction peaks of an orthorhombic PbS phase (interplane distances of 2.8 and 2.05 Å)[35] are evident from the FFT patterns (see Figure S 6.2). The ultrathin 2D geometry and crystalline nature of the NPLs is underpinned by the formation of a pronounced MOIRÉ pattern in the overlapping area of the two differently oriented diffracting crystals (see Figure S 6.2b,c for additional examples). Although not directly related to the in-depth optical studies in this work, the formation of randomly oriented MOIRÉ patterns suggests that the small $CdCl_2$ ligands used as X- and Z-type ligands in a postsynthetic surface passivation step, allow for a quasi-direct contact between some PbS NPLs (in contrast to typical bulky organic surfactants such as oleic acid, which lead to further spatially separated NPLs, see also Figure S 6.3 for grazing-incidence wide-angle X-ray scattering data of PbS NPLs and further discussion).[26,36] While twistronics are very thoroughly researched for VAN DER WAALS materials,[37] MOIRÉ superlattices based on metavalently bound materials such as PbS have only recently been accessed by WANG *et al. via* an aqueous synthesis route with readily removable ligands. We assume that metal halide passivation can yield similar formations while at the same time enhancing the optical properties of the PbS NPLs synthesized in organic medium.[36] Figure 6.1c depicts the optical characteristics of the PbS NPL ensemble in colloidal solution at room-temperature, which exhibit an excitonic absorption feature at 1.96 eV and associated NIR PL at 1.70 eV with a rather broad fwhm of 264 meV (Figure 6.1c). To gain further insight into the optical, structural and electronic properties of PbS NPLs at the single NPL level, we perform PL measurements at cryogenic temperatures (see SI, section 6.6.1). Please note that signs of MOIRÉ modulation are not expected in the characterized single NPL optical spectra since the NPLs are separated spatially by the polystyrene matrix).

Figure 6.2a shows a representative PL spectrum of individual PbS NPLs at T = 4 K. In marked contrast with typical PL spectra of PbS nanocrystals for which single broad (≥ 8 meV) emission lines are observed,[28] the PL spectra of PbS NPLs consist of a narrow, resolution-limited, zero phonon line (ZPL) together with phonon sidebands at energies of 26.5 and 5 meV that we attribute to optical (LO) and acoustic phonons (Ac), respectively[28,38] (see Table S 6.1 for the fitting results,

Figure S 6.5 and Figure S 6.6 for more spectra of individual NPLs). The statistics on more than 70 individual NPLs show that the emission energies of the ZPL (Figure 6.2b) is centered around 1.82 ± 0.06 eV, which clearly indicates a high level of uniformity in the thickness and the lateral dimensions of the PbS NPLs.

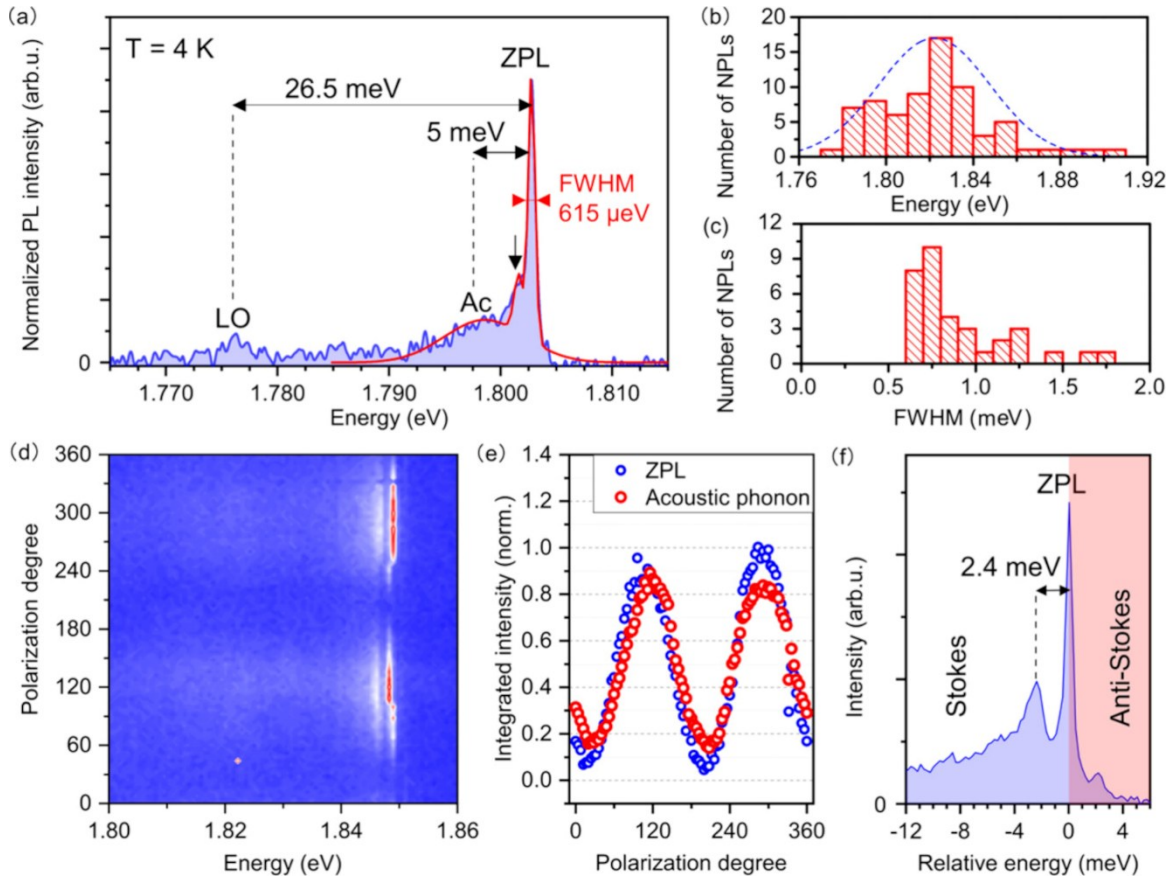

Figure 6.2. PL of single PbS NPLs at T = 4 K. (a) Micro-PL spectrum of a single PbS NPL (1 s exposure time) featuring sub-meV emission and a red-shifted phonon sideband with LO-phonon replicas (LO) and acoustic phonon (Ac) contributions. (b) Distribution of the emission energy centered around 1.82 eV and (c) fwhm of the narrowband part of single PbS NPL emissions, obtained by measuring 71 individual NPLs. 74% of the measured emission lines exhibit sub-meV line widths. (d) Polarization-dependent PL measurement of a single PbS NPL and (e) the respective normalized PL intensity obtained in different spectral ranges as a function of the linear polarization angle of the emitted light. The blue dots represent the ZPL (δ = 0.90), the red dots correspond to the acoustic phonon sideband (δ = 0.71). (f) Normalized sum of the 91 PL spectra from the measurement in (d) and illustration of STOKES and anti-STOKES PL of the acoustic phonon sidebands of a single PbS NPL.

Moreover, Figure 6.2c shows that the NPL emission line width does not exceed 2 meV and that more than 74% of the studied PbS NPLs exhibit a sub-meV line width. The detected line widths go down to 0.6 meV, approaching the resolution limit of the spectrometer. This strongly contrasts with the sharpest emission line width measured on individual PbS nanocrystals (≥ 8 meV)[28] for which the line broadening stems from the exciton fine structure,[28] the intervalley and the exciton-phonon coupling effects,[39] and the spectral diffusion.[40] Therefore, the record sharpness of the PbS NPLs studied here points to (i) an absence of spectral diffusion, (ii) a reduced exciton-phonon coupling and/or (iii) a different excitonic origin of the emission. Strikingly, we observe an additional discrete peak (arrow in Figure 6.2a) close to the ZPL on the PL spectra. A detailed analysis of the PL spectra around the ZPL (conducted on another NPL, Figure 6.2f) unveils that this discrete peak appears in both, the STOKES and anti-STOKES part of the PL spectra. Such a well-defined peak observed around 2.4 meV for most of the NPLs is most likely stemming from the thickness breathing mode (which would be 2.4 meV for a 1.6 nm thick PbS NPL, see Figure S 6.7 for TEM images of PbS NPLs exhibiting the thickness of 1–2 nm).[41,42] This feature, previously observed on PL spectra of individual CdSe[43] and InP[44] NCs at cryogenic temperatures, is the fingerprint of confined acoustic phonon modes at about 10 K, which corresponds to the base temperature in coldfinger cryostats for such sample preparation.

Notwithstanding unprecedented sharpness of their emission lines, PbS NPLs exhibit striking linear polarization properties (Figure 6.2d), which are analyzed by utilizing a rotating half-wave plate followed by a polarizer. In Figure 6.2e, integrated intensities of the ZPL and the acoustic phonon sideband for the various polarization angles are reported. From the angle dependent PL intensity, we evaluate the polarization degree, δ, as $\delta = (I_{max} - I_{min})/(I_{max} + I_{min})$ where I_{max} (I_{min}) are the maximum (minimum) PL intensities. The ZPL displays a high polarization degree $\delta = 0.90$ (for similar data from a second PbS NPL, we refer to Figure S 6.8). The acoustic phonon sideband (from -1 meV to -8 meV in Figure 6.2f) shows a slightly lower polarization degree of $\delta = 0.71$, while maintaining the same polarization angle as the ZPL.

The emission polarization of single NPLs is influenced by their aspect ratio,[31] as well as the orientation of the NPL with respect to the substrate. A dipole orientation in the plane of the substrate will show a maximum polarization degree, whereas

dipoles with orthogonal orientations are expected to appear as unpolarized emission (details in the SI, section 6.6.2, Figure S 6.8). The high degree of linear polarization in PbS NPLs indicates that the excitonic transition in individual PbS NPLs exhibits a polarization component, attributed to a linear 1D or 2D dipole. Furthermore, the alignment of the dipole is nearly ideal to the substrate plane (similar to observations shown in Figure 6.1). The aspect ratio is PbS NPLs is approximately 2, leading to anisotropic lateral electronic confinement and therefore contributing to the enhanced degree of observed polarization. It is important to note that the degree of polarization may depend on further factors that we do not study in detail here, such as selection rules of the allowed excitonic states and the respective oscillator strengths or possible effects of absorption polarization, by which the recombination of specific exciton types can be favored depending on the excitation energy and the energy spectrum of the NPL (further discussion in the SI, section 6.6.3).

Figure 6.3 shows the comparison of a PbS NPL ensemble with single NPL PL to study the origin and excitonic nature of the emission in more detail. Figure 6.3a includes the temperature-dependent PL spectra of a PbS NPL ensemble (Figure S 6.9 shows the data with an even more precise stepwise increase in temperature). We find an increasing slope of the high-energy PL edge with decreasing temperature, indicating an increased relative intensity and a decreased spectral width of the bandgap-associated emission. The PL spectrum of a single NPL at 4 K in Figure 6.3b, as well as the distribution of emission energies discussed in Figure 6.2b, shows good overlap with the emission edge of the ensemble emission at T = 4 K in Figure 6.3a.

The spectral region of the emission is then filtered (shaded gray area in Figure 6.3a,b) and detected with an avalanche photodiode to perform PL decay measurements for temperatures from 4 to 200 K (Figure 6.3c). The decay dynamics occur on two distinct time scales: a slow component ($\tau_1 \geq 6$ ns) and a fast component (τ_2 in the subnanosecond range), with detailed data provided in Figure S 6.9. As the temperature increases to 160 K, we observe a lengthening of the fast decay component from 300 to 750 ps. The fast decay component, τ_2, remains stable between 10 and 70 K, with most changes occurring above 70 K, which is consistent with the findings of CANNESON *et al.*[45] on trion emission in $CsPbBr_3$ quantum dots. At temperatures of 170 K, the fast decay component

disappears. This vanishing of the fast component could be explained by the thermal energy overcoming the binding energy of the excitonic complex, allowing us to estimate the trion binding energy to be ~14.7 meV, which is close to the theoretical values reported in the literature for PbS NPLs of similar dimensions.[46] (similar temperature-dependent results for PbS NPLs ensembles can be observed in Figure S 6.10 and Figure S 6.11). These dynamics stand compared to the PL decay of PbS nanocrystals, which typically occurs on a microsecond time scale (see Figure S 6.12 for PL lifetime measurement of ensemble PbS NPLs at RT).[47,48] We attribute the presence of the fast component to the generation of higher order excitonic complexes (such as trions), additionally favored by a pile-up effect due to the high repetition rate of the pulsed laser of 82 MHz used for photoexcitation in the temperature-dependent measurements.

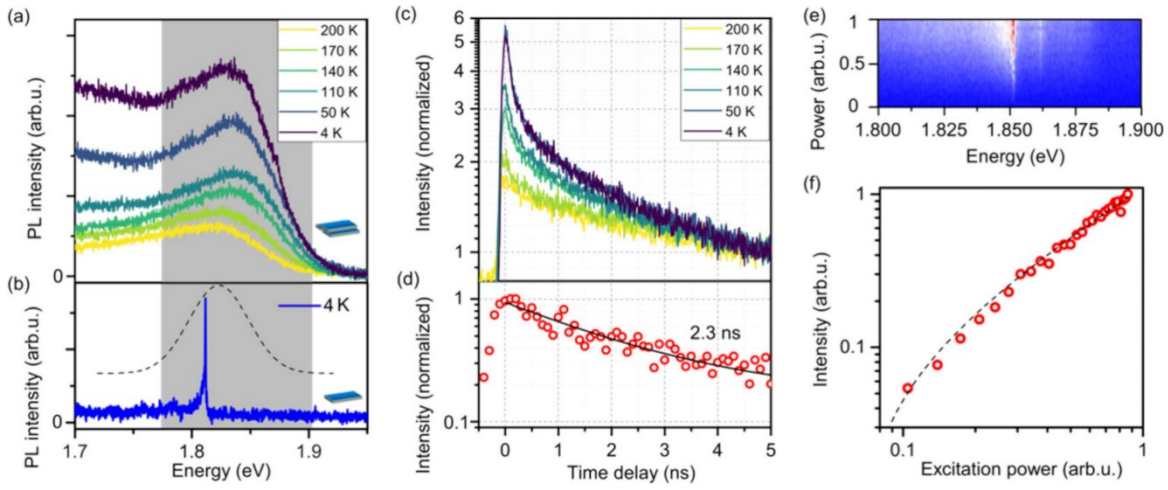

Figure 6.3. (a) Temperature-dependent PL spectra of an ensemble of PbS NPLs and (b) PL spectrum of a single PbS NPL at 4 K. The gray shaded area indicates the spectral range selected for lifetime measurements. The black dashed line represents the energy distribution of emissions from single PbS NPLs at 4 K in Figure 6.2b. (c) Fluorescence lifetime measurements of an ensemble of PbS NPLs, normalization is performed at a 'long' time scale (5 ns in this case) to emphasize the fast component and its strong temperature dependence. (d) Fluorescence lifetime measurement of a single PbS NPL. A monoexponential decay model is applied (solid, black line). (e) Excitation laser power dependent PL spectra of a single PbS NPL and (f) the respective normalized integrated PL intensity of the ZPL showing a linear increase with the excitation power.

The PL decay of a single PbS NPL at 4 K is shown in Figure 6.3d, and data is best modeled with a monoexponential decay, even though it cannot be ruled out completely that a smaller fraction with a slower decay component is present also in this case. A lifetime of 2.3 ns is extracted, which is in the realm of lifetimes reported for CdSe[49] and InP[50] NCs.

A further tool to investigate the excitonic origin of NPLs and nanocrystals are excitation power dependent measurements.[51,52] We perform these measurements under CW excitation with results shown in Figure 6.3e. A linear increase of the integrated PL intensity of the ZPL (Figure 6.3f) and the lack of additional spectral features with growing excitation power rule out multiexcitonic emissions as well as recombination processes that are independent of the excitation power (such as those involving trap or defect states).

By considering all observations up to this point, the question arises whether the narrow-band emission in single PbS NPLs can either be attributed to the presence of neutral excitons or trions, *i.e.* an exciton in the presence of an additional unpaired charge carrier. Owing to their specific spin structure,[53] optical properties of trions (positive and negative) include rather temperature-independent emission characteristics.[54] This results in trion emission having a rapid initial decay phase, which is indicative of swift radiative recombination. This phase is faster than the decay of dark excitons, yet slower than that of bright excitons.[54] The unique dynamics of neutral excitons, which are susceptible to temperature due to the interplay between optically inactive (dark) and active (bright) states, are in stark contrast with the more temperature-stable behavior of trions. However, the proportion of trion transitions is sensitive to temperature, particularly in relation to their binding energy. When thermal energy surpasses the trion binding energy, the trion emission effectively vanishes. This aligns well with observations from the PbS NPL ensemble PL decay as a function of temperature, which demonstrates that, while the rate of fast PL decay remains constant, its relative weight diminishes with an increase in temperature. Based on these factors, we assume the fast decay of the narrowband emission of single PbS NPLs at 4 K is initiated by a trion transition. The sign of the trion does not affect the conclusion but further studies on the magneto-optical properties of the trion will aim at unveiling the sign of the trion and their spin dynamics.

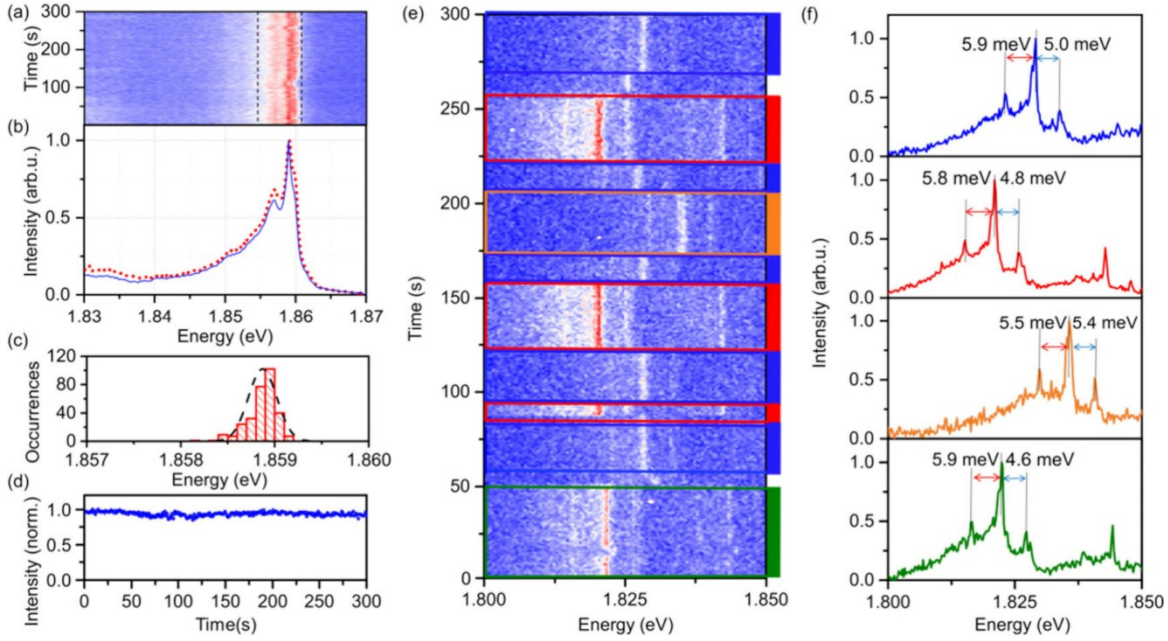

Figure 6.4. Spectral and temporal dynamics of single PbS NPLs. (a) PL time traces of a representative PbS NPL, exhibiting minimal spectral diffusion and blinking. (b) Normalized sum (red, dashed line) of the 300 PL spectra from (a). The blue line features the normalized sum of spectra which is corrected for spectral diffusion by rescaling the *x*-axis of each spectrum to the emission energy of the strongest emission peak. (c) Distribution of the central emission energy of the emission (obtained by fitting each spectrum in (a)) and (d) intensity time trace from the emission in (a) within the integration range shown by the dashed line. (e) PL time trace of a single PbS NPL, revealing combined spectral diffusion and blinking with discrete jumps. (f) Normalized sum of spectra for the four distinct emission states observed in (e), with the colors of the spectra corresponding to the selected ranges in (e).

To characterize the spectro-temporal dynamics in PbS NPLs, we analyze PL time traces of individual NPLs at a cryostat temperature of 4 K. These dynamics are key to understanding the influence of the nanomaterials' surroundings on their photophysical properties. Figure 6.4a shows 300 consecutively recorded spectra with 1 s exposure time each, exhibiting a highly stable emission of PbS NPLs. All recorded spectra are summed up and normalized to obtain a time-integrated spectrum over 300 s (dashed red line in Figure 6.4b). A second approach addresses the spectral diffusion by rescaling the *x*-axis of each individual spectrum to match the emission energy of the strongest emission peak, followed by summing up these

adjusted spectra and normalizing them (solid blue line in Figure 6.4b). The excellent overlap between the normalized sum of spectra and the spectral diffusion-compensated normalized sum of spectra underpins that the effect of spectral diffusion in the single PbS NPL emission is almost negligible over 5 min (see Figure S 6.13 and Figure S 6.14 for more time trace measurements of individual PbS NPLs). The distribution of the central emission energy, derived from applying a GAUSSIAN line shape to each spectrum, is presented in Figure 6.4c and reveals sub-meV (fwhm of 0.4 meV) spectral diffusion. The reduced fast spectral dynamics, which typically occur due to the STARK effect induced by trapped surface charges, points to a low density of surface traps. The application of $CdCl_2$ in a postsynthetic step for surface passivation has been identified as an effective strategy for addressing dangling bonds *via* X- and Z-type binding to Pb^{2+} and S^{2-} surface sites, respectively, and contributes to a reduced trap state density.[25,26] Midgap trap states are also expected to be of low level of significance due to the high crystallinity and well-balanced stoichiometry (Figure 6.1 and also MANTEIGA VÁZQUEZ *et al.*[20]), as well as an expected robustness of PbS NPLs against off-stoichiometry predicted in *ab initio* simulations.[55] Figure 6.4d shows the time-dependent intensity of the emitted signal shown in Figure 6.4a, within the spectral region indicated with dashed lines. A stable emission is observed over long times with no clear traces of blinking and only slow, low-magnitude drifts of the intensity, which is yet another argument for a low trap-state density in PbS NPLs.

While the low spectral diffusion is a common feature of the studied NPLs, the spectral characteristics can vary considerably. Figure 6.4e illustrates the spectral evolution of another PbS NPL, which displays several discrete spectral jumps over time. Four distinct spectral positions were identified, and for each of these we show the normalized sum of the respective spectra in Figure 6.4f by using the same color. Despite the differences in spectral position, the spectra are almost identical: The ZPL as well as observed STOKES and anti-STOKES PL features with phonon energies of around 5–6 meV do not change significantly. Another noteworthy feature is the lack of a memory effect[56] at the spectral jumps, which indicates that the spectral positions correspond to discrete localized states that are not correlated or affected by the previous state of the NPL. These observations could be consistent with a trion emission experiencing four different COULOMB environments (*e.g.*, four localized trapping sites) where the spectral positions are determined by the

quantum-confined STARK effect induced by a charge carrier trapping. The absence of spectral diffusion (see Figure S 6.15) at each spectral position indicates that the charges remain strongly localized as hopping charges would cause STARK effect fluctuations.

6.4 Conclusion

In conclusion, we have synthesized highly crystalline, ultrathin 2D PbS NPLs with $CdCl_2$ ligands used for surface passivation. A comprehensive analysis of the PL properties of these PbS NPLs is conducted at cryogenic temperatures. The results reveal that single PbS NPLs exhibit strong and linearly polarized emission at 4 K, showcasing sub-meV line widths significantly narrower than those observed in spherical nanocrystals of similar materials. These findings highlight the unique optical properties conferred by the 2D geometry of the PbS NPLs. Time-resolved PL measurements confirm that the narrow emission originate from trions. The trion state in PbS NPLs demonstrates stable emission with minimal spectral diffusion and the absence of blinking over minutes. Additionally, PbS NPLs exhibit new spectral diffusion characteristics, which lack a memory effect. Our findings not only advance the fundamental understanding of colloidal 2D semiconductor NPLs but also emphasize their significant potential for advancing the next generation of optical and quantum technologies.

6.5 References

(1) Kagan, C. R.; Bassett, L. C.; Murray, C. B.; Thompson, S. M. Colloidal Quantum Dots as Platforms for Quantum Information *Science. Chem. Rev.* **2021**, *121* (5), 3186–3233.

(2) Pietryga, J. M.; Park, Y.-S.; Lim, J.; Fidler, A. F.; Bae, W. K.; Brovelli, S.; Klimov, V. I. Spectroscopic and Device Aspects of Nanocrystal Quantum Dots. *Chem. Rev.* **2016**, *116* (18), 10513–10622.

(3) Diroll, B. T.; Guzelturk, B.; Po, H.; Dabard, C.; Fu, N.; Makke, L.; Lhuillier, E.; Ithurria, S. 2D II-VI Semiconductor Nanoplatelets: From Material Synthesis to Optoelectronic Integration. *Chem. Rev.* **2023**, *123* (7), 3543–3624.

(4) Ithurria, S.; Tessier, M. D.; Mahler, B.; Lobo, R. P. S. M.; Dubertret, B.; Efros, Al. L. Colloidal Nanoplatelets with Two-Dimensional Electronic Structure. *Nat. Mater.* **2011**, *10* (12), 936–941.

(5) Ithurria, S.; Dubertret, B. Quasi 2D Colloidal CdSe Platelets with Thicknesses Controlled at the Atomic Level. *J. Am. Chem. Soc.* **2008**, *130* (49), 16504–16505.

(6) Schlosser, A.; Graf, R. T.; Bigall, N. C. CdS Crown Growth on CdSe Nanoplatelets: Core Shape Matters. *Nanoscale Adv.* **2020**, *2* (10), 4604–4614.

(7) Hu, A.; Bai, P.; Zhu, Y.; Song, Z.; Wang, R.; Zheng, J.; Yao, Y.; Zhang, Q.; Ding, Z.; Gao, P.; Sui, X.; Liu, X.; Gao, Y. Green CdSe/CdSeS Core/Alloyed-Crown Nanoplatelets Achieve Unity Photoluminescence Quantum Yield over a Broad Emission Range. *Advanced Optical Materials* **2022**, *10* (13), No. 2200469.

(8) Tessier, M. D.; Mahler, B.; Nadal, B.; Heuclin, H.; Pedetti, S.; Dubertret, B. Spectroscopy of Colloidal Semiconductor Core/Shell Nanoplatelets with High Quantum Yield. *Nano Lett.* **2013**, *13* (7), 3321–3328.

(9) Tessier, M. D.; Javaux, C.; Maksimovic, I.; Loriette, V.; Dubertret, B. Spectroscopy of Single CdSe Nanoplatelets. *ACS Nano* **2012**, *6* (8), 6751–6758.

(10) Scott, R.; Heckmann, J.; Prudnikau, A. V.; Antanovich, A.; Mikhailov, A.; Owschimikow, N.; Artemyev, M.; Climente, J. I.; Woggon, U.; Grosse, N. B.; Achtstein, A. W. Directed Emission of CdSe Nanoplatelets Originating from Strongly Anisotropic 2D Electronic Structure. *Nat. Nanotechnol.* **2017**, *12* (12), 1155–1160.

(11) Morad, V.; Stelmakh, A.; Svyrydenko, M.; Feld, L. G.; Boehme, S. C.; Aebli, M.; Affolter, J.; Kaul, C. J.; Schrenker, N. J.; Bals, S.; Sahin, Y.; Dirin, D. N.; Cherniukh, I.; Raino, G.; Baumketner, A.; Kovalenko, M. V. Designer Phospholipid Capping Ligands for Soft Metal Halide Nanocrystals. *Nature* **2024**, *626* (7999), 542–548.

(12) Protesescu, L.; Yakunin, S.; Bodnarchuk, M. I.; Krieg, F.; Caputo, R.; Hendon, C. H.; Yang, R. X.; Walsh, A.; Kovalenko, M. V. Nanocrystals of Cesium Lead Halide Perovskites ($CsPbX_3$, X = Cl, Br, and I): Novel Optoelectronic Materials Showing Bright Emission with Wide Color Gamut. *Nano Lett.* **2015**, *15* (6), 3692–3696.

(13) Park, Y.-S.; Guo, S.; Makarov, N. S.; Klimov, V. I. Room Temperature Single-Photon Emission from Individual Perovskite Quantum Dots. *ACS Nano* **2015**, *9* (10), 10386–10393.

(14) Hu, F.; Zhang, H.; Sun, C.; Yin, C.; Lv, B.; Zhang, C.; Yu, W. W.; Wang, X.; Zhang, Y.; Xiao, M. Superior Optical Properties of Perovskite Nanocrystals as Single Photon Emitters. *ACS Nano* **2015**, *9* (12), 12410–12416.

(15) Rainò , G.; Nedelcu, G.; Protesescu, L.; Bodnarchuk, M. I.; Kovalenko, M. V.; Mahrt, R. F.; Stöferle, T. Single Cesium Lead Halide Perovskite Nanocrystals at Low Temperature: Fast Single-Photon Emission, Reduced Blinking, and Exciton Fine Structure. *ACS Nano* **2016**, *10* (2), 2485–2490.

(16) Cao, X.; Zopf, M.; Ding, F. Telecom Wavelength Single Photon Sources. *J. Semicond.* **2019**, *40* (7), No. 071901.

(17) Miyazawa, T.; Takemoto, K.; Sakuma, Y.; Hirose, S.; Usuki, T.; Yokoyama, N.; Takatsu, M.; Arakawa, Y. Single-Photon Generation in the 1.55-Mm Optical-Fiber Band from an InAs/InP Quantum Dot. *Jpn. J. Appl. Phys.* **2005**, *44* (5L), L620.

(18) Ward, M. B.; Karimov, O. Z.; Unitt, D. C.; Yuan, Z. L.; See, P.; Gevaux, D. G.; Shields, A. J.; Atkinson, P.; Ritchie, D. A. On-Demand Single-Photon Source for 1.3 μm Telecom Fiber. *Appl. Phys. Lett.* **2005**, *86* (20), No. 201111.

(19) Khan, A. H.; Pinchetti, V.; Tanghe, I.; Dang, Z.; Martín-García, B.; Hens, Z.; Van Thourhout, D.; Geiregat, P.; Brovelli, S.; Moreels, I. Tunable and Efficient Red to Near-Infrared Photoluminescence by Synergistic Exploitation of Core and Surface Silver Doping of CdSe Nanoplatelets. *Chem. Mater.* **2019**, *31* (4), 1450–1459.

(20) Izquierdo, E.; Robin, A.; Keuleyan, S.; Lequeux, N.; Lhuillier, E.; Ithurria, S. Strongly Confined HgTe 2D Nanoplatelets as Narrow Near-Infrared Emitters. *J. Am. Chem. Soc.* **2016**, *138* (33), 10496–10501.

(21) Xie, R.; Peng, X. Synthetic Scheme for High-Quality InAs Nanocrystals Based on Self-Focusing and One-Pot Synthesis of InAs-Based Core-Shell Nanocrystals. *Angew. Chem. Int. Ed* **2008**, *47* (40), 7677–7680.

(22) Moreels, I.; Justo, Y.; De Geyter, B.; Haustraete, K.; Martins, J. C.; Hens, Z. Size-Tunable, Bright, and Stable PbS Quantum Dots: A Surface Chemistry Study. *ACS Nano* **2011**, *5* (3), 2004–2012.

(23) Murphy, J. E.; Beard, M. C.; Norman, A. G.; Ahrenkiel, S. P.; Johnson, J. C.; Yu, P.; Mićić, O. I.; Ellingson, R. J.; Nozik, A. J. PbTe Colloidal Nanocrystals: Synthesis, Characterization, and Multiple Exciton Generation. *J. Am. Chem. Soc.* **2006**, *128* (10), 3241–3247.

(24) Pietryga, J. M.; Schaller, R. D.; Werder, D.; Stewart, M. H.; Klimov, V. I.; Hollingsworth, J. A. Pushing the Band Gap Envelope: Mid-Infrared Emitting Colloidal PbSe Quantum Dots. *J. Am. Chem. Soc.* **2004**, *126* (38), 11752–11753.

(25) Manteiga Vázquez, F.; Yu, Q.; Klepzig, L. F.; Siebbeles, L. D. A.; Crisp, R. W.; Lauth, J. Probing Excitons in Ultrathin PbS Nanoplatelets with Enhanced Near-Infrared Emission. *J. Phys. Chem. Lett.* **2021**, *12* (1), 680–685.

(26) Biesterfeld, L.; Klepzig, L. F.; Niebur, A.; Rosebrock, M.; Lauth, J. Toward Bright Colloidal Near-Infrared Emitters: Surface Passivation of 2D PbSe Nanoplatelets by Metal Halides. *J. Phys. Chem. C* **2022**, *126* (45), 19277–19285.

(27) Klepzig, L. F.; Biesterfeld, L.; Romain, M.; Niebur, A.; Schlosser, A.; Hübner, J.; Lauth, J. Colloidal 2D PbSe Nanoplatelets with Efficient Emission Reaching the Telecom O-, E- and S-Band. *Nanoscale Adv.* **2022**, *4* (2), 590–599.

(28) Hu, Z.; Kim, Y.; Krishnamurthy, S.; Avdeev, I. D.; Nestoklon, M. O.; Singh, A.; Malko, A. V.; Goupalov, S. V.; Hollingsworth, J. A.; Htoon, H. Intrinsic Exciton Photophysics of PbS Quantum Dots Revealed by Low-Temperature Single Nanocrystal Spectroscopy. *Nano Lett.* **2019**, *19* (12), 8519–8525.

(29) Krishnamurthy, S.; Singh, A.; Hu, Z.; Blake, A. V.; Kim, Y.; Singh, A.; Dolgopolova, E. A.; Williams, D. J.; Piryatinski, A.; Malko, A. V.; Htoon, H.; Sykora, M.; Hollingsworth, J. A. PbS/CdS Quantum Dot Room-Temperature Single-Emitter Spectroscopy Reaches the Telecom O and S Bands via an Engineered Stability. *ACS Nano* **2021**, *15* (1), 575–587.

(30) Correa, R. E.; Dauler, E. A.; Nair, G.; Pan, S. H.; Rosenberg, D.; Kerman, A. J.; Molnar, R. J.; Hu, X.; Marsili, F.; Anant, V.; Berggren, K. K.; Bawendi, M. G. Single Photon Counting from Individual Nanocrystals in the Infrared. *Nano Lett.* **2012**, *12* (6), 2953–2958.

(31) Nestoklon, M.; Avdeev, I. D.; Goupalov, S. V. Theory of Excitonic States in Lead Salt Quantum Dots. In *Quantum Sensing and Nano Electronics and Photonics XVII*; Razeghi, M., Lewis, J. S., Khodaparast, G. A., Khalili, P., Eds.; SPIE: San Francisco, United States, **2020**; p 30.

(32) Kang, I.; Wise, F. W. Electronic Structure and Optical Properties of PbS and PbSe Quantum Dots. *J. Opt. Soc. Am. B* **1997**, *14* (7), 1632.

(33) Schliehe, C.; Juarez, B. H.; Pelletier, M.; Jander, S.; Greshnykh, D.; Nagel, M.; Meyer, A.; Foerster, S.; Kornowski, A.; Klinke, C.; Weller, H. Ultrathin PbS Sheets by Two-Dimensional Oriented Attachment. *Science* **2010**, *329* (5991), 550–553.

(34) Bielewicz, T.; Dogan, S.; Klinke, C. Tailoring the Height of Ultrathin PbS Nanosheets and Their Application as Field-Effect Transistors. *Small* **2015**, *11* (7), 826–833.

(35) Khan, A. H.; Brescia, R.; Polovitsyn, A.; Angeloni, I.; Martín-García, B.; Moreels, I. Near-Infrared Emitting Colloidal PbS Nanoplatelets: Lateral Size Control and Optical Spectroscopy. *Chem. Mater.* **2017**, *29* (7), 2883–2889.

(36) Wang, Y.; Song, Z.; Wan, J.; Betzler, S.; Xie, Y.; Ophus, C.; Bustillo, K. C.; Ercius, P.; Wang, L.-W.; Zheng, H. Strong Structural and Electronic Coupling in Metavalent PbS Moiré Superlattices. *J. Am. Chem. Soc.* **2022**, *144* (51), 23474–23482.

(37) Carr, S.; Fang, S.; Kaxiras, E. Electronic-Structure Methods for Twisted Moiré Layers. *Nat. Rev. Mater.* **2020**, *5* (10), 748–763.

(38) Krauss, T. D.; Wise, F. W. Coherent Acoustic Phonons in a Semiconductor Quantum Dot. *Phys. Rev. Lett.* **1997**, *79* (25), 5102–5105.

(39) Cui, J.; Beyler, A. P.; Coropceanu, I.; Cleary, L.; Avila, T. R.; Chen, Y.; Cordero, J. M.; Heathcote, S. L.; Harris, D. K.; Chen, O.; Cao, J.; Bawendi, M. G. Evolution of the Single-Nanocrystal Photoluminescence Linewidth with Size and Shell: Implications for Exciton-Phonon Coupling and the Optimization of Spectral Linewidths. *Nano Lett.* **2016**, *16* (1), 289–296.

(40) Hinterding, S. O. M.; Salzmann, B. B. V.; Vonk, S. J. W.; Vanmaekelbergh, D.; Weckhuysen, B. M.; Hutter, E. M.; Rabouw, F. T. Single Trap States in Single CdSe Nanoplatelets. *ACS Nano* **2021**, *15* (4), 7216–7225.

(41) Goupalov, S. V. Low-Frequency Vibrations of Semiconductor Nanoplatelets. *J. Phys. Chem. C* **2019**, *123* (18), 11926–11932.

(42) Girard, A.; Saviot, L.; Pedetti, S.; Tessier, M. D.; Margueritat, J.; Gehan, H.; Mahler, B.; Dubertret, B.; Mermet, A. The Mass Load Effect on the Resonant Acoustic Frequencies of Colloidal Semiconductor Nanoplatelets. *Nanoscale* **2016**, *8* (27), 13251–13256.

(43) Fernée, M. J.; Littleton, B. N.; Cooper, S.; Rubinsztein-Dunlop, H.; Gómez, D. E.; Mulvaney, P. Acoustic Phonon Contributions to the Emission Spectrum of Single CdSe Nanocrystals. *J. Phys. Chem. C* **2008**, *112* (6), 1878–1884.

(44) Brodu, A.; Chandrasekaran, V.; Scarpelli, L.; Buhot, J.; Masia, F.; Ballottin, M. V.; Severijnen, M.; Tessier, M. D.; Dupont, D.; Rabouw, F. T.; Christianen, P. C. M.; de Mello Donega, C.; Vanmaekelbergh, D.; Langbein, W.; Hens, Z. Fine Structure of Nearly Isotropic Bright Excitons in InP/ZnSe Colloidal Quantum Dots. *J. Phys. Chem. Lett.* **2019**, *10* (18), 5468–5475.

(45) Canneson, D.; Shornikova, E. V.; Yakovlev, D. R.; Rogge, T.; Mitioglu, A. A.; Ballottin, M. V.; Christianen, P. C. M.; Lhuillier, E.; Bayer, M.; Biadala, L. Negatively Charged and Dark Excitons in $CsPbBr_3$ Perovskite Nanocrystals Revealed by High Magnetic Fields. *Nano Lett.* **2017**, *17* (10), 6177–6183.

(46) Macias-Pinilla, D. F.; Planelles, J.; Mora-Seró, I.; Climente, J. I. Comparison between Trion and Exciton Electronic Properties in CdSe and PbS Nanoplatelets. *J. Phys. Chem. C* **2021**, *125* (28), 15614–15622.

(47) Clark, S. W.; Harbold, J. M.; Wise, F. W. Resonant Energy Transfer in PbS Quantum Dots. *J. Phys. Chem. C* **2007**, *111* (20), 7302–7305.

(48) Moreels, I.; Lambert, K.; Smeets, D.; De Muynck, D.; Nollet, T.; Martins, J. C.; Vanhaecke, F.; Vantomme, A.; Delerue, C.; Allan, G.; Hens, Z. Size-Dependent Optical Properties of Colloidal PbS Quantum Dots. *ACS Nano* **2009**, *3* (10), 3023–3030.

(49) Califano, M.; Franceschetti, A.; Zunger, A. Temperature Dependence of Excitonic Radiative Decay in CdSe Quantum Dots: The Role of Surface Hole Traps. *Nano Lett.* **2005**, *5* (12), 2360–2364.

(50) Shirazi, R.; Kopylov, O.; Kovacs, A.; Kardynał, B. E. Temperature Dependent Recombination Dynamics in InP/ZnS Colloidal Nanocrystals. *Appl. Phys. Lett.* **2012**, *101* (9), No. 091910.

(51) Abbarchi, M.; Mastrandrea, C.; Kuroda, T.; Mano, T.; Vinattieri, A.; Sakoda, K.; Gurioli, M. Poissonian Statistics of Excitonic Complexes in Quantum Dots. *J. Appl. Phys.* **2009**, *106* (5), No. 053504.

(52) Schmidt, T.; Lischka, K.; Zulehner, W. Excitation-Power Dependence of the near-Band-Edge Photoluminescence of Semiconductors. *Phys. Rev. B* **1992**, *45* (16), 8989–8994.

(53) Califano, M.; Franceschetti, A.; Zunger, A. Lifetime and Polarization of the Radiative Decay of Excitons, Biexcitons, and Trions in CdSe Nanocrystal Quantum Dots. *Phys. Rev. B* **2007**, *75* (11), No. 115401.

(54) Shornikova, E. V.; Yakovlev, D. R.; Biadala, L.; Crooker, S. A.; Belykh, V. V.; Kochiev, M. V.; Kuntzmann, A.; Nasilowski, M.; Dubertret, B.; Bayer, M. Negatively Charged Excitons in CdSe Nanoplatelets. *Nano Lett.* **2020**, *20* (2), 1370–1377.

(55) Li, H.; Zhitomirsky, D.; Grossman, J. C. Tunable and Energetically Robust PbS Nanoplatelets for Optoelectronic Applications. *Chem. Mater.* **2016**, *28* (6), 1888–1896.

(56) Fernée, M. J.; Plakhotnik, T.; Louyer, Y.; Littleton, B. N.; Potzner, C.; Tamarat, P.; Mulvaney, P.; Lounis, B. Spontaneous Spectral Diffusion in CdSe Quantum Dots. *J. Phys. Chem. Lett.* **2012**, *3* (12), 1716–1720.

6.6 Supporting Information

6.6.1 Methods

Chemicals. Acetonitrile (≥99.5%), cadmium(II) chloride (99.99%) isopropanol (≥ 99.5%), lead(II) oxide (≥ 99.99%), methanol (≥ 99.8%), *n*-octylamine (99%), oleic acid (≥ 90%), Rhodamine 6G (~95%), triethylamine (≥ 99%), trifluoroacetic acid (99%), and trifluoracetic anhydride (≥ 99%) were purchased from SIGMA-ALDRICH/MERCK. *n*-Hexane (99.99%) and thiourea (99%) were purchased from ALFA AESAR. Ethanol (99.9%) was purchased from ACROS. Tetrachloroethylene (≥ 99.9%) was purchased from MERCK-MILLIPORE. The *n*-Octylamine and oleic acid were degassed *via* the freeze-pump-thaw method three times prior to being stored and used inside a nitrogen-filled glovebox. All other reagents were directly used as received from the listed suppliers without further purification. All synthetic steps were performed under the inert gas conditions inside a nitrogen-filled glovebox, unless explicitly stated otherwise.

Preparation of the Lead Oleate Precursor. Lead oleate was synthesized *via* an established method described by HENDRICKS *et al.*[1] For the PbS NPL synthesis, lead oleate (365 mg, 0.47 mmol) was weighed into a 8 ml screw cap vial and dissolved in a mixture of *n*-hexane (2.3 ml), *n*-octylamine (1.5 ml), and oleic acid (0.8 ml) by stirring at 35°C until complete dissolution.

Preparation of the Thiourea Precursor. The thiourea precursor was prepared by dissolving thiourea (180 mg, 2.36 mmol) in *n*-octylamine (4.5 ml) under continuous stirring at 35°C. The mixture was stirred for at least 30 h before being used in the PbS NPL synthesis.

PbS NPL Synthesis. The PbS NPLs were synthesized following a procedure by MANTEIGA VÁZQUEZ *et al.*[2] The 8 ml screw cap vial containing the premixed lead oleate solution was allowed to heat up to 35°C and 0.5 ml of the thiourea precursor solution were rapidly injected. After a reaction time of 20 minutes, the solution exhibited a bronze to dark-brown color and the PbS NPLs were passivated by adding a solution of $CdCl_2$ (2.5 ml,0.1 M) in a mixture of *n*-octylamine and oleic acid (volume ratio of 9:1) and subsequent stirring for additional 10 min. The passivated PbS NPLs were stored at -25°C in the fridge of a nitrogen-filled glovebox.

For preparing the samples for optical measurements at cryogenic temperatures the PbS NPLs were first transferred to toluene. Briefly, the NPLs were precipitated by drop-wise addition of a mixture of isopropanol and ethanol (3:1) until visible destabilization of the colloidal solution, centrifuged at 2500 rcf for 10 min, and reprecipitated in dry toluene.

The PLQY was determined using a relative method described by WÜRTH *et al.*[3] using Rhodamin 6G in dry ethanol as a reference dye with a known quantum yield of 0.95. Thereby the PLQY is given by

$$\mathrm{PLQY} = 0.95 \cdot \frac{A_{\mathrm{sample}}}{A_{\mathrm{reference}}} \cdot \frac{1 - 10^{-Abs_{\mathrm{reference}}}}{1 - 10^{-Abs_{\mathrm{sample}}}} \cdot \left(\frac{n_{\mathrm{TCE}}}{n_{\mathrm{EtOH}}}\right)^2 \qquad \text{(Eq. S6.1)}$$

with the integral area A of the PL measurement curve, the absorbance Abs, and the refractive index n of the solvent.

Transmission Electron Microscopy. Overview TEM images were obtained using a FEI TECNAI G2 F20 transmission electron microscope equipped with a field emission gun operating at 200 kV. Samples for TEM analysis were prepared by drop-casting the colloidal PbS NPLs onto carbon-coated copper grids (300 mesh) acquired from QUANTIFOIL.

High-Angle Annular Dark-Field Scanning Transmission Electron Microscopy. A FEI TITANTHEMIS 300 microscope equipped with a probe aberration corrector, which is operated at 200 kV, was used to acquire (HR)STEM images. The probe size was set to 0.1 nm with a convergence semiangle of 22.5 mrad. The collection angle of the HAADF detector was in the range 80–150 mrad. The contrast in an HAADF image is proportional to $Z \approx 1.7–2$, meaning that the bright contrast indicates relatively heavy atomic composition.

Grazing-Incidence Wide-Angle X-ray Scattering. GIWAXS diffractions patterns were measured at the beamline P03 of the PETRA III synchrotron facility (DESY, Hamburg) at an incidence angle of $\alpha_i = 0.4°$. For this, samples were prepared by drop casting the colloidal PbS solutions onto silicon wafers (5 mm x 5 mm, p-typed doped with boron, <100> surface, purchased from PLANO).

Optical Measurements at Cryogenic Temperature. The optical measurements at cryogenic temperatures for the ensembles of PbS NPLs and the individual PbS NPLs were performed using a closed-cycle helium flow cryostat (MONTANA INSTRUMENTS, CRYOSTATION C2). The drop-casted PbS NPL samples were prepared the following way: 5% weight fraction of polystyrene were added to the PbS NPL solution in toluene, which was then centrifuged at 500 rpm for 2 min. The solution was then drop-casted onto a flat silicon substrate covered with a gold film, acting as mirror to increase the yield of collected PL from the sample. For obtaining the emission spectra of NPL ensembles and single NPLs, they were excited using continuous wave diode laser light at 532 nm (THORLABS) which was focused onto the sample by an objective (MITUTOYO, M PLAN APO NIR 100X) with a numerical aperture of 0.7. The emitted PL signal was guided to a spectrometer (SPECTROSCOPY & IMAGING GMBH) with 300 l/mm grating and detected by a CCD (see Figure S 6.4). We calibrated the spectral transmission of our setup and spectrometer by guiding a broad-band white light signal (THORLABS SLS202L) through the optical setup, including the spectrometer. The recorded spectrum and the original spectrum of the white light source were used to calibrate the total spectral efficiency of our setup and spectrometer. Different NPL ensemble emissions have been studied at different positions on the sample. For the time-resolved PL measurements, the PbS NPLs were excited by pulsed laser light at

445 nm for the ensemble of NPLs, and at 500 nm for the single NPLs. The repetition rate of the pulsed laser was 82 MHz. The signal was collected by an avalanche photodiode.

For the time-resolved PL measurements on ensemble PbS NPLs, the data is fitted biexponentially:

$$I(t) = I_0 + A_1 \mathrm{e}^{-\frac{t}{\tau_1}} + A_2 \mathrm{e}^{-\frac{t}{\tau_2}}, \qquad \text{(Eq. S6.2)}$$

with the background intensity I_0 and two amplitude components A_1 and A_2. These correspond to the intensities of the slow and fast decay components, with respective lifetimes τ_1 and τ_2.

For the single PbS NPLs the data is fitted single-exponentially:

$$I(t) = I_0 + A \mathrm{e}^{-\frac{t}{\tau}}, \qquad \text{(Eq. S6.3)}$$

where I_0 represents the background intensity and A denotes the amplitude and τ is the derived lifetime.

For the polarization-dependent measurements, the degree of polarization (DOP) was determined by $\delta = (I_{\max} - I_{\min})/(I_{\max} + I_{\min})$ where $I_{\max}$ and $I_{\min}$ are the fitted maximum and minimum PL intensities, respectively.

6.6.2 Polarization-Dependent Photoluminescence Analysis

In this section, we present the theoretical model for the simulation of the polarization degree dependent on the NPL orientation on the substrate. To determine the orientation (Θ, Φ) of an individual nano-emitter, we employ the theoretical framework proposed in reference [4]. Our simulated scenario is as follows. As shown in [4], the degree of linear polarization of the emission is defined as:

$$\delta(\Theta) = \frac{I_{\max} - I_{\min}}{I_{\max} + I_{\min}}, \qquad \text{(Eq. S6.4)}$$

where $I_{\max}$ and $I_{\min}$ are the minimum and the maximum intensity.

For 1D dipoles,

$$I_{\min} = A\sin^2\Theta + B\cos^2\Theta\,, \quad \text{(Eq. S6.5)}$$

$$I_{\max} = C\sin^2\Theta + I_{\min}\,. \quad \text{(Eq. S6.6)}$$

For 2D dipoles,

$$I_{\min} = A + B + (A - B + C)\cos^2\Theta\,, \quad \text{(Eq. S6.7)}$$

$$I_{\max} = C\sin^2\Theta + I_{\min}\,. \quad \text{(Eq. S6.8)}$$

The constants A, B, and C can be determined analytically. Particularly the simple expression for δ in the limit of high numerical aperture ($\Theta_{\max} = \pi/2$) for a 1D and 2D dipoles are:

$$\delta_{\text{high NA,1D}}(\Theta) = \frac{7}{8}\sin^2\Theta\,, \quad \text{(Eq. S6.9)}$$

$$\delta_{\text{high NA,2D}}(\Theta) = \frac{7}{16}\sin^2\Theta\,, \quad \text{(Eq. S6.10)}$$

respectively. For both 1D and 2D dipoles the polarization degree δ depends on the out-of-plane Θ. Moreover, in the limit of low numerical aperture, δ for 1D and 2D dipoles[4] are:

$$\delta_{\text{low NA,1D}}(\Theta) = \frac{\sin^2\Theta}{\left(1 - \frac{\Theta_{\max}^2}{2}\right)\sin^2\Theta + \frac{\Theta_{\max}^2}{2}}, \quad \text{(Eq. S6.11)}$$

$$\delta_{\text{low NA,2D}}(\Theta) = \frac{\sin^2\Theta}{\left(\frac{\Theta_{\max}^2}{2} - 1\right)\sin^2\Theta + 2}, \quad \text{(Eq. S6.12)}$$

respectively. If we use low numerical aperture, *i.e.*, $NA = 0.7$, in the case of $n_1 = 1.5$ (polystyrene index), and $n_2 = 1$ (medium index), we can apply Equation S6.12 to show δ change with Θ, with

$$\Theta_{\max} = \arcsin\frac{NA}{n_1}. \quad \text{(Eq. S6.13)}$$

The calculation result is presented in Figure S 6.8.

6.6.3 Polarization Effects in Anisotropic PbS NPLs

In our study we investigate two-dimensional PbS NPLs. The properties of trions are often deduced from nanoycrystals where a cubic symmetry is assumed. For instance, in caesium lead halide perovskite nanocrystals it was discussed that in cubic nanocrystals (O_h point group), both electrons and holes possess Γ_6 symmetry and are two-fold degenerate.[5] As a result, the trion states formed are also of Γ_6 symmetry and similarly two-fold degenerate, with all allowed polarizations and equal dipole matrix elements along the x, y, and z axes.

However, PbS NPLs exhibit strong shape anisotropy. These NPLs are only 1–2 nm thick, but significantly larger in the other two dimensions (16.0 ± 1.6 nm x 9.2 ± 1.2 nm, in our case). This pronounced shape anisotropy breaks the cubic symmetry. With this reduced symmetry, stricter selection rules govern optical transitions, allowing transitions in certain directions while prohibiting them in others. As a result, the trion emission in PbS NPLs may become highly polarized. A finite degree of fluorescence polarization has also been observed in related systems such as PbS/CdS quantum dots.[6] Although these quantum dots are expected to show isotropic, unpolarized emission due to their symmetry, a slight linear degree of polarization is observed experimentally. Possible reasons lie in irregularities in the shape of the quantum dots, anisotropy in the CdS shell, or defects at the core/shell interface, all of which break the symmetry and lead to polarized fluorescence signals.

Another key factor contributing to polarization is the renormalization of the optical electric field within the NPLs, caused by the contrast of dielectric constants between the NPL and its environment. It leads to a significantly altered local electric field, as has been observed in CdSe/CdS NPLs.[7] For our measurements, the single PbS NPLs have been embedded in polystyrene. The resulting dielectric mismatch can increase the emission anisotropy, strengthening the in-plane dipole moment and contributing to the higher degree of PL polarization observed in our system.

On the other hand, experimental factors pose a slight overestimation to the observed polarization. For example, the use of a 0.7 NA objective lens, as well as the random orientations of the NPLs in the polystyrene matrix, may lead to deviations in the measured polarization. In future studies, advanced measurement techniques may probe the polarization in greater detail. These may include the use

of a high-NA objective lens, specially designed substrates to control the orientation and tilt angle of the NPLs, and the application of magnetic fields to further explore the underlying mechanisms and selection rules. We anticipate that these approaches will help us gain a more comprehensive understanding of the polarization behavior in PbS NPLs.

6.6.4 Phonon Sidebands in the Photoluminescence Spectra

All emissions that we observe feature sidebands which we attribute to phonon-assisted emission processes. Usually, a low energy tail of the PL is seen, which we attribute to the coupling with acoustic phonons. Coupling to distinct optical phonon related features seems to be not very prominent in the PbS NPLs. Such coupling is common in semiconductor nanocrystals and is typically explained by a mixture of surface-related and intrinsic effects.[8] The presence of localized surface-charges induces a polarization in the nanocrystal and therefore enhances coupling to longitudinal (LO) phonons. Due to the high crystal and surface quality and passivation in our PbS NPLs leading to little spectral diffusion and the presence of a narrow emission, this type of coupling is expected to be strongly reduced. Intrinsic effects include a reduced overlap of electron and hole wavefunctions in the NPL leading to an increased polarization in the nanocrystal and therefore enhanced coupling to LO phonons. In the case of PbS NPLs, the wavefunction overlap is maximized in the direction of strongest confinement, and the quality of the orthogonally oriented surface is high with negligible surface reconstruction. In contrast, coupling to acoustic phonons (as seen in the spectrum) is expected *via* deformation potential and piezoelectric interactions. Until now, this suppression of optical phonon modes has not been observed in PbS nanostructures, most likely because of strong internal dipoles caused by asymmetry in the polar facet orientation and the structure truncation. Due to the high crystal and surface quality with negligible surface reconstruction (see Figure 6.1) as well as the applied passivation in the 2D PbS NPLs, a high wavefunction overlap in the direction of strongest confinement is expected, and thereby strongly reducing the NPL polarization and LO phonon coupling. The observed low-frequency acoustic modes (both in STOKES and anti-STOKES PL) are most likely stemming from the thickness breathing mode.[9,10] The phonon energies are in the range of a few meV with slight changes from NPL to NPL (see Figure 6.4 and SI), which is reasonable for confined

acoustic phonons that are more sensitive to symmetry and size. The observed phonon energy range aligns well with transient absorption spectroscopy results in similar (slightly smaller) PbS NPLs.[2]

6.6.5 Supplementary Figures and Tables

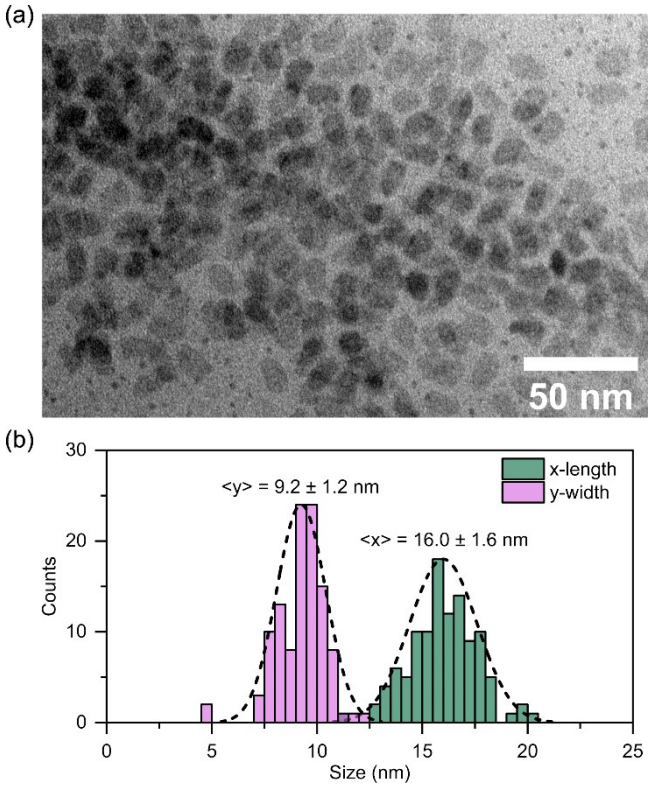

Figure S 6.1. (a) Typical overview TEM image used for determining the lateral dimensions of the PbS NPLs. Within areas of higher concentration (compared to the overview image shown in the main manuscript), individual NPLs overlap with each other. (b) Corresponding size histogram, *x*-lengths correspond to the longest dimension of the NPLs, *y*-widths are the longest distance orthogonal to the *x*-length.

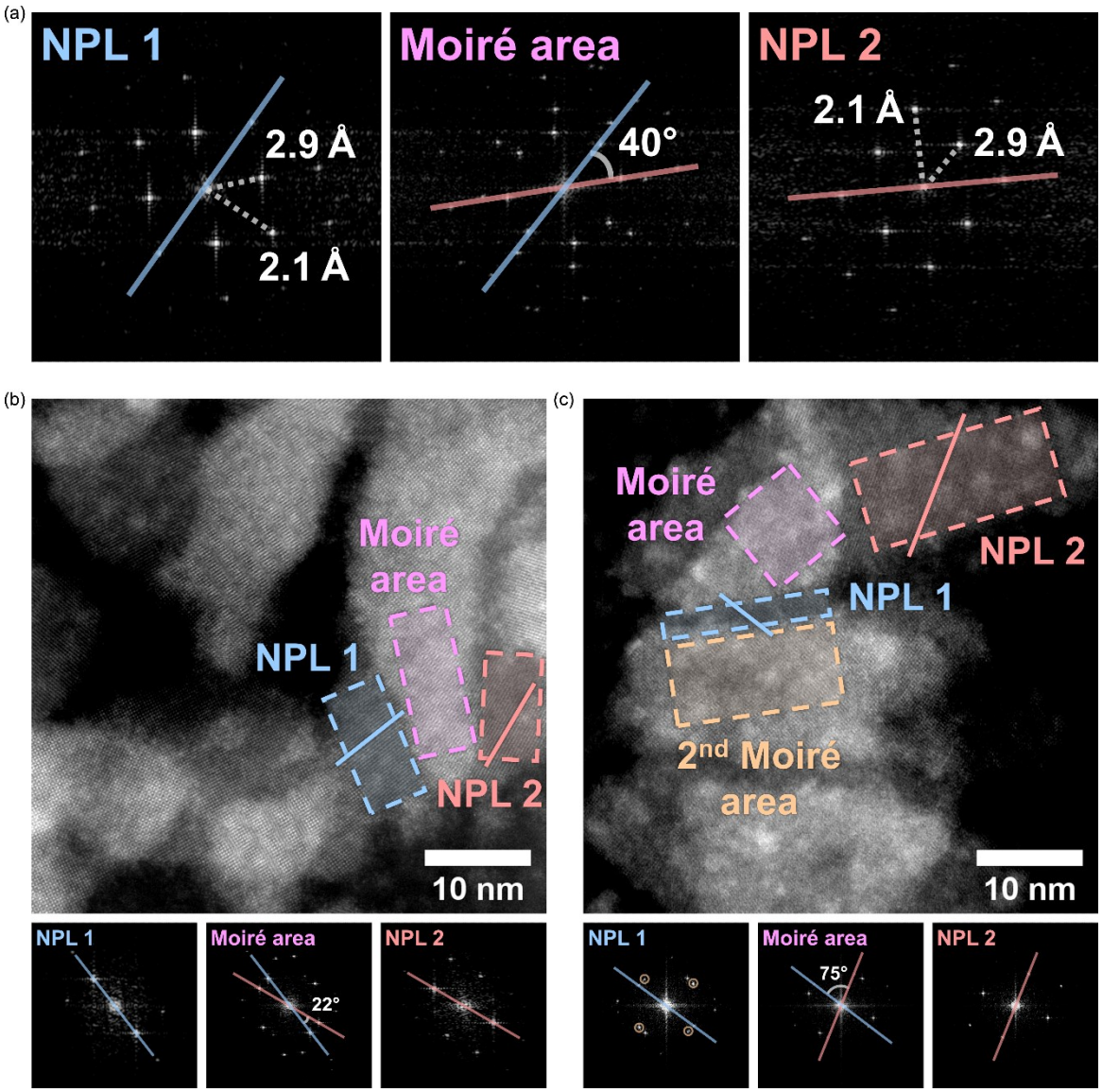

Figure S 6.2. (a) FFT patterns corresponding to the two NPLs and the MOIRÉ pattern depicted in Figure 6.1b. The two PbS NPLs overlap with a twist angle of 40°. (b, c) HR-HAADF-STEM images and corresponding FFT patterns depicting additional examples of MOIRÉ patterns formed by overlapping PbS NPLs with twist angles of (a) 22° and (b) 75°, respectively (compare to Figure 6.1b).

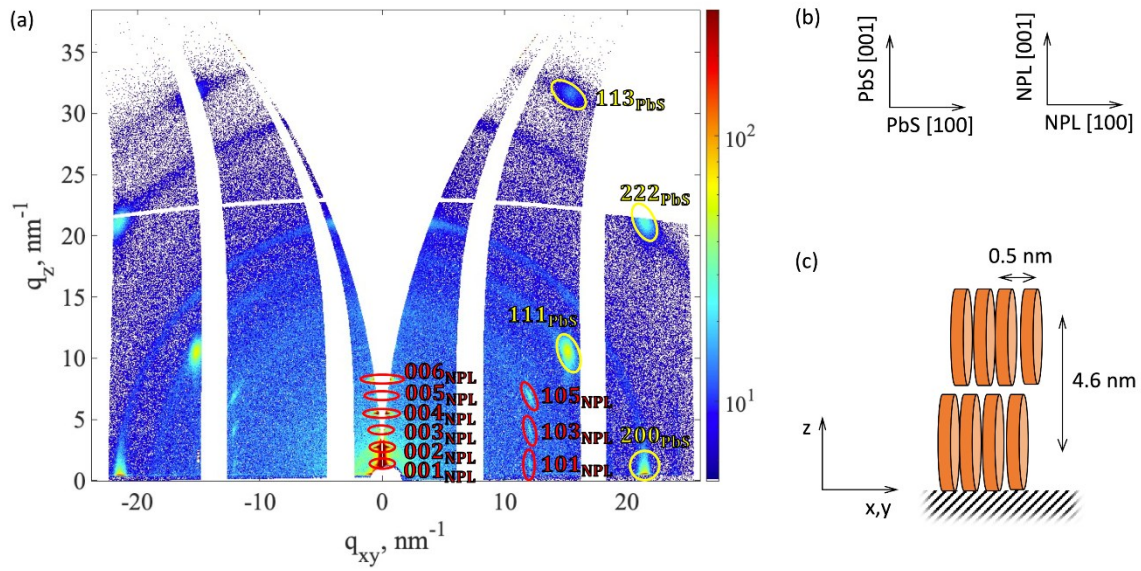

Figure S 6.3. (a) Grazing-incidence wide-angle X-ray scattering diffraction pattern (background-corrected) of PbS NPLs drop-casted onto a silicon substrate (white areas are detector gaps). The presence of superlattice peaks (marked in red) at small values of the scattering vector q indicates the formation of a superlattice of the individual NPLs. At the same time, the BRAGG peaks from the PbS atomic lattice (highlighted in yellow) allow us to confirm that the NPLs are oriented in a certain way within the formed superlattice. (b) Orientation of the crystallographic directions of the PbS atomic lattice and the superlattice of the NPLs. (c) Combining the BRAGG peaks with the superlattice peaks, we propose the shown superlattice structure with the characteristic spacings of 0.5 nm and 4.6 nm between the individual NPLs in real space. Interestingly, the low intensity of the *hkl* peaks with $h + k + l$ = odd suggests, that the rows of NPLs might be shifted by half of a unit cell with respect to each other, resembling a body-centered superlattice. The small distance of approximately 0.5 nm between the individual NPLs eliminates the possibility of relatively large organic ligands to fit between the NPLs.

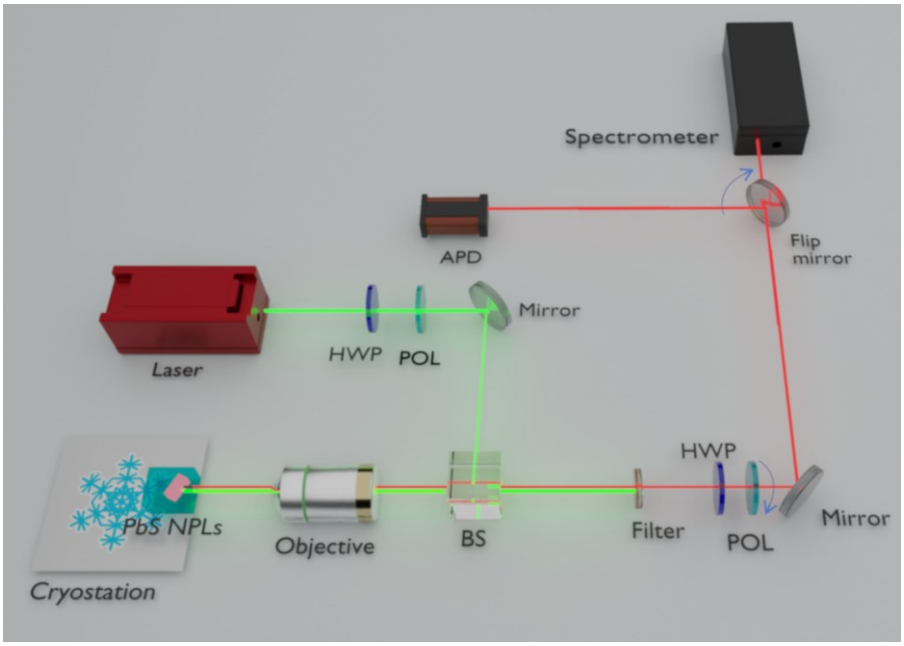

Figure S 6.4. Sketch of the optical setup for micro-PL. BS: beam splitter. HWP: half wave plate. POL: polarizer. APD: Avalanche photodiode.

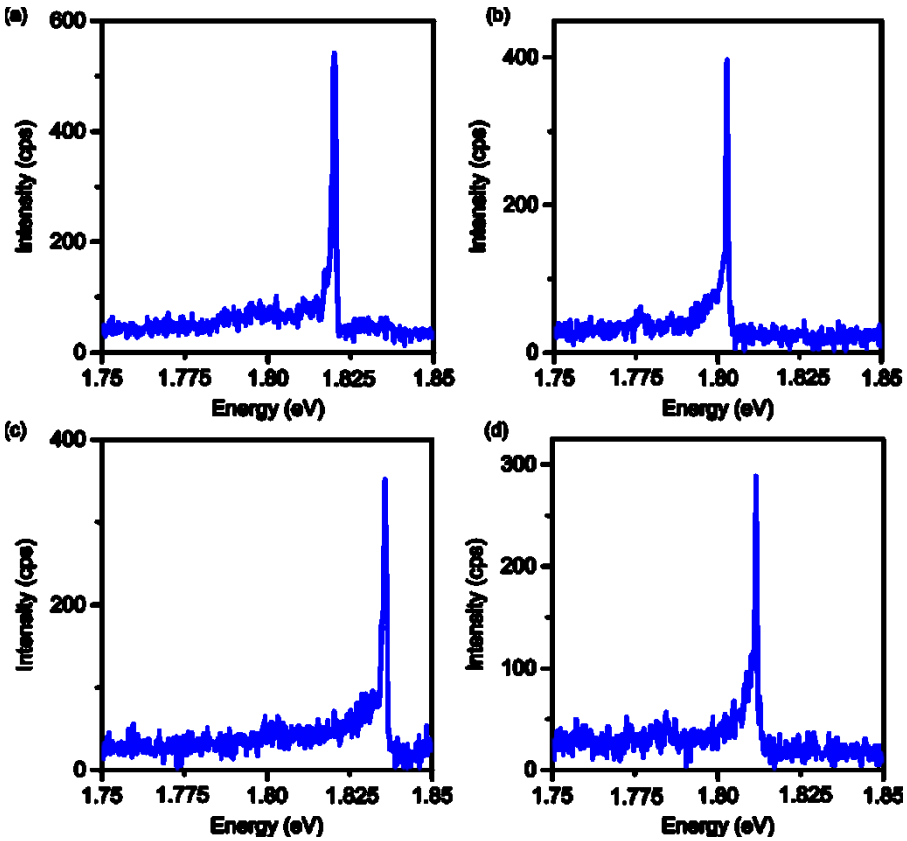

Figure S 6.5. (a)–(d) Exemplary PL Spectra of four different single PbS NPLs at T = 4 K.

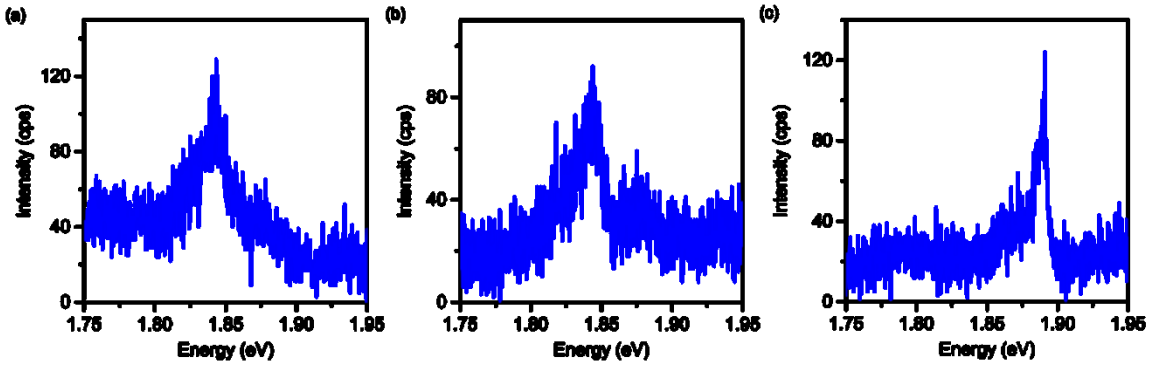

Figure S 6.6. (a)–(c) Exemplary PL spectra (T = 4 K) of other localized emissions observed in the PbS NPL sample that do not exhibit narrowband emission.

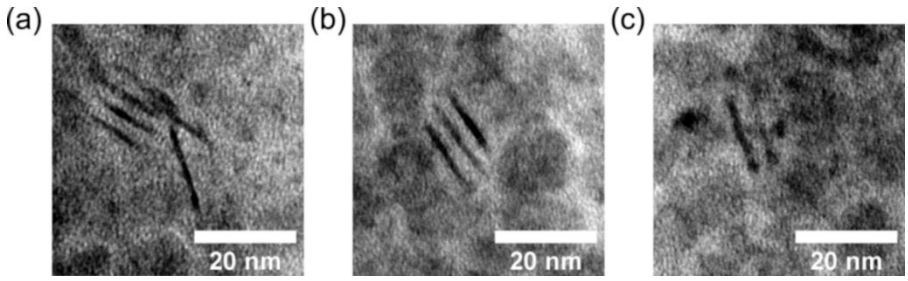

Figure S 6.7. (a)–(c) Exemplary TEM images of PbS NPLs lying on their side exhibiting a thickness of 1–2 nm.

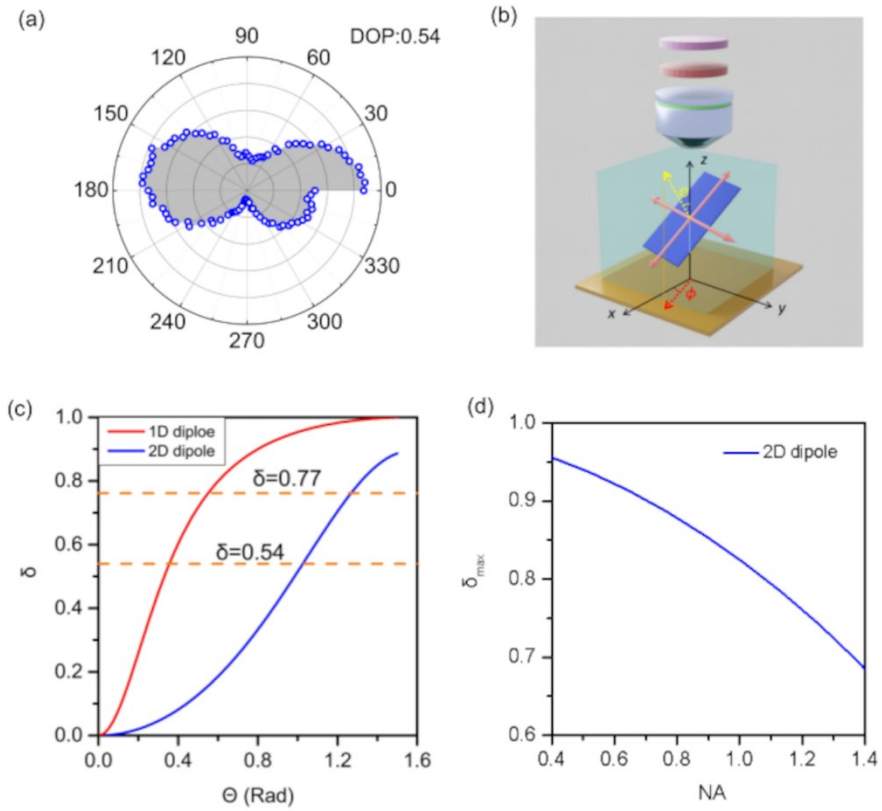

Figure S 6.8. (a) Polarization angle dependent PL intensity of a single PbS NPL. The abrupt change observed between 0° and 360° is due to photobleaching during the measurement, resulting in a discontinuity in the PL intensity. (b) Sketch of the optical set-up and relevant parameters of the model for estimating the polarization degree of a single PbS NPL. (c) Calculated polarization degree over the collection angle for an ideal 1D dipole (red) or 2D dipole (blue), assuming the experimental setup in (b). (d) Calculated maximum degree of polarization as a function of the numerical aperture of the objective, assuming the experimental setup in (b).

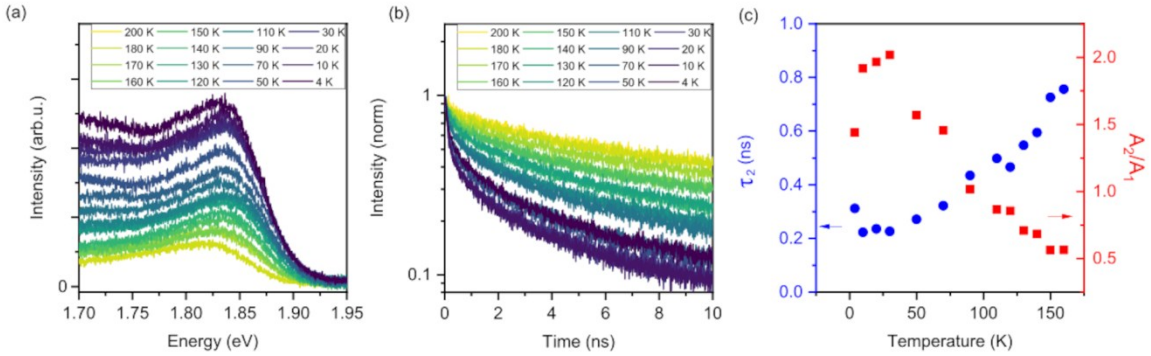

Figure S 6.9. (a) Temperature-dependent PL spectra of the PbS NPL ensemble shown in Figure 6.3. (b) Fluorescence lifetime measurements of the ensemble of PbS NPLs. (c) Temperature-dependent decay time of the short component of the PL decay τ_2 (blue dot) and Temperature-dependent amplitude of short component of the PL decay over long component of the PL decay (red dot).

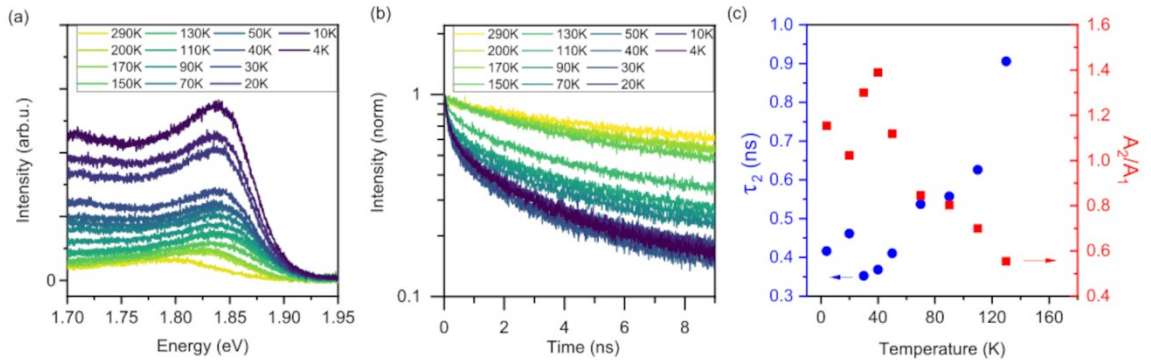

Figure S 6.10. (a) Temperature-dependent PL spectra of a different ensemble of PbS NPLs. (b) Fluorescence lifetime measurements of the ensemble of PbS NPLs. (c) Temperature-dependent decay time of the short component of the PL decay τ_2 (blue dot), the short decay component τ_2 vanished at around 150 K and Temperature-dependent amplitude of short component of the PL decay over long component of the PL decay (red dot).

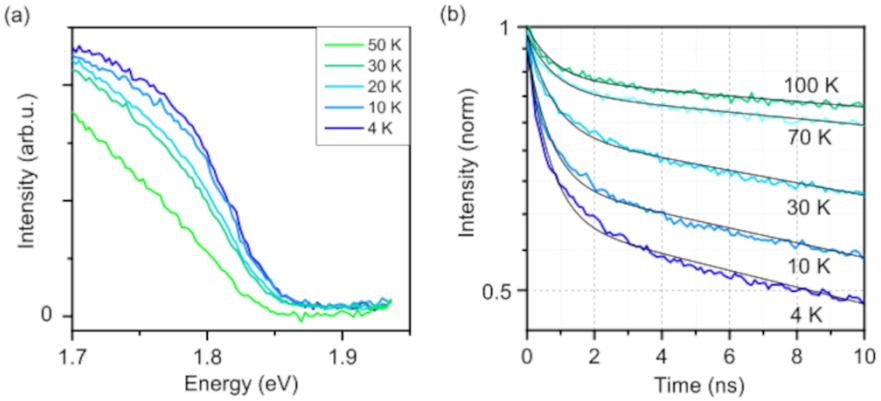

Figure S 6.11. (a) Temperature-dependent, normalized PL spectra of a different ensemble of PbS NPLs. (b) Fluorescence lifetime measurements of the ensemble of PbS NPLs.

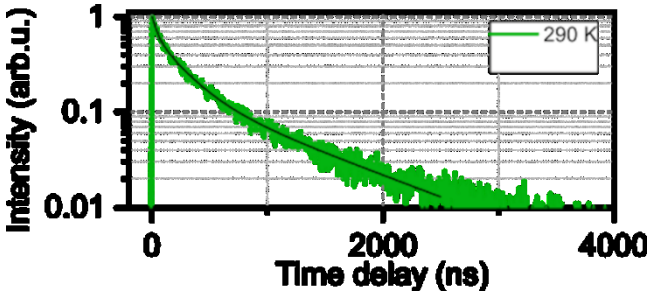

Figure S 6.12. PL lifetime measurement of an PbS NPL ensemble at room temperature. A triple-exponential decay model is employed, with τ_1 = 42.6 ns, τ_2 = 231.3 ns and τ_3 = 956.2 ns.

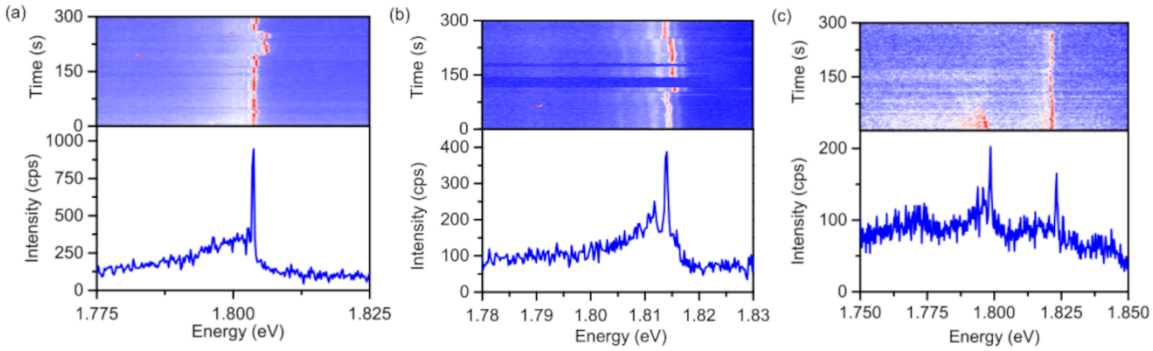

Figure S 6.13. (a)–(c) PL time traces (top) and snapshot spectra (bottom) of three exemplary PbS NPLs exhibiting spectral diffusion.

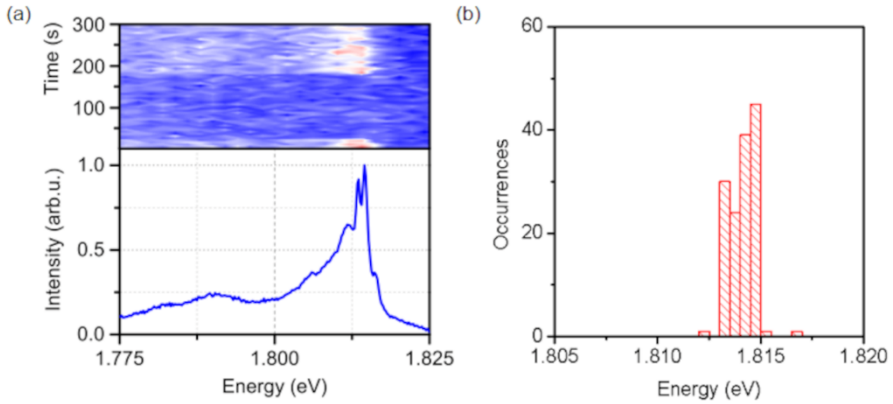

Figure S 6.14. Only minor spectral diffusion and ultra-low blinking timescales in a representative PbS NPL. (a) The top part shows the PL time trace featuring low spectral diffusion and at the same time strong blinking behavior with a long off-time of around 150 s. The bottom part shows the normalized sum of spectra with the NPL in the bright state. (b) is the distribution of the central emission energy (obtained by fitting each spectrum in (a) with the NPL in its bright state).

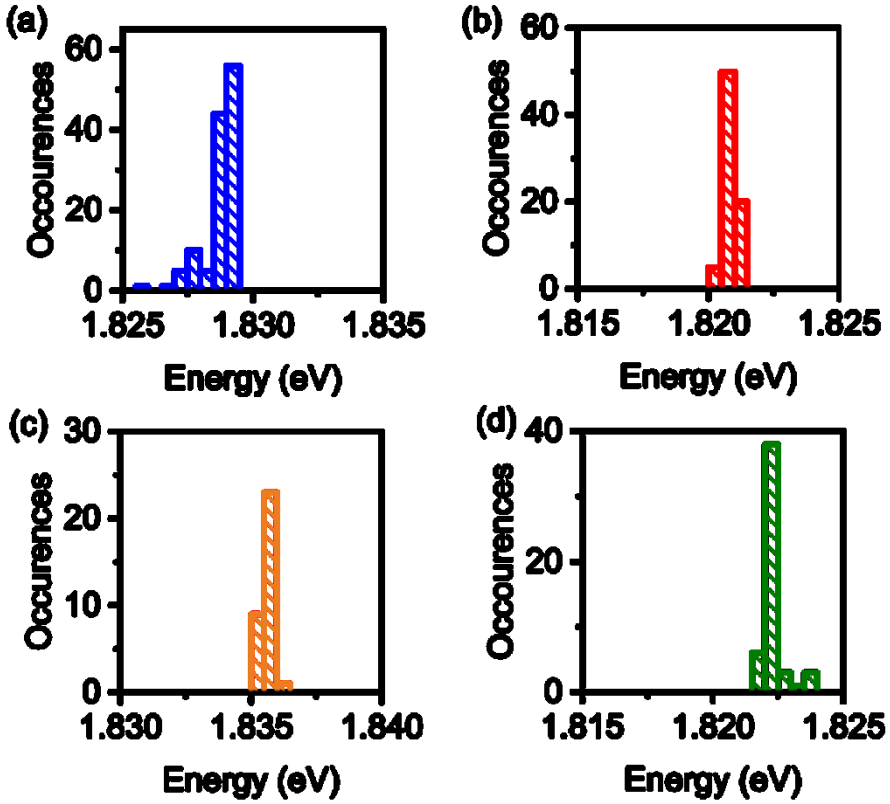

Figure S 6.15. Distribution of the central emission energy of the strongest emission peak from four trion states in Figure 6.4e (obtained by fitting each spectrum in Figure 6.4e).

Table S 6.1. The fitting results of specific PL emissions of PbS NPL derived from Figure 6.2a by using the GAUSSIAN fittings.

	ZPL	acoustic phonon
position	1.8028 eV	1.7986 eV
fwhm	0.615 eV	7.250 eV

6.6.6 References

(1) Hendricks, M. P.; Campos, M. P.; Cleveland, G. T.; Jen-La Plante, I.; Owen, J. S. A Tunable Library of Substituted Thiourea Precursors to Metal Sulfide Nanocrystals. *Science* **2015**, *348* (6240), 1226–1230.

(2) Manteiga Vázquez, F.; Yu, Q.; Klepzig, L. F.; Siebbeles, L. D. A.; Crisp, R. W.; Lauth, J. Probing Excitons in Ultrathin PbS Nanoplatelets with Enhanced Near-Infrared Emission. *J. Phys. Chem. Lett.* **2021**, *12* (1), 680–685.

(3) Würth, C.; Grabolle, M.; Pauli, J.; Spieles, M.; Resch-Genger, U. Relative and Absolute Determination of Fluorescence Quantum Yields of Transparent Samples. *Nat. Protoc.* **2013**, *8* (8), 1535–1550.

(4) Lethiec, C.; Laverdant, J.; Vallon, H.; Javaux, C.; Dubertret, B.; Frigerio, J.-M.; Schwob, C.; Coolen, L.; Maître, A. Measurement of Three-Dimensional Dipole Orientation of a Single Fluorescent Nanoemitter by Emission Polarization Analysis. *Phys. Rev. X* **2014**, *4* (2), 021037.

(5) Becker, M. A.; Vaxenburg, R.; Nedelcu, G.; Sercel, P. C.; Shabaev, A.; Mehl, M. J.; Michopoulos, J. G.; Lambrakos, S. G.; Bernstein, N.; Lyons, J. L.; Stöferle, T.; Mahrt, R. F.; Kovalenko, M. V.; Norris, D. J.; Rainò, G.; Efros, A. L. Bright Triplet Excitons in Caesium Lead Halide Perovskites. *Nature* **2018**, *553* (7687), 189–193.

(6) Hu, Z.; Kim, Y.; Krishnamurthy, S.; Avdeev, I. D.; Nestoklon, M. O.; Singh, A.; Malko, A. V.; Goupalov, S. V.; Hollingsworth, J. A.; Htoon, H. Intrinsic Exciton Photophysics of PbS Quantum Dots Revealed by Low-Temperature Single Nanocrystal Spectroscopy. *Nano Lett.* **2019**, *19* (12), 8519–8525.

(7) Ma, X.; Diroll, B. T.; Cho, W.; Fedin, I.; Schaller, R. D.; Talapin, D. V.; Wiederrecht, G. P. Anisotropic Photoluminescence from Isotropic Optical Transition Dipoles in Semiconductor Nanoplatelets. *Nano Lett.* **2018**, *18* (8), 4647–4652.

(8) Cui, J.; Beyler, A. P.; Coropceanu, I.; Cleary, L.; Avila, T. R.; Chen, Y.; Cordero, J. M.; Heathcote, S. L.; Harris, D. K.; Chen, O.; Cao, J.; Bawendi, M. G. Evolution of the Single-Nanocrystal Photoluminescence Linewidth with Size and Shell: Implications for Exciton-Phonon Coupling and the Optimization of Spectral Linewidths. *Nano Lett.* **2016**, *16* (1), 289–296.

(9) Goupalov, S. V. Low-Frequency Vibrations of Semiconductor Nanoplatelets. *J. Phys. Chem. C* **2019**, *123* (18), 11926–11932.

(10) Girard, A.; Saviot, L.; Pedetti, S.; Tessier, M. D.; Margueritat, J.; Gehan, H.; Mahler, B.; Dubertret, B.; Mermet, A. The Mass Load Effect on the Resonant Acoustic Frequencies of Colloidal Semiconductor Nanoplatelets. *Nanoscale* **2016**, *8* (27), 13251–13256.

7 Monolayer-Defined Flat Colloidal PbSe Quantum Dots in Extreme Confinement

The coming chapter comprises an in-depth study of the structural, electronic and optical properties of single layer-defined PbSe fQDs, using a combination of scanning tunneling microscopy and spectroscopy, tight-binding calculations and cryogenic ensemble PL measurements. Mono- to trilayer-thick colloidal PbSe fQDs exhibit a band gap that is free of trap states, a QD-like density of states and record exciton binding energies of up to 600 meV for (substrate-free) PbSe monolayers.

The results presented here have been published in *Nano Lett.* **2025**, *25* (31), 12019–12024. For details about the author contributions see Chapter B.

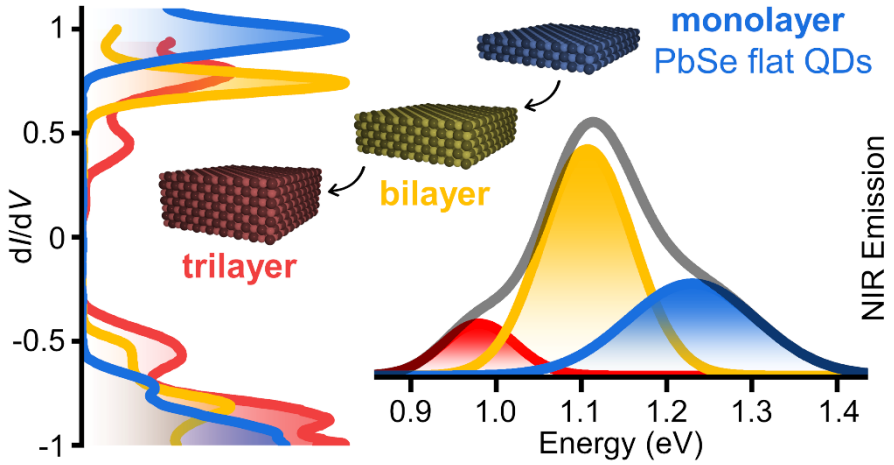

Leon Biesterfeld,[a,b,c] Huu Thoai Ngo,[d] Ahmed Addad,[e] Dominik A. Rudolph,[a,c] Wolfgang Leis,[f] Michael Seitz,[f] Gang Ji,[e] Bruno Grandidier,[d] Christophe Delerue,[d] Jannika Lauth,[a,b,c] Louis Biadala *[d]*

[e] Cluster of Excellence PhoenixD (Photonics, Optics, and Engineering – Innovation Across Disciplines), D-30167 Hannover, Germany.

[f] Institute of Physical and Theoretical Chemistry, Eberhard Karls University of Tübingen, D-72076 Tübingen, Germany.

[g] Institute of Physical Chemistry and Electrochemistry, Leibniz University Hannover, D-30167 Hannover, Germany.

[h] Université de Lille, CNRS, Centrale Lille, Université Polytechnique Hauts-de-France, F-59000 Lille, France.

[i] Université Lille, CNRS, INRAE, Centrale Lille, UMR 8207-UMET-Unité Matériaux et Transformations, F-59000 Lille, France.
[j] Institute of Inorganic Chemistry, Eberhard Karls University of Tübingen, D-72076 Tübingen, Germany.

7.1 Abstract

Colloidal 2D PbX (X = S, Se, Te) nanocrystals are innovative materials pushing the boundaries of quantum confinement by combining crystal thicknesses down to a monolayer with additional confinement in the lateral dimension. These flat PbSe quantum dots (fQDs) exhibit telecommunication band photoluminescence (1.43 – 0.83 eV), which is highly interesting for fiber optic information processing. With scanning tunneling microscopy/spectroscopy (STM/STS), we probe single-layer-defined fQD populations down to one monolayer, showing an in-gap state free QD-like density of states in excellent agreement with theoretical tight-binding (TB) calculations. Cryogenic ensemble spectra match STS/STM and TB calculations and exhibit the contribution of mono-, bi-, and trilayers to the photoluminescence. Comparing the electronic band gaps with the optical ones, we derive exciton binding energies as high as 600 meV for PbSe monolayers. Our results allow for a target-oriented synthesis of a new class of QDs with record binding energies and precisely tailored optical properties at technologically relevant wavelengths.

7.2 Introduction

Controlling the anisotropic growth of semiconductors at the nanoscale is key for tuning the degree of freedom of charge carriers, *i.e.*, by dimensionality,[1–3] and for the development of quantum technologies.[4,5] Among the available growth techniques, colloidal synthesis stands out, as it allows for a growth-by-design by thorough control over the size and the shape[6–9] of semiconductor nanocrystals (NCs), which enables fine-tuning of their (photo)physics and optoelectronic properties.[10,11] A striking example is the growth of colloidal 2D CdSe nanoplatelets (NPLs), for which the thickness is controlled at the atomic layer scale,[12] while the in-plane dimensions can be tuned over hundreds of nanometers.[13] The strong quantum confinement in the vertical dimension dominates the optical properties of the material, resulting in rapidly decaying (<10 ns at room temperature (RT)) PL associated with narrow line widths below 40 meV and exciton binding energies of ~200 meV.[12,14–16] At the same time, the lateral confinement in 2D CdSe enables a fine-tuning of the exciton energy[17] by reducing the length or width of the NPLs down to and below the exciton BOHR radius. However, the optical properties of CdSe are typically limited to visible wavelengths,

and to reach the telecommunication range, smaller band gap materials such as lead chalcogenides (PbX (X = S, Se, Te)) are required.[18–20] Notwithstanding their high potential as classical or quantum emitters for applications in fiber optics and photonics,[21,22] PbX NCs stand out for their remarkable physical properties with large exciton BOHR radii[23,24] and high dielectric constants.[25] Furthermore, PbX nanocrystals (NCs) are predicted to exhibit intriguing properties when extreme quantum confinement is reached. For example, PbSe in its monolayer (1ML) form could be a topological crystalline insulator[26,27] and a suitable material platform for defect engineering.[28] Notably, EKUMA reported on the effect of vacancy defects on the electronic and optical properties of monolayer PbSe and found that defect-induced states predominantly reside outside the band gap, which renders monolayer PbSe a rather defect-tolerant material.[28] Scarce experimental realization of monolayer-defined PbSe islands by molecular beam epitaxy has demonstrated the strong influence of the VAN DER WAALS substrate (MoS_2 [29] or VSe_2 [30]) on the growth process and the resulting material properties, caused by the induced strain between the crystal lattices of PbSe and the VAN DER WAALS substrate.[29,30] Here, we define a PbSe monolayer (1ML) according to the unit cell of cubic PbSe, namely, 0.6 nm (Pb-to-Pb distance), which consists of three atomic planes of PbSe. Recent colloidal synthesis protocols for cubic rock salt crystal-structured anisotropic PbS, PbSe, and PbTe NCs[31–34] allow to circumvent substrate interactions and are crucial for further harnessing the extreme quantum confinement in substrate-free PbX materials.

Flat PbSe NCs studied here are referred to as fQDs in the following and exhibit efficient PL (up to 61% quantum yield) in the NIR between 1.43 and 0.83 eV (860 – 1510 nm).[31,33] While highly promising, fQDs have been mostly studied with ensemble optical spectroscopic techniques, which provide average excitonic properties, but prevent comprehensive knowledge of the electronic properties, such as the dimensionality, the presence of electronic trap states in the gap, and exciton binding energies in correlation with structural properties (3D dimensions and associated size dispersion). In contrast, scanning tunneling microscopy (STM) allows for the determination of the single-particle morphology, and scanning tunneling spectroscopy (STS) enables probing excitation spectra of individual NCs, practically without any selection rules.[35] For colloidal lead chalcogenide NCs, STM/S studies have focused on spherical 0D PbSe QDs,[36,37] PbSe/PbS core-shell

QDs,[38] "molecular" aggregates of QDs,[36] and their epitaxially fused superlattices up to now.[39–41]

Here, we unveil the optical, electronic, and structural properties of 1ML-defined colloidal 2D PbSe fQDs experiencing extreme quantum confinement. By STM we show that while the lateral dimensions of PbSe fQDs remain constant, the thickness of the fQDs varies from 1.8 nm down to a monolayer of cubic PbSe, *i.e.*, 0.6 nm. Meanwhile, the corresponding STS at 77 K unambiguously shows in-gap state free DOS with well-defined electronic gap values of 1.67, 1.26, and 1.00 eV, corresponding to mono-, bi-, and trilayer cubic PbSe, accurately withstanding direct comparison with TB calculations. From these calculations we further predict that the electronic band gap is tunable by more than 0.7 eV by changing the lateral dimensions of the PbSe fQDs from 2 × 2 nm^2 to 8 × 8 nm^2. In agreement with STS, three PL contributions are observed in ensemble spectra, with their respective ratios changing for aged samples and suggesting an OSTWALD ripening mechanism of thinner (1 and 2 ML) populations of PbSe fQDs toward thicker (2 and 3 ML) ones with a smaller band gap. Strikingly, by comparing the electronic and the optical band gap, we directly obtain the exciton binding energy, which increases from 200 up to 600 meV when the thickness of PbSe fQDs is decreased from 3ML to 1ML. From our experimental results and exciton binding energies for PbSe quantum wells[42] and quantum wires,[43] we show that in PbSe nanostructures the exciton binding energy is inversely proportional to the strongest confinement dimension. These findings advance the understanding of colloidal PbSe fQDs by disentangling the vertical and lateral quantum confinement in the ultrathin structures, consequently enabling the synthetic targeting of specific fQD dimensions, leading to tailored optical properties at technologically relevant wavelengths.

7.3 Results and Discussion

NIR emitting colloidal PbSe fQDs are synthesized by a method described by us previously and stabilized by oleate and octylamine ligands.[31,33] Figure 7.1a shows an overview HR-HAADF-STEM image of PbSe fQDs exhibiting shapes with slightly anisotropic lateral dimensions of (4.9 ± 1.1) × (3.9 ± 0.6) nm^2 and a corresponding small aspect ratio of 1.25:1 (see Figure S 7.1a–c).

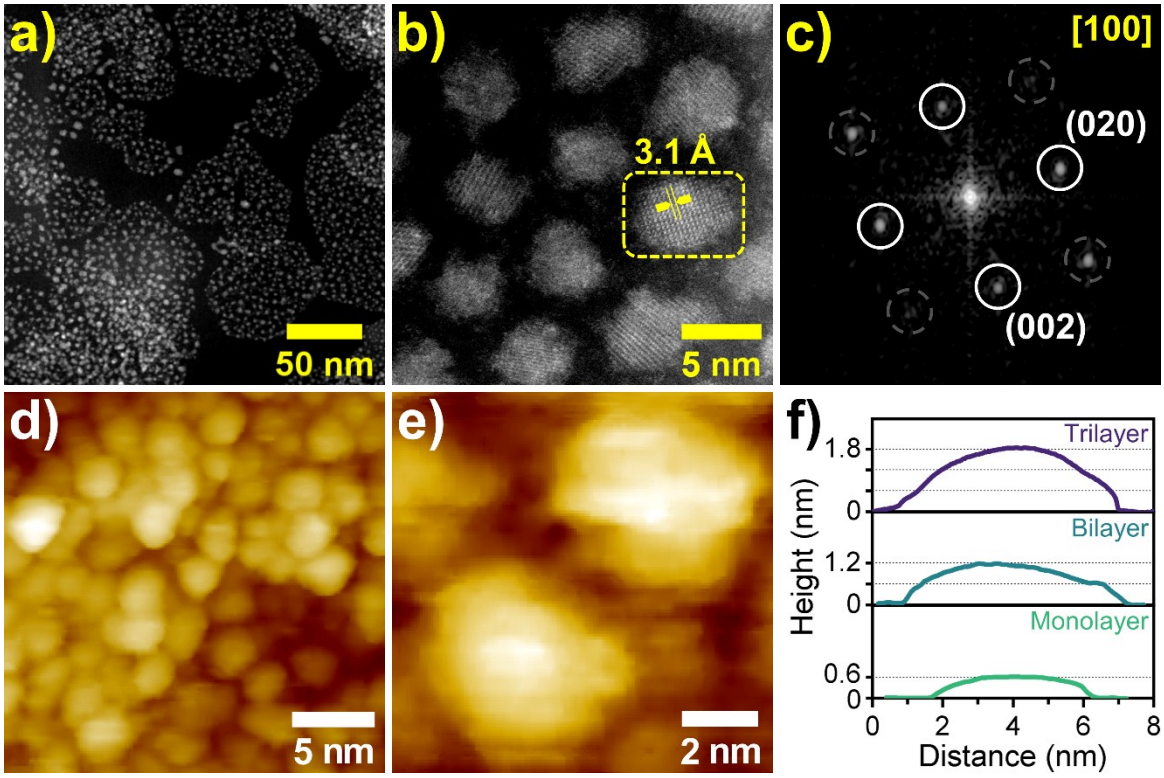

Figure 7.1. (a) Overview HR-HAADF-STEM image of PbSe fQDs with average lateral dimensions of (4.9 ± 1.1) × (3.9 ± 0.6) nm². (b) High-resolution micrograph of individual crystalline PbSe fQDs (lattice spacing 3.1 Å (200)). (c) FFT pattern of the single fQD region marked in (b), underpinning the crystallinity of the fQD and exhibiting the characteristic diffraction peaks of cubic rock salt structure PbSe. (d) STM image (V_S = 4 V; I_{set} = 50 pA) of the PbSe fQDs shown in (a), exhibiting average lateral sizes of (5.0 ± 1.7) × (3.5 ± 1.3) nm² after annealing under high vacuum. (e) Small-scale STM image (V_S = 3 V; I_{set} = 40 pA) of two PbSe fQDs. (f) STM height profiles of fQDs with thicknesses of 1.8, 1.2, and 0.6 nm.

At higher magnification (Figure 7.1b), the lattice fringes of PbSe fQDs are clearly visible, with the measured lattice spacing of 3.1 Å (200) indicating the PbSe rock salt structure. This is supported by the corresponding FFT pattern (Figure 7.1c), which exhibits a set of diffraction peaks characteristic of cubic PbSe (lattice constant a = 6.128 Å, space group $Fm\bar{3}m$, PDF card 01-077-0245). For complete structural characterization, we perform STM imaging to determine the thickness of the PbSe fQDs. Figure 7.1d depicts a large-scale STM image (23 × 23 nm² at T = 77 K) of the sample shown in Figure 7.1a–c. The size and the morphology of fQDs in STM (Figure 7.1d,e and Figure S 7.1d–f) are identical to those obtained

under STEM (see Figure S 7.1a–c) and show that fQDs are stable under the STM imaging environment without undergoing surface reconstruction. For isolated PbSe fQDs, the height, *z*, can be determined with an accuracy of ~0.1 nm from STM images collected in constant current mode. Figure 7.1f shows that, while the lateral dimension remains constant across the sample, three distinct thicknesses of 1.8, 1.2, and 0.6 nm are observed. It is noteworthy that during our experiments we have mostly observed 0.6 or 1.2 nm thick PbSe fQDs and only a few examples with a thickness of 1.8 nm. We attribute the measured thicknesses of 0.6, 1.2, and 1.8 nm to monolayer, bilayer, and trilayer fQDs, respectively, with 0.6 nm being the height of the unit cell of cubic PbSe (Pb-to-Pb distance).

To gain further insight into the electronic properties of colloidal mono- to few-layer PbSe, we performed STS measurements on isolated individual fQDs at 77 K (Figure 7.2).

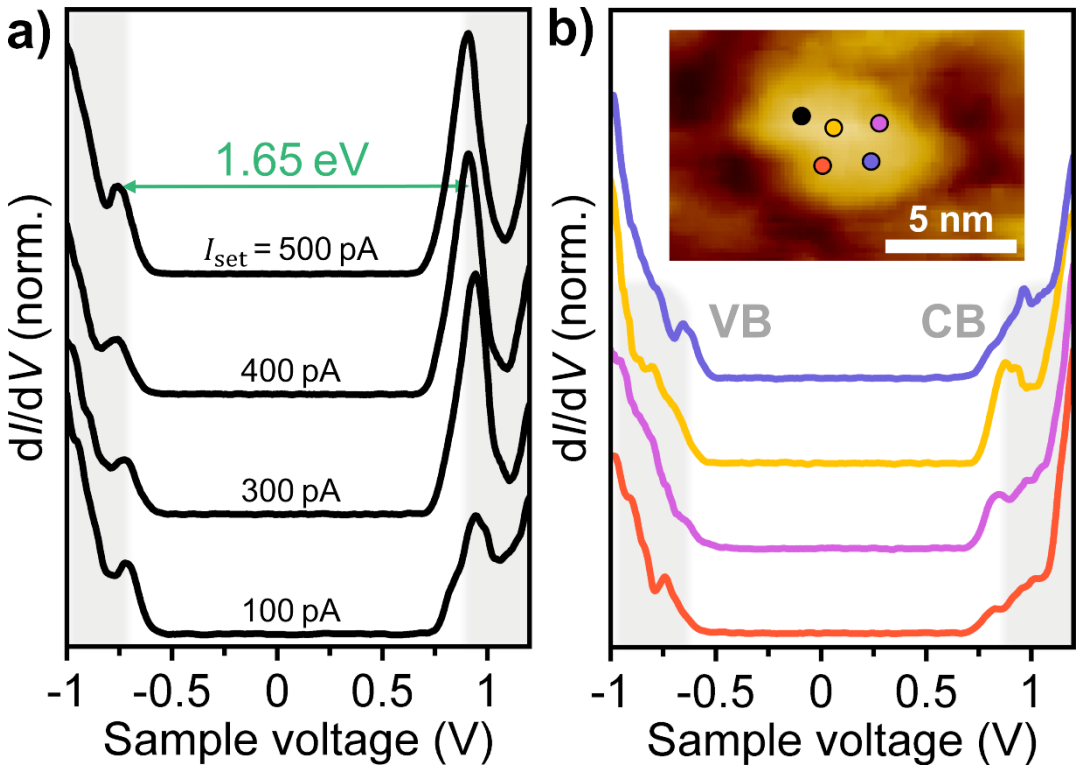

Figure 7.2. (a) Set-point current dependent STS spectra on the black dot area of the PbSe fQD ($E_{g,STS}$ = 1.65 eV) shown in the inset of panel b. (b) dI/dV spectra (V_S = -1 V; I_{set} = 200 pA) measured at four different spots on the same PbSe fQD (color-coded in the STM image inset), which consistently show a band gap free of in-gap states with only minor fluctuations in the form of the VB and CB. Inset: STM image (V_S = 4 V; I_{set} = 50 pA) of the fQD.

STS-measured dI/dV spectra depend on the parameters of the double barrier tunnel junction formed between the STS tip, the sample, and the conductive substrate. In order to extract valid energy level structures and band gaps, resonant tunneling is required (shell-tunneling regime).[35,44,45] Figure 7.2a shows current-dependent dI/dV spectra collected on a thin PbSe fQD; varying the set-point current I_{set} changes the tip to fQD distance and, thereby, the tunneling rate. When I_{set} is increased from 100 to 500 pA, the apparent band gap remains constant, which implies a single tunneling junction, *i.e.*, between the tip and the PbSe fQD, which prevents considerable charging of the sample. Please note that the lack of a double tunnel junction points toward an absence of ligands between the fQD and the gold substrate, in agreement with the height measurement by STM. A constant apparent band gap further implies resonant tunneling and that the peaks align with the actual energy levels of the PbSe fQDs, from which we can derive meaningful band gap values. In agreement with OVERGAAG *et al.*,[36] we attribute the tolerance of PbSe fQDs to high set-point currents to the low effective charge carrier masses of PbSe, which result in spatially drawn-out orbitals, and a large tunneling coupling. For the PbSe fQD shown in the STM image inset in Figure 7.2b, we find a zero-conductance region free of in-gap states, framed by single pronounced peaks on either side. The presence of sharp resonances in the dI/dV spectra, rather than a step-like energy level structure that would be expected for "truly" 2D quantum materials, provides evidence for the quantum confinement of 2D PbSe in all three dimensions ($x, y, z / a_B < 1$) and justifies the use of the term "flat QD". In accordance with the literature, we assign the two peaks at negative and positive sample voltages to the $1S_h$ and $1S_e$ energy levels, respectively.[37,46] The extracted electronic band gap of 1.65 eV is approximately 0.45 eV wider than the largest STS band gap $E_{g,STS}$ reported for spherical PbSe QDs ($E_{g,STS,spherical\ PbSe\ QDs} \approx 1.2$ eV for $d \approx 3.5$ nm) by LILJEROTH *et al.* and highlights the extreme additional confinement in the z direction in PbSe fQDs. Figure 7.2b depicts dI/dV spectra obtained from four randomly selected spots within the same single PbSe fQD (shown in the inset). Although the expression of the valence (VB) and conduction band (CB) energy levels varies slightly between the different spots, we do not find in-gap states at any of the probed spots. Furthermore, the measured band gap value is consistent throughout the fQD, underpinning that the deduced $E_{g,STS}$ values are valid.

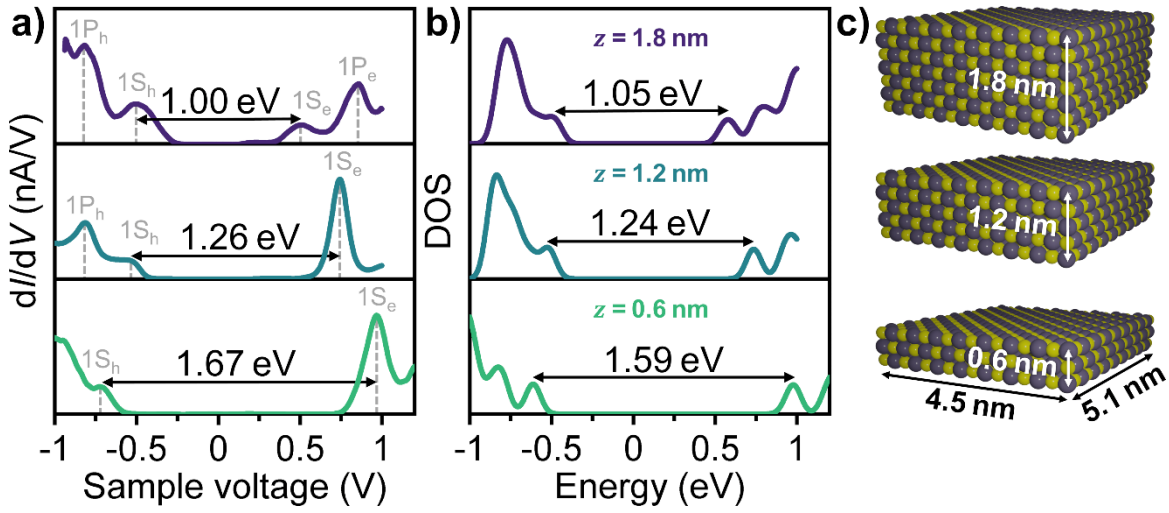

Figure 7.3. (a) Representative STS spectra at 77 K of fQDs with tri-, bi-, and monolayer thickness (top to bottom; tunneling conditions: V_S = -1 V, I_{set} = 200 pA). (b) Theoretical TB calculated DOS of PbSe fQDs with three different thicknesses *z*. Note that a broadening of 60 meV is introduced to the calculations to reproduce the experimental conditions. (c) Schematic representation of a monolayer, bilayer, and trilayer cubic rock salt PbSe fQD of 5.1 × 4.5 nm² with atomically flat (001) basal and site facets, with alternating lead (gray) and selenium (yellow) atoms.

Figure 7.3a shows representative d*I*/d*V* spectra at T = 77 K for PbSe fQDs with varying thickness. The electronic band gap increases from 1.00 to 1.67 eV when the thickness of the PbSe fQDs is decreased from 1.8 to 0.6 nm as a result of the strong quantum confinement. To further understand the correlation between the thickness/layer number and the band gap size, we performed TB calculations (Figure 7.3b) for PbSe fQDs with lateral dimensions of 4 × 4 nm².[47] The theoretical DOS quantitatively replicates the DOS and the electronic band gap derived by STS for mono-, bi-, and trilayer thick PbSe fQDs, confirming the STM height measurement shown in Figure 7.1f spectroscopically. Figure 7.3c depicts a schematic visualization of the crystal structure of a monolayer, bilayer, and trilayer cubic rock salt PbSe fQD (the crystal was built using the open-source molecular builder and visualization tool AVOGADRO version 1.2.0 with library version 1.2.048). The weak variations between the calculated and experimental electronic gaps likely arise from the slight deviation from a square shape of the fQDs.

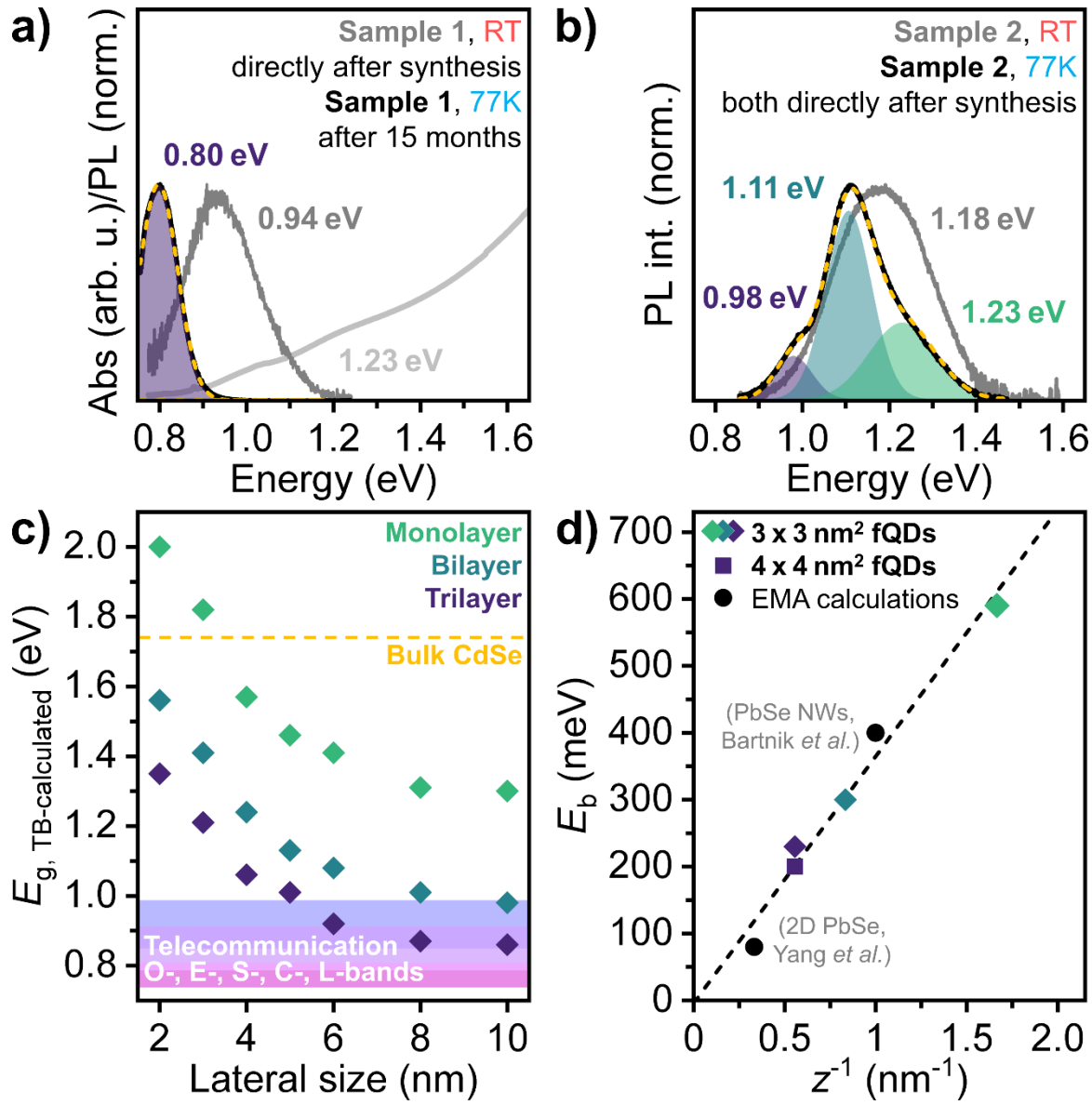

Figure 7.4. (a) Ensemble RT absorbance and PL spectrum (gray) of the colloidal PbSe fQDs studied in STM/S and cryogenic PL spectrum of the same sample over a year later (black), showing bathochromically shifted narrow PL in the third telecommunication window at 0.80 eV (1550 nm), which is attributed to OSTWALD ripening within the time frame. (b) Cryogenic PL spectrum of laterally smaller PbSe fQDs measured directly after synthesis. The three PL contributions are attributed to monolayer, bilayer, and trilayer PbSe fQD populations. (c) TB calculated correlation between the electronic band gap and lateral size of mono- to trilayer PbSe fQDs, highlighting the interplay of strong vertical confinement and the minor lateral confinement in pushing PbSe fQD emission into the low attenuation telecommunication windows. (d) Exciton binding energy *vs* the reciprocal value of

the thickness z of PbSe fQDs from this work and 2D PbSe[42] as well as PbSe nanowires (NWs)[43] (both calculated by effective mass approximation (EMA)).

In addition to their remarkable structural and electronic properties, PbSe fQDs are also appealing with regard to their optical properties. Figure 7.4a shows the RT ensemble PL and absorbance spectrum of the PbSe fQD sample investigated by STM/S (sample 1) directly after the synthesis. The PL is centered near 0.94 eV (fwhm = 197 meV) with weakly pronounced excitonic absorption at 1.23 eV. Surprisingly, cryogenic ensemble PL measurements performed 15 months after the STM/S measurements (Figure 7.4a) reveal a rather narrow PL line centered at 0.80 eV (1550 nm; fwhm = 120 meV) in the C-band telecommunication window. We infer OSTWALD ripening of PbSe fQD 1MLs and bilayers toward trilayer fQDs in the metastable colloidal solution over the extended time frame as the reason for the bathochromic PL shift (compared to the PL directly after synthesis) and the PL being governed by the emission of the thicker PbSe fQDs (see Figure S 7.2 and Table S 7.1 for further discussion on OSTWALD ripening/fusing of fQDs). To test this hypothesis, we synthesized a new batch of PbSe fQDs (sample 2) with a smaller lateral size $(3.3 \pm 0.5) \times (2.9 \pm 0.4)$ nm^2 (see Figure S 7.3), exhibiting optical features at higher energies for the following cryogenic PL discussion (Figure 7.4b). When investigating a fQD sample directly after synthesis, we find that the cryogenic PL spectrum is best fitted by the sum of three GAUSSIANS, which reflects the three distinct fQD thickness populations (1ML (0.6 nm), bilayer (1.2 nm), and trilayer (1.8 nm)) and points to an absence of major OSTWALD ripening (Figure 7.4b). The fwhm of each spectral feature at cryogenic temperature in Figure 7.4a and b is comparable to the values typically obtained for spherical PbSe QDs (50 – 100 meV)[2,20] (although it should be noted that the fwhm of 2D PbSe[31,33] strongly depends on the spectral position and is smaller the further the PL lies in the NIR), and all contributions are significantly narrower than typical values for comparable 2D PbS nanoplatelets at RT (>200 meV),[21,34] indicating the potential of PbSe fQDs for applications requiring narrow emission.

We further performed TB calculations to determine the influence of the lateral size on quantum confinement in PbSe fQDs. Figure 7.4c shows the electronic band gap deduced from the calculated DOS (see Figure S 7.4 for the calculated DOS corresponding to each of the plotted data points) for square-shaped fQDs with a

thickness from mono- to trilayers and lateral dimensions ranging from 2 to 10 nm. For each fQD thickness, the electronic gap dramatically drops by 600 meV when tuning the size from 2 to 6 nm. Beyond 6 nm, the electronic band gap weakly changes and the quantum confinement is compelled by the thickness of the fQDs. This substantiates previous reports on the PL tunability of ultrathin PbSe[31] and PbTe[32] NPLs, which was assumed to be caused by a combination of the thickness and the lateral size, with thickness as the major factor. In addition, Figure 7.4c highlights the possibility and provides a target range to access PL in the low attenuation telecommunication range of the O-, E-, and S-bands, where glass fibers exhibit negligible losses, by further tailoring the dimensions of PbSe fQDs.

It is noteworthy that the exciton binding energy of PbSe fQDs can be directly determined by our experimental results. It corresponds to the difference between the experimental values of the electronic and optical band gap with the latter including electron-hole Coulomb interactions. For the sample shown in Figure 7.4b, we evaluate the exciton binding energy as the difference between the electronic gap derived from TB calculations for 3 × 3 nm^2 and the optical spectra. We find that the binding energy E_b increases from 200 meV for 1.8 nm thick PbSe fQDs up to a record value of 600 meV for PbSe 1MLs, which is comparable to well-established layered materials such as transition metal dichalcogenides, for which E_b typically exhibits values of ~0.5 eV.[49] We emphasize that our experimental results validate previous estimations from 4-band effective mass calculations on the exciton binding energy in low-dimensional PbSe nanomaterials. Figure 7.4d shows our experimental exciton binding energies together with the ones estimated by EMA calculations for 3 nm thick PbSe nanosheets (E_b ~80 meV)[42] and ultranarrow (1 nm in diameter) PbSe NWs (E_b ~400 meV).43 The exciton binding energy is inversely proportional to the dimension that compels the quantum confinement.

7.4 Conclusion

In conclusion, we have synthesized NIR-emitting colloidal PbSe fQDs with thicknesses down to the monolayer. We directly demonstrate the strongly anisotropic nature of the fQDs by STM (height) measurements and confirm the microscopy data by a comprehensive study of the electronic properties *via* low-temperature STS and TB calculations. In-gap state free electronic band gaps of

1.67, 1.26, and 1.00 eV for mono-, bi-, and trilayers and a QD-like DOS with defined peaks on either side of the zero-conductance region, in excellent agreement with theoretical DOS, are demonstrated. Associated ensemble cryogenic PL spectra contain three distinct contributions, which are attributed to the different thickness populations in PbSe fQD syntheses and show consistent results between structural, electronic, and optical properties. From a shift of the PL contributions on longer time scales after synthesis, we infer OSTWALD ripening and a possible fusing mechanism of thinner fQDs to thicker populations with PL shifting to longer telecommunication wavelengths, which can be slowed down by PbI_2 surface passivation. Our study showcases the extreme quantum confinement of PbSe fQDs exhibiting high exciton binding energies up to 600 meV for PbSe 1MLs and emphasizes their potential as innovative classical or quantum light sources for fiber optics-based photonics.

7.5 References

(1) Cho, K.-S.; Talapin, D. V.; Gaschler, W.; Murray, C. B. Designing PbSe Nanowires and Nanorings through Oriented Attachment of Nanoparticles. *J. Am. Chem. Soc.* **2005**, *127* (19), 7140–7147.

(2) Murray, C. B.; Sun, S.; Gaschler, W.; Doyle, H.; Betley, T. A.; Kagan, C. R. Colloidal Synthesis of Nanocrystals and Nanocrystal Superlattices. *IBM J. Res. Dev.* **2001**, *45* (1), 47–56.

(3) Koh, W.-K.; Bartnik, A. C.; Wise, F. W.; Murray, C. B. Synthesis of Monodisperse PbSe Nanorods: A Case for Oriented Attachment. *J. Am. Chem. Soc.* **2010**, *132* (11), 3909–3913.

(4) D'Amato, M.; Fu, N.; Glorieux, Q.; Giacobino, E.; Le Jeannic, H.; Ithurria, S.; Lhuillier, E.; Bramati, A. Room-Temperature Efficient Single-Photon Generation from CdSe/ZnS Nanoplatelets. *ACS Nano* **2025**, *19* (14), 14404–14409.

(5) Ma, X.; Diroll, B. T.; Cho, W.; Fedin, I.; Schaller, R. D.; Talapin, D. V.; Gray, S. K.; Wiederrecht, G. P.; Gosztola, D. J. Size-Dependent Biexciton Quantum Yields and Carrier Dynamics of Quasi-Two-Dimensional Core/Shell Nanoplatelets. *ACS Nano* **2017**, *11* (9), 9119–9127.

(6) Rabani, E.; Hetényi, B.; Berne, B. J.; Brus, L. E. Electronic Properties of CdSe Nanocrystals in the Absence and Presence of a Dielectric Medium. *J. Chem. Phys.* **1999**, *110* (11), 5355–5369.

(7) Banin, U.; Cao, Y.; Katz, D.; Millo, O. Identification of Atomic-Like Electronic States in Indium Arsenide Nanocrystal Quantum Dots. *Nature* **1999**, *400* (6744), 542–544.

(8) Ji, B.; Rabani, E.; Efros, A. L.; Vaxenburg, R.; Ashkenazi, O.; Azulay, D.; Banin, U.; Millo, O. Dielectric Confinement and Excitonic Effects in Two-Dimensional Nanoplatelets. *ACS Nano* **2020**, *14* (7), 8257–8265.

(9) Ma, D. D. D.; Lee, C. S.; Au, F. C. K.; Tong, S. Y.; Lee, S. T. Small-Diameter Silicon Nanowire Surfaces. *Science* **2003**, *299* (5614), 1874–1877.

(10) Alivisatos, A. P. Perspectives on the Physical Chemistry of Semiconductor Nanocrystals. *J. Phys. Chem.* **1996**, *100* (31), 13226–13239.

(11) Murray, C. B.; Norris, D. J.; Bawendi, M. G. Synthesis and Characterization of Nearly Monodisperse CdE (E = Sulfur, Selenium, Tellurium) Semiconductor Nanocrystallites. *J. Am. Chem. Soc.* **1993**, *115* (19), 8706–8715.

(12) Ithurria, S.; Dubertret, B. Quasi 2D Colloidal CdSe Platelets with Thicknesses Controlled at the Atomic Level. *J. Am. Chem. Soc.* **2008**, *130* (49), 16504–16505.

(13) Bouet, C.; Mahler, B.; Nadal, B.; Abecassis, B.; Tessier, M. D.; Ithurria, S.; Xu, X.; Dubertret, B. Two-Dimensional Growth of CdSe Nanocrystals, from Nanoplatelets to Nanosheets. *Chem. Mater.* **2013**, *25* (4), 639–645.

(14) Ithurria, S.; Tessier, M. D.; Mahler, B.; Lobo, R. P. S. M.; Dubertret, B.; Efros, A. L. Colloidal Nanoplatelets with Two-Dimensional Electronic Structure. *Nat. Mater.* **2011**, *10* (12), 936–941.

(15) Ithurria, S.; Bousquet, G.; Dubertret, B. Continuous Transition from 3D to 1D Confinement Observed during the Formation of CdSe Nanoplatelets. *J. Am. Chem. Soc.* **2011**, *133* (9), 3070–3077.

(16) Shornikova, E. V.; Yakovlev, D. R.; Gippius, N. A.; Qiang, G.; Dubertret, B.; Khan, A. H.; Di Giacomo, A.; Moreels, I.; Bayer, M. Exciton Binding Energy in CdSe Nanoplatelets Measured by One-and Two-Photon Absorption. *Nano Lett.* **2021**, *21* (24), 10525–10531.

(17) Di Giacomo, A.; Rodà, C.; Khan, A. H.; Moreels, I. Colloidal Synthesis of Laterally Confined Blue-Emitting 3.5 Monolayer CdSe Nanoplatelets. *Chem. Mater.* **2020**, *32* (21), 9260–9267.

(18) Wehrenberg, B. L.; Wang, C.; Guyot-Sionnest, P. Interband and Intraband Optical Studies of PbSe Colloidal Quantum Dots. *J. Phys. Chem. B* **2002**, *106* (41), 10634–10640.

(19) Du, H.; Chen, C.; Krishnan, R.; Krauss, T. D.; Harbold, J. M.; Wise, F. W.; Thomas, M. G.; Silcox, J. Optical Properties of Colloidal PbSe Nanocrystals. *Nano Lett.* **2002**, *2* (11), 1321–1324.

(20) Pietryga, J. M.; Schaller, R. D.; Werder, D.; Stewart, M. H.; Klimov, V. I.; Hollingsworth, J. A. Pushing the Band Gap Envelope: Mid-Infrared Emitting Colloidal PbSe Quantum Dots. *J. Am. Chem. Soc.* **2004**, *126* (38), 11752–11753.

(21) Li, P.; Biesterfeld, L.; Klepzig, L. F.; Yang, J.; Ngo, H. T.; Addad, A.; Rakow, T. N.; Guan, R.; Rugeramigabo, E. P.; Zaluzhnyy, I.; Schreiber, F.; Biadala, L.; Lauth, J.; Zopf, M. Sub-millielectronvolt Line Widths in Polarized Low-Temperature Photoluminescence of 2D PbS Nanoplatelets. *Nano Lett.* **2024**, *24* (51), 16293–16300.

(22) Krishnamurthy, S.; Singh, A.; Hu, Z.; Blake, A. V.; Kim, Y.; Singh, A.; Dolgopolova, E. A.; Williams, D. J.; Piryatinski, A.; Malko, A. V.; Htoon, H.; Sykora, M.; Hollingsworth, J. A. PbS/CdS Quantum Dot Room-Temperature Single-Emitter Spectroscopy Reaches the Telecom O and S Bands via an Engineered Stability. *ACS Nano* **2021**, *15* (1), 575–587.

(23) Wise, F. W. Lead Salt Quantum Dots: the Limit of Strong Quantum Confinement. *Acc. Chem. Res.* **2000**, *33* (11), 773–780.

(24) Murphy, J. E.; Beard, M. C.; Norman, A. G.; Ahrenkiel, S. P.; Johnson, J. C.; Yu, P.; Mićić, O. I.; Ellingson, R. J.; Nozik, A. J. PbTe Colloidal Nanocrystals: Synthesis, Characterization, and Multiple Exciton Generation. *J. Am. Chem. Soc.* **2006**, *128* (10), 3241–3247.

(25) Ravindra, N. M.; Srivastava, V. K. Properties of PbS, PbSe, and PbTe. *Phys. Status Solidi A* **1980**, *58* (1), 311–316.

(26) Wrasse, E. O.; Schmidt, T. M. Prediction of Two-Dimensional Topological Crystalline Insulator in PbSe Monolayer. *Nano Lett.* **2014**, *14* (10), 5717–5720.

(27) Shao, Z.; Zheng, F.; Zhang, Z.; Sun, H.; Li, S.; Yuan, H.; Li, Q.; Zhang, P.; Pan, M. Epitaxial Growth of PbSe Few-Layers on SrTiO3: The Effect of Compressive Strain and Potential Two-Dimensional Topological Crystalline Insulator. *ACS Nano* **2019**, *13* (2), 2615–2623.

(28) Ekuma, C. E. Effects of Vacancy Defects on the Electronic and Optical Properties of Monolayer PbSe. *J. Phys. Chem. Lett.* **2018**, *9* (13), 3680–3685.

(29) Chen, T.; Fan, C.; Zhou, W.; Zou, X.; Xu, X.; Wang, S.; Wan, Q.; Zhang, Q. Epitaxial Growth of Non-Layered PbSe Nanoplates on MoS_2 Monolayer for Infrared Photoresponse. *Appl. Phys. Express* **2019**, *12* (5), 55005.

(30) Cordova, D. L. M.; Fender, S. S.; Hooshmand, M. S.; Buchanan, M. R.; Davis, J.; Kam, T. M.; Gannon, R. N.; Fischer, R.; Lu, P.; Hanken, B. E.; Asta, M.; Johnson, D. C. The Instability of Monolayer-Thick PbSe on VSe_2. *Chem. Mater.* **2020**, *32* (18), 7992–8003.

(31) Biesterfeld, L.; Klepzig, L. F.; Niebur, A.; Rosebrock, M.; Lauth, J. Toward Bright Colloidal Near-Infrared Emitters: Surface Passivation of 2D PbSe Nanoplatelets by Metal Halides. *J. Phys. Chem. C* **2022**, *126* (45), 19277–19285.

(32) Biesterfeld, L.; Vochezer, M. T.; Kögel, M.; Zaluzhnyy, I. A.; Rosebrock, M.; Klepzig, L. F.; Leis, W.; Seitz, M.; Meyer, J. C.; Lauth, J. Solving the Synthetic Riddle of Colloidal Two-Dimensional PbTe Nanoplatelets with Tunable Near-Infrared Emission. *Chem. Mater.* **2024**, *36* (15), 7197–7206.

(33) Klepzig, L. F.; Biesterfeld, L.; Romain, M.; Niebur, A.; Schlosser, A.; Hübner, J.; Lauth, J. Colloidal 2D PbSe Nanoplatelets with Efficient Emission Reaching the Telecom O-, E- and S-Band. *Nanoscale Adv.* **2022**, *4*, 590–599.

(34) Manteiga Vázquez, F.; Yu, Q.; Klepzig, L. F.; Siebbeles, L. D. A.; Crisp, R. W.; Lauth, J. Probing Excitons in Ultrathin PbS Nanoplatelets with Enhanced Near-Infrared Emission. *J. Phys. Chem. Lett.* **2021**, *12* (1), 680–685.

(35) Banin, U.; Millo, O. Tunneling and Optical Spectroscopy of Semiconductor Nanocrystals. *Annu. Rev. Phys. Chem.* **2003**, *54*, 465–492.

(36) Overgaag, K.; Liljeroth, P.; Grandidier, B.; Vanmaekelbergh, D. Scanning Tunneling Spectroscopy of Individual PbSe Quantum Dots and Molecular Aggregates Stabilized in an Inert Nanocrystal Matrix. *ACS Nano* **2008**, *2* (3), 600–606.

(37) Liljeroth, P.; Zeijlmans van Emmichoven, P. A.; Hickey, S. G.; Weller, H.; Grandidier, B.; Allan, G.; Vanmaekelbergh, D. Density of States Measured by Scanning-Tunneling Spectroscopy Sheds New Light on the Optical Transitions in PbSe Nanocrystals. *Phys. Rev. Lett.* **2005**, *95* (8), 86801.

(38) Grinbom, G. A.; Saraf, M.; Saguy, C.; Bartnik, A. C.; Wise, F.; Lifshitz, E. Density of States in a Single PbSe/PbS Core-Shell Quantum Dot Measured by Scanning Tunneling Spectroscopy. *Phys. Rev. B* **2010**, *81* (24), 245301.

(39) Kavrik, M. S.; Hachtel, J. A.; Ko, W.; Qian, C.; Abelson, A.; Unlu, E. B.; Kashyap, H.; Li, A.-P.; Idrobo, J. C.; Law, M. Emergence of Distinct Electronic States in Epitaxially-Fused PbSe Quantum Dot Superlattices. *Nat. Commun.* **2022**, *13* (1), 6802.

(40) Notot, V.; Walravens, W.; Berthe, M.; Peric, N.; Addad, A.; Wallart, X.; Delerue, C.; Hens, Z.; Grandidier, B.; Biadala, L. Quantum Dot Acceptors in Two-Dimensional Epitaxially Fused PbSe Quantum Dot Superlattices. *ACS Nano* **2022**, *16* (2), 3081–3091.

(41) Liljeroth, P.; Overgaag, K.; Urbieta, A.; Grandidier, B.; Hickey, S. G.; Vanmaekelbergh, D. Variable Orbital Coupling in a Two-Dimensional Quantum-Dot Solid Probed on a Local Scale. *Phys. Rev. Lett.* **2006**, *97* (9), 96803.

(42) Yang, J.; Wise, F. W. Electronic States of Lead-Salt Nanosheets. *J. Phys. Chem. C* **2015**, *119* (48), 26809–26816.

(43) Bartnik, A. C.; Efros, A. L.; Koh, W.-K.; Murray, C. B.; Wise, F. W. Electronic States and Optical Properties of PbSe Nanorods and Nanowires. *Phys. Rev. B* **2010**, *82* (19), 195313.

(44) Bakkers, E. P. A. M.; Hens, Z.; Zunger, A.; Franceschetti, A.; Kouwenhoven, L. P.; Gurevich, L.; Vanmaekelbergh, D. Shell-Tunneling Spectroscopy of the Single-Particle Energy Levels of Insulating Quantum Dots. *Nano Lett.* **2001**, *1* (10), 551–556.

(45) Jdira, L.; Liljeroth, P.; Stoffels, E.; Vanmaekelbergh, D.; Speller, S. Size-Dependent Single-Particle Energy Levels and Interparticle Coulomb Interactions in CdSe Quantum Dots Measured by Scanning Tunneling Spectroscopy. *Phys. Rev. B* **2006**, *73* (11), 115305.

(46) Allan, G.; Delerue, C. Confinement Effects in PbSe Quantum Wells and Nanocrystals. *Phys. Rev. B* **2004**, *70* (24), 245321.

(47) Niquet, Y. M.; Delerue, C.; Allan, G.; Lannoo, M. Interpretation and Theory of Tunneling Experiments on Single Nanostructures. *Phys. Rev. B* **2002**, *65* (16), 165334.

(48) Hanwell, M. D.; Curtis, D. E.; Lonie, D. C.; Vandermeersch, T.; Zurek, E.; Hutchison, G. R. Avogadro: An Advanced Semantic Chemical Editor, Visualization, and Analysis Platform. *J. Cheminform.* **2012**, 4 (1), 17.

(49) Wang, G.; Chernikov, A.; Glazov, M. M.; Heinz, T. F.; Marie, X.; Amand, T.; Urbaszek, B. Colloquium: Excitons in Atomically Thin Transition Metal Dichalcogenides. *Rev. Mod. Phys.* **2018**, *90* (2), 21001.

7.6 Supporting Information

7.6.1 Methods

Chemicals. Acetonitrile (≥ 99.5%), anhydrous ethanol (max. 0.01% H_2O), isopropanol (≥ 99.5%), lead(II) oxide (≥ 99.99%), methanol (≥ 99.8%), *n*-octylamine (99%), anhydrous tetrachloroethylene (TCE, ≥ 99%), triethylamine (≥ 99%), trifluoroacetic acid (99%), and trifluoroacetic anhydride (≥ 99%) were purchased from SIGMA-ALDRICH/MERCK. Anhydrous *n*-hexane (97%) was purchased from ACROS ORGANICS. Lead(II) iodide (99.99%) and selenourea (99.97%) were purchased from ALFA AESAR. Oleic acid (90%) was purchased from ABCR. *n*-Octylamine and oleic acid were degassed *via* the freeze-pump-thaw technique three times prior to being used and stored inside a N_2-filled glovebox. All other reagents were used as received from the listed suppliers without any further purification steps.

PbSe fQDs Synthesis. 2D PbSe fQDs were synthesized following a procedure previously described by our group;[1,2] all synthetic steps were performed under N_2 atmosphere. Prior to the actual synthesis, a selenourea precursor solution was prepared by dissolving selenourea (193 mg, 1.57 mmol) in a mixture of octylamine (2.025 ml, 12.2 mmol), oleic acid (0.225 ml, 0.71 mmol), and *n*-hexane (0.75 ml) at 35°C for 24 – 72 h. For a typical 2D PbSe fQDs synthesis, lead oleate (1.83 g, 2.7 mmol) (synthesized *via* an established method of Hendricks *et al.*)[3] was stirred in a mixture of octylamine (2.0 ml, 12.0 mmol), oleic acid (4.0 ml, 12.5 mmol), and *n*-hexane (18 ml) at 35°C until complete dissolution and subsequently cooled to 0°C using an ice bath. The selenourea solution (2.5 ml) was injected rapidly into the vigorously stirred lead oleate solution, causing an immediate color change from colorless/slightly yellow to dark brown. After 10 min the dark reaction mixture was

quenched by adding dry ethanol (18.5 ml). The cloudy quenched solution was then centrifuged at 2500 rcf for 10 min, the supernatant discarded, and the precipitate was redispersed in *n*-hexane (10 ml). This process was repeated until the supernatant was transparent, usually requiring a total of three cycles. At this point, pristine PbSe fQDs were sealed under N_2 atmosphere and stored in a refrigerator. PbI_2 passivated PbSe fQDs were prepared by diluting pristine fQDs (0.5 ml) with *n*-hexane (0.75 ml) and injecting 1.0 ml of a 0.1 M PbI_2 solution in *n*-octylamine and oleic acid (molar ratio 9:1). After 40 min at 35°C the passivated PbSe fQDs were likewise sealed and stored in a refrigerator.

High-Angle Annular Dark-Field Scanning Transmission Electron Microscopy. HR-HAADF-STEM images were obtained using a FEI TITAN THEMIS 300 microscope equipped with a probe aberration corrector, operated at 200 kV. The probe size was set to 0.1 nm with a convergence semi-angle of 22.5 mrad. The collection angle of the HAADF detector was in the range of 80 – 150 mrad. The contrast in HAADF images is proportional to $Z \approx 1.7 - 2$, meaning that bright contrast indicates relatively heavy atomic composition.

Transmission Electron Microscopy. TEM images were acquired using a FEI TECNAI G2 F20 transmission electron microscope with a field emission gun operating at 200 kV. For TEM measurements the colloidal PbSe fQDs were drop-cast onto carbon-coated copper grids (300 mesh) from QUANTIFOIL.

Scanning Tunneling Microscopy and Spectroscopy. Colloidal solutions of PbSe fQDs were drop-cast onto gold substrates, which were immediately loaded into the load lock chamber of an ultra-high vacuum (UHV) system (base pressure below 1×10^{-10} Torr) for annealing at 80°C for several hours. The samples were probed with tungsten tips that were thoroughly annealed in UHV. The STM experiments were performed with a low temperature STM from OMICRON at 77 K. The STM images were typically obtained with a sample bias between -5.5 and -4.5 V and set-point currents less than 30 pA. Tunneling spectroscopy measurements were performed at constant tip-sample separation by varying the feedback bias between -2.0 and -1.0 V and increasing the set-point current between hundreds of pA. The dynamic conductance was measured with a lock-in amplifier typically

using a 9 mV modulation at 500 Hz on the bias voltage. During the acquisition of a sequence of spectra, ramping up the voltage between the sample and the tip took 4.6 s to measure a single dI/dV trace.

NIR (Cryogenic) PL and Ultraviolet-Visible-NIR Absorbance Spectroscopy. NIR (cryogenic) PL spectra were collected using an EDINBURGH FLS 1000 UV-Vis-NIR spectrometer and a PTI QUANTAMASTER QM4 spectrofluorometer. The EDINBURGH FLS 1000 is equipped with a 450 W ozone-free xenon arc lamp for excitation; PL was monitored using a liquid N_2 cooled InGaAs NIR photomultiplier tube 1650 detector from EDINBURGH. The PTI QUANTAMASTER QM4 is equipped with a 75 W steady-state xenon short arc lamp for excitation and PL was monitored using a liquid N_2 cooled PTI P1.7R detector module (HAMAMATSU PMT R5509-72). To avoid higher order excitation light, a RG780 long pass filter glass (thickness of 3 mm) was mounted in the emission path. Spectral selection was achieved using single grating monochromators (excitation: 1200 grooves/mm, 300 nm blaze; NIR emission 600 grooves/mm, 1200 nm blaze). Samples for RT optical ensemble spectroscopy were prepared by diluting the colloidal PbSe fQD solutions in TCE (optical density below 0.2 at 500 nm) in a quartz cuvette (quartz glass high performance QS 200 – 2500 nm with an optical path length of 1 cm by HELLMA). Absolute PLQYs were determined with the FLS 1000 using an integrating sphere. For this, scattering at 450 nm and the PL in the NIR of TCE and the fQDs were measured separately, accounting for the difference in sensitivity of both detectors with a correction factor. Cryogenic PL spectra measured with the FLS 1000 were acquired using an OPTISTAT CF sample-in-vacuum cryostat system by OXFORD INSTRUMENTS operated with liquid N_2 at regulated temperatures between 293 K and 77 K. Samples were prepared by drop-casting the colloidal PbSe fQD solutions onto high purity fused silica substrates from ESCO OPTICS. Cryogenic PL spectra obtained with the QUANTAMASTER QM4 were collected using a special liquid N_2 filled dewar accessory with a fused silica base at the level of the optical path. For this, samples were prepared by dip-coating magnesia sticks (from SIGMA-ALDRICH/MERCK) in the colloidal PbSe fQD solutions, which were then directly submerged in the liquid N_2, achieving operating temperatures of ~80 K. All PL spectra were acquired by exciting the PbSe fQDs at 450 nm. UV-Vis-NIR absorbance spectra were collected by using a double beam

CARY 5000 spectrophotometer from AGILENT TECHNOLOGIES equipped with a tungsten halogen (Vis) and deuterium arc (UV) lamp and a PbSmart NIR detector for monitoring.

Tight-Binding Calculations. We calculate the electronic structure of QDs in TB. Pb and Se atoms are described by 20 atomic orbitals, 10 orbitals ($sp^3d^5s^*$) for each spin. The HAMILTONIAN matrix is written from parameters that have been adjusted to give a good description of the electronic structure of PbSe over a wide energy range and the entire BRILLOUIN zone. Spin-orbit coupling is included. We present here the results obtained with parameters by PODDUBNY *et al.*,[4] but very similar results are obtained with parameters by ALLAN *et al.*[5] Due to the large number of atoms in QDs, full diagonalization of the HAMILTONIAN is impossible, and only electronic states close to the gap are calculated. The DOS is obtained by expanding each DIRAC by a GAUSSIAN with a half-value width of 100 meV. QD surfaces are not passivated. Despite this, in the case of IV-VI semiconductors, there are no surface states for reasons discussed in Ref. [5], which was confirmed by *ab initio* calculations by HENS *et al.*[6]

7.6.2 Supplementary Figures and Tables

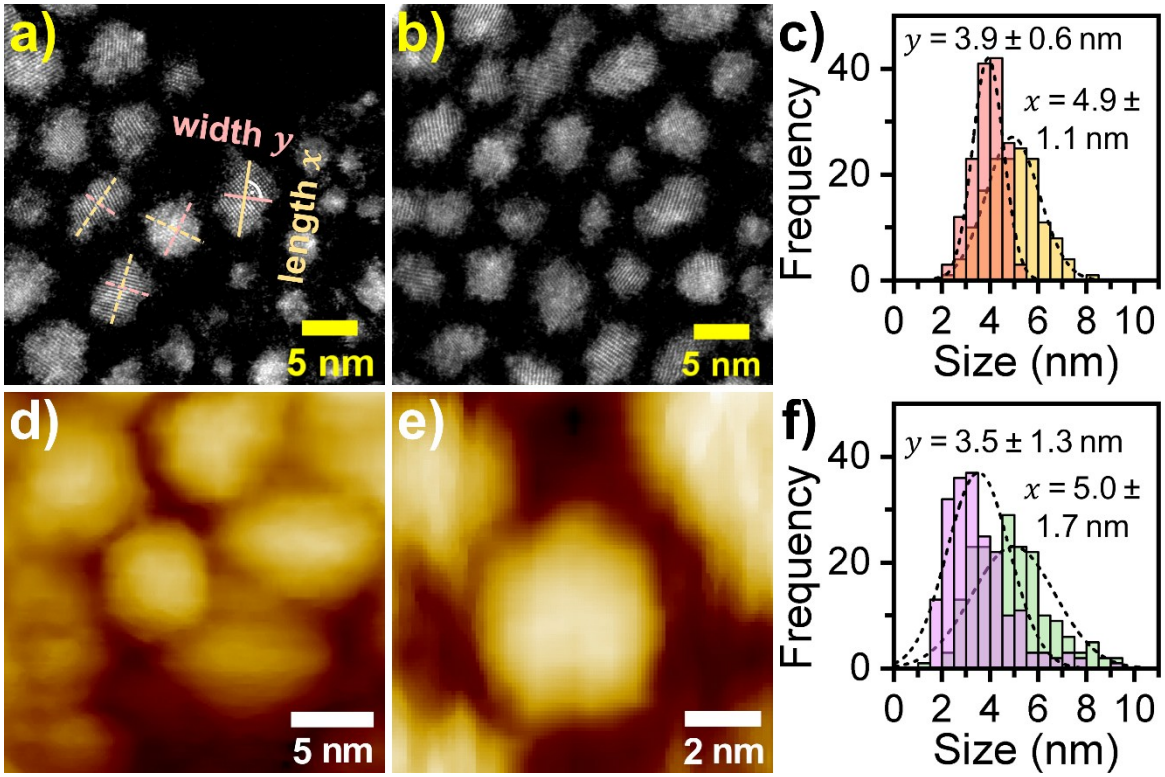

Figure S 7.1. (a, b) Typical STEM images used for lateral size determination of PbSe fQDs. *x*-Lengths were determined by measuring the longest dimension of the NPLs, *y*-widths are the largest distance orthogonal to the *x*-length. (c) Lateral size histogram of PbSe fQDs, values determined from STEM images. (d, e) Typical STM images used for lateral size determination after annealing under high vacuum. (f) Lateral size histogram of PbSe fQDs determined from STM images, demonstrating that the size of the fQDs does not change drastically during annealing.

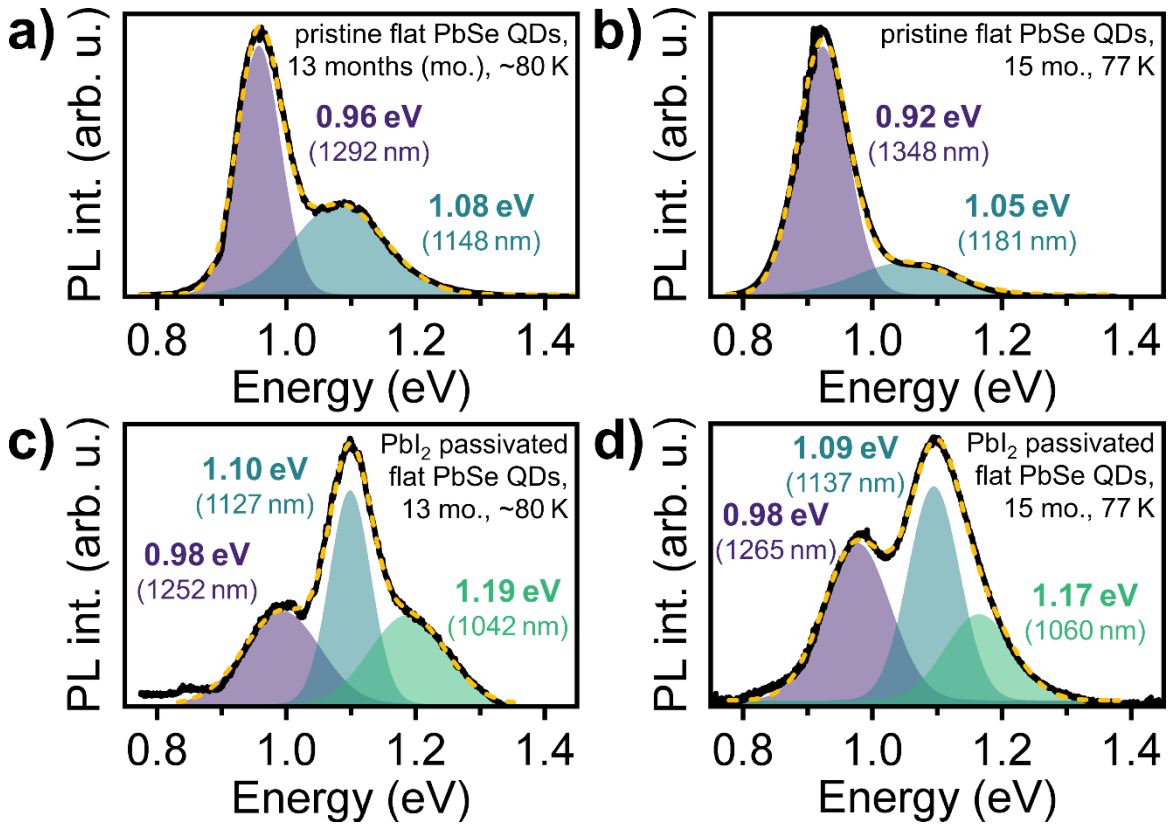

Figure S 7.2. Cryogenic PL spectra of pristine (a, b) and PbI_2 passivated (c, d) PbSe fQDs,[1] measured two months apart (during this time the samples were stored at ambient temperature under N_2 atmosphere). (a, b) The low temperature PL of pristine fQDs is best fitted by the sum of two GAUSSIANS, assigned to bi- and trilayer PbSe, resp. (c, d) For PbI_2 passivated PbSe fQDs, the PL is best fitted by three GAUSSIANS in both cases. The third and highest energy PL contribution is attributed to 1ML PbSe fQDs. Notably, the ratio between the two/three PL contributions changes within the studied time frame; after two months, we observe an increased population of the lower energy contributions (bilayer and trilayer PbSe fQDs), while the higher energy contributions (1ML and bilayer PbSe fQDs) decrease (see Table S 7.1 for details on PL contributions of all samples). We infer OSTWALD ripening in solution (and fusing in deposited samples) as the cause of shifted PL maxima in aged fQD samples and the ratio changes of the three contributions. In particular, we observe more pronounced ageing in pristine PbSe fQDs (a, b) with a surface mainly passivated by oleate in octylamine as a solvent (no 1ML contribution after 13 and 15 months, compared to the new sample 2 shown in Figure 7.4b, which shows all three contributions). In contrast, PbI_2 passivation appears to be a valuable tool for slowing down/hindering the fusing of fQDs (c, d) and we find three PL contributions at both time points. These observations are consistent with

previous reports for 2D CdSe NPLs by DUFOUR *et al.*,[7] who reported an increased colloidal stability for mixed halide- and octylamine-passivated 2D CdSe NPLs compared to purely organically passivated NPLs with a tendency to stack over time. Directly related to PbSe, KOH *et al.* found that oriented attachment of PbSe QDs is disfavored when PbI_2/I^- is introduced, since the mismatch between Pb-I and Pb-Se bond lengths prevents the formation of bridges between adjacent NCs,[8] which likewise could hinder the vertical fusing of fQDs in our case. Similarly, we have previously reported the necessity of PbI_2 passivation for the colloidal stabilization of 2D PbTe NPLs synthesized under comparable conditions.

Table S 7.1. Position and ratio of all PL contributions for the PL spectra shown in Figure 7.4a and b and Figure S 7.2.

sample	1 ML PL contribution		bilayer PL contribution		trilayer PL contribution	
	position (eV)	ratio (%)	position (eV)	ratio (%)	position (eV)	ratio (%)
STM/S sample, 77 K, after 15 mo. (Figure 7.4a)	-	-	-	-	0.80	100
laterally smaller PbSe fQDs, 77 K, directly after synthesis (Figure 7.4b)	1.23	33	1.11	56	0.98	11
pristine PbSe fQDs, 13 mo., ~80 K (Figure S 7.2a)	-	-	1.08	43	0.96	57
pristine PbSe fQDs, 15 mo., 77 K (Figure S 7.2b)	-	-	1.05	20	0.92	80
PbI_2 passivated PbSe fQDs, 13 mo., ~80 K (Figure S 7.2c)	1.19	30	1.10	39	0.98	31
PbI_2 passivated PbSe fQDs, 15 mo., 77 K (Figure S 7.2d)	1.17	22	1.09	40	0.98	38

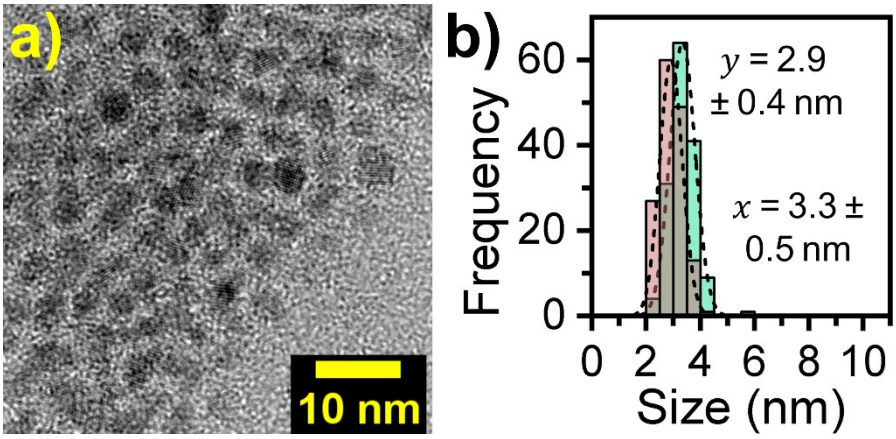

Figure S 7.3. (a) Exemplary TEM image of the laterally smaller PbSe fQDs ((3.3 ± 0.5) x (2.9 ± 0.4) nm²) shown in Figure 7.4b of the main manuscript. (b) Corresponding lateral size histogram.

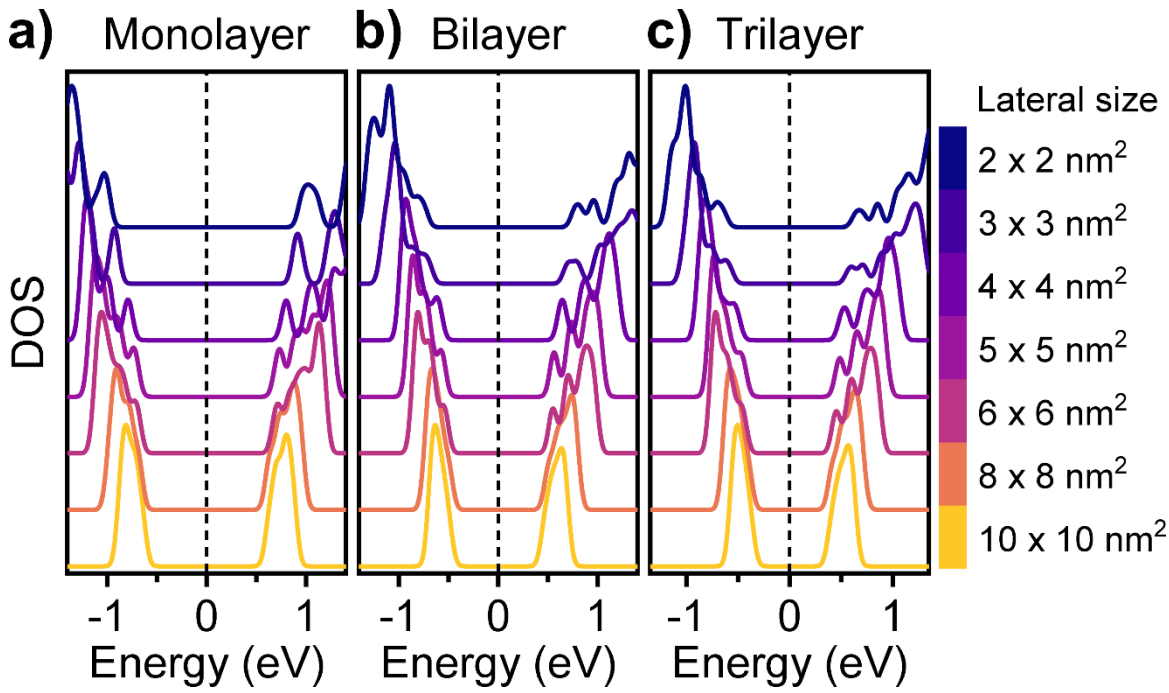

Figure S 7.4. TB calculated DOS for 1ML (a), bilayer (b), and trilayer (c) PbSe fQDs with increasing lateral size from 2 x 2 nm² to 10 x 10 nm², used to determine the calculated electronic band gaps for the band gap *vs.* lateral size plot shown in Figure 7.4c of the main manuscript.

7.6.3 References

(1) Biesterfeld, L.; Klepzig, L. F.; Niebur, A.; Rosebrock, M.; Lauth, J. Toward Bright Colloidal Near-Infrared Emitters: Surface Passivation of 2D PbSe Nanoplatelets by Metal Halides. *J. Phys. Chem. C* **2022**, *126* (45), 19277-19285.

(2) Klepzig, L. F.; Biesterfeld, L.; Romain, M.; Niebur, A.; Schlosser, A.; Hübner, J.; Lauth, J. Colloidal 2D PbSe Nanoplatelets with Efficient Emission Reaching the Telecom O-, E- and S-Band. *Nanoscale Adv.* **2022**, *4*, 590-599.

(3) Hendricks, M. P.; Campos, M. P.; Cleveland, G. T.; Jen-La Plante, I.; Owen, J. S. A Tunable Library of Substituted Thiourea Precursors to Metal Sulfide Nanocrystals. *Science* **2015**, *348* (6240), 1226-1230.

(4) Poddubny, A. N.; Nestoklon, M. O.; Goupalov, S. V. Anomalous Suppression of Valley Splittings in Lead Salt Nanocrystals without Inversion Center. *Phys. Rev. B* **2012**, *86* (3), 35324.

(5) Allan, G.; Delerue, C. Confinement Effects in PbSe Quantum Wells and Nanocrystals. *Phys. Rev. B* **2004**, *70* (24), 245321.

(6) Hens, Z.; Llusar, J.; Infante, I. Fuzzy Band Structure of Quantum Dots by Bloch Orbital Expansion: Unconventional Insights into Geometric-Electronic Structure Relations. *ACS Nano* **2025**, *19* (8), 8227-8237.

(7) Dufour, M.; Qu, J.; Greboval, C.; Méthivier, C.; Lhuillier, E.; Ithurria, S. Halide Ligands to Release Strain in Cadmium Chalcogenide Nanoplatelets and Achieve High Brightness. *ACS Nano* **2019**, *13* (5), 5326-5334.

(8) Koh, W.-K.; Dandu, N. K.; Fidler, A. F.; Klimov, V. I.; Pietryga, J. M.; Kilina, S. V. Thickness-Controlled Quasi-Two-Dimensional Colloidal PbSe Nanoplatelets. *J. Am. Chem. Soc.* **2017**, *139* (6), 2152–2155.

(9) Biesterfeld, L.; Vochezer, M. T.; Kögel, M.; Zaluzhnyy, I. A.; Rosebrock, M.; Klepzig, L. F.; Leis, W.; Seitz, M.; Meyer, J. C.; Lauth, J. Solving the Synthetic Riddle of Colloidal Two-Dimensional PbTe Nanoplatelets with Tunable Near-Infrared Emission. *Chem. Mater.* **2024**, *36* (15), 7197-7206.

8 Near-Infrared Emitting Fibers: Stable Jet Electrospinning Flat PbSe Quantum Dots into Poly(methyl methacrylate)

This chapter demonstrates the incorporation of colloidal PbSe fQDs into poly(methyl methacrylate) fibers using stable jet electrospinning. The fabricated highly aligned nanocomposite fibers are easy-to-handle, exhibit a well-defined structure and retain the NIR PL of the embedded PbSe fQDs in the solid-state. Energy transfer within perpendicularly aligned stacks of PbSe fQDs results in PL that is narrower and bathochromically shifted compared to that of the colloidal PbSe fQDs.

The results presented here have been published in *J. Phys. Chem. Lett.* **2026**, *17* (4), 955–965. For details about the author contributions see Chapter B.

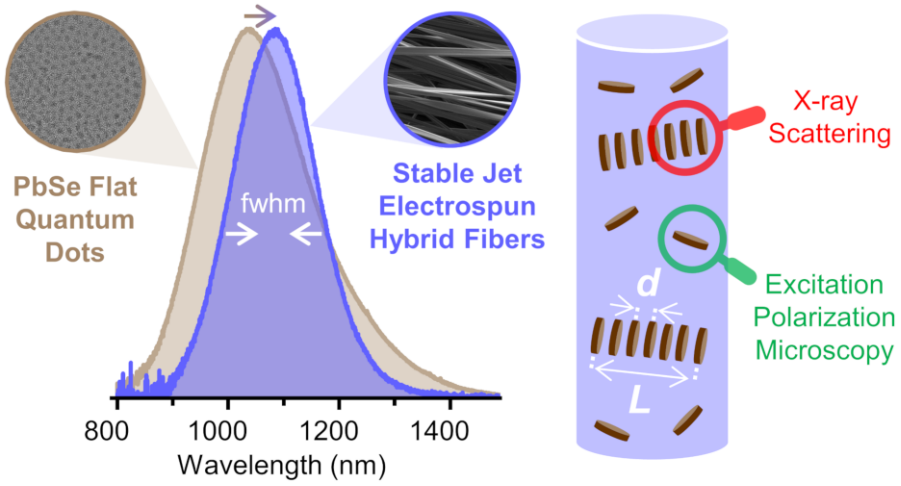

Leon Biesterfeld,[a,b,c] *Dennis Kühn,*[d] *Fuzhao Li,*[a,d] *Franka Gädeke,*[e] *Dominik A. Rudolph,*[a,c,f] *Frank Schreiber,*[g] *Peter J. Walla,*[a,e] *Ivan Zaluzhnyy,*[g] *Henning Menzel,*[a,d] *Jannika Lauth* *[a,b,c,f]

[a] Cluster of Excellence PhoenixD (Photonics, Optics, and Engineering – Innovation Across Disciplines), D-30167 Hannover, Germany.

[b] Institute of Physical and Theoretical Chemistry, Eberhard Karls University of Tübingen, D-72076 Tübingen, Germany.

[c] Institute of Physical Chemistry and Electrochemistry, Leibniz University Hannover, D-30167 Hannover, Germany.
[d] Institute for Technical Chemistry, Technische Universität Braunschweig, D-38106 Braunschweig, Germany.
[e] Institute for Physical and Theoretical Chemistry, Technische Universität Braunschweig, D-38106 Braunschweig, Germany.
[f] Laboratory of Nano and Quantum Engineering, Leibniz University Hannover, D-30167 Hannover, Germany.
[g] Institute of Applied Physics, Eberhard Karls University of Tübingen, D-72076 Tübingen, Germany.

8.1 Abstract

Flat colloidal PbSe QDs (fQDs) represent an innovative class of 2D near-infrared (NIR) photoluminescent QDs, which combine extreme thickness with additional lateral confinement. PbSe fQDs exhibit efficient NIR photoluminescence (860 – 1550 nm) that is adjustable to the low-loss transmission windows of (optical) fibers and makes them highly promising nanoemitters for fiber-based applications. Here, we demonstrate the incorporation of PbSe fQDs into easy-to-handle functional and stable jet electrospun poly(methyl methacrylate) (PMMA) fibers. Within these electrospun nanocomposites, we find perpendicularly aligned stacks of PbSe fQDs, which give rise to a narrowed and bathochromically shifted photoluminescence (*e.g.*, at 1073 nm, with a quantum yield of 5%) that is caused by an energy transfer into the smallest band gap tail of the PbSe fQD thickness distribution. Embedding PbSe fQDs into solid-state nanocomposite fibers represents an important step forward for implementing near-infrared (NIR)-emitting 2D PbX nanocrystals in fiber optics.

8.2 Introduction

Colloidal semiconductor nanocrystals (NCs) are highly valued for their unique size-tunable properties, while being easy to synthesize, modify and process in solution.[1,2] In particular, two-dimensional (2D) nanoplatelets (NPLs) and nanosheets with a thickness of a few monolayers (ML) exhibit highly interesting photophysics different from their 0D NC counterparts.[3,4] For instance, 2D CdSe NPLs[5,6] have received significant recognition due to their efficient,[7] color pure[8] and directed[9] photoluminescence (PL) throughout the visible range, and consequently have prompted the concurrent exploration of near-infrared (NIR) photo-luminescent 2D NCs, such as lead[10–12] and mercury[13,14] chalcogenides. Among NIR-emitters, 2D lead chalcogenide PbX (X = S, Se and Te) NPLs[10,15–17] and flat quantum dots (fQDs)[18] stand out as a material class with large bulk exciton Bohr radii a_B (PbS, 20 nm; PbSe, 46 nm; PbTe, ~82 nm)[19,20] and interesting properties when forced into the strong confinement regime ($x, y/a_B < 1$ and $z/a_B \ll 1$).[21–23] For example, ultrathin 2D PbS NPLs exhibit linearly polarized, blinking-free emission (at ~681 nm) with a significantly narrower linewidth than their spherical counterparts at low temperatures (down to 0.6 meV with a polarization degree of 0.9).[24] When using PbSe fQDs rather than CdSe or PbS NPLs, the low-

loss transmission windows of optical fibers located further into infrared at ~850 nm, ~1350 nm and ~1550 nm[25] can be covered.[15,18,26] 2D PbSe fQDs exhibit efficient PL at NIR to short-wave infrared wavelengths (860 – 1550 nm, with up to 61% quantum yield (QY))[26] and thus have the potential to be used as nano-sized light sources in optical fibers, either as classical emitters (*e.g.*, to periodically reamplify a signal that is transmitted through a fiber)[25,27] or as quantum emitters for emerging quantum information science.[28] However, colloidal PbSe fQDs (similar to most colloidal NCs in general) face an inherent discrepancy between their finely dispersed colloidal state in solution and the demands of predominantly solid-state applications. Therefore, efficient methods are needed to fabricate macroscopic functional nanocomposites from colloidal NCs. Common strategies for bridging this gap include depositing colloidal solutions of PbX NCs (or NCs in general) in thin films *via* drop-casting (and doctor-blading),[29] spin coating,[30] spray coating,[31] or dip coating,[30] and layer-by-layer deposition in conjunction with polymers.[32,33] Films produced like this have been used as, or have been further processed into, field-effect transistors (ionic ligand passivated PbSe QDs)[29], photodetectors (I^--capped PbSe NPLs synthesized *via* cation exchange from CdSe NPLs)[31] and solar cells (metal halide passivated PbS and PbSe QDs).[30] More specialized manufacturing options for bringing colloidal NCs into solid-state are, *e.g.*, ink-jet printing[34] or embedding colloidal NCs into electrospun polymer fibers.[35–38] For the latter, Liu *et al.* have reported the incorporation of CdSe/ZnS core-shell QDs into disordered electrospun fibers consisting of a polymeric photoresist and have demonstrated their potential as waveguiding structures.[37] However, an advanced operating mode of electrospinning is stable jet electrospinning (SJES), which allows producing a few micrometers thin, highly aligned unidirectional fibers with macroscopic length scales.[39,40] With this approach, the chaotic whipping of the spun fiber that is inherent to conventional electrospinning is prevented by adjusting the viscoelastic properties of the spinning solution. In particular, the polymer concentrations and molecular weight must be high enough to achieve the overlap concentration. Typically, the solutions then exhibit non-Newtonian viscoelastic behaviour.[41,42] By adding organic dye molecules[42,43] or inorganic nanocrystalline emitters[36,43] to the polymer solution used for SJES, functional composite microfibers can be fabricated *via* a straight-forward yet versatile and cost-efficient approach. The obtained inorganic-organic

(or organic-organic) composite fibers are easy to handle and possess the optical functionality of the embedded emitters, which makes them highly interesting for telecommunication applications, waveguiding and solid-state fiber lasing.[36,42] We previously embedded green light-emitting (512 nm) colloidal 2D CdSe/CdS core-crown NPLs (4.5 ML) into SJES fibers and have found an unexpected perpendicular alignment of the 2D NPLs relative to the fiber. This orientation is beneficial for light harvesting and guiding light along the fiber direction and was found to be caused by normal forces that occur when the viscoelastic spinning solution leaves the spinneret nozzle due to die swell of the polymer.[36,44] As a consequence, SJES not only represents an advanced method for integrating colloidal NCs into solid state form but also offers a way to control their orientation by carefully adjusting the rheological properties of the spinning solution *via* its composition and polymer characteristics, as well as the spinning parameters. However, to the best of our knowledge, nanocomposite (SJES) fibers with similar characteristics containing nanocrystalline emitters with PL at technologically relevant NIR wavelengths, have not yet been demonstrated, despite their potential for (quantum) optical applications.

Here, we report on the incorporation of NIR-emissive 2D PbSe fQDs into poly(methyl methacrylate) (PMMA) fibers *via* stable jet electrospinning. The fibers are well-defined with a smooth surface and unidirectional alignment, while exhibiting the narrow and efficient NIR PL of the embedded PbSe fQDs, *e.g.*, at 1073 nm with a fwhm of 185 meV and a PLQY of 5%. Small-angle X-ray scattering reveals that the fQDs are arranged within the fibers such that individual fQDs are stacked in vertical columns, which are then oriented perpendicular to the fiber direction. Contextualizing these findings within a previously derived alignment mechanism driven by the die swell of the polymer advances the understanding of SJES for obtaining solid-state nanocomposites containing macroscopically ordered anisotropic fQDs. The PbSe fQD stack formation results in a bathochromic shift and narrowing of the PL due to energy transfer into the smaller band gap tail of the fQD thickness distribution.

8.3 Results and Discussion

Figure 8.1a and b respectively depict an overview and a high-magnification TEM image of PbSe fQDs, which were synthesized from lead oleate and selenourea by using a method described previously.[15,18,26] PbSe fQDs used here exhibit average lateral dimensions of (4.6 ± 0.9) nm x (3.5 ± 0.6) nm and a corresponding aspect ratio of 1.3 : 1, which is in perfect agreement with reported values (see Figure S 8.1a for a lateral size histogram). The higher-magnification micrograph (Figure 8.1b) reveals the lattice fringes of the individual PbSe fQDs, confirming their highly crystalline nature and cubic rock salt structure (see Figure S 8.1b for a corresponding FFT pattern of a single fQD). The rather low contrast in TEM, compared to conventional spherical QDs, points toward the ultrathin geometry of the fQDs, which has been characterized by scanning tunneling microscopy. We have probed distinct, atomic-layer-defined thicknesses corresponding to monolayered, bilayered and trilayered PbSe fQDs (see Figure S 8.2 for height/thickness measurements).[18]

Stable jet electrospinning was performed to embed the shown PbSe fQDs into PMMA fibers (Figure 8.1c). The spinning solution was prepared by dissolving 35 wt% PMMA in 2-butanone,[36,42] which was subsequently mixed with 0.6 – 1.8 wt% PbSe fQDs dispersed in toluene (relative to the PMMA amount). Figure 8.1c displays a schematic representation of the SJES setup (see Figure S 8.3 for a photograph of the custom-built system). To spin the fibers, an electric field of 30 kV was applied between the steel needle of a syringe, mounted on an automated pump, and a rotating drum collector. The final hybrid microfibers were collected between layers of aluminum foil (see Figure S 8.4 for a photograph). Figure 8.1d and e show SEM images of 1.2 wt% PbSe fQD-containing SJES PMMA fibers. With this PbSe fQD concentration, the parallel aligned fibers show a smooth surface and a rather narrow size distribution, with an average diameter of 20.3 ± 2.8 μm (see Figure S 8.5 for SEM images of fibers containing 0.6 and 1.8 wt% PbSe fQDs). Likewise, the lowest concentration of 0.6 wt% PbSe fQDs results in fibers with a uniform and even surface [d = 21.9 ± 3.4 μm], which is essential for minimizing surface-roughness scattering losses when guiding light through the fibers, *e.g.*, in telecommunication applications.[45,46] These well-defined composite fibers exhibit a ribbon-like cross section (see Figure S 8.6), which is consistent with previous

studies on purely organic PMMA SJES fibers without any emitters,[42] and is presumably related to the drying process of freshly spun fibers.[47,48]

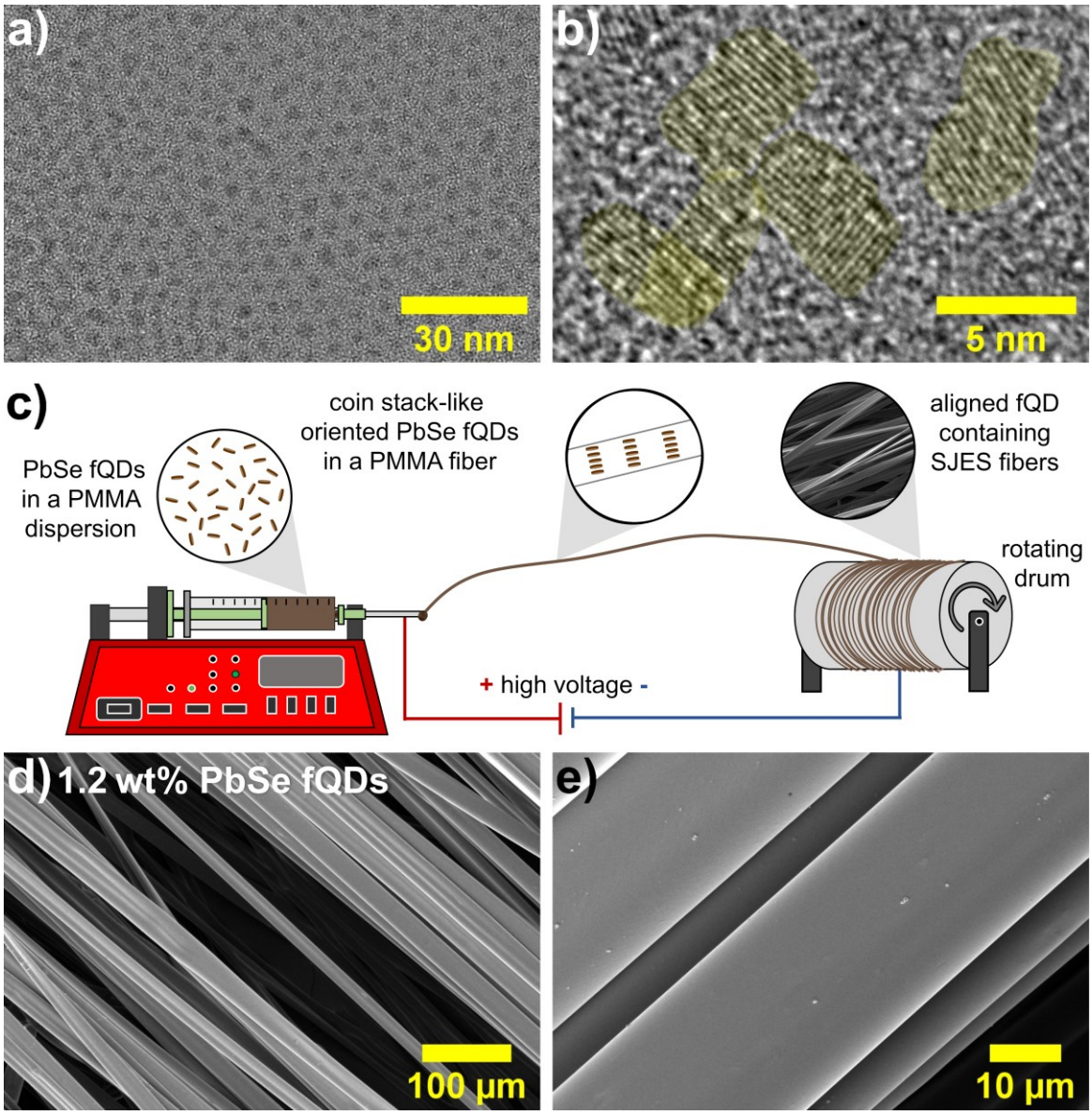

Figure 8.1. (a, b) TEM images of PbSe fQDs with an average lateral dimension of 4.6 ± 0.9 nm x 3.5 ± 0.6 nm and a slightly rectangular shape (aspect ratio = 1.3 : 1). (c) Schematic representation of the stable jet electrospinning method used to produce PbSe fQD-containing SJES PMMA fibers. (d, e) SEM images of SJES PMMA fibers containing 1.2 wt% PbSe fQDs. The resulting fibers are highly aligned and evenly shaped, with a smooth surface and an average diameter of (20.3 ± 2.8) µm.

In contrast, adding a high concentration of 1.8 wt% PbSe fQDs to the PMMA spinning solution leads to fibers with a compromised morphology, showing branching between irregularly shaped domains (Figure S 8.5c and d). Accordingly, we consider the upper limit of PbSe fQD concentration that can be added to obtain structurally intact SJES fibers to be 1.8 wt% or lower. Notably, the studied concentration range (0.6 – 1.8 wt%) is considerably higher than all concentrations reported previously by us for SJES fibers containing 2D CdSe/CdS core-crown NPLs (0.003 – 0.3 wt%), and it highlights not only the versatility of the approach, but also the robustness of stable jet electrospinning for embedding different colloidal NC systems.[36] In the final fibers, the PMMA matrix fully encapsulates the pristine PbSe fQDs (*i.e.*, without post-synthetic surface passivation), so that the obtained nanocomposite fibers are highly stable under environmental conditions and can be easily handled for further investigation or processing *e.g.* by simply cutting out pieces from a fiber mat using scissors. To test the optical functionality of the produced PbSe fQD-containing fibers, we conducted absorption and PL and PL quantum yield measurements on fiber samples and the initial colloidal PbSe fQDs.

Figure 8.2 shows absorption and PL spectra of colloidal PbSe fQDs (blue) and PbSe fQD-containing SJES fibers (red); their optical characteristics are listed in Table 8.1. The initial colloidal PbSe fQDs exhibit excitonic absorption at ~941 nm and PL centered at 1033 nm (STOKES shift of ~130 meV), with a fwhm of ~275 meV as well as a PL quantum yield of 18%, which is representative of previous measurements of as-synthesized oleic acid/octylamine passivated PbSe fQDs.[26] In previous work, we describe that the ensemble PL of PbSe fQDs is governed by three contributions which correspond to the aforementioned monolayer, bilayer and trilayer PbSe fQD populations.[18] For the fQDs used here, which were processed into fibers within a few days after the synthesis (*i.e.*, without significant aging), the PL is expected to be dominated almost entirely by bilayer PbSe fQDs (lateral dimensions of ~4.6 nm x 3.5 nm with a thickness of 1.2 nm), with minor contributions from monolayers and trilayers, causing the ensemble PL to deviate slightly from a symmetric GAUSSIAN shape.

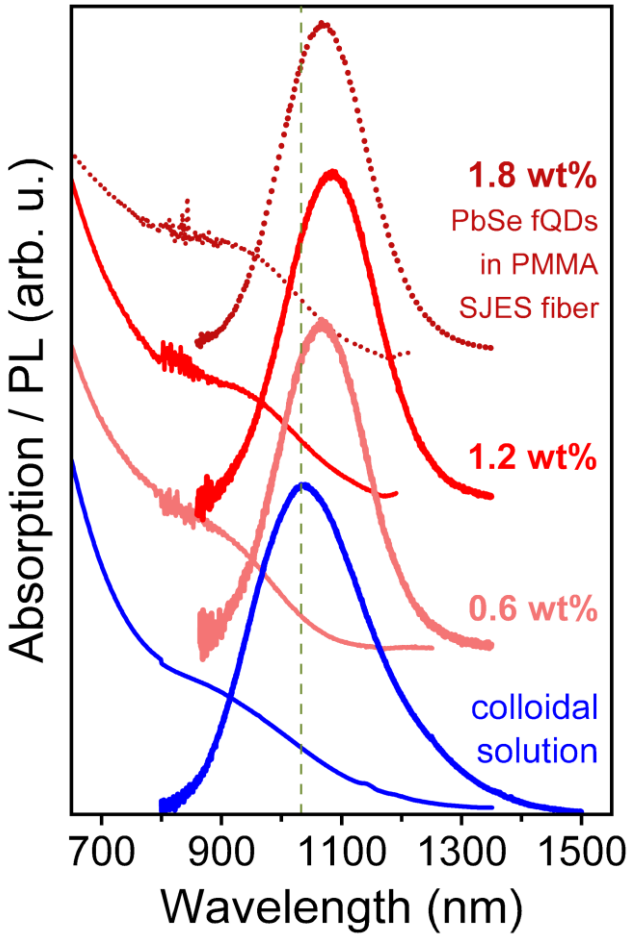

Figure 8.2. NIR absorption and PL spectra of PbSe fQDs in solution (blue) and in PMMA SJES fibers (red). PbSe fQDs in solution exhibit efficient PL at 1033 nm with a PLQY of 18%, which is retained in the fibers and accompanied by a bathochromic shift to 1070 – 1085 nm and a PLQY of 3 – 6%.

Table 8.1. Excitonic absorption λ_{Abs} (based on the local minimum of the 2nd derivative of the absorption), PL position λ_{PL}, STOKES shift, fwhm of the PL and PLQY of colloidal PbSe fQDs and PbSe fQD-containing PMMA SJES fibers.

sample	λ_{Abs} (nm)	λ_{PL} (nm)	STOKES shift (meV)	PL fwhm (meV)	QY (%)
colloidal PbSe fQDs	941	1033	130	275	18
0.6 wt% fQD fiber	916	1073	198	185	5
1.2 wt% fQD fiber	935	1085	183	190	3
1.8 wt% fQD fiber	939	1070	162	186	6

Regarding the fiber measurements, notably, the optical properties of the 2D PbSe fQDs are retained without any drastic changes for all three nanocomposite samples, which is a prerequisite for any fiber optical application. In detail, the PL of the fibers is bathochromically shifted compared to the colloidal fQDs, with maxima at 1073 nm and 1085 nm for the 0.6 wt% (light red) and 1.2 wt% PbSe-containing fibers (red), respectively. The PL of the 1.8 wt% fibers (dark red, dotted) is shifted to 1070 nm; however, due to their irregular shapes and rough fiber surfaces, this sample is disregarded in the following (see Figure S 8.5c and d). The absorbance features of the fibers are slightly hypsochromically shifted to ~916 and ~935 nm with respect to the colloidal fQDs, the fwhm of the fiber PL spectra is decreased by ~100 meV, and the PLQY is reduced to 5% and 3%, respectively (see Table 8.1). The decrease in PLQY by a factor of ~0.22, from 18% to ~4%, upon embedding the fQDs into the PMMA fiber is consistent with values typically reported for the incorporation of core-only NCs into polymers[33,49] or their deposition into solid-state thin films,[50,51] and has been ascribed to changes in the NCs' surface chemistry exposing previously saturated surface trap states.[52] This may be overcome in future work by stabilizing the optical properties of PbSe fQDs through additional ligand passivation, for example with a polymer-compatible surface ligand,[52] and/or by shelling,[53–55] prior to incorporation into the polymer matrix. The bathochromic PL shift (from 1033 nm to 1073 and 1085 nm) and the thereby increased STOKES shift (from ~130 meV to 198 and 183 meV), as well as the change to more symmetric GAUSSIAN PL linewidths in PbSe fQD-containing fibers, may be attributed to energy transfer between fQDs that are spatially closer to each other and fixed locally in the polymer matrix, compared to the colloidal solution. VOZNYY *et al.* reported on a concentration-dependent energy transfer in colloidal 0D PbS QD ensembles, whereby charge carriers funnel into the lowest-energy tail of the QD distribution, thus increasing the apparent STOKES shift with higher QD concentration.[56] In the case of the PbSe fQDs studied here, this could be energy transfer from monolayer to bilayers/trilayers and bilayers to trilayers, as well as to laterally larger PbSe fQDs within a given thickness population. Similar energy transfers have been thoroughly studied for coupled QD films,[57,58] and are amplified by long photoluminescence lifetimes and spatial proximity of (f)QDs (*e.g.*, due to agglomeration in colloidal solution or stacking in solid state).[56] For example, ROWLAND *et al.* and GUZELTURK *et al.* have demonstrated efficient homo-

fluorescence resonance energy transfer in ordered stacks of 2D CdSe NPLs in which the spatial separation between donor and acceptor is minimized.[59–63] PbSe fQDs typically exhibit rather long PL lifetimes in the range of 1 – 2 μs[12,15,26] and we have previously observed the formation of stacked superlattices with short interparticle distances of ~0.5 nm for colloidal PbS and PbTe NPLs (chloride/iodide-passivated) when depositing them as thin films.[10,24] Consequently, energy transfer between PbSe fQDs (stacked or randomly oriented in close proximity) in the fiber is possible and assumed as an additional reason for the lowered PLQY in the fibers, as charge carriers can be transferred to defective fQDs.[60] It is important to note that this type of energy transfer does not preclude the possibility of the fQDs' surface chemistry changing simultaneously, thereby causing shifts of their optical features when they are encapsulated in the polymer, as discussed in the context of PLQY.

To gain insight into the relative orientation and the spacing of the PbSe fQDs within the fibers, specifically the possible presence of stacks of PbSe fQDs, we have performed 3D single-particle excitation polarization microscopy (Figure 8.3) and X ray diffraction (Figure 8.4), which are possible due to the comparatively high PbSe fQD concentrations used.

Figure 8.3a shows polar plots of the radiation patterns of single PbSe fQDs and reference individual 4.5 ML CdSe/CdS core-crown NPLs in SJES PMMA fibers. CdSe NPL-containing SJES fibers were produced as described in reference [36]. In brief, the 2D CdSe/CdS NPLs exhibit a lateral size of ~47 nm x 12 nm x 1.2 nm, meaning that their 2D geometry is much more pronounced than in PbSe fQDs (~4.6 nm x 3.5 nm x 1.2 nm), which are confined in all three dimensions (with particular strong confinement in the thickness).[18,36] Regardless of the smaller lateral dimensions in PbSe fQDs, we observe a clear variation in the PL intensity of PbSe fQDs, depending on the polarization excitation light (see Figure 8.3b), which suggests an anisotropic dipole distribution in PbSe fQDs, different from that of (quasi-)spherical QDs.[36] However, this variation is considerably lower than has been observed for CdSe/CdS NPLs, for which the in-plane dipole distribution leads to highly directional PL orthogonal to the NPLs' plane.[9,36] Notably, with 3D single-particle excitation polarization microscopy, we only probe individual PbSe fQDs that are not part of a closely packed stack. Therefore, unlike in our previous work on CdSe/CdS NPLs,[36] it is not possible to draw conclusions about the presence (and

possible orientation) of PbSe fQDs inside the SJES PMMA fibers based on optical measurements alone, which is why we have conducted X-ray diffraction experiments.

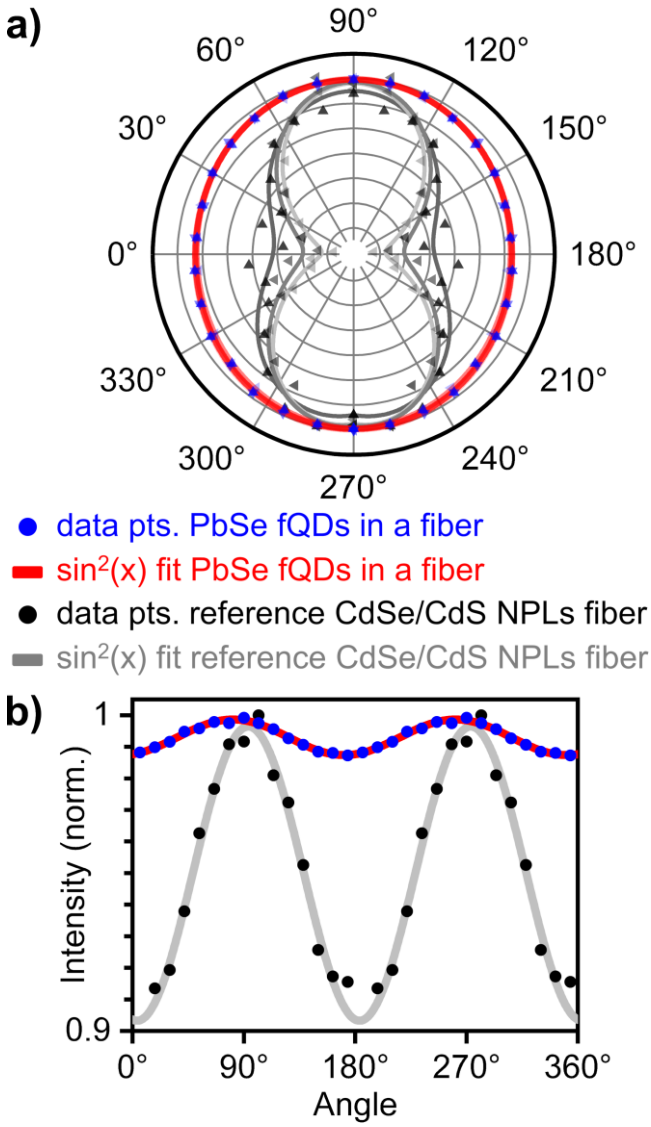

Figure 8.3. 3D single-particle excitation polarization microscopy measurements. (a) Polar plots of the radiation pattern of PbSe fQDs (0.6 wt%) and CdSe NPLs (0.03 wt%) inside a SJES PMMA fiber fitted with a $\sin^2(x)$ function (average of 10 analyzed particles). The NPLs/fQDs were excited from three different angles (0°, 120°, and 240°) to ensure excitation of all NPLs/fQDs at the focus point of the objective (shown in three shades of grey for CdSe NPLs; for PbSe fQDs all three red lines overlap). (b) Corresponding averaged $\sin^2(x)$ amplitudes.

Figure 8.4 depicts X-ray diffraction patterns of 0.6 to 1.8 wt% PbSe fQD-containing SJES PMMA fibers (see Figure S 8.8a for an in-depth description of the 1.8 wt% fiber). All three fiber samples exhibit an anisotropically shaped scattering signal at $q = \sqrt{{q_x}^2 + {q_y}^2} \approx 1.26$ nm^{-1}, indicating the presence of stacks of PbSe fQDs oriented perpendicular to the fiber axis (Figure 8.4a,c,e as well as Figure S 8.9a–c; see Figure S 8.10 for X-ray diffraction patterns of complementary drop-casted PbSe-polymer samples containing randomly oriented stacks for comparison).

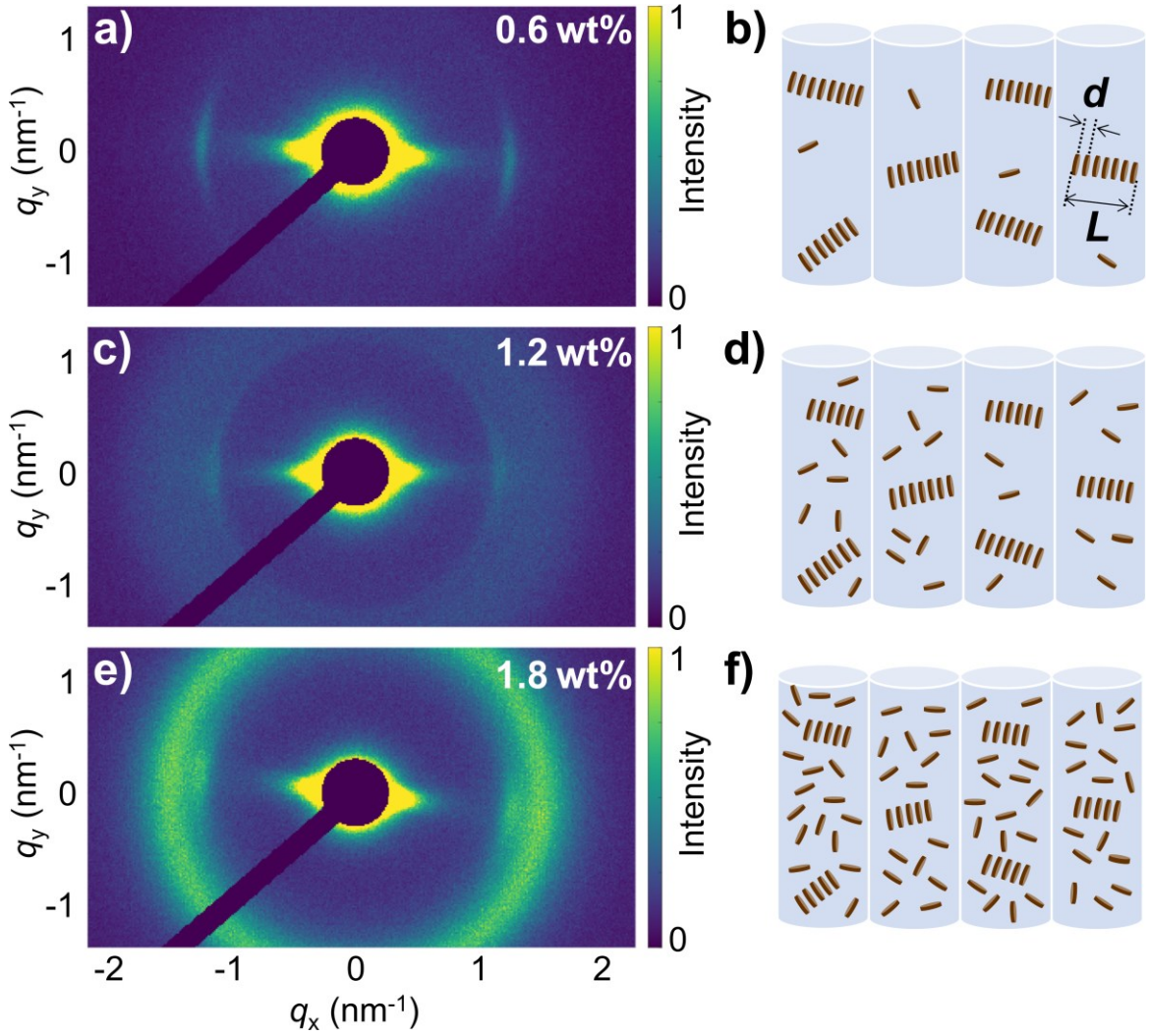

Figure 8.4. X-ray diffraction experiments conducted on PbSe fQD-containing SJES PMMA fibers. (a, c, e) 2D diffraction patterns of fibers with a PbSe fQD mass fraction of 0.6 wt% (a), 1.2 wt% (c), and 1.8 wt% (e). (b, d, f) Schematic representation of the arrangement of the PbSe fQDs inside the PMMA fibers.

The distance between the PbSe fQDs within a stack can be estimated as $d = 2\pi/q$ = 5.0 ± 0.2 nm (Figure 8.4b,d,f, as well as Figure S 8.8b), which is in good agreement with the expected center-to-center distance of stacked 1.2 nm thick fQDs/NPLs separated by oleic acid ligands.[64] The angular width of the peak at 1.26 nm^{-1} is ~25 ± 5° for all three mass fractions (see Figure S 8.9d–f), indicating a high degree of orientational order of the stacks perpendicular to the PMMA fiber. From a single fQD point of view, this observation differs strikingly from our previous report on the perpendicular orientation of individual CdSe NPLs in SJES PMMA fibers, since each individual PbSe fQD in the present configuration is oriented parallel to the fiber direction.[36] However, considering the small dimensions of the PbSe fQDs (~4.6 nm x 3.5 nm x 0.6 – 1.8 nm) and the dimensions of the formed stacks, it is evident that the same mechanism that vertically aligns CdSe/CdS NPLs can result in a seemingly different arrangement for significantly smaller 2D fQDs: The length of the stack is estimated from the radial width of the scattering peak as $L = 2\pi/\Delta q$ and decreases from approximately L = 65 nm for 0.6 wt% to 40 nm for 1.8 wt%. This means that the rod-like shaped stacks of PbSe fQDs (see Figure 8.4b,d,f) exhibit dimensions similar to those of larger individual CdSe/CdS NPLs, and that they show similar behavior when stable jet electrospun with PMMA. We assume that the PbSe fQDs prestack in the spinning solution (a process that is further promoted by the generally high fQD mass fractions used in this work, see Figure S 8.10) with the stacks being randomly oriented within the likewise randomly coiled PMMA chains in solution. At the same time, in the spinneret nozzle the coiled polymer chains become stretched into the flow direction due to the velocity gradient, equally causing the PbSe fQD stacks to orient in the same direction. Upon leaving the nozzle, the polymer chains recoil, inducing a normal force (die swell), that reorients the fQD stacks into an upright orientation perpendicular to the fiber direction.[44] In this orientation, in turn, each individual PbSe fQD is then oriented parallel to the fiber. For larger PbSe fQD weight fractions, a broad uniform ring emerges in the scattering patterns at $q \approx 1.6$ nm^{-1} (Figure 8.4c,e, as well as Figure S 8.8a and Figure S 8.9b,c), corresponding to the appearance of individual PbSe fQDs with no preferred orientation. These findings highlight that the comparatively small single PbSe fQDs cannot be oriented by the polymer and that a higher aspect ratio (as in NPLs) is needed for the normal forces to induce a rotation into an upright position, as is the

case for the stacks of PbSe fQDs or individual CdSe/CdS NPLs. These single randomly oriented PbSe fQDs correspond to the ones observed in 3D single-particle excitation polarization microscopy measurements shown in Figure 8.3.

The stack formation revealed by X-ray scattering underpins the discussed assumption that energy transfer between spatially close PbSe fQDs is the reason for the apparent shift of their PL inside the fibers, compared to that of their initial colloidal state in solution. Since this effect not only shifts the PL to higher wavelengths/lower energies, but is also accompanied by a narrowing of the PL signal, it may be leveraged to tailor the optical properties of the nanocomposite fibers to the 2nd and 3rd telecommunication windows at ~1350 and ~1550 nm in the future.

8.4 Conclusion

To conclude, we have demonstrated the incorporation of NIR-emissive colloidal 2D PbSe fQDs into stable jet electrospun PMMA fibers. The obtained functional nanocomposite fibers are unidirectionally aligned, have a smooth surface and possess the optical properties of the embedded PbSe fQDs. For fibers containing 0.6 wt% PbSe fQDs, we measured narrow PL at 1073 nm (fwhm 185 meV) with a quantum yield of 5%, rendering them highly interesting for classical and quantum communication applications. X-ray scattering revealed that the PbSe fQDs in the fibers are distributed in a quasi-hierarchical structure made of stacks of individual fQDs, which are oriented perpendicular to the fiber direction due to die swelling during the SJES process. Within the stacks of PbSe fQDs, the energy transfer toward the smallest band gap tail of the fQD thickness/size distribution results in hybrid fibers with a PL that is narrower than that of their colloidal PbSe fQD building blocks. Our findings underscore the potential of SJES for producing functional hybrid materials and are an important step in developing easy-to-handle solid state nanocomposites with PL at technologically relevant NIR wavelengths.

8.5 Experimental Section

Chemicals. Acetonitrile (≥ 99.5%), ethanol (EtOH, max. 0.01% H_2O), *iso*-propanol (≥ 99.5%), lead(II) oxide (≥ 99.99%), methanol (≥ 99.8%), *n*-octylamine (99%), tetrachloroethylene (TCE, ≥ 99%), triethylamine (≥ 99%), trifluoroacetic acid (99%), and trifluoracetic anhydride (≥ 99%) were purchased from SIGMA-ALDRICH/MERCK. 2-Butanone (> 99%) and *n*-hexane (97%) were purchased from ACROS ORGANICS. Oleic acid (90%) was purchased from ABCR. Selenourea (99.97%) was purchased from ALFA AESAR. Poly(methyl methacrylate) (PMMA-8N, 83000 g/mol) was purchased from RÖHM GMBH. *n*-Octylamine and oleic acid were degassed by freeze-pump-thawing prior to being stored and handled inside a N_2-filled glove box. All other reagents were used as received from the listed suppliers.

PbSe Flat Quantum Dot Synthesis. Colloidal PbSe fQDs were synthesized by a method previously described by us.[15,18,26] The lead oleate used was synthesized *via* an established protocol by HENDRICKS *et al.*[65] First, a solution of selenourea (193 mg, 1.57 mmol) in octylamine (2.03 ml), oleic acid (0.23 ml), and hexane (0.75 ml) was prepared and stirred at 35°C for at least two days prior to the fQD synthesis. To synthesize the PbSe fQDs, lead oleate (1.83 mg, 2.7 mmol) was dissolved in a mixture of octylamine (2 ml), oleic acid (4 ml), and hexane (18 ml) at 35°C. After complete dissolution (~5 min), the sealed mixture was cooled to 0°C using an ice bath. The selenourea solution (2.5 ml) was then quickly injected into the vigorously stirred lead oleate mixture. After 10 min of reaction time, the dark brown reaction mixture was quenched by the addition of dry EtOH (18.5 ml). To purify the already destabilized PbSe fQDs, dry EtOH was added dropwise until a precipitate formed at the bottom of the flask. This mixture was then centrifuged at 2500 rcf, the supernatant was discarded, and the precipitate was redispersed in dry toluene (10 ml). This process was repeated two more times before sealing and storing the purified PbSe fQDs under N_2 atmosphere. All steps of the PbSe fQD synthesis, except for cooling, were performed under inert gas conditions in a N_2-filled glove box.

Stable Jet Electrospinning of PbSe fQD-containing PMMA Fibers. SJES was performed using a custom-built electrospinning setup (see Figure S 8.3 for a photograph of the setup and details about its components). The spinning

solution was prepared by stirring 35 wt% of PMMA in 2-butanone for 24 h at room temperature, resulting in a clear, viscous solution. Then, PbSe flat quantum dots dispersed in toluene were added at varying concentrations (0.6 – 1.8 wt% of Pb) and ultrasonicated for 10 min prior to spinning. For SJES, 4 mL of the PMMA/fQD dispersion was loaded into a syringe equipped with a stainless-steel needle (inner diameter of 0.8 mm) and mounted on an automated syringe pump. The rotating drum collector, which was covered in aluminum foil to make fiber removal easier, was placed 30 cm from the needle tip inside the SJES chamber. Prior to spinning, nitrogen was used to flush the chamber atmosphere to maintain a relative humidity of approximately 10%. A +15 kV voltage was applied to the steel needle and a voltage of -15 kV was applied to the drum collector, resulting in a total potential difference of 30 kV across the spinning gap. The solution flow rate was kept at 25 mL/h, and the drum collector was rotated at 2000 rpm to improve fiber alignment. All parameters were kept constant across experiments. After each spinning run, the chamber was flushed with nitrogen for 15 min to remove any residual organic solvent vapors.

Transmission Electron Microscopy. TEM images were obtained using a FEI TECNAI G2 F20 transmission electron microscope with a field emission gun operating at 200 kV. For this, the colloidal PbSe fQDs were crop-cast onto carbon-coated copper grids (300 mesh) from QUANTIFOIL. The average lateral size of the PbSe fQDs was determined using the IMAGEJ software.

Scanning Electron Microscopy. To image the fiber surfaces, a 1 cm x 1 cm section was cut from the electrospun fiber mat and mounted on an aluminum SEM sample carrier using conductive adhesive carbon tape. To obtain cross-sectional images, another 1 cm x 1 cm fiber sample was placed between two layers of carbon tape and immersed in liquid nitrogen for 1 min. The frozen sample was then broken at the midpoint between the tapes to expose the cross-section, after which it was mounted on a sample carrier. To improve conductivity, all samples were sputter-coated with a thin layer of gold using a LEICA SCD050 sputter coater (from LEICA MICROSYSTEMS). SEM images were captured using a combined system consisting of a ZEISS EVO LS 25 and BRUKER EVO system at magnifications ranging from 500x to 35000x. The average diameter of the electrospun fibers was determined using the IMAGEJ software. For each sample, SEM images acquired at different locations and orientations were measured using manual line profiling across well-resolved

fibers (sample size n = 40) and the values were then averaged to obtain the mean fiber diameter.

NIR Photoluminescence and UV-Vis-NIR Absorption Spectroscopy. Near-infrared photoluminescence spectra were acquired using an EDINBURGH FLS 1000 UV-Vis-NIR spectrometer equipped with a 450 W ozone-free xenon arc lamp for excitation. The PL was monitored using an InGaAs NIR photomultiplier tube (Model 1650 detector cooled with liquid N_2) from EDINBURGH INSTRUMENTS. Colloidal samples for optical ensemble spectroscopy were prepared by diluting the colloidal PbSe fQD solutions in TCE (with an optical density below 0.2 at 500 nm) in a quartz cuvette (quartz glass, high-performance Model QS 200 – 2500 nm, with an optical path length of 1 cm by HELLMA). For fiber samples, a 3 cm × 1 cm was cut from the electrospun fiber mat and placed on the solid sample holder of the FLS 1000. Absolute PLQYs were determined using an integrating sphere with the FLS 1000. For this, the scattering at 450 nm and the PL in the NIR of TCE or a blank PMMA fiber sample and the fQDs or PMMA/fQD fibers, respectively, were measured separately, accounting for the difference in sensitivity of both detectors with a correction factor. UV-Vis-NIR absorption spectra were collected using a double beam CARY 5000 spectrophotometer from AGILENT TECHNOLOGIES equipped with a tungsten halogen (Vis) and deuterium arc (UV) lamp and a PbSmart NIR detector for monitoring. For fiber samples, an integrating sphere (diffuse reflectance accessory from AGILENT TECHNOLOGIES) was used. The absorption maxima/shoulders were determined by the local minima of the second derivative of the smoothed absorption (locally estimated scatterplot smoothing). The increased noise present in all absorption spectra around 800 nm stems from the NIR detector changes at this wavelength

Excitation Polarization Microscopy. For 3D excitation polarization microscopy, PbSe fQD-(0.6 wt%) and CdSe NPLs-containing (0.03 wt%) PMMA SJES fibers were placed between a microscope slide and a cover slip and fixated using NORLAND optical adhesive 148 glue (NORLAND PRODUCTS). The NCs were excited using a COHERENT CHAMELEON ULTRA II laser that generates 900 nm light, which was frequency-doubled to 450 nm using a β-BaB_2O_4 crystal (THORLABS). The beam was broadened using a lens system and the polarization of the laser beam was rotated using a rotating half-wave plate (achromatic $\lambda/2$ plate, 400 – 800 nm, THORLABS). Sending the beam through a rotatable wedge prism (4° beam deviation,

375 – 700 nm, THORLABS), allowed entering the back aperture of the objective (NA = 1.35, oil immersion, UPlanApo, 60x, OLYMPUS) from three different positions, thus hitting the sample from three different angles. The emitted light passed through a dichroic mirror (SP 556, AHF) and onto an electron-multiplying charge-coupled device camera (iXonEM +897, back-illuminated, ANDOR TECHNOLOGY). Consequently, the intensity of the radiation pattern is a function of the excitation angle. It is important to note that this method only analyzes individual fQDs: stacks are not taken into account.

Small-Angle X-ray Scattering. X ray diffraction experiments were performed using a XEUSS 2.0 instrument with a copper anode. The diffraction patterns from the vertically aligned fibers were recorded by a PILATUS 300K detector in transmission geometry. The X-ray beam was focused to approximately 1.2 µm x 1.2 µm. The direct beam was covered with a beam stop.

8.6 References

(1) Houtepen, A. J.; Sargent, E. H.; Infante, I.; Owen, J. S.; Green, P. B.; Schaller, R. D.; Bals, S.; Zeiske, S.; Stöferle, T.; Hens, Z. Colloidal Quantum Dots for Optoelectronics. *Nat. Rev. Methods Primers.* **2025**, *5* (1), 1–29.

(2) Ibáñez, M.; Boehme, S. C.; Buonsanti, R.; Roo, J. de; Milliron, D. J.; Ithurria, S.; Rogach, A. L.; Cabot, A.; Yarema, M.; Cossairt, B. M.; Reiss, P.; Talapin, D. V.; Protesescu, L.; Hens, Z.; Infante, I.; Bodnarchuk, M. I.; Ye, X.; Wang, Y.; Zhang, H.; Lhuillier, E.; Klimov, V. I.; Utzat, H.; Rainò, G.; Kagan, C. R.; Cargnello, M.; Son, J. S.; Kovalenko, M. V. Prospects of Nanoscience with Nanocrystals: 2025 Edition. *ACS Nano* **2025**, *19* (36), 31969–32051.

(3) Nasilowski, M.; Mahler, B.; Lhuillier, E.; Ithurria, S.; Dubertret, B. Two-Dimensional Colloidal Nanocrystals. *Chem. Rev.* **2016**, *116* (18), 10934–10982.

(4) Diroll, B. T.; Guzelturk, B.; Po, H.; Dabard, C.; Fu, N.; Makke, L.; Lhuillier, E.; Ithurria, S. 2D II-VI Semiconductor Nanoplatelets: From Material Synthesis to Optoelectronic Integration. *Chem. Rev.* **2023**, *123* (7), 3543–3624.

(5) Ithurria, S.; Dubertret, B. Quasi 2D Colloidal CdSe Platelets with Thicknesses Controlled at the Atomic Level. *J. Am. Chem. Soc.* **2008**, *130* (49), 16504–16505.

(6) Ithurria, S.; Tessier, M. D.; Mahler, B.; Lobo, R. P. S. M.; Dubertret, B.; Efros, A. L. Colloidal Nanoplatelets with Two-Dimensional Electronic Structure. *Nat. Mater.* **2011**, *10* (12), 936–941.

(7) Tessier, M. D.; Mahler, B.; Nadal, B.; Heuclin, H.; Pedetti, S.; Dubertret, B. Spectroscopy of Colloidal Semiconductor Core/Shell Nanoplatelets with High Quantum Yield. *Nano Lett.* **2013**, *13* (7), 3321–3328.

(8) van der Bok, J. C.; Dekker, D. M.; Peerlings, M. L. J.; Salzmann, B. B. V.; Meijerink, A. Luminescence Line Broadening of CdSe Nanoplatelets and Quantum Dots for Application in w-LEDs. *J. Phys. Chem. C* **2020**, *124* (22), 12153–12160.

(9) Scott, R.; Heckmann, J.; Prudnikau, A. V.; Antanovich, A.; Mikhailov, A.; Owschimikow, N.; Artemyev, M.; Climente, J. I.; Woggon, U.; Grosse, N. B.; Achtstein, A. W. Directed Emission of CdSe Nanoplatelets Originating from Strongly Anisotropic 2D Electronic Structure. *Nat. Nanotechnol.* **2017**, *12* (12), 1155–1160.

(10) Biesterfeld, L.; Vochezer, M. T.; Kögel, M.; Zaluzhnyy, I. A.; Rosebrock, M.; Klepzig, L. F.; Leis, W.; Seitz, M.; Meyer, J. C.; Lauth, J. Solving the Synthetic Riddle of Colloidal Two-Dimensional PbTe Nanoplatelets with Tunable Near-Infrared Emission. *Chem. Mater.* **2024**, *36* (15), 7197–7206.

(11) Khan, A. H.; Pal, S.; Dalui, A.; Pradhan, J.; Sarma, D. D.; Acharya, S. Solution-Processed Free-Standing Ultrathin Two-Dimensional PbS Nanocrystals with Efficient and Highly Stable Dielectric Properties. *Chem. Mater.* **2017**, *29* (3), 1175–1182.

(12) Galle, T.; Samadi Khoshkhoo, M.; Martin-Garcia, B.; Meerbach, C.; Sayevich, V.; Koitzsch, A.; Lesnyak, V.; Eychmüller, A. Colloidal PbSe Nanoplatelets of Varied Thickness with Tunable Optical Properties. *Chem. Mater.* **2019**, *31* (10), 3803–3811.

(13) Tenney, S. M.; Vilchez, V.; Sonnleitner, M. L.; Huang, C.; Friedman, H. C.; Shin, A. J.; Atallah, T. L.; Deshmukh, A. P.; Ithurria, S.; Caram, J. R. Mercury Chalcogenide Nanoplatelet-Quantum Dot Heterostructures as a New Class of Continuously Tunable Bright Shortwave Infrared Emitters. *J. Phys. Chem. Lett.* **2020**, *11* (9), 3473–3480.

(14) Izquierdo, E.; Robin, A.; Keuleyan, S.; Lequeux, N.; Lhuillier, E.; Ithurria, S. Strongly Confined HgTe 2D Nanoplatelets as Narrow Near-Infrared Emitters. *J. Am. Chem. Soc.* **2016**, *138* (33), 10496–10501.

(15) Klepzig, L. F.; Biesterfeld, L.; Romain, M.; Niebur, A.; Schlosser, A.; Hübner, J.; Lauth, J. Colloidal 2D PbSe Nanoplatelets with Efficient Emission Reaching the Telecom O-, E- and S-Band. *Nanoscale Adv.* **2022**, *4*, 590–599.

(16) Manteiga Vázquez, F.; Yu, Q.; Klepzig, L. F.; Siebbeles, L. D. A.; Crisp, R. W.; Lauth, J. Probing Excitons in Ultrathin PbS Nanoplatelets with Enhanced Near-Infrared Emission. *J. Phys. Chem. Lett.* **2021**, *12* (1), 680–685.

(17) Biesterfeld, L.; Vochezer, M.; Rudolph, D.; Lauth, J. Aqueous Phase Near-Infrared Emitters: Water Transfer of Colloidal 2D PbS, PbSe and PbTe Nanoplatelets. *Nanoscale* **2025**, *17*, 24006–24016.

(18) Biesterfeld, L.; Ngo, H. T.; Addad, A.; Rudolph, D. A.; Leis, W.; Seitz, M.; Ji, G.; Grandidier, B.; Delerue, C.; Lauth, J.; Biadala, L. Monolayer-Defined Flat Colloidal PbSe Quantum Dots in Extreme Confinement. *Nano Lett.* **2025**, *25* (31), 12019–12024.

(19) Wise, F. W. Lead Salt Quantum Dots: The Limit of Strong Quantum Confinement. *Acc. Chem. Res.* **2000**, *33* (11), 773–780.

(20) Murphy, J. E.; Beard, M. C.; Norman, A. G.; Ahrenkiel, S. P.; Johnson, J. C.; Yu, P.; Mićić, O. I.; Ellingson, R. J.; Nozik, A. J. PbTe Colloidal Canocrystals: Synthesis, Characterization, and Multiple Exciton Generation. *J. Am. Chem. Soc.* **2006**, *128* (10), 3241–3247.

(21) Ramin Moayed, M. M.; Bielewicz, T.; Zöllner, M. S.; Herrmann, C.; Klinke, C. Towards Colloidal Spintronics Through Rashba Spin-Orbit Interaction in Lead Sulphide Nanosheets. *Nat. Commun.* **2017**, *8* (1), 15721.

(22) Lauth, J.; Failla, M.; Klein, E.; Klinke, C.; Kinge, S.; Siebbeles, L. D. A. Photoexcitation of PbS Nanosheets Leads to Highly Mobile Charge Carriers and Stable Excitons. *Nanoscale* **2019**, *11* (44), 21569–21576.

(23) Aerts, M.; Bielewicz, T.; Klinke, C.; Grozema, F. C.; Houtepen, A. J.; Schins, J. M.; Siebbeles, L. D. A. Highly Efficient Carrier Multiplication in PbS Nanosheets. *Nat. Commun.* **2014**, *5*, 3789.

(24) Li, P.; Biesterfeld, L.; Klepzig, L. F.; Yang, J.; Ngo, H. T.; Addad, A.; Rakow, T. N.; Guan, R.; Rugeramigabo, E. P.; Zaluzhnyy, I.; Schreiber, F.; Biadala, L.; Lauth, J.; Zopf, M. Sub-millielectronvolt Line Widths in Polarized Low-Temperature Photoluminescence of 2D PbS Nanoplatelets. *Nano Lett.* **2024**, *24* (51), 16293–16300.

(25) Harrison, M. T.; Kershaw, S. V.; Burt, M. G.; Rogach, A. L.; Kornowski, A.; Eychmüller, A.; Weller, H. Colloidal Nanocrystals for Telecommunications. Complete Coverage of the Low-Loss Fiber Windows by Mercury Telluride Quantum Dot. *Pure Appl. Chem.* **2000**, *72* (1–2), 295–307.

(26) Biesterfeld, L.; Klepzig, L. F.; Niebur, A.; Rosebrock, M.; Lauth, J. Toward Bright Colloidal Near-Infrared Emitters: Surface Passivation of 2D PbSe Nanoplatelets by Metal Halides. *J. Phys. Chem. C* **2022**, *126* (45), 19277–19285.

(27) Zhu, Z.; Sun, S.; Chai, X.; Gao, J.; Lu, M.; Wu, Z.; Gao, Y.; Feng, T.; Bai, X.; Zhang, Y.; Yan, F.; Yu, W. W.; Ke, C. Quantum Dot-Doped Optical Fibers. *Laser Photonics Rev.* **2024**, *18* (9), 2301388.

(28) Kagan, C. R.; Bassett, L. C.; Murray, C. B.; Thompson, S. M. Colloidal Quantum Dots as Platforms for Quantum Information Science. *Chem. Rev.* **2021**, *121* (5), 3186–3233.

(29) Lin, Q.; Yun, H. J.; Liu, W.; Song, H.-J.; Makarov, N. S.; Isaienko, O.; Nakotte, T.; Chen, G.; Luo, H.; Klimov, V. I.; Pietryga, J. M. Phase-Transfer Ligand Exchange of Lead Chalcogenide Quantum Dots for Direct Deposition of Thick, Highly Conductive Films. *J. Am. Chem. Soc.* **2017**, *139* (19), 6644–6653.

(30) Crisp, R. W.; Kroupa, D. M.; Marshall, A. R.; Miller, E. M.; Zhang, J.; Beard, M. C.; Luther, J. M. Metal Halide Solid-State Surface Treatment for High Efficiency PbS and PbSe QD Solar Cells. *Sci. Rep.* **2015**, *5* (1), 9945.

(31) Galle, T.; Spittel, D.; Weiß, N.; Shamraienko, V.; Decker, H.; Georgi, M.; Hübner, R.; Metzkow, N.; Steinbach, C.; Schwarz, D.; Lesnyak, V.; Eychmüller, A. Simultaneous Ligand and Cation Exchange of Colloidal CdSe Nanoplatelets toward PbSe Nanoplatelets for Application in Photodetectors. *J. Phys. Chem. Lett.* **2021**, *12* (21), 5214–5220.

(32) Suarez, I.; Munoz, R.; Chirvony, V.; Martinez-Pastor, J. P.; Artemyev, M.; Prudnikau, A.; Antanovich, A.; Mikhailov, A. Multilayers of CdSe/CdS/ZnCdS Core/Wings/Shell Nanoplatelets Integrated in a Polymer Waveguide. *IEEE J. Sel. Top. Quantum Electron.* **2017**, *23* (5), 1–8.

(33) Li, F.; Klepzig, L. F.; Keppler, N.; Behrens, P.; Bigall, N. C.; Menzel, H.; Lauth, J. Layer-by-Layer Deposition of 2D CdSe/CdS Nanoplatelets and Polymers for Photoluminescent Composite Materials. *Langmuir* **2022**, *38* (37), 11149–11159.

(34) Sliz, R.; Lejay, M.; Fan, J. Z.; Choi, M.-J.; Kinge, S.; Hoogland, S.; Fabritius, T.; García de Arquer, F. Pelayo; Sargent, E. H. Stable Colloidal Quantum Dot Inks Enable Inkjet-Printed High-Sensitivity Infrared Photodetectors. *ACS Nano* **2019**, *13* (10), 11988–11995.

(35) Tomczak, N.; Gu, S.; Han, M.; van Hulst, N. F.; Julius Vancso, G. Single Light Emitters in Electrospun Polymer Nanofibers: Effect of Local Confinement on Radiative Decay. *Eur. Polym. J.* **2006**, *42* (10), 2205–2210.

(36) Liu, X.; Li, F.; Hohgardt, M.; Klepzig, L. F.; Willich, M. M.; Christ, H.-A.; Schaate, A.; Behrens, P.; Lauth, J.; Menzel, H.; Walla, P. J. Perpendicular Alignment of 2D Nanoplatelet Emitters in Electrospun Fibers: A Result of the Barus Effect? *Macromol. Mater. Eng.* **2023**, *308* (9), 2300027.

(37) Liu, H.; Edel, J. B.; Bellan, L. M.; Craighead, H. G. Electrospun Polymer Nanofibers as Subwavelength Optical Waveguides Incorporating Quantum Dots. *Small* **2006**, *2* (4), 495–499.

(38) Li, M.; Zhang, J.; Zhang, H.; Liu, Y.; Wang, C.; Xu, X.; Tang, Y.; Yang, B. Electrospinning: A Facile Method to Disperse Fluorescent Quantum Dots in Nanofibers without Förster Resonance Energy Transfer. *Adv. Funct. Mater.* **2007**, *17* (17), 3650–3656.

(39) Carnell, L. S.; Siochi, E. J.; Holloway, N. M.; Stephens, R. M.; Rhim, C.; Niklason, L. E.; Clark, R. L. Aligned Mats from Electrospun Single Fibers. *Macromolecules* **2008**, *41* (14), 5345–5349.

(40) Zhang, Y. Z.; Su, B.; Ramakrishna, S.; Lim, C. T. Chitosan Nanofibers from an Easily Electrospinnable UHMWPEO-Doped Chitosan Solution System. *Biomacromolecules* **2008**, *9* (1), 136–141.

(41) Zhou, Q.; Bao, M.; Yuan, H.; Zhao, S.; Dong, W.; Zhang, Y. Implication of Stable Jet Length in Electrospinning for Collecting Well-Aligned Ultrafine PLLA Fibers. *Polymer* **2013**, *54* (25), 6867–6876.

(42) Christ, H.-A.; Ang, P. Y.; Li, F.; Johannes, H.-H.; Kowalsky, W.; Menzel, H. Production of Highly Aligned Microfiber Bundles from Polymethyl Methacrylate via Stable Jet Electrospinning for Organic Solid-State Lasers. *J. Polym. Sci.* **2022**, *60* (4), 715–725.

(43) Li, F.; Menzel, H. Electrospinning of Cyclic Olefin Copolymer for the Production of Highly Aligned Dye-Doped Optical Fibers. *Macromol. Mater. Eng.* **2024**, *309* (3), 2300292.

(44) Li, F.; Liu, X.; Klepzig, L. F.; Rudolph, D.; Lauth, J.; Walla, P. J.; Menzel, H. Origin and Manipulation of the Orientation of Colloidal 2D Nanoplatelets in Electrospun Fibers, *ACS Appl. Opt. Mater.*, **2025**, DOI: 10.1021/acsaom.5c00494.

(45) Osório, J. H.; Amrani, F.; Delahaye, F.; Dhaybi, A.; Vasko, K.; Melli, F.; Giovanardi, F.; Vandembroucq, D.; Tessier, G.; Vincetti, L.; Debord, B.; Gérôme, F.; Benabid, F. Hollow-Core Fibers with Reduced Surface Roughness and Ultralow Loss in the Short-Wavelength Range. *Nat. Commun.* **2023**, *14* (1), 1146.

(46) Avram, E.; Mahmood, W.; Ozer, M. Quantification of Scattering From Fiber Surface Irregularities. *J. Lightwave Technol.* **2002**, *20* (4), 634.

(47) Li, L.; Jiang, Z.; Li, M.; Li, R.; Fang, T. Hierarchically Structured PMMA Fibers Fabricated by Electrospinning. *RSC Adv.* **2014**, *4* (95), 52973–52985.

(48) Dayal, P.; Kyu, T. Porous Fiber Formation in Polymer-Solvent System Undergoing Solvent Evaporation. *J. Appl. Phys.* **2006**, *100*, 043512.

(49) Lesser, C.; Gao, M.; Kirstein, S. Highly Luminescent Thin Films from Alternating Deposition of CdTe Nanoparticles and Polycations. *Mater. Sci. Eng. C* **1999**, *8–9*, 159–162.

(50) Naskar, S.; Miethe, J. F.; Sánchez-Paradinas, S.; Schmidt, N.; Kanthasamy, K.; Behrens, P.; Pfnür, H.; Bigall, N. C. Photoluminescent Aerogels from Quantum Wells. *Chem. Mater.* **2016**, *28* (7), 2089–2099.

(51) Akselrod, G. M.; Weidman, M. C.; Li, Y.; Argyropoulos, C.; Tisdale, W. A.; Mikkelsen, M. H. Efficient Nanosecond Photoluminescence from Infrared PbS Quantum Dots Coupled to Plasmonic Nanoantennas. *ACS Photonics* **2016**, *3* (10), 1741–1746.

(52) Scholtz, L.; Eckert, J. G.; Elahi, T.; Lübkemann, F.; Hübner, O.; Bigall, N. C.; Resch-Genger, U. Luminescence Encoding of Polymer Microbeads with Organic Dyes and Semiconductor Quantum Dots During Polymerization. *Sci. Rep.* **2022**, *12* (1), 12061.

(53) Krishnamurthy, S.; Singh, A.; Hu, Z.; Blake, A. V.; Kim, Y.; Singh, A.; Dolgopolova, E. A.; Williams, D. J.; Piryatinski, A.; Malko, A. V.; Htoon, H.; Sykora, M.; Hollingsworth, J. A. PbS/CdS Quantum Dot Room-Temperature Single-Emitter Spectroscopy Reaches the Telecom O and S Bands via an Engineered Stability. *ACS Nano* **2021**, *15* (1), 575–587.

(54) Hanson, C. J.; Hartmann, N. F.; Singh, A.; Ma, X.; DeBenedetti, W. J. I.; Casson, J. L.; Grey, J. K.; Chabal, Y. J.; Malko, A. V.; Sykora, M.; Piryatinski, A.; Htoon, H.; Hollingsworth, J. A. Giant PbSe/CdSe/CdSe Quantum Dots: Crystal-Structure-Defined Ultrastable Near-Infrared Photoluminescence from Single Nanocrystals. *J. Am. Chem. Soc.* **2017**, *139* (32), 11081–11088.

(55) Saidzhonov, B. M.; Zaytsev, V. B.; Vasiliev, R. B. Effect of PMMA Polymer Matrix on Optical Properties of CdSe Nanoplatelets. *J. Lumin.* **2021**, *237*, 118175.

(56) Voznyy, O.; Levina, L.; Fan, F.; Walters, G.; Fan, J. Z.; Kiani, A.; Ip, A. H.; Thon, S. M.; Proppe, A. H.; Liu, M.; Sargent, E. H. Origins of Stokes Shift in PbS Nanocrystals. *Nano Lett.* **2017**, *17* (12), 7191–7195.

(57) Kagan, C. R.; Murray, C. B.; Nirmal, M.; Bawendi, M. G. Electronic Energy Transfer in CdSe Quantum Dot Solids. *Phys. Rev. Lett.* **1996**, *76* (9), 1517–1520.

(58) Choi, J. J.; Luria, J.; Hyun, B.-R.; Bartnik, A. C.; Sun, L.; Lim, Y.-F.; Marohn, J. A.; Wise, F. W.; Hanrath, T. Photogenerated Exciton Dissociation in Highly Coupled Lead Salt Nanocrystal Assemblies. *Nano Lett.* **2010**, *10* (5), 1805–1811.

(59) Rowland, C. E.; Fedin, I.; Zhang, H.; Gray, S. K.; Govorov, A. O.; Talapin, D. V.; Schaller, R. D. Picosecond Energy Transfer and Multiexciton Transfer Outpaces Auger Recombination in Binary CdSe Nanoplatelet Solids. *Nat. Mater.* **2015**, *14* (5), 484–489.

(60) Guzelturk, B.; Erdem, O.; Olutas, M.; Kelestemur, Y.; Demir, H. V. Stacking in Colloidal Nanoplatelets: Tuning Excitonic Properties. *ACS Nano* **2014**, *8* (12), 12524–12533.

(61) Liu, J.; Guillemeney, L.; Abécassis, B.; Coolen, L. Long Range Energy Transfer in Self-Assembled Stacks of Semiconducting Nanoplatelets. *Nano Lett.* **2020**, *20* (5), 3465–3470.

(62) Guillemeney, L.; Lermusiaux, L.; Landaburu, G.; Wagnon, B.; Abécassis, B. Curvature and Self-Assembly of Semi-Conducting Nanoplatelets. *Commun. Chem.* **2022**, *5* (1), 7.

(63) Guzelturk, B.; Demir, H. V. Near-Field Energy Transfer Using Nanoemitters For Optoelectronics. *Adv. Funct. Mater.* **2016**, *26* (45), 8158–8177.

(64) Jana, S.; Phan, T. N. T.; Bouet, C.; Tessier, M. D.; Davidson, P.; Dubertret, B.; Abécassis, B. Stacking and Colloidal Stability of CdSe Nanoplatelets. *Langmuir* **2015**, *31* (38), 10532–10539.

(65) Hendricks, M. P.; Campos, M. P.; Cleveland, G. T.; Jen-La Plante, I.; Owen, J. S. A Tunable Library of Substituted Thiourea Precursors to Metal Sulfide Nanocrystals. *Science* **2015**, *348* (6240), 1226–1230.

8.7 *Supporting Information*

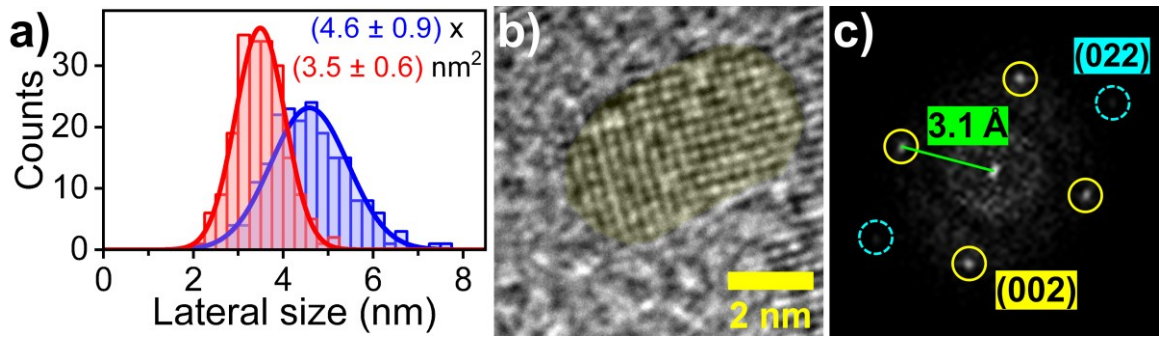

Figure S 8.1. (a) Lateral size histogram of the PbSe fQDs used in this study (sample size n = 200). The x-lengths (blue) correspond to the longest dimension of the fQDs and the y-widths (red) were determined by measuring the longest perpendicular distance. (b) High-magnification TEM image of a single PbSe fQD. (c) FFT pattern of the PbSe fQD shown in (b), composed of a set of diffraction peaks that are characteristic of cubic rock-salt-structured PbSe (with a lattice constant a = 6.1 Å and space group $Fm\bar{3}m$, as referenced in PDF card 01-077-0245).

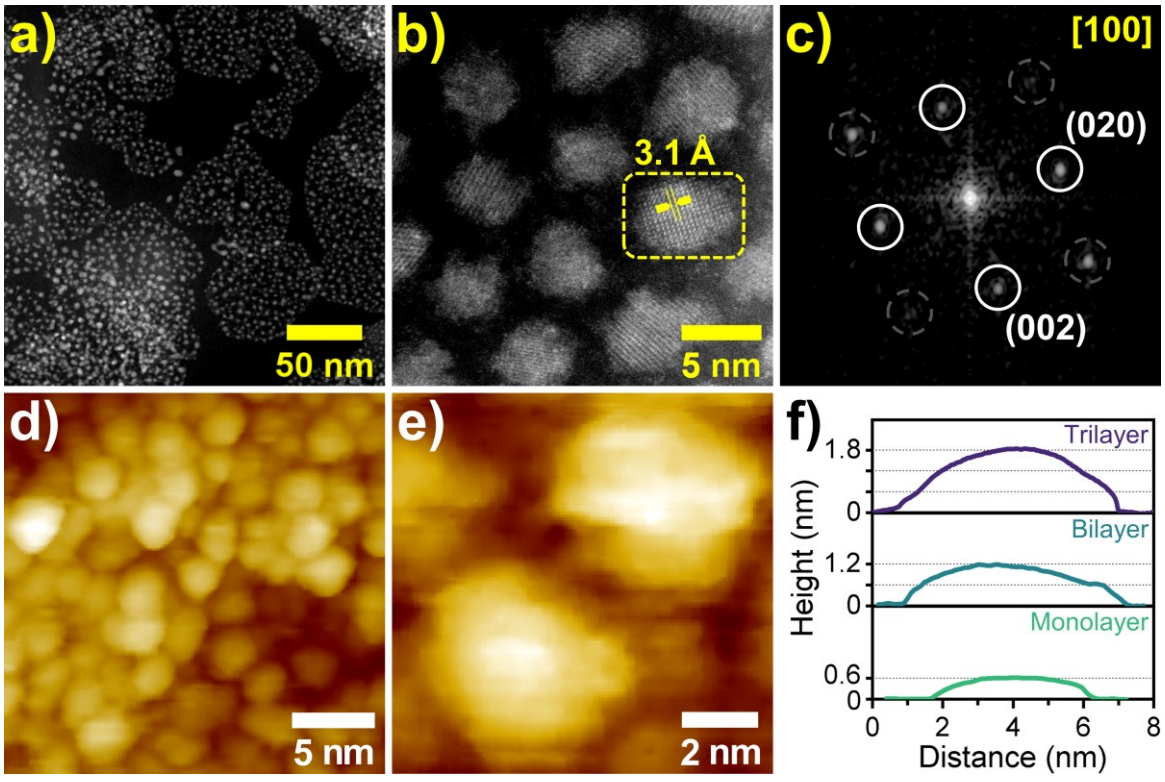

Figure S 8.2. Overview on the morphology of PbSe fQDs, as previously published.[1] (a, b) HR-HAADF-STEM images of PbSe fQDs. (c) FFT of the region marked in (b). (d, e) STM images (V_S = 4 V; I_{set} = 50 pA) of PbSe fQDs (shown in (a) and (b)). **(f) STM height profiles of colloidal PbSe fQDs showing**

distinct atomic layer-defined thicknesses of 1.8, 1.2 and 0.6 nm, corresponding to tri- to monolayer cubic PbSe, respectively.

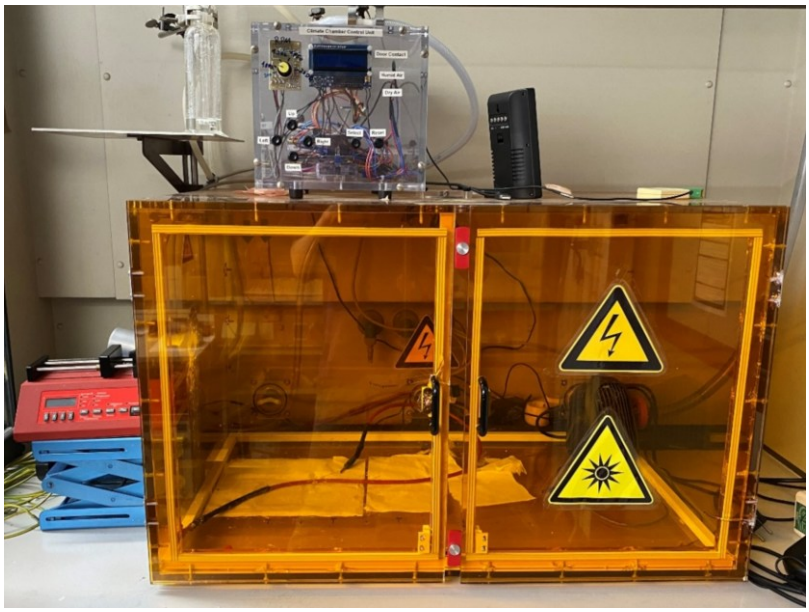

Figure S 8.3. Custom-built stable jet electrospinning setup used to fabricate PbSe fQD-containing PMMA SJES fibers, consisting of: a tinted acrylic glass chamber (80 x 50 x 50 cm^3), two highvoltage generators (from HEINZINGER ELECTRONIC) to apply an electric potential, a spinneret (21-gauge needle from B. BRAUN) connected to the positive voltage, and a custom-made rotating drum collector (hollow aluminum cylinder with 10 cm diameter and 17 cm length, rotated at 8–33 Hz) connected to the negative voltage. The spinning solution was injected *via* a syringe pump LA-30 (left side) from LANDGRAF LABORSYSTEME HLL.[2] The gas atmosphere inside the orange chamber was controlled using a custom-built ARDUINO-based climate chamber control unit (top).

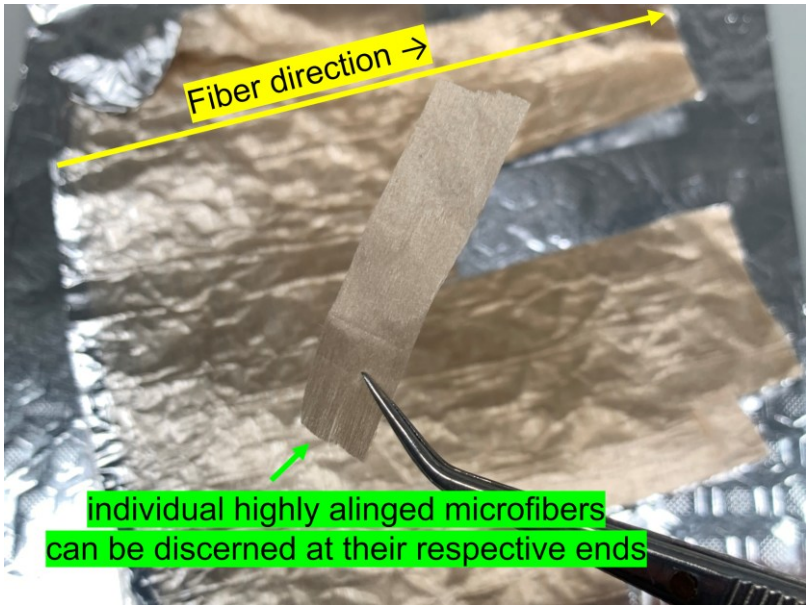

Figure S 8.4. Photograph of stable jet electro spun PbSe fQD-containing PMMA microfibers on aluminum foil (used to facilitate fiber separation).

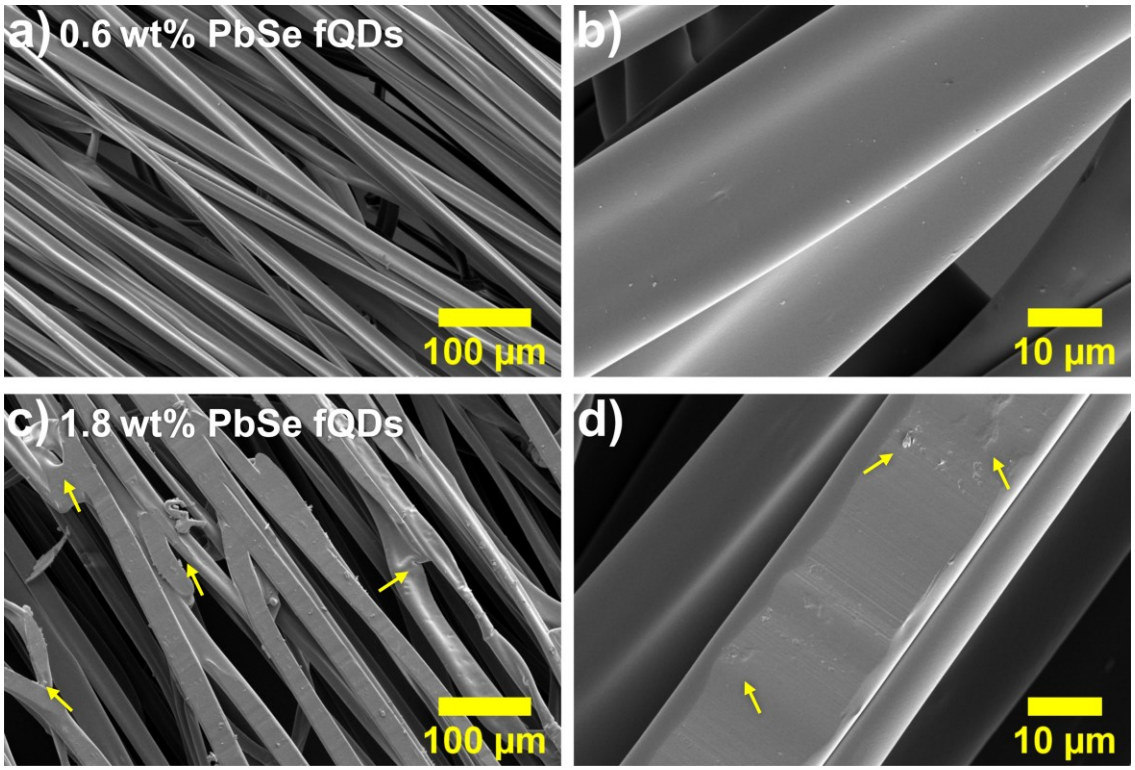

Figure S 8.5. SEM overview images of SJES PMMA fibers containing 0.6 wt% (a, b) and 1.8 wt% PbSe fQDs (c, d). At the lower PbSe fQD concentration, the aligned fibers exhibit a smooth, regular surface and a mean diameter of (21.9 ± 3.4) µm, which is similar to the 1.2 wt% sample shown in Figure 8.1d,e of

the main manuscript. However, adding 1.8 wt% PbSe fQDs results in unevenly shaped SJES fibers with a rougher surface, as well as considerable crosslinking between adjacent fibers and splitting of individual fibers (indicated by the yellow arrows in panel c). Consequently, 1.8 wt% PbSe fQDs are considered the upper limit for obtaining high-quality PbSe fQD-containing SJES PMMA fibers within the parameter space of this work.

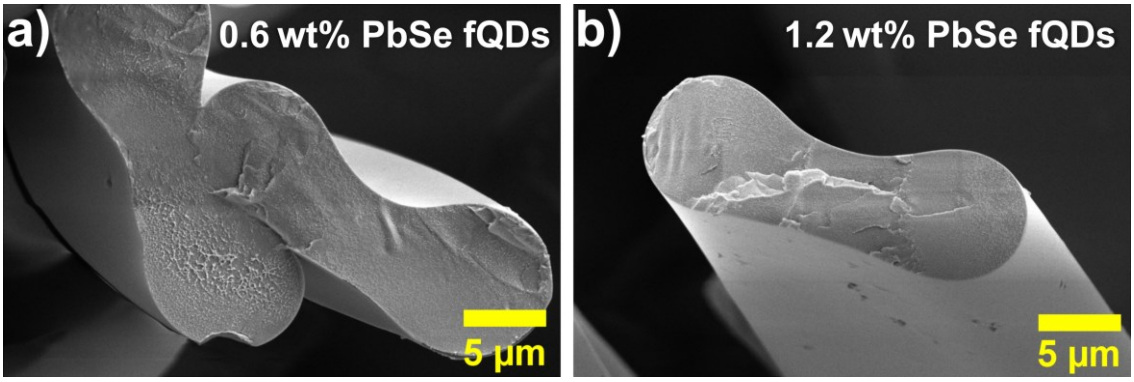

Figure S 8.6. Cross sectional SEM images of individual PbSe fQD-containing fibers highlighting their ribbon-/dog-bone-like shape.

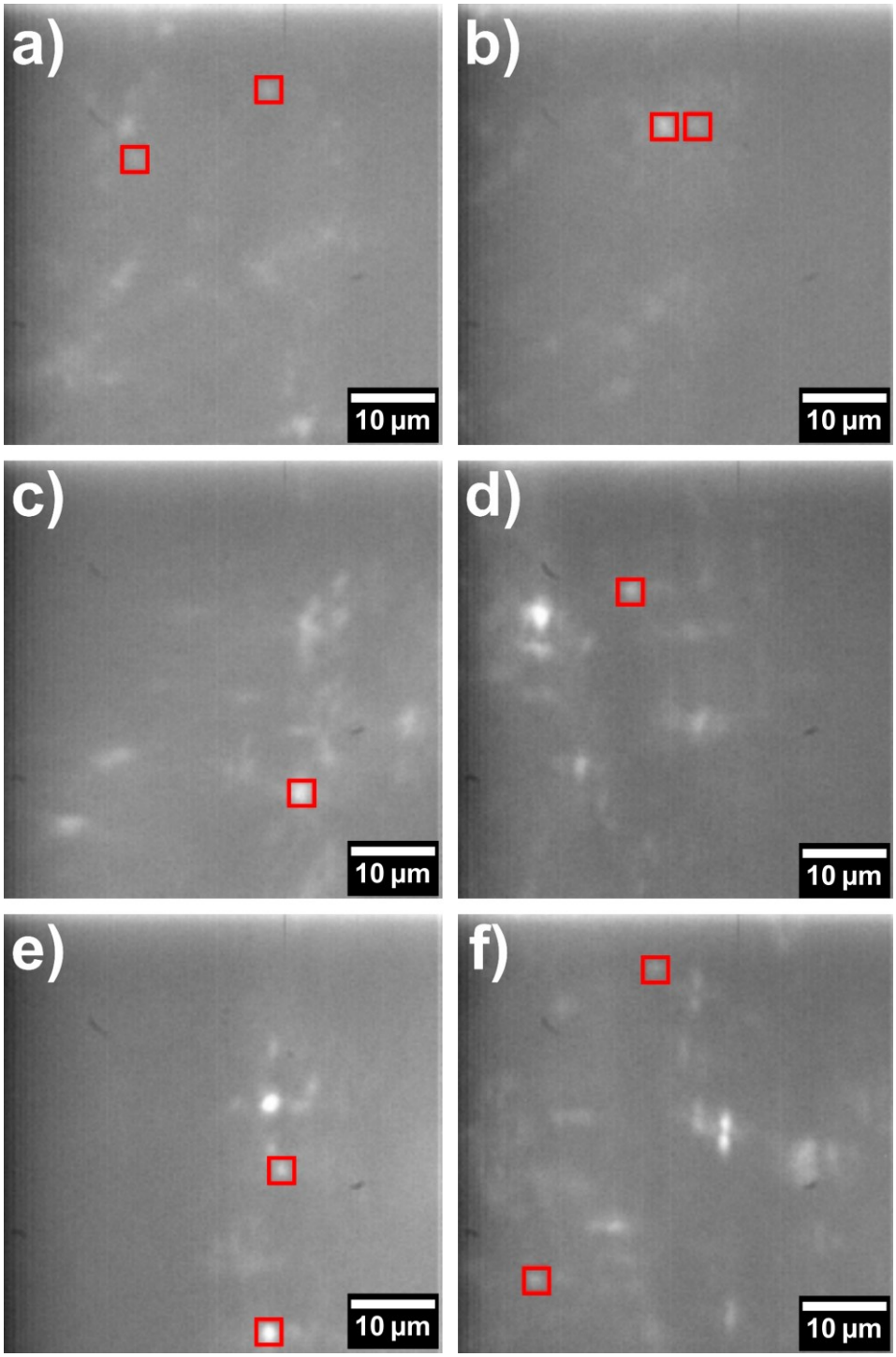

Figure S 8.7. 3D single-particle excitation polarization microscopy images. The data shown in Figure 8.3 were collected by analyzing the signal from the spots indicated in red. Spots with a regular round shape and clear sinusoidal modulation of the signal when varying the polarization orientation were selected for analysis. Spot brightness does not play a role in the selection process, because the brightness only reflects the angle-dependent absorption probability of a given fQD; therefore, different excitation angles lead to different brightness levels.

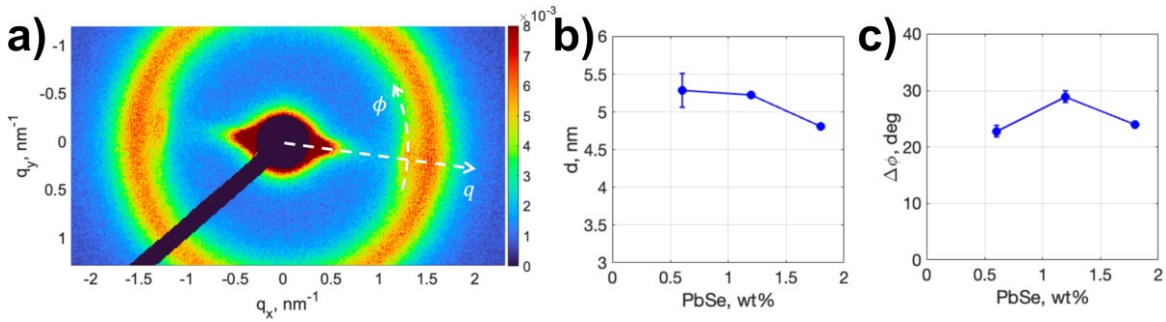

Figure S 8.8. (a) SAXS diffraction pattern of SJES fibers containing 1.8 wt% PbSe fQDs. The white dashed lines indicate the radial (q) and angular (ϕ) directions in polar coordinates. The scattering signal of PbSe fQDs within stacks is visible at q = 1.3 nm^{-1}. This signal can be used to estimate the distance between the PbSe fQDs in a stack and their orientational order. The uniform scattering ring at q = 1.5 nm^{-1} originates from the unordered individual PbSe fQDs. This ring is only visible for the samples with PbSe fQD mass fractions of 1.2 and 1.8 wt%. (b) Distance d between the PbSe fQDs within a stack, determined from the radial position of the scattering peak, plotted against the PbSe fQD weight fractions. (c) Fwhm in angular direction of the scattering peak originating from the PbSe stack, plotted against the PbSe fQD weight fractions.

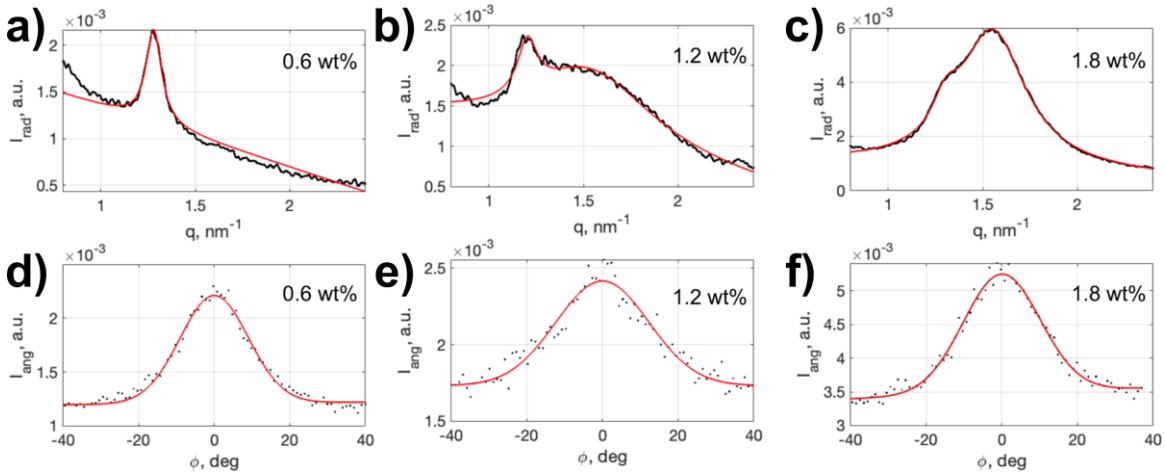

Figure S 8.9. Radial (a–c) and angular (d–f) cross-sections of the scattered intensity through the peak corresponding to the stacks of PbSe fQDs in fibers with PbSe fQD mass fractions of 0.6 wt% (a, d), 1.2 wt% (b, e) and 1.8 wt% (c, f). Black points represent the experimental data, and the red lines correspond to fits with GAUSSIAN functions with a linear background. For the radial profiles at 1.2 wt% and 1.8 wt% (panels (b) and (c)), two GAUSSIAN functions were used to take into account

two contributions: (1) PbSe fQDs within a stack (small peak at around q = 1.3 nm^{-1}) and (2) individual PbSe fQDs (large peak at around q = 1.5 nm^{-1}). The results of the fits, *i.e.* the corresponding distances between the PbSe fQDs and the angular fwhm of the peaks, are shown in Figure S 8.8b, c above.

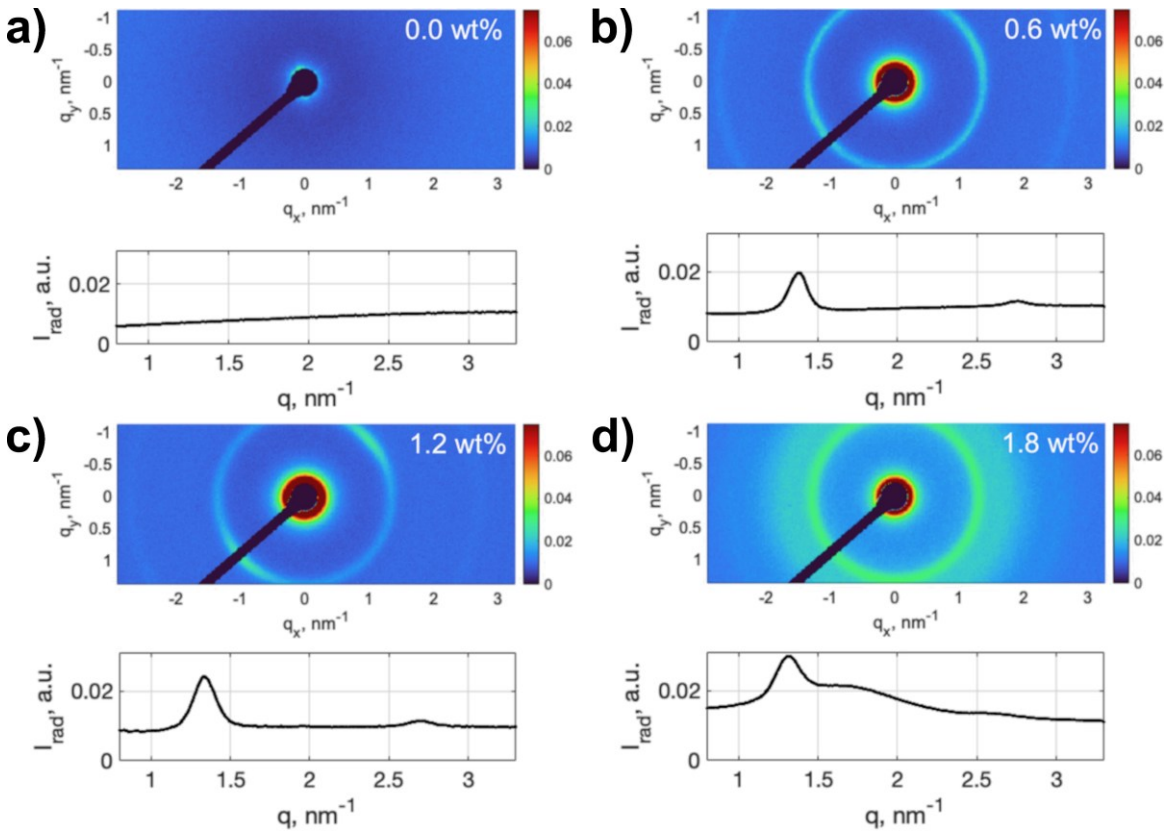

Figure S 8.10. X-ray diffraction patterns of complementary drop-casted chip-like PbSe fQD-polymer samples of the same composition that was used for the SJES fibers. All samples containing PbSe fQDs (b–d) exhibit an isotropic scattering ring at $q \approx 1.34$ nm^{-1}, corresponding to stacks of PbSe fQDs with a random orientation (indicated by an isotropic ring instead of an anisotropically shaped scattering signal). The interparticle spacing within these stacks is similar to that observed in the SJES fibers (~4.7 nm here *vs* ~5.0 nm in the fibers), supporting the assumption that the PbSe fQDs pre-stack in the spinning solution, while the alignment of the stacks is an effect of the SJES technique. (The minor anisotropy of the scattering signal in panel (c) is presumably caused by accidental stress during sample preparation, because the spinning solution is optimized for SJES rather than for drop-casting and drying under ambient conditions.)

8.7.1 References

(1) Biesterfeld, L.; Ngo, H. T.; Addad, A.; Rudolph, D. A.; Leis, W.; Seitz, M.; Ji, G.; Grandidier, B.; Delerue, C.; Lauth, J.; Biadala, L. Monolayer-Defined Flat Colloidal PbSe Quantum Dots in Extreme Confinement. *Nano Lett.* **2025**, *25* (31), 12019–12024.

(2) Christ, H.-A.; Ang, P. Y.; Li, F.; Johannes, H.-H.; Kowalsky, W.; Menzel, H. Production of Highly Aligned Microfiber Bundles from Polymethyl Methacrylate via Stable Jet Electrospinning for Organic Solid-State Lasers. *J. Polym. Sci.* **2022**, *60* (4), 715–725.

7 Summary

This thesis provides insights into the chemistry and photophysics of colloidally synthesized two-dimensional lead chalcogenide nanocrystals and underscores their potential for cutting-edge technologies operating in the NIR. The presented findings span from the material development in 2D NC synthesis over in-depth analyses of their morphology, electronic structure and optical properties to the incorporation of 2D NCs in to functional hybrid fibers.

Chapter 1 and 2 introduce the field of colloidal 2D NIR emitters, providing a broad foundation for the following research articles.

Chapter 3 reports on the surface passivation of colloidal 2D PbSe NPLs using a selection of metal halides to adress surface-related trap states and thereby increase the PLQY of the NPLs. The best enhancement was achieved using PbI_2 with PLQY values of 27% for PbSe NPLs with PL centered around 1265 nm and 61% for PL at 989 nm. This increase is interpreted in terms of the HSAB principle: undercoordinated Pb^{2+} surface sites preferably interact with the soft iodide rather than with the harder fluoride to bromide. In addition, it was found that introducing foreign cations, *e.g.* by adding ZnI_2, to saturate undercoordinated Se^{2-} surface atoms is less favorable than using lead halides, which is in line with earlier reports and presumably due to undesired cation exchange side reaction starting to occur. By using XPS in conjuction with experiments employing organic halides, it was further determined that the PLQY enhancement is the result of a combined passivation by X-type binding halides X^- from the dissociated treatment agent, as well as direct Z-type binding of metal halides MX_2. The developed surface passivation method yields 2D PbSe NPLs with the highest reported PLQYs to date and later proved to be a crucial step in the development of a new 2D PbTe NPLs synthesis.

Chapter 4 describes a synthesis of colloidal 2D PbTe nanoplatelets with tunable NIR PL in the range of 910 – 1460 nm with a PLQY of 1 – 15% based on aminophosphine precursor chemistry. To obtain a tellurium source that is sufficiently reactive at the low temperatures required to synthesize 2D NPLs, tris(dimethylamino)phosphine was let to react with elemental tellurium and transaminated with octylamine at 100°C. This *ex-situ* transamination is monitored by ^{31}P NMR and results in the weakening of the Pb^+-Te^-/Pb=Te bond in the

aminophosphine precursor, *i.e.* an increase in its reactivity. The PL position of the final PbTe NPL can be controlled by the Pb/Te ratio as well as by the alkyl chain length of the amine used for transamination. Further, it is hypothesized that post-synthesis PbI_2 treatment plays a vital double role by (1) passivating the NPL surface and (2) quenching the precursor by forming a stable iodophosphonium salt. GIWAXS was used to confirm the 2D shape of the NPLs, by revealing the formation of superlattices with anisotropic interparticle spacings. A small interplanar distance of ~0.5 nm points toward single atomic layers of PbTe separated by iodide ligands. This study is the first to report a straightforward synthesis of colloidal PbTe NPLs, thereby complementing the group of colloidal 2D PbX NCs.

Chapter 5 describes a water transfer protocol for 2D PbX NCs. Exchanging the native oleic acid and octylamine ligands for bifunctional 11-mercaptoundecanoic acid yields aqueous phase near-infrared emitters. The phase tranfer retains the PL, crystallinity and shape of all three lead chalcogenides. Aqueous PbSe fQDs exhibit relatively efficient PL with a QY of 13% for emission centered at ~1023 nm, matching the performance of water-soluble spherical PbX NCs. Furthermore, the combination of XPS and NMR studies enables following the phase transfer on a molecular level, and revealing two binding motifs of the mercaptocarboxylic acid to the 2D NCs: X-type bound thiolate and L-type bound thiol. These results highlight the chemical robustness of 2D PbX NCs, which is higher than one might initially expect of a material class deemed to be water and oxygen sensitive. Aqueous phase 2D PbX NCs bridge the gap between their intriguing photophysics and the solubility requiremens of downstream processing techniques used for producing functional nanocomposites, such as layer-by-layer deposition.

Chapters 6 and 7 focus on spectroscopy. In Chapter 6 the PL of single PbS NPLs at cryogenic temperatures is investigated. At 4 K, the 2D PbS NPLs exhibit narrow PL with a degree of linear polarization of up to 90%. Single NPL spectra consist of a zero-phonon line with sub-meV line widths around 0.6 meV (resolution-limited), and two lower-energy phonon sidebands at -26.5 and -5 meV, which are attributed to acoustic and optical phonons, respectively. Time-resolved PL spectra reveal that the PL, which decays biexponentially at cryogenic temperatures, is dominated by a fast decay component, that is attributed to trion emission. Above 170 K, this fast component vanishes, implying a trion binding energy of ~14.7 meV. Further analysis of the PL over a period of 5 min reveals that the single NPL PL shows no

blinking as well as minimal spectral diffusion without a memory effect. These unique properties distinguish 2D PbS NPLs from their spherical counterparts, highlighting the influence of their 2D shape on their photophysical properties. Additionally, the crystalline quality and ultrathin 2D geometry of PbS NPLs are underpinned by the formation of randomly oriented MOIRÉ patterns, which suggest a thickness of one to a few atomic layers and quasi-direct contact between these NPLs.

Chapter 7 presents research on the morphology and extreme quantum confinement of 2D PbSe fQDs. Using scanning tunneling microscopy (STM), the thickness of 2D PbSe fQDs was directly assessed for the first time. Investigating an ensemble of fQDs, three distinct single-layer defined populations of mono-, bi- and trilayer PbSe were found. These findings represent the first realization of substrate-free PbSe monolayers. Scanning tunnelling spectroscopy (STS) of these three fQD populations reveals that they exhibit in-gap free density of states (DOS) with defined peaks on either side of the zero-conductance region. This QD-like DOS differs from the step-like profile of confined 2D systems and is the reason why these QDs are termed “flat QDs”. Flat quantum dots are a class of QDs that exhibit extreme vertical confinement combined with additional confinement in their lateral dimension. Comparing the experimental band gaps with theoretical tight-binding (TB) calculations confirms the presence of mono- to trilayer PbSe. Additionally, the different layer populations can be distinguished in ensemble PL spectra when the fQDs are cooled to 77 K. Such cryo-PL measurements over longer timescales suggest OSTWALD ripening of monolayers into bilayers and later trilayers taking place, which can be considerably slowed down by surface passivation of the fQDs with PbI_2. Comparing the fundamental band gaps obtained from STS and TB calculations with the optical band gaps obtained from cryo-PL, allows the direct determination of exciton binding energies of 200 meV in trilayers up to a record 600 meV in monolayer PbSe. This work ties together in-depth insights into the morphology and electronic structure of PbSe fQDs with synthetic considerations, paving the way for future growth-by-design-approaches.

Chapter 8 builds on the previous findings and brings PbSe fQDs one step closer to a fiber optical application by incorporating them into easy-to-handle solid-state nanocomposite fibers *via* stable jet electrospinning with poly(methyl methacrylate). Electrospinning a dispersion of PMMA and PbSe fQDs results in

highly aligned NIR-emissive nanocomposite fibers (*e.g.* PL at 1073 nm with a QY of 5%), which have a well-defined shape and smooth surface, suitable for *e.g.* waveguiding. SAXS experiments reveal stacks of individual PbSe fQDs within these fibers, that are oriented perpendicular to the fiber direction, which supports a previously proposed die swelling mechanism for the alignment of 2D nanocrystalline emitters by SJES. Within these PbSe fQD stacks, energy transfer into the smallest band gap tail of the thickness/size distribution of the fQD ensemble results in a narrowing (*e.g.* from a fwhm of 275 meV to 185 meV) and a bathochromic shift (~40 – 50 nm) of the fiber PL compared to colloidal fQDs, which could be leveraged to further tailor the optical properties of these interesting nanocomposites.

To conclude, the research presented in this thesis expands the synthetic horizon for future chemical and photophysical studies on 2D lead chalcogenide nanocrystals and deepens the understanding of their optical properties, laying a foundation for up-coming physical and application-oriented research. The next chapter outlines possible directions for future work in this field, highlighting open ends of this work and presenting general ideas that seem worthwhile to pursue.

10 Outlook

To address the open questions that arose thoughout this thesis, future studies on colloidal NIR-emissive 2D lead chalcogenide NCs should further combine synthetic chemistry with advanced spectroscopic investigations.

Chapter 3, which focuses on the surface passivation of 2D PbSe NPLs concludes with the determination of MCS PL lifetimes of around ~2 µs for PbSe NPLs. However, this method has a rather low time resolution of ~10 ns and is naturally limited to radiative recombination processes. This calls for further ultrafast spectroscopic studies of PbSe NPLs and 2D PbX NCs in general. Transient absorption spectroscopy will provide insights into short-lived radiative and non-radiative recombination dynamics of charge carriers in as-synthesized and surface-passivated PbSe NPLs (with a ~130 fs time resolution). Combining broadband transient absorption studies (350 – 2400 nm) with the findings presented herein from STS and tight-binding calculations (Chapter 7) might allow the unambiguous assignment of observed transient signals to specific transitions in PbSe fQDs (and subsequently in PbS and PbTe NPLs). Comparison with existing studies on spherical PbX NCs could provide a deeper understanding on how the ultrathin 2D shape affects the unique optical properties of NPLs/fQDs, including the PL characteristics observed for single PbS NPLs in Chapter 6. The next logical step could be low-temperature transient absorption measurements, which may allow distinguishing 2D PbX NCs with different layer numbers, similar to the PL measurements presented in Chapter 7.

In terms of synthetic questions, a long-term goal would be achieving precise control over the obtained number of layers, or more generally the thickness of the 2D NCs, for all three 2D PbX systems, as is standard for 2D cadmium chalcogenides. This will undoubtedly be a challenging task. One possible starting point would be revisiting the surface passivation/quenching of 2D PbX syntheses using metal halides, as this was proven to significantly slow down the OSTWALD ripening of mono- and bilayers to trilayer PbSe (Chapter 7). Stopping the 2D PbX syntheses after different (and presumably short) reaction times by adding MX_2 and rigorously purifying the product may allow the isolation of populations with distinct atomic-layer-defined thicknesses. Similarly, a better control over the lateral dimensions and specifically the growth of laterally significantly larger NPLs,

i.e. 20 x 20 nm² and beyond could be pursued. To achieve this, first experiments could involve a prolonged dropwise precursor addition (rather than the rapid injection of the complete solution at once) to extend the growth time of the NPLs without generating additional nuclei.

One possible mid-term synthetic goal could be the growth of heterostructured 2D lead chalcogenides, *i.e.* core/shell or core/crown NPLs/fQDs. For applications requiring efficient PL, *e.g.* for use as classical or quantum emitters at telecommunication wavelengths, the goal includes specifically designing structures with a type-I band alignment. In this configuration, the shell or crown has a lower-energy valence band edge and a higher-energy conduction band edge, so that both charge carriers are confined to the 2D NCs core for radiative recombination. Well-established materials with similar crystal structure and lattice parameters would good first canditates for such heterostructures. For example, CdX (X = S, Se, Te) exhibit comparable lattice constants to PbX and can crystallize in a cubic structure (zinc blende), and all possible material combinations result in a type-I band alignement. To achieve combinations with more uneven lattice matching, such as 2D PbSe/CdS core/crown or shell NCs, gradient shelling, *e.g.* 2D PbSe/PbS/CdS core/shell/shell structures, could be considered.

Regarding the aqueous phase-transfer presented in Chapter 5, immidiate follow-up research could start with further processing of aqueous 2D PbX NCs to create nanocomposite materials. A starting point could be layer-by-layer deposition with different polyelectrolytes or incorporation into metal organic frameworks, as was previously done with CdSe NPLs by our group and cooperation partners. Further in the future, combining a water transfer with the mentioned synthesis of heterostructured 2D PbX NCs – for example by shelling PbX with thick layers of low-toxicity materials, such as ZnS – could open up possibilities for fundamental research in biological environments.

Concerning the findings from STM/STS measurements (Chapter 7), future studies may focus on surface-passivated PbSe fQDs, which have not yet been studied in the same manner. Beyond that, 2D PbTe NPLs are arguably the most interesting material for in-depth physical studies, due to the materials very large exciton BOHR radius and inherent band structure anisotropy. In this context alloying of PbTe with SnTe may be a long-term goal, that introduces the relative

composition of Pb to Sn as a new parameter for controlling the materials band gap and opens up a different line of research into the world of topological insulators.

The incorporation of PbSe fQDs into SJES PMMA fibers (Chapter 10) opens up various options for future research. From a fundamental 2D PbX NC perspective, the next step would be to investigate the presumed energy transfer within PbSe fQD stacks using transient absorption spectroscopy, for example. In terms of the polymer chemistry, it would be interesting to apply this proof of concept for stable jet electrospinning PbSe fQD to more sophisticated transparent polymers with lower optical loss at telecommunication wavelengths than PMMA, to further improve the quality of the nanocomposites.

In conclusion, there are many exciting avenues for future research on colloidal two-dimensional lead chalcogenide nanocrystals, each of which will undoubtedly give rise to new questions in the years to come. The present work provides a broad foundation for future studies to build upon.

A Publications and Scholarly Contributions

A.1 Publications Included in this Thesis

1. **Toward Bright Colloidal Near-Infrared Emitters: Surface Passivation of 2D PbSe Nanoplatelets by Metal Halides**
   Leon Biesterfeld, Lars F. Klepzig, André Niebur, Marina Rosebrock, and Jannika Lauth.*
   J. Phys. Chem. C **2022**, *126* (45), 19277–19285.
2. **Solving the Synthetic Riddle of Colloidal Two-Dimensional PbTe Nanoplatelets with Tunable Near-Infrared Emission**
   Leon Biesterfeld, Mattis T. Vochezer, Marco Kögel, Ivan A. Zaluzhnyy, Marina Rosebrock, Lars F. Klepzig, Wolfgang Leis, Michael Seitz, Jannik C. Meyer, and Jannika Lauth.*
   Chem. Mater. **2024**, *36* (15), 7197–7206.
3. **Sub-millielectronvolt Line Widths in Polarized Low-Temperature Photoluminescence of 2D PbS Nanoplatelets**
   Pengji Li,‡ Leon Biesterfeld,‡ Lars F. Klepzig, Jingzhong Yang, Huu Thoai Ngo, Ahmed Addad, Tom N. Rakow, Ruolin Guan, Eddy P. Rugeramigabo, Ivan Zaluzhnyy, Frank Schreiber, Louis Biadala,* Jannika Lauth,* and Michael Zopf.*
   Nano Lett. **2024**, *24* (51), 16293–16300.
4. **Monolayer-Defined Flat Colloidal PbSe Quantum Dots in Extreme Confinement**
   Leon Biesterfeld, Huu Thoai Ngo, Ahmed Addad, Dominik A. Rudolph, Wolfgang Leis, Michael Seitz, Gang Ji, Bruno Grandidier, Christophe Delerue, Jannika Lauth,* and Louis Biadala.*
   Nano Lett. **2025**, *25* (31), 12019–12024.
5. **Aqueous Phase Near-Infrared Emitters: Water Transfer of Colloidal 2D PbS, PbSe and PbTe Nanoplatelets**
   Leon Biesterfeld, Mattis T. Vochezer, Dominik A. Rudolph, and Jannika Lauth.*
   Nanoscale, 2025, **17**, 24006–24016.

6. **Near-Infrared Emitting Fibers: Stable Jet Electrospinning Flat PbSe Quantum Dots into Poly(methyl methacrylate)**
   Leon Biesterfeld, Dennis Kühn, Fuzhao Li, Franka Gädeke, Dominik A. Rudolph, Frank Schreiber, Peter J. Walla, Ivan Zaluzhnyy, Henning Menzel and Jannika Lauth.*
   J. Phys. Chem. Lett. **2026**, *17* (4), 955–965.

‡ Equal contributions, * Corresponding author(s)

A.2 Publications Not Included in this Thesis

1. **Colloidal 2D PbSe nanoplatelets with efficient emission reaching the telecom O-, E-, and S-band**
   Lars F. Klepzig, Leon Biesterfeld, Michel Romain, André Niebur, Anja Schlosser, Jens Hübner, and Jannika Lauth.*
   Nanoscale Adv. **2022**, 4, 590.

* Corresponding author(s)

A.3 Invited Talks

1. **Future Optics from Solution: Wet-Chemical Synthesis of Ultrathin 2D Semiconductors**
   RenewPV Special Symposium **2024** on "Quantum Dots for Solution-Processed Devices", online.

A.4 Contributed Talks

1. **Surface Treatment of Colloidal 2D Lead Chalcogenide NPLs for Emission Enhancement at Telecom Wavelengths**
   Bunsen-Tagung **2022** on "Understanding Dispersion Interactions in Molecular Chemistry", Deutsche Bunsen-Gesellschaft, Giessen, Germany.
2. **Colloidal 2D PbSe Nanoplatelets for Efficient Near-Infrared Emission**
   NANOHYBRID **2022** "Hamburg Conference on Complex Nanostructures", GrK Nanohybrid, Hamburg, Germany.

3. **Colloidal 2D Lead Chalcogenide Nanoplatelets as Efficient Near-Infrared Emitters**

Materials for Sustainable Development Conference Spring **2023** at the symposium on “Materials for Quantum Technology”, nanoGe, Valencia, Spain.

4. **Perpendicular Alignment of 2D Nanoplatelet Emitters in Electrospun Fibers: A Result of the Barus Effect?**
   PhoenixD Retreat **2023**, Schneverdingen, Germany (trio-talk with Prof. Dr. P. J. Walla and Prof. Dr. H. Menzel).
5. **Strong Confinement in Colloidal Flat PbSe Quantum Dots: New Optical and Electronic Properties**
   Materials for Sustainable Development Conference Spring **2024** at the symposium on “Solution-Processed 2D Materials”, nanoGe, Barcelona, Spain.
6. **Strong Confinement in Colloidal Flat PbSe Quantum Dots: New Optical and Electronic Properties**
   Bunsen-Tagung **2024** on “High-Resolution Structural Methods in Material and Life Sciences”, Deutsche Bunsen-Gesellschaft, Aachen, Germany.
7. **Solving the Synthetic Riddle of Colloidal 2D PbTe Nanoplatelets with Tunable Near-Infrared Emission**
   Materials for Sustainable Development Conference Fall **2024** at the symposium “Functional Nanomaterials: from materials to applications”, nanoGe, Lausanne, Switzerland.

In addition, I presented several posters at different international conferences (*e.g.* at the “Optoelectronic Processes at Nanostructured Interfaces – 763. WE-Heraeus Seminar” conference 2022 in Bad Honnef or at the “Chemical Coding at the Atomic Scale: Designing Hybrid and Quantum Nanostructures for Applications in Optical Biosensing, Light Harvesting, Chiral Catalysis, and More” international workshop 2024 in Dresden) as well as at various university internal and cluster of excellence events (e.g. at the “International Advisory Committee of PhoenixD Meetings” 2022 and 2025 in Hannover).

B Declaration of Contributions

Toward Bright Colloidal Near-Infrared Emitters: Surface Passivation of 2D PbSe Nanoplatelets by Metal Halides

Leon Biesterfeld	PbSe NPL syntheses and development of a new (purification and) surface treatment procedure; absorbance, PL, and PLQY measurements and data interpretation; TEM data interpretation; PXRD data interpretation; XPS data fitting and interpretation; ATR-FTIR measurements and data interpretation; discussion; preparation of all figures and the TOC graphic; writing of the original draft; answering of reviewer questions; editing and rewriting of the reviewed draft *Estimated contribution of my own: ~80%*
Lars F. Klepzig	Reproduction of PbSe NPL syntheses and surface treatments, XRD measurements; PL LT measurements, data inter-pretation, and writing of the corresponding paragraph; discussion; critical review; proof reading
André Niebur	TEM measurements; discussion; proof reading
Marina Rosebrock	XPS measurements
Jannika Lauth *	Conceptualization; supervision; discussion; critical review and correction; proof reading; correspondence with the journal; funding acquisition; access to laboratory equipment

Solving the Synthetic Riddle of Colloidal Two-Dimensional PbTe Nanoplatelets with Tunable Near-Infrared Emission

Leon Biesterfeld	Conceptualization; development of a new PbTe NPL synthesis and surface passivation method; absorbance, PL, and PLQY measurements and data interpretation; TEM data interpretation; SAED data interpretation; PXRD data interpretation; syntheses of ^{1}H, $^{31}P\{^{1}H\}$ and HMBC NMR samples and data interpretation; XPS data fitting and interpretation; discussion; preparation of all figures and the TOC graphic; writing of the original draft; answering of reviewer questions; additional experiments requested in the revision; editing and rewriting of the reviewed draft *Estimated contribution of my own: ~80%*
Mattis T. Vochezer	Reproduction of PbTe NPL syntheses; support with absorbance and PL measurements; discussion
Marco Kögel	HR-TEM and SAED measurements; discussion of the SAED interpretation
Ivan A. Zaluzhnyy	GIWAXS and XRR measurements, data interpretation, preliminary visualization, and writing of a corresponding short paragraph in the main manuscript and a figure caption for the SI; proof reading
Marina Rosebrock	XPS measurements
Lars F. Klepzig	PXRD measurements; discussion; proof reading
Wolfgang Leis	Support with NMR techniques; proof reading
Michael Seitz	Proof reading; access to laboratory equipment

Jannik C. Meyer	Supervision of HR-TEM and SAED measurements; proof reading; access to laboratory equipment
Jannika Lauth *	Conceptualization; supervision; discussion; critical review and correction; proof reading; correspondence with the journal; funding acquisition; access to laboratory equipment

Sub-millielectronvolt Line Widths in Polarized Low-Temperature Photoluminescence of 2D PbS Nanoplatelets

Pengji Li ‡	Low-temperature PL measurements, sample preparation and data interpretation; polarization simulations; discussion; preparation of figures; writing of the original draft; proof reading; answering of the reviewer questions; additional experiments requested in the revision; editing and rewriting of the reviewed draft
Leon Biesterfeld ‡	PbS NPL syntheses; HAADF-STEM and TEM data interpretation; room-temperature PL measurements and data interpretation; discussion; preparation of figures; writing of the original draft; proof reading; answering of the reviewer questions; additional experiments requested in the revision; editing and rewriting of the reviewed draft *Estimated contribution of my own: ~35%*

‡ Equal contributions

Lars F. Klepzig	PbS NPL syntheses; room-temperature PL measurements and data interpretation; writing of early text fragments
Jingzhong Yang	Support with low-temperature PL measurements; proof reading

Huu Thoai Ngo	HAADF-STEM measurements
Ahmed Addad	HAADF-STEM measurements
Tom N. Rakow	Support with low-temperature PL data interpretation; proof reading
Ruolin Guan	Polarization simulations; proof reading
Eddy P. Rugeramigabo	Sample preparation for low-temperature PL measurements; proof reading
Ivan Zaluzhnyy	GIWAXS measurements, data interpretation, and preparation of a corresponding figure and figure caption for the SI; proof reading
Frank Schreiber	Supervision of X-ray experiments; proof reading
Louis Biadala *	Supervision of HAADF-STEM experiments; discussion; data interpretation; critical review and correction; proof reading; access to laboratory equipment
Jannika Lauth *	Conceptualization; supervision; discussion; data interpretation; critical review and correction; proof reading; funding acquisition; access to laboratory equipment
Michael Zopf *	Conceptualization, supervision of low-temperature PL measurements; discussion; data interpretation; critical review and correction; proof reading; correspondence with the journal; funding acquisition; access to laboratory equipment

Monolayer-Defined Flat Colloidal PbSe Quantum Dots in Extreme Confinement

Leon Biesterfeld	Conceptualization; PbSe fQD syntheses; absorbance, room-temperature PL, and low-temperature PL measurements and data interpretation; HAADF-STEM/TEM data interpretation; discussion; preparation of all figures and the TOC graphic; writing of the original draft; answering of reviewer questions; editing and rewriting of the reviewed draft *Estimated contribution of my own: ~75%*
Huu Thoai Ngo	STM/S measurements, early discussion
Ahmed Addad	HAADF-STEM measurements
Dominik A. Rudolph	TEM measurements
Wolfgang Leis	Consultation on part of the low-temperature PL measurements using magnesia sticks; proof reading
Michael Seitz	Access to laboratory equipment
Gang Ji	Supervision of HAADF-STEM measurements; access to laboratory equipment
Bruno Grandidier	Discussion; proof reading
Christoph Delerue	TB calculations; discussion; proof reading

Jannika Lauth *	Conceptualization; supervision; discussion; critical review and correction; proof reading; correspondence with the journal; answering of reviewer questions; funding acquisition; access to laboratory equipment
Louis Biadala *	Conceptualization; supervision of STM/S measurements and data interpretation; discussion; critical review and correction; proof reading; answering of reviewer questions; funding acquisition; access to laboratory equipment

Aqueous Phase Near-Infrared Emitters: Water Transfer of Colloidal 2D PbS, PbSe and PbTe Nanoplatelets

Leon Biesterfeld	Conceptualization; PbX NPL/fQD syntheses; absorbance, PL, and PLQY measurements and data interpretation; TEM data interpretation; XPS measurements, fitting and interpretation; ^{1}H NMR data interpretation; discussion; preparation of all figures and the TOC graphic; writing of the original draft; answering of reviewer questions; editing and rewriting of the reviewed draft *Estimated contribution of my own: ~85%*
Mattis T. Vochezer	Support with PbX NPL/fQD syntheses and phase transfers; support with absorbance and PL measurements; discussion
Dominik A. Rudolph	TEM measurements; XPS measurements; discussion; proof reading
Jannika Lauth *	Conceptualization; supervision; discussion; critical review and correction; proof reading; correspondence with the journal; funding acquisition; access to laboratory equipment

Near-Infrared Emitting Fibers: Stable Jet Electrospinning Flat PbSe Quantum Dots into Poly(methyl methacrylate)

Leon Biesterfeld	PbSe fQD syntheses; PL, PLQY and absorption measurements and data interpretation; TEM data interpretation; compilation and processing of all collected data; discussion; preparation of all figures and the TOC graphic; writing of the original draft; answering of the reviewer questions; additional experiments requested in the revision; editing and rewriting of the reviewed draft *Estimated contribution of my own: ~60%*
Dennis Kühn	Optimization of the SJES process for embedding PbSe fQDs and fabrication of PbSe fQD-containing fibers; sample preparation for SEM; discussion
Fuzhao Li	SJES of CdSe NPL-containing fiber and support with SJES of PbSe fQDs with PMMA
Franka Gädeke	3D single-particle excitation polarization microscopy measurements and data analysis; discussion
Dominik A. Rudolph	Support with absorption measurements; TEM measurements
Frank Schreiber	Proof reading; access to laboratory equipment
Peter J. Walla	Supervision; discussion; proof reading; access to laboratory equipment
Ivan Zaluzhnyy	X-ray scattering experiments and data interpretation; discussion; proof reading; additional experiments requested in the revision

Henning Menzel	Conceptualization; supervision; discussion; critical review and correction; proof reading; funding acquisition; access to laboratory equipment
Jannika Lauth *	Conceptualization; supervision; discussion; critical review and correction; proof reading; correspondence with the journal; funding acquisition; access to laboratory equipment; in-depth discussion of the revision

* Corresponding author(s)

C Acknowledgements

Looking back on the past four years, I rarely think about the daily learning and the initial frustrations and final rewarding moments that often came with it. Instead, I think about the people I got to know, who accompanied me along the way. You made this time an invaluable experience and I am very grateful for that.

First, I would like to thank Jun.-Prof. Jannika Lauth. Jannika, I am thankful for the freedom and trust you gave me in my work and research, whether it has been in Tübingen, Hannover or in between. At the same time, you were there when I needed your help and I have learnt most of what I know about research, writing and publishing from you. Our outside meetings during the pandemic feel like ages ago, and I think it is remarkable how far things have come since then.

I would like to thank Prof. Reinhold Fink for agreeing to evaluate my thesis at short notice, for acting as an examiner at my defense, and for taking on the additional workload associated with these tasks.

I thank Prof. Sandrine Ithurria Lhuillier for promptly agreeing to evaluate my thesis as the third external referee, and for joining my defense as an online listener.

I thank apl. Prof. Heiko Peisert for agreeing to step in as an examiner and committee chair for my oral defense.

I want to thank Dr. Louis Biadala for not only joining my defense as an oral examiner, but also for introducing me to scanning tunneling spectroscopy, as well as for the interesting collaborations and valuable discussions we had in the last two years. Meeting you at the nanoGe in Valencia two years ago was definitely the most enriching conference encounter I have had.

I am truly pleased to have had the opportunity to work with all of the co-authors of the publications included in this thesis. Thank you all for investing your time in measurements, data interpretation, and writing, and for the fruitful meetings we have had.

I am very grateful to my office colleagues, Onno and Markus, and I am incredibly thankful that we quickly became good friends. You two made my time at work so much more enjoyable. Onno, I especially thank you for proofreading this thesis.

I would also like to thank Theresa and Jonas for regularly joining us for coffee breaks. I always looked forward to you coming up.

I would further like to thank the newer and sometimes temporary members of the Lauth group who joined us for various theses and research internships. In particular, I thank Mattis for all of his efforts as an undergraduate student and a research assistant, your work ethic is remarkable.

I am grateful for my colleagues and former colleagues in Hannover. Dominik, it has always been great to come to the LNQE knowing you would be there, and I thank you for the time you spent measuring my samples at the TEM. Artsiom, thank you for your feedback during our group meetings and for the way you deliver it, which often put a smile on our faces. I would also like to thank Lars and André for teaching me everything PhD-related in the early months in Hannover, and their welcoming nature when I initially joined the group. I am also thankful to all former members of the Functional Nanostructures group in Hannover for letting me be a part of their group. I would especially like to thank Hadir and Denis for teaching me how to use the XPS and for helping me troubleshooting at the NIR PL spectrometer, even after they had finished their studies.

I would like to thank the administrative staff who kept the non-scientific processes going, in particular Kerstin Janze, who helped me with ordering chemicals even after I left Hannover, and the PhoenixD office team around Katrin Pfennig, who kept up with my back-and-forth between Tübingen and Hannover.

I also thank my friends from the canoe polo team for welcoming me back everytime I visited Hannover for measurements as if I had never left.

I am grateful for my family and their support during my studies. I thank my brother Peer for proof reading this thesis at an early stage.

Lilli, I thank you for your loving nature and support ever since we know each other, for moving to Tübingen with me and for putting up with me when I had a bad day in the lab.